Optically Detected Cyclotron Resonance of GaAs-Based Semiconductors

Joseph Gerard Michels

A thesis submitted for the degree of Doctor of Philosophy

Pembroke College, Oxford

Trinity Term, 1994

Optically Detected Cyclotron Resonance of GaAs-Based Semiconductors

Joseph Gerard Michels

A thesis submitted for the degree of Doctor of Philosophy
Pembroke College
Oxford
Trinity Term, 1994

Abstract

Cyclotron resonance has been measured in GaAs and related compounds through the use of a new experimental technique developed for the study of very pure semiconductors called optically detected cyclotron resonance (ODCR).

ODCR differs from other forms of magnetospectroscopy in that the intensity of luminescence excited by a visible laser is monitored rather than the direct absorption of far-infrared radiation. The ODCR technique is initially used on an exceptionally pure sample of GaAs and resolves impurity transitions and central cell effects. An accurate measure of the electron effective mass including band nonparabolicity is made. The ODCR signal represents an interaction between the donor bound electron states and the donor bound exciton states.

Standard cyclotron resonance measurements on high mobility GaAs/$Ga_{1-x}Al_xAs$ heterojunctions are performed with tilted magnetic fields. Resonant coupling between the Landau levels and electric subbands gives rise to a splitting of the cyclotron resonance lineshape which can be used to determine the subband energy spacings. This allows for a direct determination of the shape of the confinement potential which changes dramatically under different illumination conditions.

A dilution refrigerator is modified in order to measure the cyclotron resonance (CR) to 100 mK of the low density, two dimensional electron system in a heterojunction. Anomalies in the CR spectrum are explained in terms of an interacting electron system composed of carriers in the two spin states of the lowest Landau level. Experimental results are presented in terms of a recent theory offered for cyclotron resonance.

A series of undoped GaAs quantum wells is studied with ODCR. The conduction band mass was measured for different well widths. An offset is observed in the cyclotron resonance energy which is strongly dependent on the well width.

ODCR is measured on $In_{0.05}Ga_{0.95}As$/GaAs superlattices using both the Faraday and Voigt magnetic field orientations. Cyclotron resonance in the Voigt geometry reveals a band structure in the growth direction. The impurity transition in the Voigt configuration shifts dramatically, moving from the bulk 1s-$2p_+$ to close to the bulk free electron field.

Acknowledgements

I would like to thank all those who have helped me in the preparation of this thesis, in particular:

Professors P G H Sandars and R A Cowley, and Dr. J M Baker for extending to me the facilities of the Clarendon Laboratory.

My supervisor, Dr. Robin Nicholas for his invaluable guidance along with constant enthusiasm and encouragement. Robin rescued me from the hazy world of pure mathematics and has fought innumerable battles on my behalf over the past four years.

My research colleagues, particularly Richard Warburton, Alice Wong and Rob Martin. Richard was an excellent teacher and co-worker who introduced me to experimental physics and is now a great friend; Alice Wong a trusted confidant with an indomitable spirit; Rob Martin formulated the idea of talking to Robin and sat with me as bow pair of a very special unit. Other close friends and co-workers: M'hamed Lakrimi for his advice on physics, immigration matters and tales of civil disobedience; Matt Daley for the four hour block sleep theory and tidiness; Dave Symons for reflections on life and useful theoretical calculations; Glen Summers for helping with the Bruker, ^{3}He system, and the many programs he wrote that made data analysis a less formidable task. Tom Vaughan, a late comer from the colonies for simultaneously being Mr. Matrix and Mr. Separation of Variables, Dave Leadley for explanations of the fractional quantum Hall effect, and also: David Kinder, Henry Cheng, Karen Dalton, Chen Yifang and Maarten van der Burgt.

The staff and workshop of the Clarendon Laboratory, especially George Matthews, Simon Moulder, Terry Holiday, Ken Rumble and Dick Thompson. If the day was going particularly badly, my mates in the workshops could always be counted on for a laugh.

All the organizations that have provided financial support: Nigel Blackwell and the committee of the Blackwell Scholarship, Pembroke College for the Junior Dean position and the British government for the Overseas Research Award Scheme.

My friends from the Oxford University Boat Club and the many other people far too numerous to mention who have welcomed me to this strange land over the past four years.

Special thanks and love go to Jenny and my brothers and sisters.

This thesis is dedicated to my parents for their unceasing love, support and encouragement throughout my education.

Contents

Chapter 1

GaAs quantum wells, heterojunctions and superlattices

1.1 Overview

Research and development of semiconductor materials is carried out along two fronts. The first involves the fabrication and characterization of increasingly pure semiconductor crystals composed of single elements or compounds which are collectively referred to as 'bulk material.' The second front began only 24 years ago following the introduction by Esaki and Tsu of the semiconductor superlattice[1] where alternating layers of two different semiconductors are grown on top of one another. This marked the real beginning of 'band structure engineering' where tremendous advances in the fabrication of semiconductors made it possible to control or tune the electronic properties of a material. The ability to tailor the band characteristics of semiconductors has led to an explosion in their use in a multitude of commercial applications, many of which are based on simple heterojunctions. By far the most frequently used materials are GaAs and $Ga_{1-x}Al_xAs$. This thesis is a detailed investigation of GaAs based systems, primarily using a novel experimental technique that allows optical measurements to be made on very pure samples with a low residual density of carriers. The GaAs alloy is studied in bulk (Chapter 3) and then combined in thin sheets with layers of $Ga_{1-x}Al_xAs$ forming quantum wells (Chapter 6). A specially grown high mobility $GaAs/Ga_{1-x}Al_xAs$ heterojunction where the electrons are confined in the plane of the interface is examined in Chapters 4 and 5. Study of a series of $In_{0.05}Ga_{0.95}As/GaAs$ superlattices in Chapter 7 concludes the thesis. Unabashedly experimental in its focus, this thesis places emphasis on both the technique and results of the many different experiments that were performed on the material systems detailed above.

The current chapter introduces the basic background ideas of the field including description of the heterojunction, quantum well and superlattice configurations fashioned from GaAs and its derivatives. This is followed by an overview of electrical and magnetic quantization effects possible in semiconductor materials. The chapter concludes with a survey of previous experimental and theoretical work on the high mobility heterojunctions. A survey is necessary because the cyclotron resonance experiment described in Chapter 5 must be presented against the backdrop of currently accepted understanding regarding the two-dimensional electron system - a topic which has recently been the

topic of much animated debate and discussion.

1.2 GaAs-based semiconductor structures

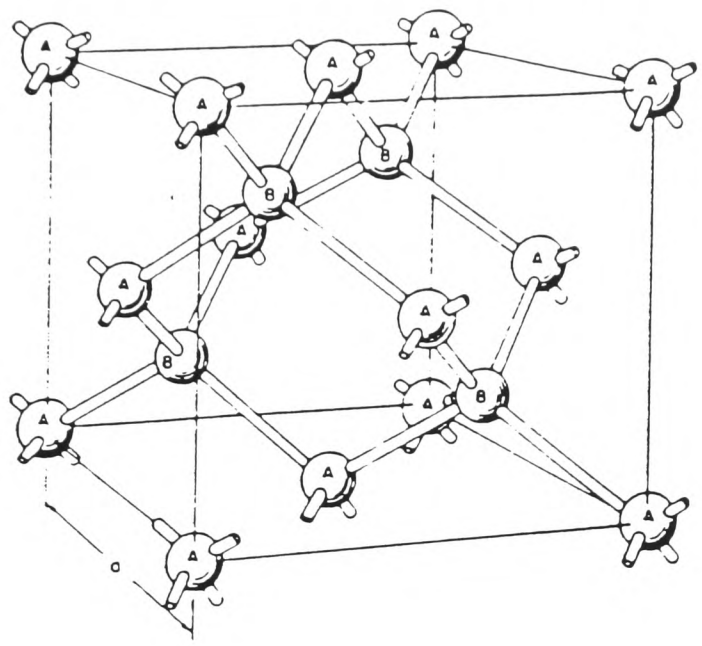

Figure 1.1: The crystal structure of a III-V compound

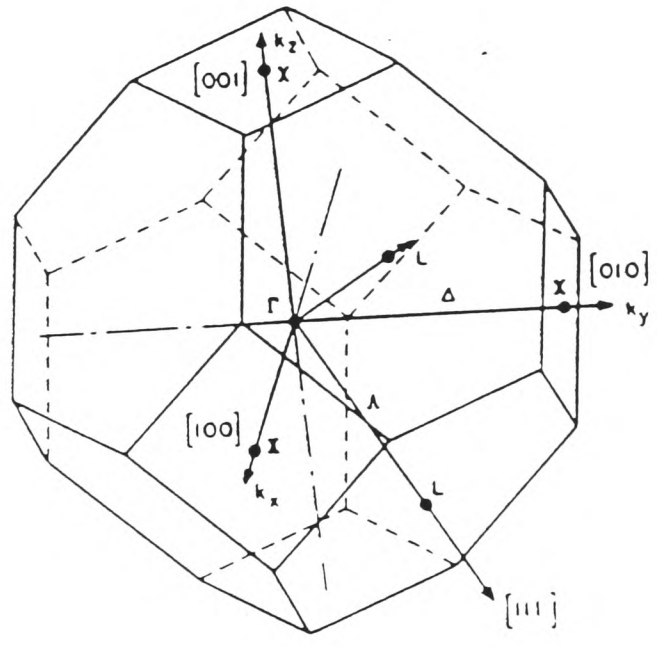

Figure 1.2: The first Brillouin zone for the body-centered cubic lattice in reciprocal space. The high symmetry directions are labelled.

All the materials studied in this thesis are III-V compounds, which crystallize in a lattice with the zinc-blende structure that consists of two interpenetrating face centered cubic (f.c.c.) lattices, displaced from one another by one quarter of the main cube diagonals (Figure 1.1). Consequently, the corresponding reciprocal lattice is body-centered cubic (b.c.c.) whose first Brillouin zone is a truncated octahedron (Figure 1.2). The high

symmetry points are labelled Γ (zone-center), X (intersection of $\langle 100 \rangle$ and the first Brillouin zone boundary) or L (intersection of $\langle 111 \rangle$ with first Brillouin zone boundary).

In each unit cell there are eight electrons which participate in the chemical bonding. The orbitals of each atom hybridise with those of neighbouring atoms to produce bonding and anti-bonding levels, which broaden into bands due to the presence of many surrounding unit cells. The valence band results from bonding of the p-orbitals, and is divided into three bands; namely the heavy and light hole bands and the lower energy spin-orbit band. The splitting of the valence bands is due to the differences in the total angular momentum $\mathbf{J}$ which is the combination of the orbital and spin angular momenta ($\mathbf{J} = \mathbf{L} + \sigma$). Here the addition of $\mathbf{L} = 1$ and $\sigma \pm \frac{1}{2}$ gives either $\mathbf{J} = \frac{1}{2}$ (Γ_7 symmetry) or $\mathbf{J} = \frac{3}{2}$ (Γ_8 symmetry).

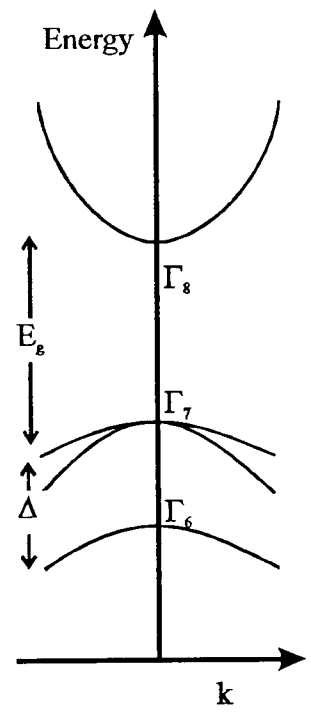

Figure 1.3: The band structure of a direct gap III-V semiconductor in the vicinity of the Γ point showing the ordering of the Γ_6, Γ_7 and Γ_8 states. The energy gap E_g and the spin orbit splitting Δ are marked. The conduction band is 2-fold degenerate while the valence band is 6-fold degenerate.

The remaining two electrons lie deep in the anti-bonding s-orbitals and form the conduction band, which is separated by the band gap E_g from the top of the valence band. The band structure for GaAs is complex but for the experiments considered in this thesis only small regions of k-space around the band extrema are important, which is often the case in semiconductor physics. A simplified picture for a direct-gap III-V material is shown in Figure 1.3. As can be seen from Figure 1.3, the four-fold degenerate $\mathbf{J} = \frac{3}{2}$ edge lies higher in energy than the two-fold degenerate $\mathbf{J} = \frac{1}{2}$ edge by an amount

known as the spin orbit splitting, $\Delta(= 0.34$ eV for GaAs). The bands are approximately parabolic and can be approximated by an effective mass m^* which is defined as

$$\frac{1}{m^*} = \frac{1}{\hbar^2}\frac{d^2E(k)}{dk^2} \tag{1.1}$$

Corrections to this approximation must be made especially at higher energies where the slope of the band deviates from parabolic.

1.2.1 High mobility heterojunctions

A heterojunction is the interface between two semiconductor materials with similar lattice constants but different bandgaps, leading to a bandgap discontinuity. When a heterojunction is formed, charge transfer occurs until the Fermi energy is balanced across the interface. The charge flow creates regions of space charge on either side of the junction and the resulting electrostatic potential causes bending of the bands. Far away from each side of the interface, the Fermi energy corresponds to charge neutrality in each material. The heterojunctions examined in this thesis are formed by growing a layer of $Ga_{1-x}Al_xAs$ on very pure GaAs and are classified as n-type Type I structures. In these materials electrons will move from the higher band gap material ($Ga_{1-x}Al_xAs$) to the lower gap material (GaAs) which creates a region of positive space charge in the $Ga_{1-x}Al_xAs$ and an accumulation layer of negative space charge in the GaAs. The resulting band bending when combined with the bandgap discontinuity, leads to a nearly triangular potential well formed in the GaAs. Electrons that fall into the well are confined to a quasi two dimensional sheet where they are free to move parallel to the plane of the interface but restricted by the potential from movement perpendicular to the interface. This is illustrated schematically in Figure 1.4. The electrons that are trapped at the interface are referred to as comprising a two dimensional electron system (2DES) or, for the specific case when they behave as a nearly free Fermi gas as a two dimensional electron gas (2DEG).

All the measurements presented in Chapters 4 and 5 were performed on a series of ultra-high mobility GaAs/$Ga_{1-x}Al_xAs$ heterojunctions grown by MBE at Philips Research Laboratory by C.T. Foxon and J.J. Harris. The Al fraction x was set at $33 \pm 1\%$ which kept the barrier height constant at about 0.27 eV. The Philips' samples are examples

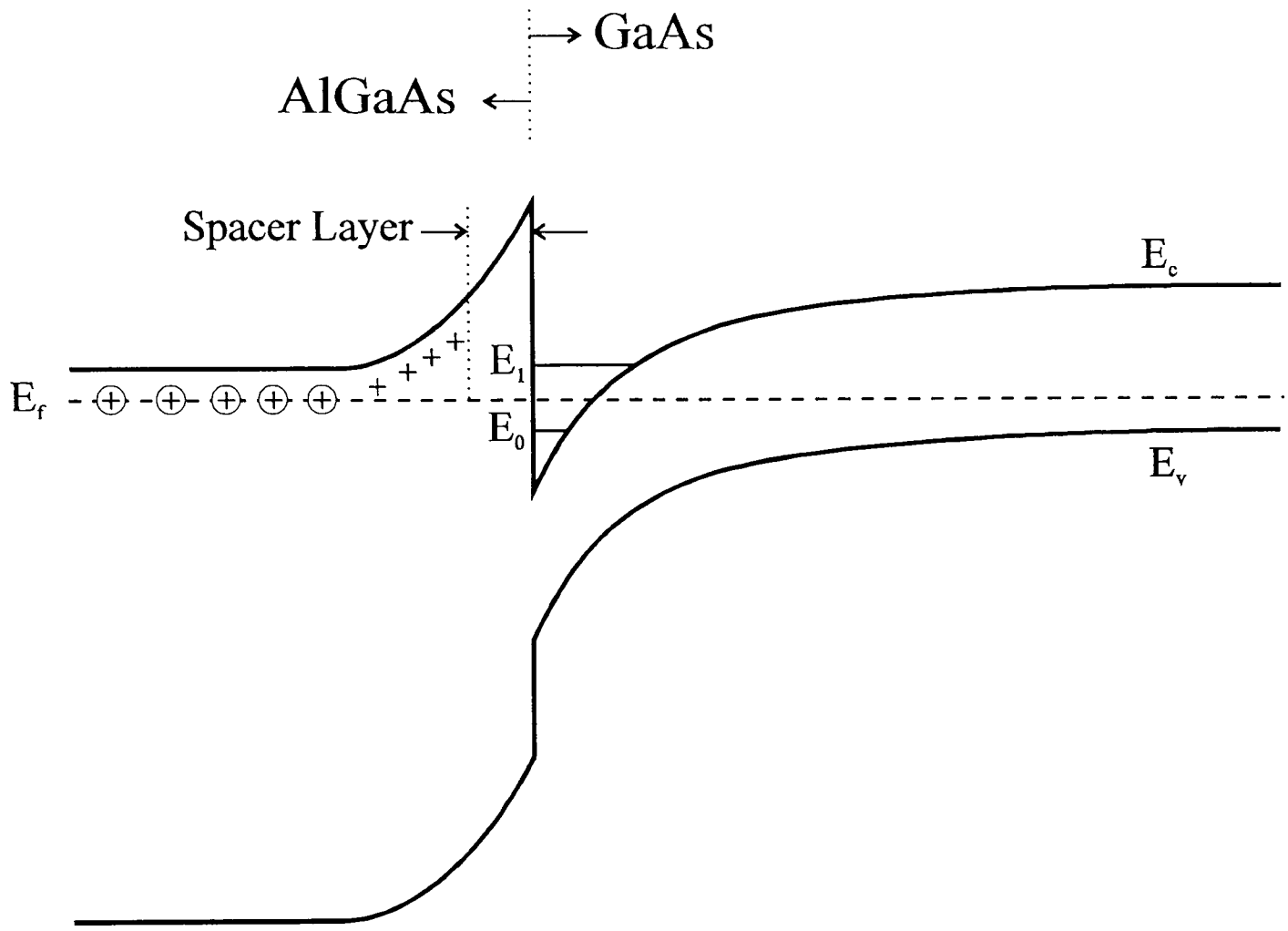

Figure 1.4: Schematic band profile of a typical modulation doped GaAs/$Ga_{1-x}Al_xAs$ heterojunction, with two confined energy levels shown. After Summers[5].

of modulation-doped heterostructures where the doping impurities introduced into the larger bandgap material are separated from the undoped lower bandgap material by a nominally undoped spacer layer. The electrons migrate into the well where they are trapped and remain separated from the impurities. This reduces the scattering from the impurity centers and greatly increases the mobility. Foxon *et al* employed many optimization techniques that enabled them to achieve high carrier densities without the simultaneous decrease in mobility due to impurity scattering[6]. These included:

- the use of a lightly doped layer of $Ga_{1-x}Al_xAs$ separated from the 2DES by an undoped spacer layer. Increasing widths of the spacer layer reduced the carrier density of the 2DES with insulating samples produced for spacer layers of 3200 Å and above. The concentration of Si donors in the 2000 Å-wide lightly doped region was $n = 1.0 \times 10^{17}\,\mathrm{cm}^{-3}$. The optimum mobility of $4.6 \times 10^6 \mathrm{cm}^2\mathrm{V}^{-1}\mathrm{s}^{-1}$ at 4 K was measured for samples with spacer layers of between $400 - 800$ Å.

- the use of a superlattice in the GaAs buffer. A 50 period GaAs/$Ga_{1-x}Al_xAs$ superlattice was grown as a prelayer to the GaAs buffer in order to trap any

residual impurities into the superlattice. As a result, the GaAs buffer layer has a very low residual acceptor impurity level of $\sim 1 \times 10^{14}\,\mathrm{cm}^{-3}$.

Mobility measurements extrapolated down to zero temperature give a value of $1.26 \times 10^{6}\mathrm{cm}^{2}\mathrm{V}^{-1}\mathrm{s}^{-1}$ and are an indication of the ionised impurity scattering rate. The mobility measured in this way is significantly higher than the 4 K value which suggests that the dominant scattering process is due to acoustic phonons. It is not an exaggeration to say that the Philips' heterojunctions are the best in the world.

1.2.2 Quantum wells and superlattices

A quantum well is formed by sandwiching a thin layer of one semiconductor material within a second semiconductor material and thus involves two back-to-back heterojunctions. If the quantum well is sufficiently thin ($\sim$ 100 Å) then little band bending occurs and the carriers are confined by the band discontinuities which approximate a square well potential. For wider wells or higher carrier densities, the band bending becomes significant and the quantum well behaves as a pair of heterojunctions.

Quantum wells are classified as Type I if both the electrons and holes are localized within the well formed by the narrower band gap material. Figure 1.5[a] represents a Type I quantum well showing how both the conduction and valence band of the narrow gap material fit within the bandgap of the barrier material. The carriers in the well are provided either through modulation doping or by residual impurities found in the barrier region. A series of quantum wells grown together to produce a number of two dimensional systems is referred to as a multi-quantum well (MQW) structure. Each of the GaAs/$\mathrm{Ga}_{1-x}\mathrm{Al}_{x}$As MQW's studied in Chapter 6 consisted of 50 well/barrier periods; the barrier width was fixed at 50 Å while the well width was varied from sample to sample. Very careful monitoring of the growth process, primarily using RHEED oscillations, resulted in high quality interfaces that displayed well and barrier width uniformity to within one monolayer[7].

If the barriers between the wells of a MQW structure are made thin enough, the wavefunctions from adjacent wells overlap and the structure is known as a superlattice (Fig-

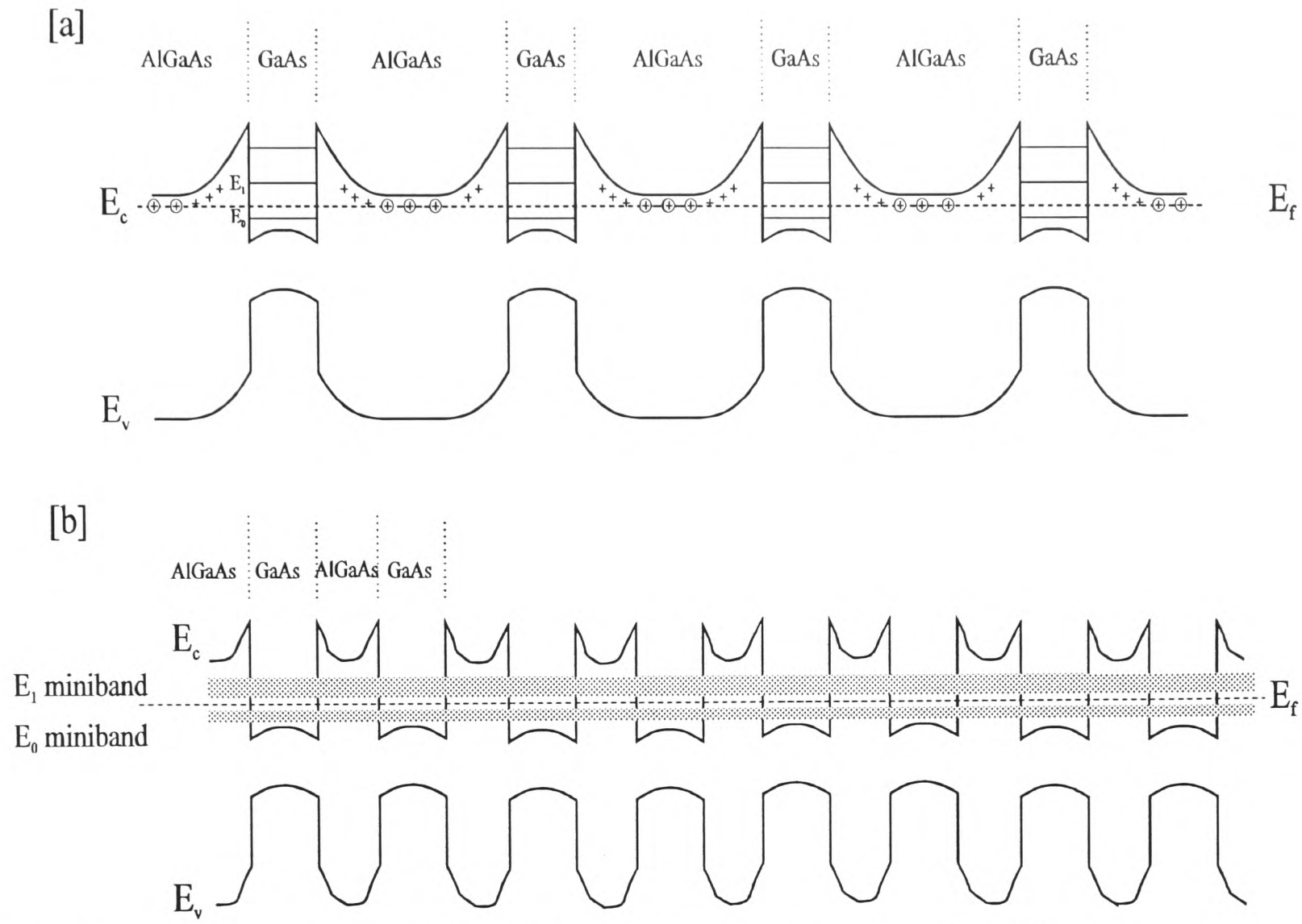

Figure 1.5: [a] The band profile of a typical modulation doped multi quantum well structure showing three confined subbands within each well. [b] Reduction of the barrier width enables the formation of minibands and a superlattice is formed.

ure 1.5[b]). The coupling causes the quantized energy levels to broaden into a series of minibands. The width or energy dispersion of the minibands can be varied by changing the sample parameters. For example, an increase in band width is achieved by either decreasing the barrier thickness or decreasing the well thickness at a fixed barrier thickness. The MQW's superlattices studied in Chapter 7 are made from (In,Ga)As-GaAs rather than the more commonly studied GaAs-(Al,Ga)As system. An advantage of the $In_{0.05}Ga_{0.95}As/GaAs$ material system is that significant miniband widths are achieved for relatively large barrier widths.

1.2.3 Growth techniques

Samples used in this research were grown by MBE (molecular beam epitaxy). MBE is a refined form of vacuum evaporation where thermally generated beams of atoms from pure solids are directed at a heated and rotating substrate under ultra-high vacuum[2].

It is energetically favorable for atoms reaching the surface to adhere to imperfection sites so it is possible to grow crystals one monalayer at a time. Growth rates are typically $0.3-30$ Ås^{-1}. Mechanical shutters are placed over the cells, allowing different materials to be grown. The shutters are controlled by computers and have switching times which are short when compared to the time required to grow one monolayer. Reflection high energy electron diffraction or RHEED allows each monolayer to be detected as it is grown which is a significant advantage of this technique. A drawback however, is that phosphorous is difficult to handle in a MBE environment because of its high vapor pressure. The process also is rather costly and it is difficult to reconfigure growth kits to produce a different material system. The ultra-high vacuum requirement means that the growing chamber is seldom opened to atmospheric pressure with the result that the detritus of past growth runs collects on the sides of the vessel in eerily shaped structures.

A second growth technique is metal organic vapour phase epitaxy or MOVPE which is a gas flow process. Here the group III elements enter the reactor as an organic metal called an alkyl (e.g. trimethylgallium $Ga(CH_3)_3$) and the group V elements as hydrides (e.g. arsine AsH_3). The compounds react and are deposited on the heated substrate. The method is cheaper than MBE and there are no significant problems with phosphorous compounds. Interfaces of MOVPE-grown material tend to be graded over several monolayers and are less sharp when compared to MBE samples. The continual gas flow through the growth chamber makes in-situ RHEED characterization impossible although a new technique is being developed in the Clarendon that uses absorption of ultra-violet light to monitor the growth process. The UV matches electronic transitions within the alkyl molecule and so very small fluctuations in the gas concentration are indicated by a change in the absorption of the light directed through the sample chamber[3]. This technique has produced the world's best $InAs/In_xGa_{1-x}Sb$ structures as signified by completely intrinsic behavior[4].

1.3 Quantization in heterostructures

An observable quantity is said to be quantized if its magnitude is restricted to a discrete set of values. Electrical quantization occurs in heterojunctions, quantum wells

and superlattices because the carriers are not able to freely move in three dimensions. Reduction in the dimensionality of the system and the resulting electric quantization, is usually caused by confinement of the carriers within a potential well present either at the interface of a heterojunction or formed in the narrow bandgap material of a quantum well or superlattice. In either case, movement of the carriers is restricted to a thin plane that is perpendicular to the growth direction of the structure which is conventionally set as the z axis. Therefore, energy levels associated with the z-component of the momentum are quantized. A further quantization occurs when a magnetic field is applied perpendicular to this plane defined by the x and y axes. This is referred to as magnetic quantization.

1.3.1 Electric quantization

It is helpful to begin discussion of low dimensional systems by examining the quantum mechanical problem of an electron trapped in a three dimensional potential box of sides a, b and c with the potential defined such that it is null in the interior and finite outside the box. In solving the related Schrödinger equation by separating the variables such that the eigenfunction $\psi(x,y,z) = X(x)Y(y)Z(z)$ and accounting for the boundary conditions requiring that $\psi(x,y,z) = 0$ for $0 > x > a$, $0 > y > b$ and $0 > z > c$ it follows that the eigenenergy E is given by:

$$E = \frac{\pi^2\hbar^2}{2m_o}\left(\frac{l^2}{a^2} + \frac{m^2}{b^2} + \frac{n^2}{c^2}\right) \tag{1.2}$$

where m_o is the electron rest mass and l, m and n are integers. In a three dimensional system, a, b and c are of the same order of magnitude and the net result is that the energy spectrum is a continuum. If the box is constricted in the z-direction as is the case for the heterojunction pictured in Figure 1.4, then the energy levels become discrete and are referred to as subbands. The concept of two dimensional systems is purely quantum mechanical because the potential well is usually at least 50 Å thick. At low temperatures and low carrier densities, the carriers will occupy only the ground subband.

Solution of the Schrödinger equation for the specific case of a heterojunction is described in Chapter 4. To a first approximation, the shape of the potential is assumed

to be triangular and the wavefunctions $\phi(z)$ and eigenenergies E_i are found by guessing a solution of Schrödinger's equation. In the modelling of experimental data from heterostructures, however, the triangular approximation is often not sufficient and the potential must be obtained through a solution of Poisson's equation. The Schrödinger and Poisson equations are now linked as the shape of the potential influences the subband wavefunction or vice versa, the wavefunction influences the charge distribution and therefore the potential. A self-consistent solution is therefore required.

1.3.2 Effect of a magnetic field

Magnetic fields are often used in semiconductor physics to help with band structure determination. A magnetic field can complete the quantization of a two dimensional system: the confinement potential quantizes motion in the z-direction and the magnetic field quantizes motion in the (x, y) plane into the allowed cyclotron orbits. The research presented in this thesis utilizes high magnetic fields primarily through cyclotron resonance measurements. Magneto-transport experiments are also used in Chapter 5 as a secondary check on the heterojunction carrier density. Each technique is described below.

1.3.2.1 Landau levels, density of states and the filling factor

When a magnetic field is applied to an electron gas it reorganizes the electronic states into the celebrated Landau levels due to the Lorentz force and orbit quantization. This section will derive the energy levels of a two dimensional system using the following assumptions which greatly simplify the mathematics: effective mass theory can be applied, the energy bands are isotropic and non-parabolicity effects resulting in a varying effective mass are disallowed.

The effect of the magnetic field is accounted for by the momentum transformation $\mathbf{p} \rightarrow \mathbf{p} - e\mathbf{A}$ in the Schrödinger equation, where $\mathbf{A}$ is the vector potential. The Landau gauge is used to represent a general magnetic field perpendicular to the interface planes

so that for example, $\mathbf{A} = (-yB, 0, 0)$. The Schrödinger equation becomes:

$$\left(\frac{1}{2m^*}\left\{[p_x + eyB]^2 + p_y^2 + p_z^2\right\} + eV(z)\right)\psi = E\psi \tag{1.3}$$

Since we know that the z-component leads only to the electrical quantization, it is reasonable to make a separation of variables by rewriting Equation 1.3 as follows:

$$[H_{xy} + H_z]\psi = E\psi \tag{1.4}$$

with solutions of the form $\psi(x, y, z) = f(x, y)\phi(z)$. This produces two equations, one dependent only on x, y and the other involving z terms, recalling that $\phi(z)$ is the wavefunction associated with electric quantization. The effect of the magnetic field is contained within the equation involving x and y,

$$\frac{1}{2m^*}\left\{[p_x + eyB]^2 + p_y^2\right\} f(x, y) = E_{||} f(x, y) \tag{1.5}$$

with the eigenenergy $E_{||}$ due only to motion in the interface plane. The total energy is then found by adding E_i, the energy due to confinement in the z-direction, to $E_{||}$.

In order to solve for $E_{||}$, a solution is guessed of the form $f(x, y) = exp(ik_x x)\theta(y)$ which makes a further separation of variables possible. Equation 1.5 becomes:

$$\frac{\hbar\omega_c}{2}\left\{-l_0^2\frac{\delta^2}{\delta y^2} + \left[\frac{y}{l_0} - l_0 k_x\right]^2\right\} exp(ik_x x)\theta(y) = E_{||} exp(ik_x x)\theta(y) \tag{1.6}$$

where $w_c = eB/m^*$ is the cyclotron frequency and $l_0 = \sqrt{\frac{\hbar}{eB}}$ is the magnetic length.

Equation 1.6 describes a harmonic oscillator centered at $y = l_0^2 k_x$ with the eigenvalues given by

$$E_{||} = \hbar\omega_c\left(N + \frac{1}{2}\right) \tag{1.7}$$

The Landau level index is $N(= 0, 1, 2, ...)$. If the effects of spin are included, each of these states will be split into two levels with the energy of each spin state given by $\pm|m_J|g^*\mu_B B$, where m_J is the projection of the angular momentum in the direction of the magnetic field. Adding all the different contributions to the energy together, the total energy of the Landau levels is then

$$E = E_i + \hbar\omega_c(N + \frac{1}{2}) \pm |m_J|g^*\mu_B B \tag{1.8}$$

Since $E_{||}$ is independent of k, the Landau levels are highly degenerate. A sample with dimensions l_x, l_y gives allowed values of $(2\pi/l_x)i$ in k-space where i is an integer. There are then $l_x/2\pi$ allowed values of k_x per unit length along the k_x direction. An additional constraint is that the center of the cyclotron orbit must be located within the sample extent which is expressed as:

$$\begin{aligned} 0 < y < l_y \\ 0 < l_0^2 k_x < l_y \end{aligned} \tag{1.9}$$

Each level therefore contains $l_x l_y / 2\pi l_0^2$ allowed values of k_x. Since the quantization is complete, the levels are discrete and the density of states which is the number of states per Landau level per unit area is

$$\begin{aligned} D(E) &= \frac{l_x l_y}{2\pi l_0^2} \\ D(E) &= \frac{eB}{h} \end{aligned} \tag{1.10}$$

The density of states consists of a series of singularities at the Landau level energies and any phenomenon that depends on the density of states at the Fermi energy $g(E_f)$ will show strong oscillatory behavior when sweeping the magnetic field. If the carrier concentration is N_s per unit area, then the number of filled Landau levels ν is

$$\nu = \frac{N_s}{D(E)} = \frac{N_s h}{eB} \tag{1.11}$$

where ν is called the filling factor. For integral values of ν, the Fermi energy lies between two Landau levels and $g(E_f)$ is small. When ν is half-integral, $g(E_f)$ is large. Oscillations are periodic in ν or equivalently, periodic in $1/B$.

No matter how carefully grown, samples will always exhibit randomness arising from impurities and rough semiconductor interfaces. These effects are grouped together under the descriptive term 'disorder' and result in a broadening of the Landau levels and correspondingly, the density of states as is shown in Figure 1.6.

Application of a magnetic field in a three dimensional semiconductor will also produce Landau levels along similar lines as described above. The absence of confinement in the z-direction, however, results in much broader levels and a $\sqrt{E}$ dependence to the density of states.

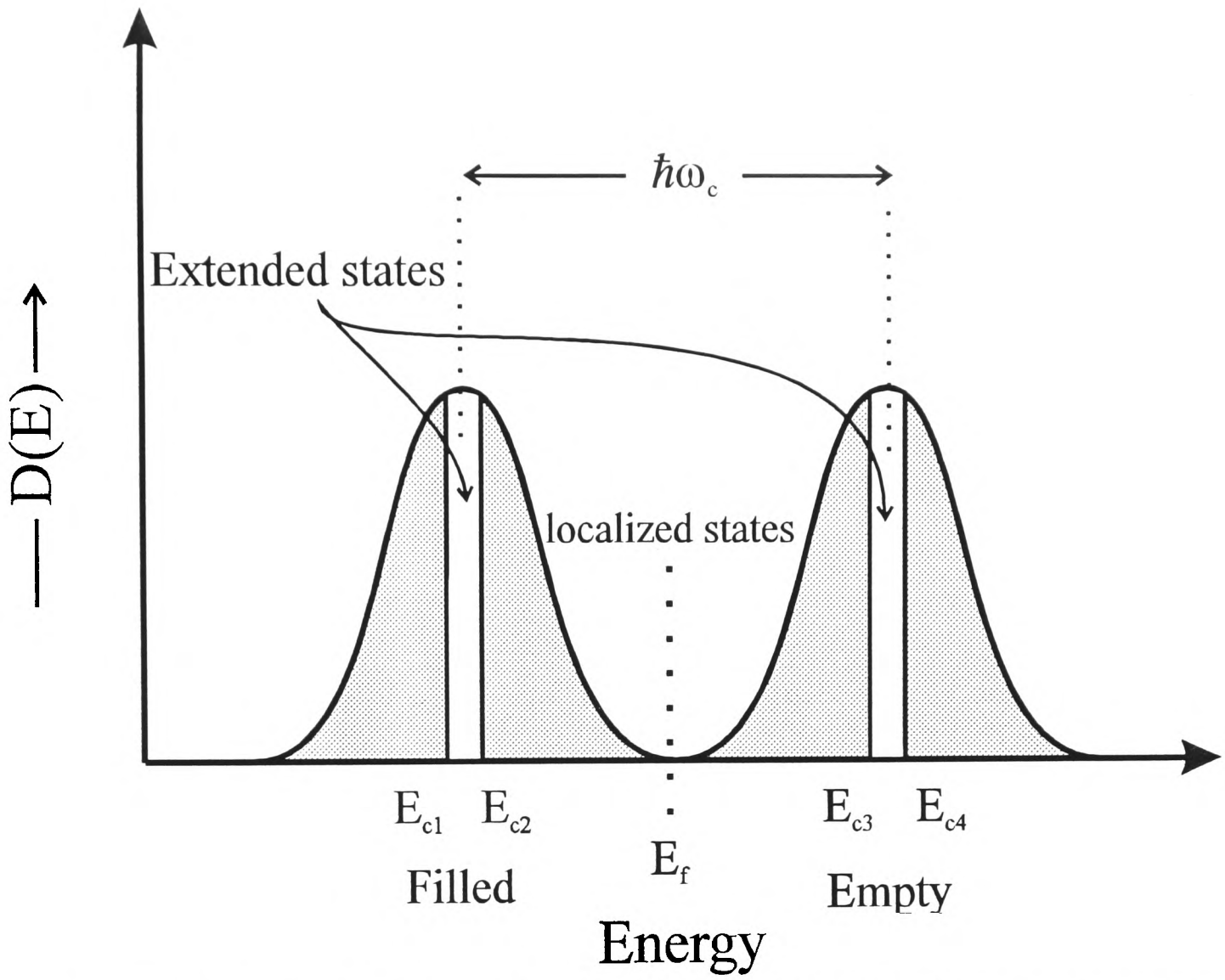

Figure 1.6: The broadened density of states of a two dimensional gas in a strong magnetic field. Localized and extended states are indicated.

1.3.2.2 Magneto-transport

The density of states of a 2DES is fundamental to the understanding of transport phenomenon such as the Shubnikov-de Haas (SdH) and Quantum Hall Effects (QHE). Carriers occupying states in the tails of the broadened Landau levels are localized by the disorder potential to small regions in the xy-plane and so are unable to carry current through the sample. These are called localized states. Carriers that lie at the center of the Landau levels are free to move within the xy-plane and are referred to as extended states. When ν is half-integral, E_F lies in the extended states and so the conductivity is large. When ν is integral, E_F lies in the localized states and so the diagonal conductivity σ_{xx} is small. This is because the electrons cannot scatter between two adjacent states and so become frozen or localized. The conductivity thus oscillates with $\frac{1}{B}$. This is the Shubnikov-de Haas effect. An example of SdH oscillations from a $GaAs/Ga_{1-x}Al_xAs$ heterojunction is shown in Figure 1.7.

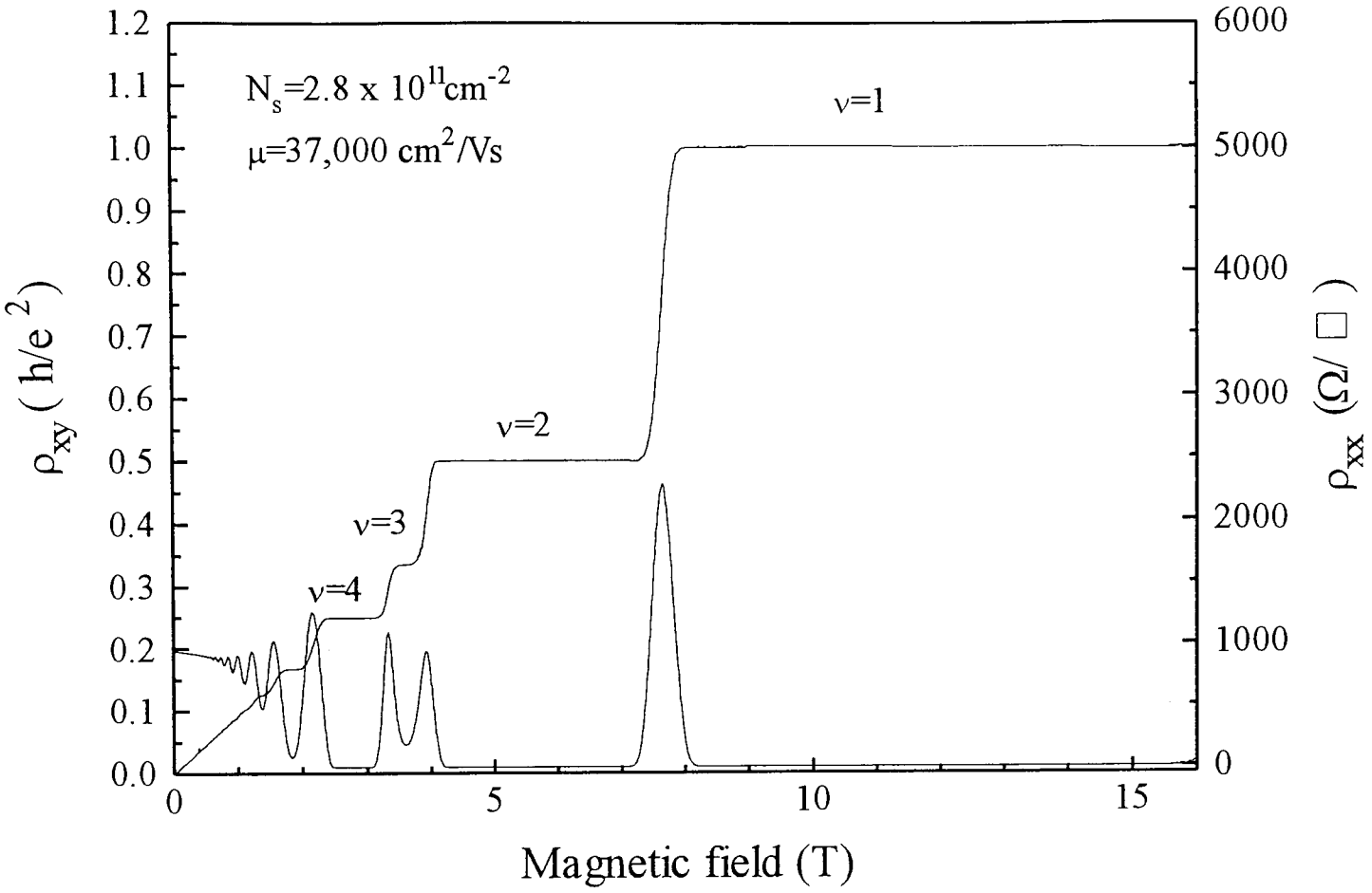

Figure 1.7: Experimental recordings of the quantum Hall effect and Shubnikov-de Haas oscillations for a GaAs/$Ga_{1-x}Al_xAs$ heterojunction with a carrier concentration of $2.8 \times 10^{11}cm^{-2}$. The plateaux of the Hall resistance are marked, scaled to Equation 1.13 to match the Landau level filling factor. Data courtesy of P. Gee.

An obvious application from Equation 1.11 is to use the periodicity of the oscillations to provide a carrier density. In practice, the diagonal resistance ρ_{xx} is measured rather than the conductivity. The resistivity is related to the conductivity through a tensor relation:

$$\begin{aligned} \rho xx &= \frac{\sigma_{xx}}{\sigma_{xx}^2 + \sigma_{xy}^2} \\ \rho xy &= \frac{-\sigma_{xy}}{\sigma_{xx}^2 + \sigma_{xy}^2} \end{aligned} \tag{1.12}$$

where ρ_{xy} is known as the Hall resistivity. If $\sigma_{xy} \gg \sigma_{xx}$ which is generally the case, then when $\sigma_{xx} \simeq 0$, $\rho_{xx} \simeq 0$ also.

The magnetoresistance minima in Figure 1.7 are seen to correspond to plateaux in the Hall resistivity, ρ_{xy}. From Equation 1.12, the diagonal resistivity has a constant value of $-\frac{1}{\sigma_{xy}}$ over a region in which σ_{xx} vanishes. The quantized resistance values given by:

$$\rho_{xy} = \frac{1}{\nu}\frac{h}{e^2} \tag{1.13}$$

occur when ν Landau levels are fully occupied. This is the integral quantum Hall effect or IQHE. Because of the quantization of the magnetic flux in units of h/e the IQHE serves to demonstrate the fundamental nature of e as the unit of charge and is now used as an international reference for resistance.

1.3.2.3 Cyclotron resonance

Cyclotron resonance corresponds to the intra-band excitation of an electron or hole from one Landau level to another. The selection rule is given by the electric dipole operator $\delta N = \pm 1$ with the transition also spin conserving making $\delta s = 0$. The technique is principally used to determine the carrier effective mass. A cyclotron resonance transition can only be observed if the initial level is occupied and the final level partially unoccupied. It will be shown later in Chapter 2 that the integrated strength of the resonant absorption is set by the classical Drude conductivity. Since the Drude conductivity is dependent on the carrier density, cyclotron resonance also allows for a direct optical measurement of the carrier densities of the initial state.

Cyclotron resonance in a two dimensional system is more complicated than can be described by a simple single particle picture, however, as it can be influenced by electron-electron interactions and disorder potentials. Chapter 5 discusses cyclotron resonance measurements of the Philips' heterojunctions and so necessarily addresses these topics.

1.4 Two dimensional electron systems and the fractional quantum Hall effect

Armed with the basic terminology used to describe the physics of two dimensional systems in place, we turn to a survey of recent experimental and theoretical work on the subject. This survey excludes the much more detailed discussion of experimental cyclotron resonance results and relevant theory for two dimensional systems that is the topic of Chapter 5

While the IQHE can be explained using a straightforward single particle picture, the

1982 discovery of the fractional quantum Hall effect (FQHE) has demanded a more sophisticated approach. Found only in very high mobility heterojunctions and at low temperatures, the FQHE is manifested by plateaux in the Hall resistance where ν is now a simple rational fraction. Plateaux in the Hall resistance have now been observed at $\nu = 2/5, 3/5, 3/7, 4/7, 4/9, etc.$ with increasing denominators that follow the 'principle' sequence $\nu = p/(2p+1)$ where p is a positive integer. Although there are several different theoretical approaches to the FQHE, all accept the major role that electron-electron correlations play in the effect.

The majority of current theoretical work demonstrates that the ground state of the electron system is a liquid, with Laughlin making the major step in arriving at this conclusion[9]. Laughlin's radical suggestion was that the lowest energy charge excitations are pairs of quasielectrons and quasiholes with an apparent charge $e^* = e/q$ and q generally an odd integer. These particles of fractional charge necessitate a treatment using fractional statistics and, to borrow a phrase, life gets very complicated. In very simple terms, however, a deviation from the stable state which occurs at experimentally observed rational values of ν would serve to create both quasielectrons and quasiholes. When a sufficient number of quasiparticles are formed they interact between themselves to form a new ground state, which occurs at the next fractional value of ν. A comprehensive survey of the FQHE can be found in *The Fractional Quantum Hall Effect* by Chakraborty and Pietiläinen [10].

Equating the vanishing of the diagonal resistivity with creation of quasielectrons and quasiholes is equivalent to asserting that an energy gap exists in the excitation of the correlated many-electron ground state. The usual method for measuring the gap is through the temperature dependence of the Shubnikov-de Haas oscillations of the resistivity ρ_{xx} as $\rho_{xx} \propto \exp(-W/k_B T)$ where $W = \frac{1}{2}E_g$ is the activation energy and k_B is Boltzmann's constant. In traditional activation measurements the actual value of the resistivity is recorded at the FQHE or IQHE minimum for each temperature. A plot of $\log(\rho_{xx})$ vs $1/T$ provides the activation energy which is essentially the gap between the edges of localised states in adjacent Landau levels.

Very recently, a modified form of activation measurements have been used to support a

new model for the FQHE based on interacting composite Fermions (CF) in an effective magnetic field B*[11]. In the CF picture, a gauge transformation is made, equivalent to attaching $q = 2$ flux quanta Φ_0 to each electron. The fractional states belonging to the principal sequence of $\nu = p/(2p + 1)$ are converted into a system of fermions in an effective magnetic field which results in p Landau levels filled by the fermions. As a result, the energy gap of the fractional states is interpreted as the cyclotron energy of the transformed particles. $\nu = \frac{1}{2}$ marks the point of zero effective magnetic field, defined as $B^* = B\text{-}2N_S\Phi_0$. Setting $q = 2$ has converted the electron system into a system of fermions in zero external magnetic field which is consistent with the absence of fractional Hall quantization at this fraction. The composite Fermion picture makes it unnecessary to invoke the fractional charge of quasielectrons and quasiholes and converts the FQHE to the IQHE of composite Fermions.

Experiments which have been used to support the composite Fermion picture use a formula which describes SdH oscillations at low fields, when the oscillations are a small ($< 50\%$) fraction of the background resistance. In this case the SdH oscillations can be modelled as a cosine function enclosed within an exponential envelope. The size of the envelope depends on kT/E_c. E_c is the cyclotron rather than an activation energy and does not depend on the width of the localised states. The real advantage is that this method works for any field and not just at the minima of the oscillations. As a result, proponents of the CF theory argue that it offers a better picture than the ideas of bose condensations which can only work properly at the resistivity minima.

Transport measurements in high mobility heterojunctions are limited by the samples becoming insulating at low temperatures and carrier densities. An alternative approach is looking at the photoluminescence spectra. This technique uses weak photoexcitation with energy just below the AlGaAs barrier to excite electrons and holes in the GaAs; the excited holes relax to the valence band edge where they recombine with the electrons that have been trapped in the potential well at the interface. Both the energy and the intensity of the photoluminescence have shown to be sensitive to the two dimensional interacting liquid of electrons. The appearance of extra peaks in the luminescence spectrum has also been correlated with the many different fractions of filling factor where the FQHE states are seen in transport measurements. [12][13]. For $\nu = \frac{1}{3}$,

a broad peak is observed containing three individual peaks which are interpreted in terms of different numbers of fractionally charged quasi-particles participating in the recombination process[14]. This spectra is compared to the luminescence peak at $\nu = \frac{1}{2}$ which is more symmetrical in shape. If the gauge transformation used in composite Fermion theory is made, then $\nu = \frac{1}{2}$ corresponds to an effective field of zero and the luminescence linewidth should be a measure of the Fermi energy. The authors report a value of $\sim$ 0.5 meV, which corresponds to an effective mass of $0.35m_e$ close to a theoretically predicted value of $0.27m_e$.

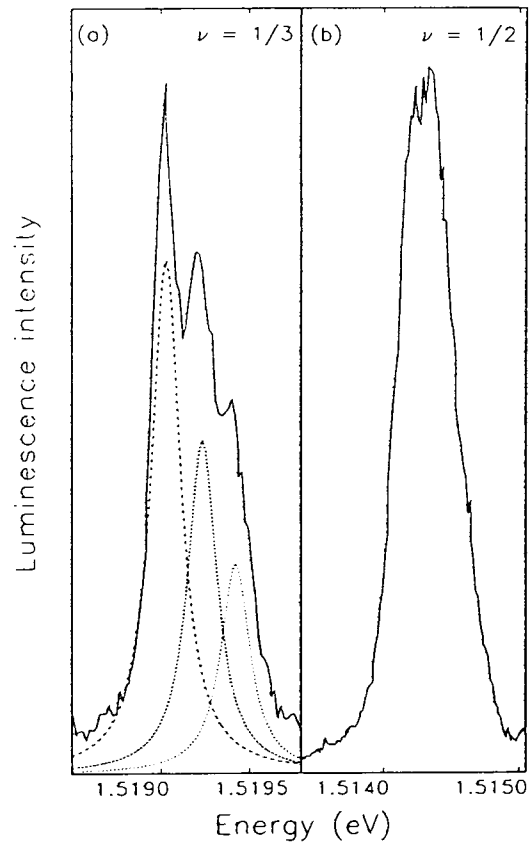

Figure 1.8: Luminescence spectra of the Philips G641 sample at 100 mK (a) $\nu = \frac{1}{3}$; (b)$\nu = \frac{1}{2}$. Taken from [14].

Luminescence has also been proposed to test the extent of crystalline ordering that is predicted to occur as the high field, low temperature ground state of the two dimensional electron system. Harris et al. [14] argue that crystallization of electrons in the ground (E_0) subband would result in a non-uniform charge distribution due to pinning of the Crystal by variations in the interface potential. This would perturb the higher lying subbands but have the greatest effect on E_1 which is principal source for the observed luminescence. Crystallization could then be detected through its effect on the luminescence spectrum. Near to $\nu = \frac{1}{5}$ luminescence originating from the lowest Landau level of the first (E_1) excited subband in a GaAs heterojunction initially broadens and then develops a high-energy shoulder. These changes in the width and structure of the E_1

luminescence are ascribed to the effect of crystallization on the E_0 subband[14].

Other experimental techniques used to probe the FQHE regime have been transport generated ac 'noise' [15], diagonal resistance versus temperature [16] and surface acoustic wave propagation[17]. All these measurements have provided evidence for possible crystal formation just below and re-entrant above filling factor $\nu = \frac{1}{5}$. These experiments are not inconsistent with the best currently available theoretical estimates of a 'critical' filling factor below which crystallization would occur of $\nu_c = \frac{1}{6.5}$ [18] and $\nu_c = \frac{1}{9}$ [19].

An attempt to combine optical and transport data has been made by Kukushkin and co-workers [20] who monitored luminescence intensity while applying an electric field. A crystalline solid indicated by the appearance of the low energy photoluminescence peak, exists in regions below $\nu_c = 0.27$ and surprisingly, up to temperatures of 1.5 K. Only the low energy luminescence peak intensity is affected by the electric field; showing an enhancement attributed to depinning of the Wigner crystal. Indication is also given for a two-stage melting process which agrees with earlier experiments on classical systems [21] and theoretical predictions for the existence of an intermediate 'hexatic' phase between the liquid and solid phases in a 2DES [22].

Characterization of the two dimensional electron system in high magnetic fields remains a hotly debated issue among researchers. Each type of experiment - cyclotron resonance, photoluminescence, magneto-transport, *etc.* has provided valuable clues but an overarching consensus that spans the field has yet to be developed.

1.5 References

[1] Esaki and R. Tsu, IBM J. Res. Dev. **14**, 61 (1970).

[2] B.A. Joyce, Rep. Prog. Phys. **48**, 1637 (1985).

[3] N. Mason and P.J. Walker, *Private communication*

[4] M. Lakrimi, R.W. Martin, C. Lopez, D.M. Symons, E.T.R. Chidley, R.J. Nicholas and P.J. Walker, *Semicon. Sci. Tech.* **8**, S367 (1993).

[5] G. Summers, *D.Phil thesis, Oxford*, (1993)

[6] C.T. Foxon, J.J. Harris, D. Hilton, J. Hewett and C. Roberts, *Semicon. Sci. Tech.* **4**, 582 (1989).

[7] J.W. Orton, P.F. Fewster, J.P. Gowers, P. Dawson, K.J. Moore, P.J. Dobson, C.J. Curling, C.T. Foxon, K. Woodbridge, G. Duggan and H.I. Ralph, *Semicon. Sci. Tech.* **2**, 597 (1987).

[8] M.A. Brummel, *D.Phil thesis, Oxford*, (1984)

[9] R.B. Laughlin, *Phys. Rev. Lett.* **50**, 1395 (1983).

[10] T. Chakraborty and P.Pietiläinen, *The Fractional Quantum Hall Effect*, Solid-State Sciences vol. **85**, Springer-Verlag (1988)

[11] D.R. Leadley, R.J. Nicholas, C.T. Foxon and J.J Harris, *Phys. Rev. Lett.* **72**, 1906 (1994).

[12] A.J. Turberfield, S.R. Haynes, P.A. Wright, R.A. Ford, R.G. Clark and J.F. Ryan, *Phys. Rev. Lett.* **65**, 637 (1990).

[13] B.B. Goldberg, D. Heimann, A. Pinczuk, L. Pfeiffer and K. West, *Phys. Rev. Lett.* **65**, 641 (1990).

[14] I.N. Harris, H.D.M. Davies, R.A. Ford, J.F. Ryan, A.J. Turberfield, C.T. Foxon and J.J. Harris, *Surface Science* **305**, 61 (1994).

[15] V.J. Goldman, M. Santos, M. Shayegan and J.E. Cunningham, *Phys. Rev. Lett.* **65**, 2189 (1990).

[16] H.W. Jiang, R.L. Willet, H.L. Stormer, D.C. Tsui, L.N. Pfeiffer and K.W. West, *Phys. Rev. Lett.* **65**, 633 (1990).

[17] M.A. Paalanen, R.L. Willet, P.B. Littlewood, R.R. Ruel, K.W. West, L.N. Pfieffer and D.J. Bishop, *Phys. Rev.* B **45**, 11342 (1992).

[18] P.K. Lam and S.M. Girvin, *Phys. Rev.* B **30**, 473 (1984).

[19] D. Levesque, J.J. Weis and A.H. MacDonald, *Phys. Rev.* B **30**, 1056 (1984).

[20] I.V. Kukushkin, N.J. Pulsford, K. von Klitzing, K. Ploog, R.J. Haug and S. Koch, *Phys. Rev.* B **45**, 4532 (1992).

[21] C.A. Murray and D.H. Van Winkle, *Phys. Rev. Lett.* **58**, 1200 (1987).

[22] B.I. Halperin and D.R. Nelson, *Phys. Rev. Lett.* **41**, 121 (1978).

[23] R.L. Willet, H.L. Störmer, D.C. Tsui, L.N. Pfeiffer, K.W. West and K.W. Baldwin, *Phys. Rev.* B **38**, 7881 (1989).

[24] V.J. Goldman, M. Shayegan and D.C. Tsui, *Phys. Rev. Lett.* **61**, 881 (1988).

[25] F.I.B. Williams, P.A. Wright, R.G. Clark, E.Y. Andrei, G. Deville, D.C. Glattli, O. Probst, B. Etienne, C. Dorin, C.T. Foxon and J.J. Harris, *Phys. Rev. Lett.* **66**, 3285 (1991).

[26] E.Y. Andrei, G. Deville, D.C. Glattli and F.I.B. Williams, *Phys. Rev. Lett.* **60**, 2765 (1988).

[27] H. Buhmann, W. Joss, K. von Klitzing, I.V. Kukushkin, A.S. Plaut, G. Martinez, K. Ploog and V.B. Timofeev, *Phys. Rev. Lett.* **66**, 926 (1991).

[28] U. Rössler, F. Malcher and G. Lommer, in *High Magnetic Fields in Semiconductor Physics II* Springer Series in Solid-State Sciences Vol. 87 (Springer-Verlag, Berlin, 1989), p. 376.

Chapter 2

Experimental Details

2.1 Introduction

The measurements described in this thesis were accomplished through the use of three different experimental configurations: optically detected cyclotron resonance, Fourier transform spectroscopy, and standard far-infrared absorption. All three monitor the resonant absorption of light by a semiconductor material or structure when the cyclotron frequency of the carriers matches the frequency of the incident light. Given the electron effective masses of GaAs based systems and the field range possible with modern superconducting magnets, the frequencies that were of use to my work were in the far-infrared (FIR) region of the spectrum from 47 to 1223 μm.

Most experiments were at the helium liquid temperature of 4 K although many were performed at 2 K or even well into the millikelvin range by using commercially available ^{3}He or ^{3}He/^{4}He dilution refrigerator systems. Since the principles and working procedures of these systems are well documented, I will only refer to modifications that were made in order to enable optical measurements. More attention will be placed on optically detected cyclotron resonance, which although conceived almost seventeen years ago, has largely been developed into a demonstrably successful tool of semiconductor research by Richard Warburton, Robin Nicholas and myself here in Oxford. An effort is made to include hints or 'tricks' that resulted in better signal output for all three of the experimental configurations so that future experimentalists might not have to learn so much by experience.

Shared by each experimental setup is the phenomenon of cyclotron resonance (CR), where electromagnetic radiation can be resonantly absorbed when the energy of the radiation is equal to the energy separation between the Landau levels. This makes the condition for resonance

$$\omega_c = \frac{eB}{m^*} \tag{2.1}$$

where ω_c is the cyclotron frequency and B the resonant field. CR was first suggested as an experimental technique by Shockley in 1953 for determining the band structure within the Brillouin zone. Since then it has become a classic tool for study of semiconductors. When the electric vector of the far-infrared light is aligned at right angles to the magnetic field, as is the case for all of the experiments surveyed, the selection rule

that governs this absorptive process is to $\Delta N = \pm 1$ where N is the Landau level index.

A key feature of cyclotron resonance is that the integrated strength of the resonant absorption is determined by the classical Drude conductivity which allows a direct contactless measurement of the carrier densities within whatever initial states are populated. The Drude formalism begins with the equation of motion for a carrier of mass m^* in a static magnetic field $\mathbf{B}$ and ac electric field $\mathbf{E}$:

$$m^* \frac{d\nu}{dt} + \frac{m^* \nu}{\tau} = e\,(\mathbf{E} + [\nu \times \mathbf{B}) \tag{2.2}$$

where ν is the carrier velocity and τ is the collision time which is assumed to be independent of energy[1]. For $\mathbf{E} \propto exp(i\omega\tau)$ and $ne\nu = \sigma\mathbf{E}$, Equation 2.2 is solved to determine the nonzero components of the conductivity tensor σ which takes the form:

$$\sigma = \begin{bmatrix} \sigma_{xx} & \sigma_{xy} & 0 \\ \sigma_{yx} & \sigma_{yy} & 0 \\ 0 & 0 & \sigma_{zz} \end{bmatrix} \tag{2.3}$$

For linearly polarised radiation, which can be decomposed into two counter-rotating circularly polarised components, the effective conductivity for each component is $\sigma_\pm = \sigma_{xx} \pm i\sigma_{xy}$. Solving Equation 2.2 gives

$$\sigma_\pm = \frac{\sigma_0 \tau^{-1}}{\tau^{-1} + i(\omega \pm \omega_c)} \tag{2.4}$$

where the dc conductivity is $\sigma_0 = N_s e^2/m^*$. When the electric field is perpendicular to the magnetic field (Faraday configuration) the power absorbed by the carriers is given by

$$\mathbf{P} = \frac{1}{2}\Re(\mathbf{J} \cdot \mathbf{E}). \tag{2.5}$$

Since the ac current density $\mathbf{J}$ is related to $\mathbf{E}$ by the expression

$$\mathbf{J} = \sigma(\omega\tau) \cdot \mathbf{E}, \tag{2.6}$$

the absorption of the incident radiation can be described using only the ac conductivity. For the linearly polarized case, the total power absorption is equal to the sum of the two circular polarizations and after some manipulation can be written as

$$\frac{P}{P_0} = \frac{1 + (\omega^2 + \omega_c^2)\tau^2}{[1 + (\omega^2 - \omega_c^2)\tau^2]^2 + 4\omega_c^2\tau^2} \tag{2.7}$$

where P_0 is the absorption for ω_c and $\omega = 0$. Figure 2.1 shows power absorbed by an electron gas for several values of $\omega\tau$. The absorption spectrum is only clearly defined when the cyclotron frequency is comparable or larger than the collision frequency which means that the carrier is able to complete at least one radian of the cyclotron orbit before being scattered.

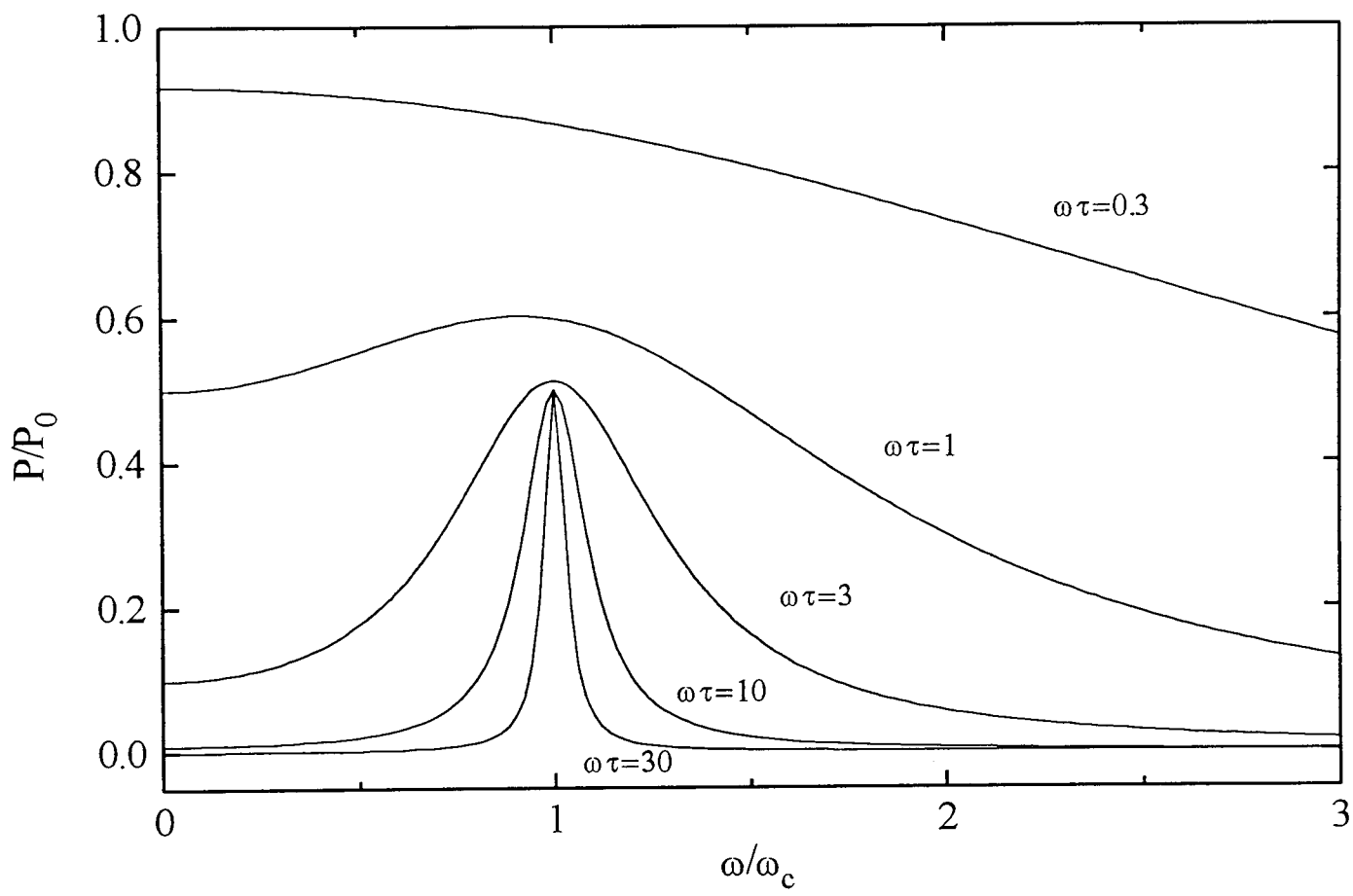

Figure 2.1: The cyclotron resonance lineshape is only defined for the case when $\omega_c\tau \geq 1$.

In order to arrive at the carrier density from a cyclotron resonance, the area underneath the curve must be determined, which is then proportional to the number of carriers. The constant of proportionality is given directly by Equation 2.7 and was verified by a comparison between optical and transport measurements. In practice the conversion from area under the CR curve to carrier density was made much easier through the use of a computer program written by Glen Summers which automatically fits the experimental resonance to a combination of Gaussian and Lorentzian lineshapes[2]. In a careful analysis of the accuracy of the predicted carrier densities, Summers established that error was not greater than 5% over a range of carrier densities from 1 to 14 $\times 10^{10}\text{cm}^{-2}$[2]. This serves to reaffirm the usefulness of the Drude model which provides an accurate

description of the cyclotron resonance despite its simplicity.

For all of its success, the Drude model does not accurately explain all observed experimental results, especially in two dimensional systems when the cyclotron resonance mode can couple to the collective modes of the electron plasma (Chapter 5). In particular, the quantity τ which accounts for scattering effects has no reason to be energy independent as postulated in the Drude model.

2.2 Optically Detected Cyclotron Resonance

Optically detected cyclotron resonance or ODCR differs from CR in that the intensity of visible laser excited luminescence from the sample is monitored rather than the direct absorption of far-infrared (FIR) radiation. ODCR is a potentially valuable tool in the study of semiconductor materials for several reasons. Firstly, experiments on undoped samples are possible as the optical pumping of the visible laser provides the necessary carriers. Secondly, photomultiplier tubes used to detect luminescence offer far more sensitivity than their counterpart microwave or FIR detectors, and finally, the possibility now exists for a simultaneous study of electrons *and* holes.

The feasibility of ODCR at microwave frequencies was first demonstrated by Romestain and Weisbuch who used the method for determining band masses in CdTe and GaAs[3]. Extension of the resonant frequencies to the far-infrared has been shown to provide an enhancement in the resolution and sensitivity of the technique[4]-[6]. In this thesis, I have used the ODCR technique in a comprehensive study of bulk GaAs, establishing the conduction band effective mass and offset effects in undoped GaAs/AlGaAs quantum well structures, and to probe superlattice orbits and impurity states in $In_{0.05}Ga_{0.95}As/GaAs$.

The ODCR experimental configuration pictured in Figure 2.2 is the result of much trial and experimentation with different components and techniques. It is convenient to organise the instrumentation into three parts, each discussed in detail.

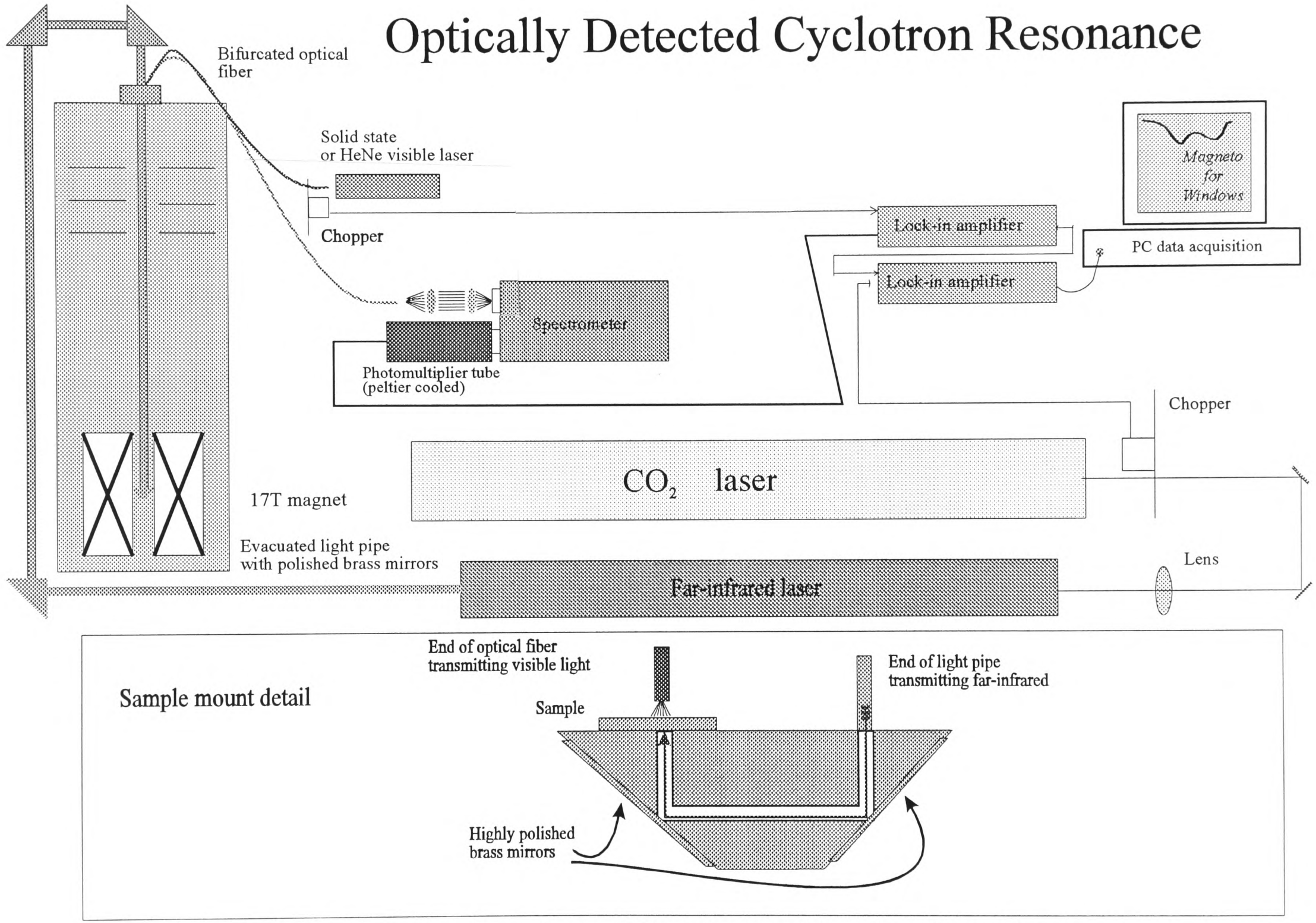

Figure 2.2: The experimental setup for far-infrared ODCR and standard cyclotron resonance. Detail of the sample mount is shown in the inset.

2.2.1 Insert, sample mount and bolometers

The ODCR insert consists of two tubes, one of which holds the fiber bundle and the other which serves as a continuation of the waveguide for the FIR radiation. Care was taken while machining the insert components to eliminate any ridges at joints in the light pipe that might scatter the FIR. A ten pin electrical board at the bottom of the insert provides the necessary connections for bolometer leads. The twin pipes are held together by a series of radiation baffles which reduce the heat travelling to the bottom end. Once fitted with the sample mounting block, the entire unit is slipped into a stainless steel cylindrical sheath, evacuated and filled with a small amount of He exchange gas, and then pre-cooled with liquid N_2 before inserting into the magnet core.

The sample mount block employs two 45^o reflectors and a tapered cone to focus the incident FIR radiation on the sample substrate. It also provides an adjustable mounting for the fiber bundle so that the visible laser light coincides with the area immersed by the FIR radiation. Samples were generally wedged to avoid interference effects and were fastened to the block with nail polish or silver paint, the latter substance prevented FIR radiation from leaking around the sample edges in standard CR experiments. The largest photoluminscence signal and therefore optimum ODCR data, was obtained when the fiber bundle was positioned less than 1.0 mm above the sample.

In order to tune the CO_2 laser and make sure enough FIR was getting down into the insert, there had to be a very sensitive detector of long wavelength light, placed near the sample. This would be in addition to a golay detector that was external to the cryostat. Bolometers, a name given to devices that respond to slight variations in temperature by exhibiting a variation in a material property such as resistance, are often used to detect in the far-infrared. For ODCR experiments, bolometers served primarily as confirmation that the strength of the FIR laser line remained constant during a scan. Often two bolometers were mounted, one above and the other below the sample, with their outputs ratioed together so that the direct absorption of the FIR could be monitored as well as changes in the luminescence intensity. The bolometers were fashioned from 470Ω Allen-Bradley resistors, which were delicately ground down until they were flat and extremely thin, with a room temperature resistance of $4-6K\Omega$.

When cooled, the resistance across the bolometer increased to $150K\Omega$ at $4K$ and the $2K$ resistance approached $1M\Omega$. Placement of the bolometer over the sample was made just outside the circumference of the fiber so as to receive the maximal amount of transmitted FIR without interfering with the bundle luminescence collection. Typically, a current of $10\,\mu$A was sent through the bolometer, with the voltage signal amplified and monitored on the oscilliscope.

The ODCR insert was equally suited for standard cyclotron resonance absorption measurements. For this type of work, the fiber bundle would be drawn back from the sample surface to allow for better placement of the bolometer over the sample. Having the fiber bundle available was often convenient, especially in studies of the GaAs heterojunctions where visible light was used to reduce the electron density.

2.2.2 The far-infrared laser

The laser used to produce the far-infrared radiation actually consists of two separate lasers that are coupled together: a CO_2 laser with output between $9-11\,\mu$m and a molecular gas laser whose lasing cavity is usually filled with a low pressure gas of methanol or methanol derivative. The CO_2 laser optically pumps the molecular laser which emits a series of discrete energy laser lines generated by the vibrational and rotational modes of the gas. Such a system is described in detail in [7] and so will not be more fully covered here. Of some interest, however, is the *modus operandi* useful for optimizing the power output of a specific line (wavelength) of FIR radiation and transporting the light with a minimal amount of transmission loss to the sample.

Like any complex optical apparatus, operating the FIR laser is part direct instruction from manual and part fine adjustment learned from continual use. Experience has shown that the instrument works best after a prolonged warm-up period of as long as four hours. An accessory device was built that circulated cooling water around the molecular lasing cavity to minimize thermal expansion which improved both power output and stability.

The CO_2 laser grating usually reads slightly below that for a specific line listed in the manual. The pressure of the gas within the molecular lasing cavity, controlled by a

needle valve regulator, has an enormous effect on the power output with some lines (notably 163, 57 and 53μm) liking higher pressures. The pressure of the CO_2 laser gas mixture is held to 15 torr at start-up and 28 torr during normal operation. There is little difference in FIR power output at either setting, but the gain goes down if the pressure is placed at an intermediate setting.

The procedure for finding a 'clean' line is straightforward. Initially, the line is dialled up by setting the CO_2 laser grating and watching the golay and bolometer signal on an oscilliscope. Differentiation between long and short wavelengths on the same pump line is achieved by observing the attenuation of signal caused by a single sheet of British standard grade of graph paper. 57 μm is attenuated by exactly a factor of ten, with longer wavelengths reduced proportionally less. The golay's tendency to see longer wavelengths more strongly (perhaps not detect shorter wavelengths at all) is useful when compared with the bolometer's tendency to be transparent to longer wavelengths. For weaker lines, especially those that come on a pump with many other possible nodes, the index on the micrometer that controls the cavity length can be useful. A node will reappear at regular intervals, spaced by integral multiples of its wavelength. To fully utilize this property, a small step driver motor attached to the micrometer, turns the knob while the bolometer output is monitored on a chart recorder. It then becomes much easier to differentiate between the different frequencies.

When possible, the magnetic field is set close to the expected resonance point and the mode on the line that optimizes ODCR signal is selected by adjusting the cavity length of the laser. This last step serves the important function of ensuring the incident wavelength is what you think it is (not always trivial!) and, more importantly, is uncontaminated by other lines with the same pump. In some early ODCR experiments on bulk GaAs, as many as four different free electron resonances were observed as the field was swept due to line contamination. ODCR gives the user of the FIR laser system the unique opportunity to tune modes precisely provided the resonance field is known.

An additional problem is getting the FIR radiation to a sample buried deep within a superconducting magnet. For this purpose, a brass pipe waveguide is used, with highly polished plates at the corners to direct the radiation. The waveguide has optical

Wavelength μm	Gas	$C0_2$ laser grating reading	CO_2 pump line	Cavity pressure (torr)	Comments
47.6	DMA	4025-6	9R08	0.1-0.15	
53.9	MA	4400	10R36	0.13-0.17	likes high press.
44.3	MAD	3971	9R28	0.12-0.13	
56.7	MAD	4415	10R30	0.1	
57.20	DMA	4025-6	9R08	0.1-0.15	
61.61	MA	4000	10R18	0.1	
63.37	MA	4178	9P34	0.095	comes w/70,699
70.51	MA	4177-82	9P34	0.08-0.1	comes w/63,699
81.9	DMA	4161	9P30	0.12	
89.6	DMA	4160-2	9P30	0.09	
96.52	MA	4018-9	9R10	0.15+	
103.13	DMA	4160-4	9P30	0.15	
118.83	MA	4187-9	9P36	0.1+	the best
129.55	MA	4404	10R34	0.2	
133.12	MA	4135	9P24	0.07	
145.5	MA	4408	10R32	0.1	
163.03	MA	4391	10R38	0.2	pressure sens.
170.58	MA	4188	9P36	-	
202.40	MA	4187	9P36	0.08	
215.37	DMA	4006	9R14	0.12	
232.94	MA	4018-9	9R10	0.2+	comes w/ 96
251.14	MA	4393-4	10R38	0.09	comes w/ 163
294.81	DMA	4025-9	9R08	0.06	
305.73	DMA	4025-9	9R08	0.06	
570.57	MA	4104-11	9P16	0.1-.2	
699.42	MA	4177-9	9P34	0.07	comes w/63,70
871.58	MAD	4486	10R18	0.1	
1223.66	MA	4104-11	9P16	0.1	

Table 2.1: Far-infrared laser lines used for cyclotron resonance experiments. Wavelengths are quoted to two decimal places unless not sufficiently accurately known. For the gases MA=CH_3OH, DMA=CH_3OD and MAD = CD_3OH. 57 μm is attenuated a factor of 10 by a sheet of graph paper.

windows made of TPX at the entrance port by the FIR laser and top of the insert assembly and is evacuated using a standard rotary pump. TPX was found to be ideal for maintaining a high vacuum while only slightly attenuating the intensity of the radiation. The waveguide and its composite metal mirrors require regular cleaning to prevent build-up of oil droplets and dust. In the first attempt at ODCR, a 3% modulation of the photoluminescence signal was observed. After cleaning the light pipes, polishing the TPX windows and making small improvements on the waveguide through the insert, the modulation had increased to 40%.

Care was taken to periodically re-align the mirrors and lens that linked the CO_2 laser beam with the molecular lasing cavity. Aiding in the realignment is a sensitive audio microphone that detects the pulses of near infrared light in the molecular lasing cavity. The alignment of output mirrors within the lasing cavity is checked using a visible HeNe laser.

2.2.3 Visible lasers and optical fibers

The visible laser light used to excite carriers in the sample is provided by one of three sources: a solid-state laser diode, a standard HeNe laser or a HeCd laser. The Applied Laser Systems diode emits 5 mW of power at 670 nm (1.85 eV). The unit comes in a small case with self-contained power regulating circuit and focusing lens and is powered by a 9V rechargeable battery. The diode was found to be superior for most experiments due to the low noise levels on the PL signal, a consequence of power output stability. The HeNe laser is a small, conventionally powered unit emitting 5 mW at 632 nm (1.96 eV), slightly shorter than the diode

The HeCd laser is a much larger unit, with separate power supply and control unit, emitting approximately 50 mW of blue light at 433 nm. This laser was used in an attempt to increase the magnitude of the PL signal in the hope that the signal to noise ratio on the ODCR signal would increase. A slight increase in luminescence was observed but the ODCR signal remained much the same so usage of the HeCd has been limited. The HeCd laser caused greater levels of electrical noise in the detection and amplification system and suffered from poor output power stability.

A randomized bifurcated optical bundle carries the visible light to the sample and collects the emitted luminescence. It was found that a two lens collection and focusing setup for the luminescence between the fiber and the spectrometer resulted in optimum PL signal levels. The lenses were picked to match the f-number of the spectrometer and cover the large solid angle of light leaving the fiber. Despite the resulting magnification ($\sim 3\times$), this system was found to be superior to butting the end of the fiber directly against the spectrometer slits.

Several fiber bundles have been made using six individual fibers, 600 or 1000 μm in diameter, joined together around a central fiber. The central fiber is used to transmit the visible laser light, while the remaining six fibers are collected together in a 'fishtail' assembly made to match the spectrometer slit configuration. These home-made fibers have been extremely successful and are now used for most experiments. The chief problem in the construction of these bundles has been making them suitable for use in high vacuums. Simply sealing to the TPX coating of the fiber has shown to be insufficient. Fibers with alternative coatings such as polyamide have been tried with greater success although the fibers themselves are more brittle and prone to breakage than the TPX coated variety.

2.2.4 Signal detection

Generally, the ODCR system would be used to collect three types of data: (1) photoluminescence (PL) measurements, (2) ODCR and (3) infrared modulated photoluminescence or IMPL. IMPL measures the ODCR signal as a function of PL wavelength and will be discussed in more detail in Chapter 3. The visible laser beam was chopped to provide a reference signal for a lock-in amplifier in PL measurements. ODCR and IMPL involved the additional step of taking output from the lock-in amplifier connected to the luminescence signal and feeding it into a second lock-in whose reference was provided by chopping the CO_2 laser beam. This configuration maximized the ODCR signal to noise ratio and ensured that effects seen were not spurious in origin. The PL signal was chopped at ~ 2 kHz and the FIR signal at ~ 20 Hz.

The light back from the sample is dispersed with a 0.5 m Czerney-Turner spectrometer

fitted with either a 1200 or 600 lines/mm grating and blaze wavelength of 630 nm or 1.2 μm. A red band pass filter is usually placed inside the housing to prevent second order laser lines from coming through and overburdening the photomultiplier tube.

For all the ODCR experiments covered in this thesis, the PL intensity is converted to current through the use of a GaAs photomultiplier tube, selected for its high responsivity between $400 - 800$ nm and its relatively low dark current. The tube rests in a magnetically shielded housing and is Peltier cooled to about -25°C. Several other detection systems have been tried including silicon diodes and a Germanium detector useful for longer wavelengths. The Germanium detector has a slower response time and so the chopping frequency cannot be set as high as for the photomultiplier tube. It also suffers from annoying cosmic ray spikes.

The current from the photomultiplier was sent through a large resistor to convert into a voltage signal with an isolated ground. The signal is then amplified with a battery powered pre-amplifier before being sent to the main lock-in amplifier. Extreme care was taken to minimize signal cable length and encase the current to voltage converter in a shielded box. Output from the lock-in amplifier is directed into an IEEE analog to digital converter and entered into a PC-based data collection program written by Glen Summers called *Magneto for Windows*. *Magneto* allows the magnet and amplifiers to be controlled automatically through the menu driven program and enables simultaneous recording of up to 6 channels.

Recently the principle behind ODCR has been extended to monitoring FIR induced changes in the photocurrent from a sample with multiple GaAs quantum wells. Low levels of HeNe laser light excite the photocurrent. The amount of current is dependent on a bias voltage which brings the energy subband levels in adjacent wells coincident with each other. Early results show promise for this technique in monitoring intersubband absorption of the far-infrared.

2.3 Fourier transform spectroscopy

A limitation of the far-infrared laser is that it is only capable of producing discrete lines that correspond to an excited state of the gas mixture in the lasing cavity. Although by using different gases, thousands of FIR wavelengths are possible, in practice only a limited number are of sufficient strength to be useful. When a fine mesh of energy values are needed, such as for the heterojunction subband coupling measurements in Chapter 4, Fourier transform spectroscopy is an extremely useful technique. Here, a globar or metal wire replaces the laser as the source of the infrared and an idealized Michelson interferometer is used to divide the energy spectrum, with the intensity of the transmitted light measured at each energy value for a set magnetic field. For my work, I have used an extremely high precision fast Fourier transform spectrometer (FTS) made by Bruker of Germany, which are leaders in infrared spectroscopic equipment.

The process by which the Bruker produces a spectral trace is straightforward, although a certain amount of mathematical manipulation is involved. The optical heart of the system is the interferometer pictured in Figure 2.3. Light from the source is passed through a mylar beam splitter, with half the light traveling to a fixed mirror and bouncing back again to the beam splitter with a total optical path length of $2L$. The remainder of the light travels to a second mirror which also a distance L from the mirror but can be moved very precisely back and forth a distance x about L. When the halves recombine at the beam splitter, the moving mirror results in a path difference of $2x$.

The beam leaving the interferometer is passed through the sample and finally onto a very sensitive silicon bolometer. The quantity measured by the detector is the intensity $I(x)$ of the combined beams as a function of the moving mirror displacement x. This is referred to as the *interferogram*. The partial waves interfere constructively yielding maximum detector signal if their path difference is an integer multiple of the wavelength λ and destructively if the path difference is an integer multiple of $\lambda/2$. This dependence can be described by the cosine function:

$$I(x) = S(\nu)\cos(2\pi\nu x) \tag{2.8}$$

where $\nu = 1/\lambda$ and $S(\nu)$ is the intensity of the monochromatic line at wavenumber ν.

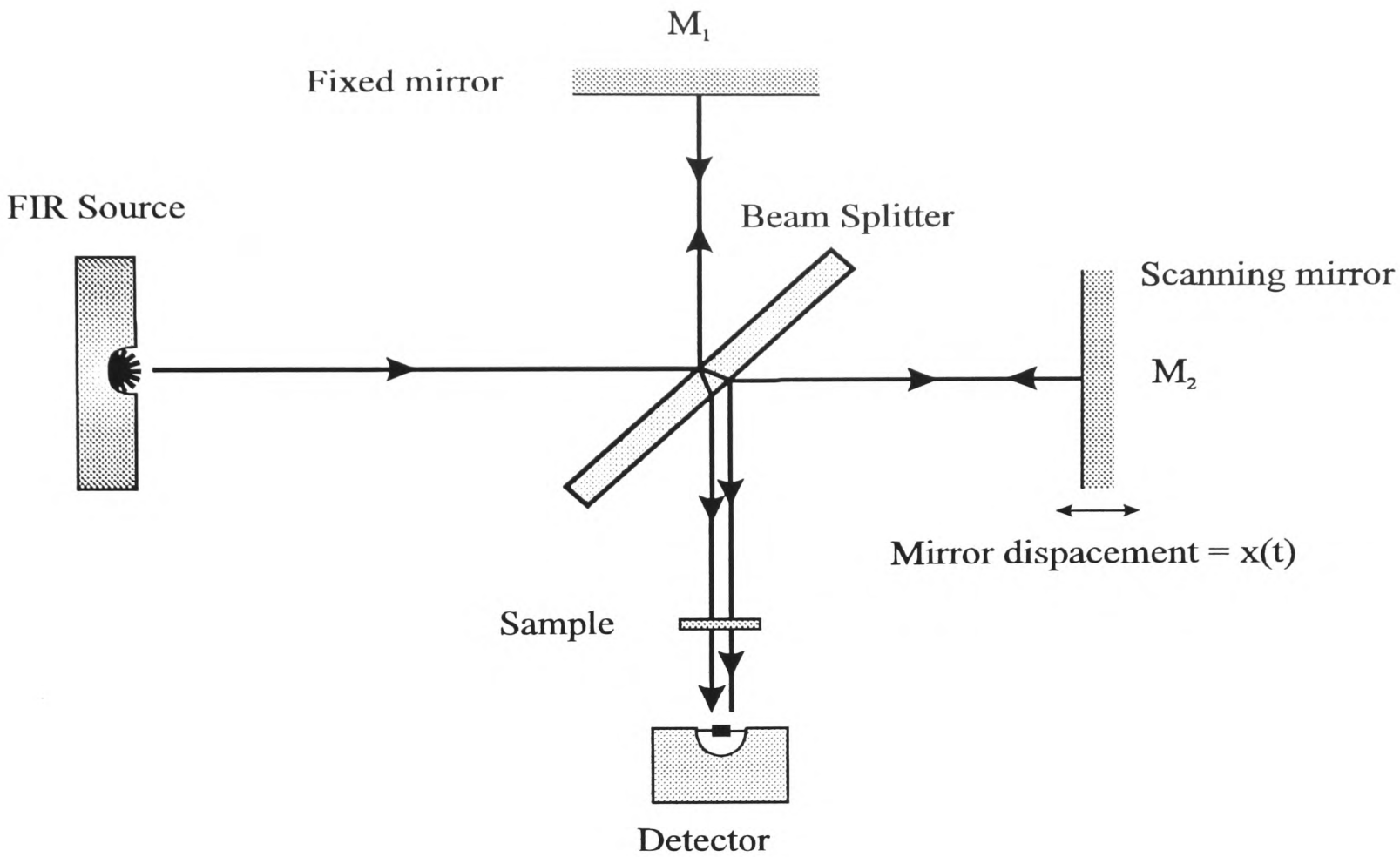

Figure 2.3: The Michelson interferometer at the heart of the Fourier transform spectrometer showing the FIR source, detector, fixed mirror and moveable mirror. From G. Summers D.Phil Thesis[2].

Since very accurate tracking of the moving mirror is possible by using the interference pattern of a HeNe laser to control the change in optical path difference, the system has a built-in accuracy proportional to Δx which is usually at least $0.01\,\mathrm{cm}^{-1}$. Other advantages of the system include the larger area of the circular apertures used in FTS which allows for increased input and the ability to move the mirror very fast, enabling the measurement of complete spectra in fractions of a second.

For a monochromatic source of wavenumber ν, the intensity measured by the detector for optical path difference $y = 2x$ will be:

$$I(\nu, y) = \frac{1}{4} S(\nu) T(\nu) D(\nu) \left[1 + e^{-i(2\pi\nu y)}\right]^2 = \frac{1}{2} f(\nu)[1 + cos(2\pi\nu y)] \qquad (2.9)$$

where $S(\nu)$ is the intensity of the source at wavenumber ν, $T(\nu)$ is the transmission spectrum of the sample, $D(\nu)$ is the detector response and $f(\nu) = S(\nu)T(\nu)D(\nu)$ is a compound function that describes the complete response of the system. When a

broadband source is used, the output of the interferometer must be integrated over ν.

$$\begin{aligned} I(y) &= \frac{1}{2}\int_0^\infty f(\nu)[1+cos(2\pi\nu y)]d\nu \\ &= \frac{1}{2}I(0)+\frac{1}{2}\int_0^\infty f(\nu)[1+cos(2\pi\nu y)]d\nu \end{aligned} \tag{2.10}$$

This makes $I(y)$ the cosine Fourier transform of the function $f(\nu)$ plus a constant term. In order to create the spectrum from the interferogram the inverse Fourier transform is then taken:

$$f(\nu) = 4\int_0^\infty \left[I(y)-\frac{1}{2}I(0)\right] cos(2\pi\nu y)dy \tag{2.11}$$

In practice, the intensity is measured as a function of mirror displacement, converted into digital form and then fed into the computer to calculate $f(\nu)$ describing the transmission of the sample. The Bruker instrument is equipped with a special fast Fourier transform processor that greatly speeds the mathematical computation. Since $f(\nu)$ is also influenced by the source spectrum and detector response, an interferogram must be taken both with and without the sample in the optical path. These two interferograms are converted to spectra and then ratioed to obtain the final transmission spectrum.

In the Fourier transform of the interferogram, several data processing techniques are used to overcome spectral artifacts that can arise due the approximation of a continuous spectrum by the discrete Fourier transform. An excellent review of FT data processing can be found in [2] and references therein. The remainder of this section will center on improvements made to the ^{3}He insert to try to improve the quality of the spectra taken in the low carrier density limit of GaAs heterojunctions.

Previous resonant subband Landau level coupling experiments on the GaAs heterojunctions used the 2 K insert and examined samples with higher carrier densities[2]. Since the aim of my experiment was to determine the shape of the confinement potential under conditions similar to the millikelvin cyclotron resonance measurements, I decided to use the ^{3}He system. With its many pumps, the ^{3}He cryostat added much more electrical and mechanical noise to the spectra than its 2 K counterpart. Compounding the problem was the low carrier density present in the heterojunction after illumination with visible light. This resulted in resonance absorptions of often less than 10%.

The first series of spectra taken had a noise level of $\sim 5\%$ which made the data unworkable as it was impossible to separate noise induced features from real resonance effects.

To solve this problem several steps were taken. Chief among the projects was moving the field effect transistor (FET) which formed part of the bolometer detection circuit, to be adjacent to the bolometer. This shortened the length of wiring that the high impedance signal from the bolometer had to travel before the impedance was reduced by the FET. The remaining wires were replaced by miniature coax cable to reduce the amount of r-f pickup. Attempts to improve the optical part of the system were made as well. The light pipe down the center of the insert was carefully cleaned and a new focusing light cone was made to fit above the sample. The combined effect of these measures was to largely eliminate the electrical and mechanical noise when the magnetic field was off. Once the magnet was switched on, noise levels were generally reduced to under 3% which greatly improved the quality of the spectra. Random noise spikes were largely eliminated. It is not clear why the magnet influences the noise characteristics of the system but it could reflect a slight misalignment of the insert relative to the magnet core. Despite many hours of trial and error attempts to reduce the noise levels further, the ^{3}He system never produced the noise-free spectra of the 2 K insert.

2.4 References

[1] K. Seeger, *Semiconductor Physics*, Springer-Verlag, 358,(1982)

[2] Glen Summers, *D.Phil thesis*, *Oxford*, (1993)

[3] R. Romestain and C. Weisbuch, *Phys. Rev. Lett.* **45**, 2067 (1980).

[4] M.G. Wright, N. Ahmed, K. Mitchell, A. Koohian, C.R. Pidgeon, B.C. Cavenett, C.R. Stanley and A.H. Kean, *Semicon. Sci. Tech.* **5**, 438 (1990).

[5] N. Ahmed, I.R. Agool, M.G. Wright, K. Mitchell, A. Koohian, S.J. Adams, C.R. Pidgeon, B.C. Cavenett, C.R. Stanley and A.H. Kean, *Semicon. Sci. Tech.* **7**, 352 (1992).

[6] A. Moll, C. Wetzel, B.K. Meyer, P. Omling, and F. Scholz, *Phys. Rev.* B **45**, 1504 (1992).

[7] Mark Brummel, *D.Phil thesis*, *Oxford*, (1984)

[8] Mark Watts, *D.Phil thesis*, *Oxford*, (1991)

Chapter 3

An Optically detected cyclotron resonance study of bulk GaAs

3.1 Introduction

In this chapter, an exceptionally pure sample of n-type GaAs is studied using optically detected cyclotron resonance (ODCR). Extremely good resolution of the system enabled observation of the free electron cyclotron resonance, with a spin split peak discernible above 4.3 T, and a complete range of bound and metastable impurity transitions. Chemical shifts due to the presence of different donor species are clearly resolved. Comment is offered on an anomaly in the ODCR signal at high fields. A critical factor in the experimental success of ODCR is the magnitude of the ODCR signal, which reflected up to a 50% modulation of the PL intensity.

Apart from demonstrating the effectiveness of the ODCR technique and the high quality of the sample, the experimental results in this chapter have been extremely useful in all of my subsequent work on GaAs-based systems. Later chapters in this thesis contain many references to the effective mass at a specific field, nonparabolicity corrections and impurity levels; all values that are provided by this study. Before moving to the experimental results, however, it is appropriate to begin the chapter with a quick survey of the basic theory that governs free carriers and bound impurity states in GaAs.

With the application of a magnetic field, energy levels of free carriers in a semiconductor are quantized into Landau levels (LL) separated by $\hbar\omega_c$. Below each LL exists an additional series of states due to carriers bound to impurities in the sample. Observed experimental transition energies of these impurity states are in good agreement with numerical solutions of the Schrödinger equation for a single electron under the simultaneous action of a static Coulomb potential and uniform magnetic field. Prominent among these studies is that of Makado and McGill[1] who calculated the energy eigenvalues of such a hydrogen-like system in a large magnetic field for the complete spectrum of bound states. These values have been successfully used to identify the origin of experimentally observed transitions for several photoexcitation and transmission spectra[2]-[6].

Further refinement in the calculation of energy levels was offered by Simola and Virtamo [6] who considered the solution of the Schrödinger equation in the high field limit and found that a series of so called metastable states exist in the continuum below each

Landau level. Unlike bound states, the metastable states have no zero field analogue and consequently cannot be labelled using hydrogen spectrum notation.

The characterization of impurity states can be confusing because it employs different labelling systems for the weak ($\gamma \leq 1$), intermediate ($\gamma \sim 1$) and high field ($\gamma \geq 1$) regions, with

$$\gamma = \frac{1}{2}\frac{\hbar\omega_c}{R_y^*},$$

where R_y^* is the effective Rydberg or binding energy of the impurity, and $\omega_c = eB/m^*$ is the cyclotron frequency. γ is then a dimensionless parameter, being the ratio of the zero point cyclotron energy to the effective Rydberg. The situation has become somewhat muddled as various authors have labelled high field states with their corresponding low field label, a correspondence that further theoretical work has shown does not exist[4][7].

At weak fields, the energy eigenvalues are characterized by the Zeeman splitting nomenclature and atomic numbers (n, l, m). In the high field limit, states may be assigned quantum numbers (N, m, ν) where N denotes the Landau level from which the state is derived, m ($m = N, N-1, ..., -\infty$), is the magnetic quantum number, and ν ($\nu = 0, 1, ..., \infty$) equals the number of nodes of the eigenstate in the direction of the magnetic field. The parity of the eigenstate is given by $\pi = (-1)^{m+\nu}$. m and π remain good quantum numbers throughout the field spectrum. Also applying to the entire field range are the electric dipole selection rule, $\Delta m = \pm 1$ for a Faraday configuration, and the parity restriction $\pi_i \pi_f = -1$, where π_i and π_f are the parities of the initial and final states respectively.

No quantitative theoretical information existed concerning the metastable states until recently, when $E_{N,m,\nu} - E_{N-m,-m,\nu}$, the energy difference between states (N, m, ν) and $(N-m, -m, \nu)$ was shown experimentally to be $m\hbar\omega_c$ [3]. Optical $\Delta m = \pm 1$ transitions thus yield pairs of lines separated by ω_c in frequency. Klarenbosch *et al*[2] used this to label many experimentally observed low field transitions with energy above the $N = 0$ LL as metastable states. The energy level calculations of Makado and McGill and the experimental results of Klarenbosch *et al* are used to classify the observed bound and metastable impurity transitions.

3.2 Experimental setup

The optically detected cyclotron resonance experimental setup is described in detail in Chapter 2. For bulk GaAs measurements, the photoluminescence (PL) was excited with a 3 mW solid state laser diode operating at 670 nm, used for its greater amplitude stability over conventional HeNe lasers. A CO_2 pumped molecular gas laser provided the FIR radiation in a series of lines from $47 - 570$ μm. This was directed through a highly polished brass waveguide and series of mirrors onto the sample substrate, mounted in a Faraday configuration at the field center of an 18 T superconducting magnet. The 670 nm radiation arrived at the sample by means of one arm of a bifurcated optical bundle; the second arm collected the luminescence and returned it to a 0.5 m spectrometer where the intensity was measured with a GaAs photomultiplier tube. The GaAs sample was grown in Glasgow, has a transport measured peak mobility $\mu \sim 402,000\ cm^2\ V^{-1}\ s^{-1}$, carrier concentration $(N_D - N_A)$ of $2.8 \times 10^{13}\ cm^{-3}$ and is characterized more fully in a paper by its growers, C.R. Stanley and A.H. Keane[8]. Luminescence spectra will be presented in Section 3.4 as part of the discussion relating to ODCR mechanisms.

Three types of data were collected: 1) Photoluminescence (PL) measurements, 2) ODCR and 3) infrared modulated photoluminescence or IMPL. IMPL involves measuring the ODCR signal as a function of PL wavelength with the FIR allowed to illuminate the sample and the magnetic field fixed to correspond to a resonance position. The IMPL would then be compared to a PL spectra taken at the same magnetic field to determine how the FIR radiation impacted on the differing PL transitions. For PL and IMPL measurements, the spectrometer slits were narrowed in order to resolve the principle triad of peaks in the PL spectrum while ODCR work was performed with the slits set wide enough to take in all three without distinguishing between them (approximately 0.5 cm). In this way, luminescence intensity was maximized for ODCR traces and the system resolution was comparable to the diamagnetic shift of the luminescence peak, making it unnecessary to continually adjust the detection wavelength when sweeping the field.

All ODCR data was taken with the sample at $\sim$ 2.2 K. Figure 3.1 is a representative

ODCR trace for FIR wavelength of 163 μm showing the wealth of impurity transitions and a spin-split cyclotron resonance at 4.41 T.

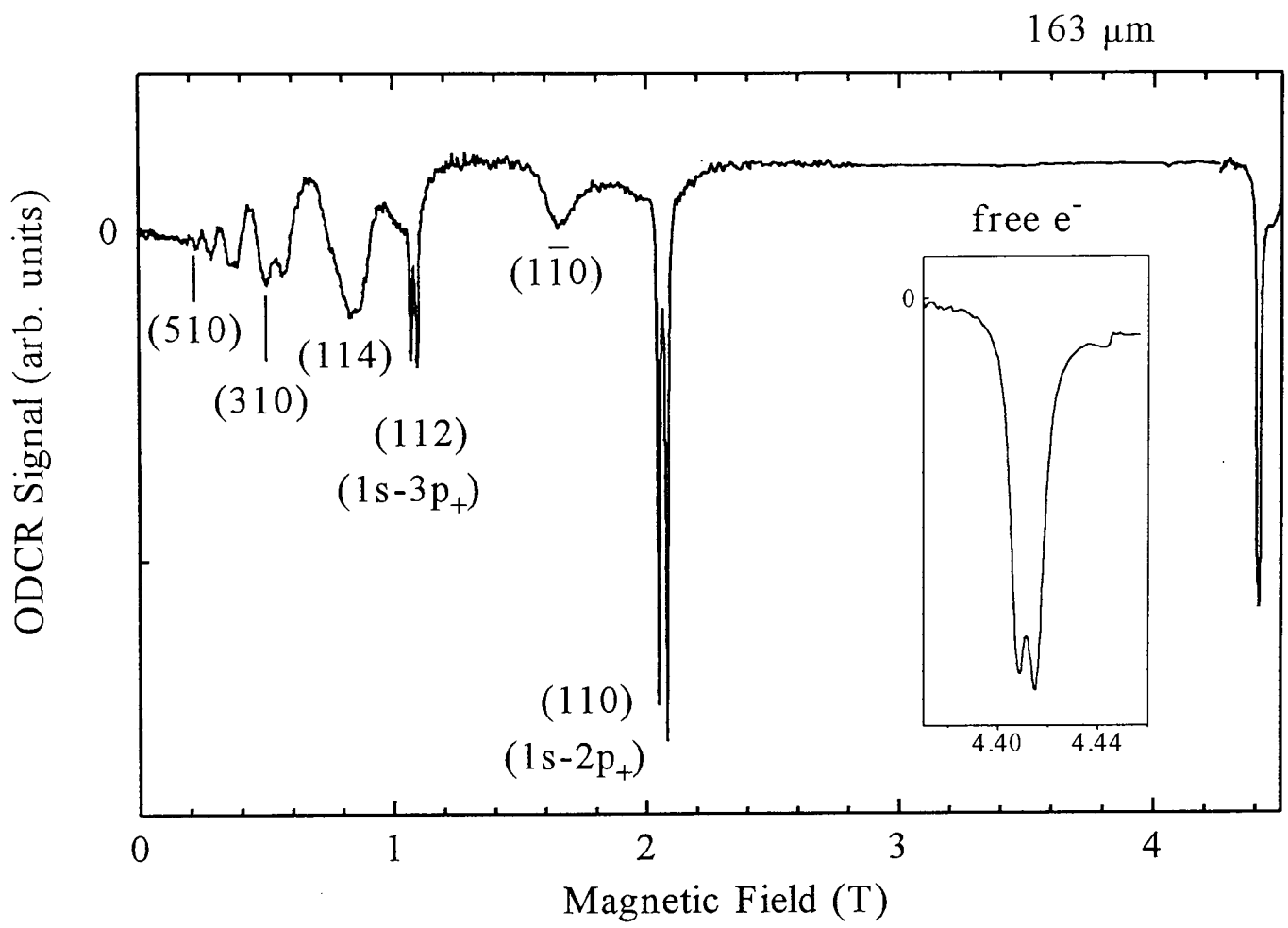

Figure 3.1: ODCR signal for FIR wavelength of 163 μm. Transitions with hydrogen-like analogues are sharply defined (ie. $1s - 2p_+, 3p_+$). The splitting is due to central cell effects of different impurities. Low field, higher energy metastable transitions show broad profiles (310, 510 etc.). The free electron transition is at 4.41 T with enough resolution to show a spin-split peak.

3.3 Experimental results

3.3.1 Free electron cyclotron resonance

Free-electron cyclotron resonance energies for the eighteen different FIR frequencies used are collected together in Figure 3.2[a], a plot of the cyclotron energy, $E_{CR} = \hbar eB/m^*$, against resonant field position,B where m^* is the carrier effective mass. The data points lie on a curve resulting from the combined effect of polaron coupling and the band structure. Figure 3.2[b] shows the cyclotron mass, m^*, as a function of energy.

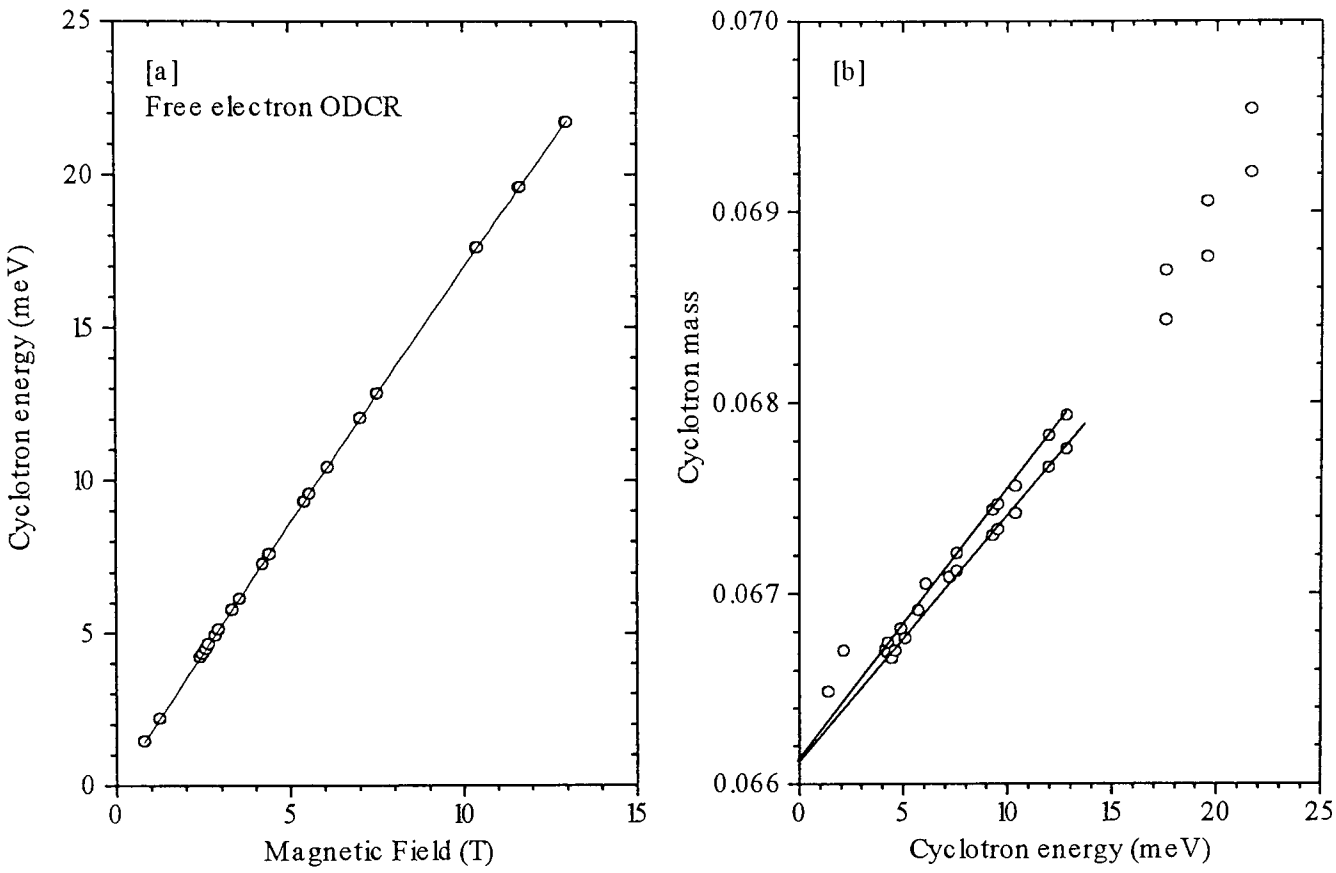

Figure 3.2: [a] Free electron cyclotron resonance energies as a function of field. The slightly non-linear slope is a consequence of polaron coupling and nonparabolic band structure. [b] Experimentally determined electron effective mass. The lines show a linear fit at low energies to determine the value(s) of K_2 (cf. text and [9]).

Extrapolated to B=0 T, the data gives an effective mass of $m_o^* = 0.0661 m_o \pm 0.0001$ which agrees well with a previous cyclotron resonance study of bulk GaAs by Hopkins *et al*[9]. These authors fitted the effective mass at low E_{CR} to

$$m^* = m_o^*[1 - \frac{2K_2}{E_g} E_{CR}] \tag{3.1}$$

with E_g the band gap and K_2 empirically determined from the slope of the energy-mass relationship. The data indicate K_2 values of -1.67 and -1.45, for the spin up and spin down transitions, slightly lower than the Hopkins data.

Spin splitting of the Landau levels, observable due to the energy dependence of the g-factor, becomes visible in our data at fields above 4.4 T. Following the work of Sigg *et al*[10] on the field dependence of splitting in GaAs, the magnitude of the spin-splitting is plotted against B^2 and shows excellent agreement with their result based on a five band k.p model. (Figure 3.3) This result will be used in Chapter 5 as evidence that spin splitting underlies anomalies seen in the cyclotron resonance spectra of $GaAs/Ga_{1-x}Al_xAs$ heterojunctions.

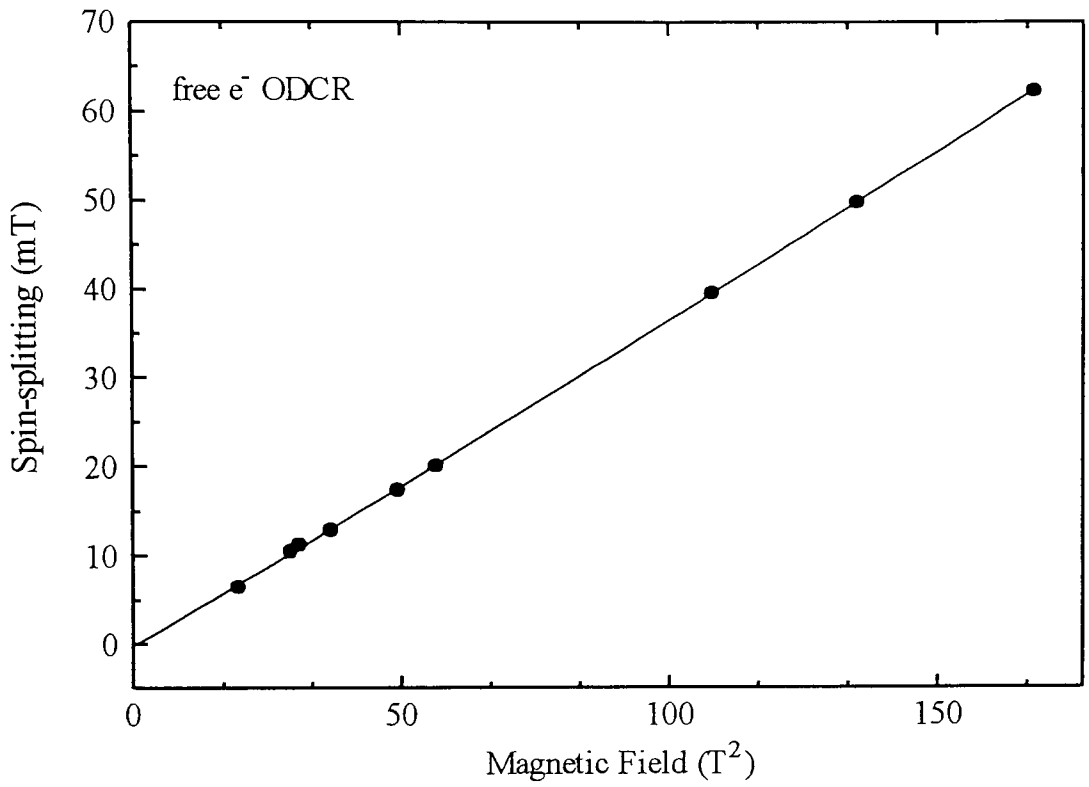

Figure 3.3: The splitting between the spin↑ and spin↓ free electron transitions follows a characteristic B^2 dependence. After Reference [10].

3.3.2 Low energy impurity transitions & central cell effects

In addition to the free electron cyclotron resonance, a full range of transitions was observed from the ground to excited states of shallow donor impurities present in the sample. In describing these transitions it is convenient to split them into two groups: those with low-field bound hydrogen-like analogues and those without, the latter being the previously mentioned metastable states. Experimentally, those transitions with hydrogen-like analogues appeared as sharp resonances, with a hyperfine separation caused by central cell effects of the different impurities present in the sample, while metastable states had broad resonance profiles. (Figure 3.4)

The experimental transition energies from the $1s$ ground state to the hydrogen-like states up to and including the $3p_+$ energy level were found to match the theoretical results of Makado and McGill through the intermediate field region. An effective rydberg R_y^* of 5.72 meV was used in the calculations. The energy of these resonances is plotted

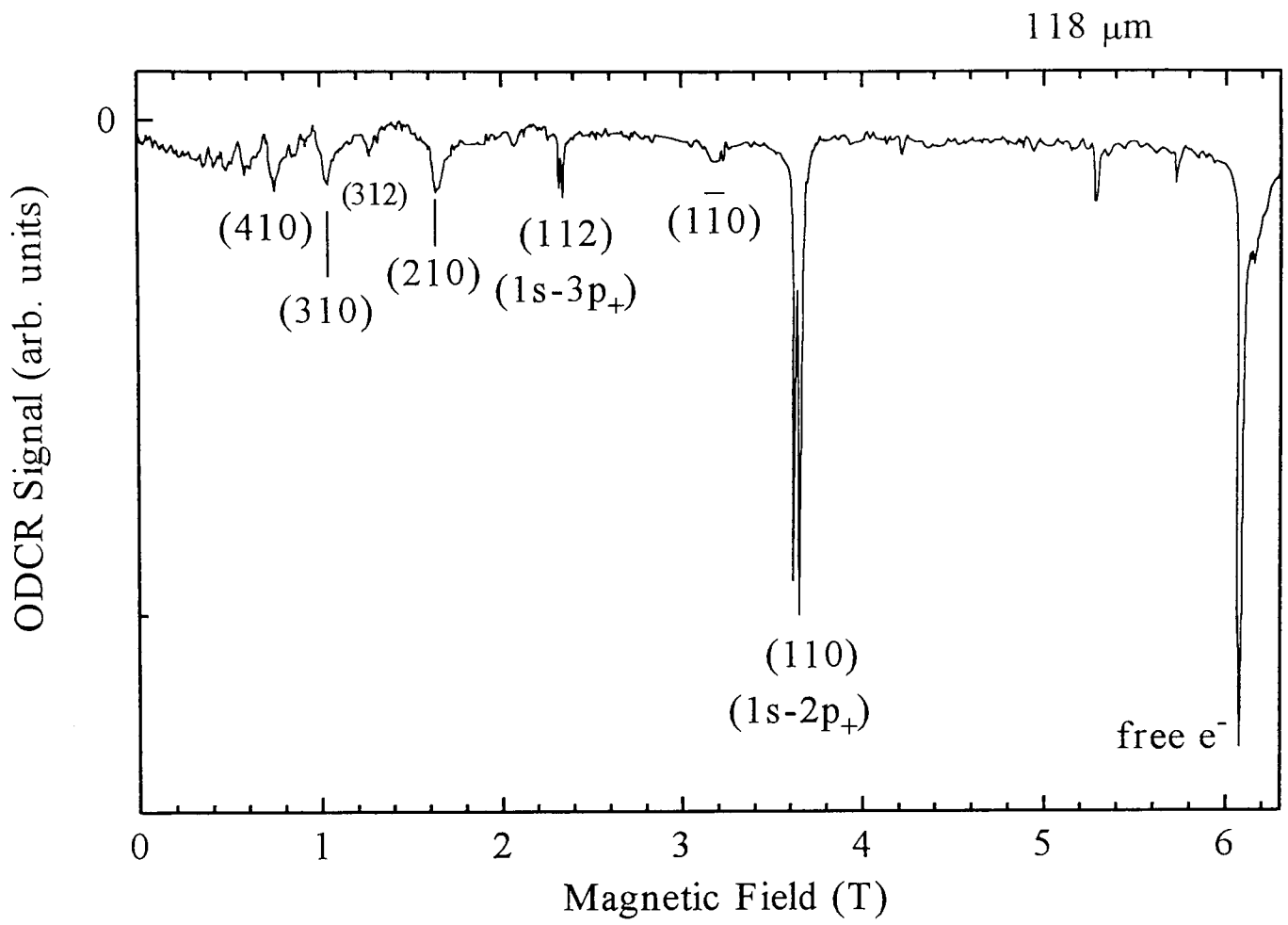

Figure 3.4: ODCR signal for FIR wavelength of 118 μm. Differences in hydrogen-like and metastable state signatures are apparent (cf. Figure 3.1).

as a function of field in Figure 3.5 with the solid lines representing the energy spectrum determined by the Makado and McGill analysis. The slight discrepancy between theory and experiment at high fields is caused by band nonparabolicity which was not considered in the Makado and McGill calculations.

The large number of incident frequencies coupled with high resolution of the ODCR technique provide a detailed picture of the central cell effects in this GaAs sample. Previous studies [11, 12] employed pressure to increase the resolution on transitions with steeper gradients and also used the lower energy transitions $1s - 2p_-$, $1s - 2p_o$, $1s - 3p_-$ and $1s - 3p_o$ whose flatter slopes served the same function. In the most extreme case, the small change in energy with increasing field on the $1s - 2p_-$ transition resulted in a 1.5 T wide split of the three chemically shifted resonances (Figure 3.6[a]). Pictured in Figure 3.6[b] is the $1s - 3p_+$ transition with laser wavelength of 163 μm. The three peaks are due to S, Sn/Se and Si donors present in the sample[8]. The lines are narrower than photoconductivity spectra obtained previously from high mobility MBE-

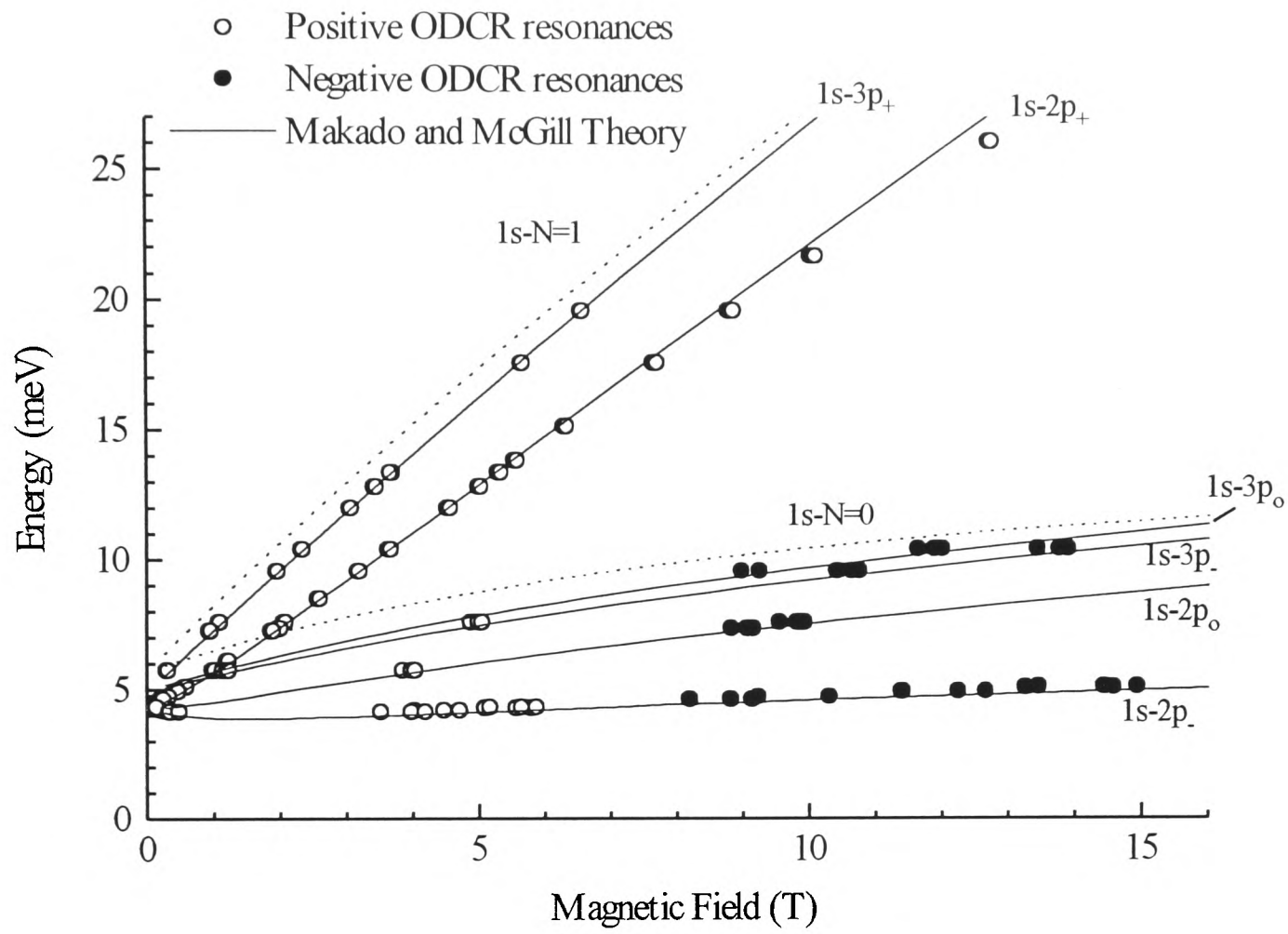

Figure 3.5: Transitions with hydrogen-like state analogues are fitted to the Makado and McGill theory which calculates the energy spectrum of a hydrogen atom in a large magnetic field. An effective Rydberg of 5.72 meV was used in the calculation. Central cell shifts of different impurities are resolved as repeating groups of triplets especially on the flatter lower energy transitions. Also shown are the predicted energy levels of the $1s - N = 0, 1$ Landau level transitions.

grown n-GaAs, an indication of the purity and highest ever recorded peak mobility of this sample.

3.3.3 High energy impurity transitions

In addition to lower energy transitions of the bound hydrogen-like states, shallow donor transitions to metastable states were also observed (cf. Figure 3.1 and 3.4). The hyperfine separation of peaks due to central cell corrections of different donors is absent as the energy levels of the final metastable states are considerably broader than the hydrogen-like bound states. ODCR spectra of these low field features is equivalent or better than photoconductivity traces taken with the same sample or ones of comparable quality [2, 4]. More importantly, the troublesome adjustment of sample voltage bias is

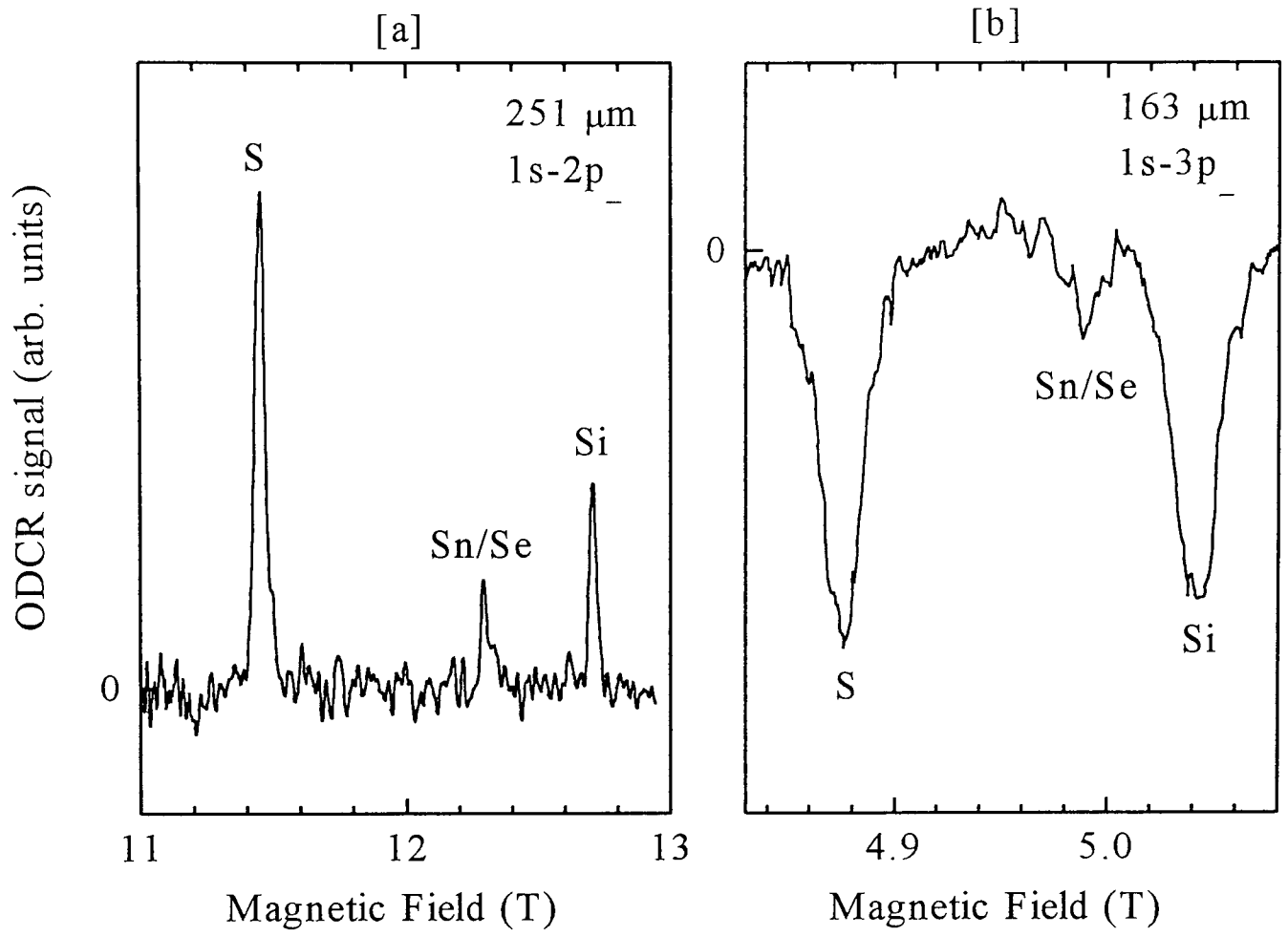

Figure 3.6: [a] $1s - 2p_-$ transition for 251 μm. The flat slope of the transition at high fields results in chemical shifts due to S, Sn/Se and Si donors being spread over 1.5 T. [b] $1s - 3p_-$ transition for 163 μm. Even for transitions with much steeper energy vs. field gradients, the high resolution of the ODCR technique enabled observation of central cell effects. The discrepancy in linewidth between the two figures is due to the larger extent in real space of the $3p_+$ wavefunction relative to the $2p_-$ state. [a] represents a positive ODCR signal and [b] a negative ODCR signal (cf. Section 3.4).

eliminated with ODCR.

In Figure 3.7 the experimentally observed transitions to final states above the $1s - 3p_+$ impurity level are given. The solid lines are taken from the Klarenbosch *et al*[2] photoconductivity study which labels energy levels following the Simola and Virtamo analysis[6]. No (200) or $(2\bar{2}0)$ metastable states were seen. This is consistent with the hypothesis of Klarenbosch *et al*[2] that above band gap radiation decreases the number of ionized impurities and thereby minimizes the mixing of electron states (210) and $(2\bar{1}0)$ responsible for the formation of the (200) and $(2\bar{2}0)$ states. Klarenbosch *et al*[2] use band gap radiation as an additional check on the identification of transitions. In our case, above band gap radiation is inherent in the ODCR system to excite the PL.

For FIR wavelengths 70 and 118 μm, a high field tail to the free electron cyclotron

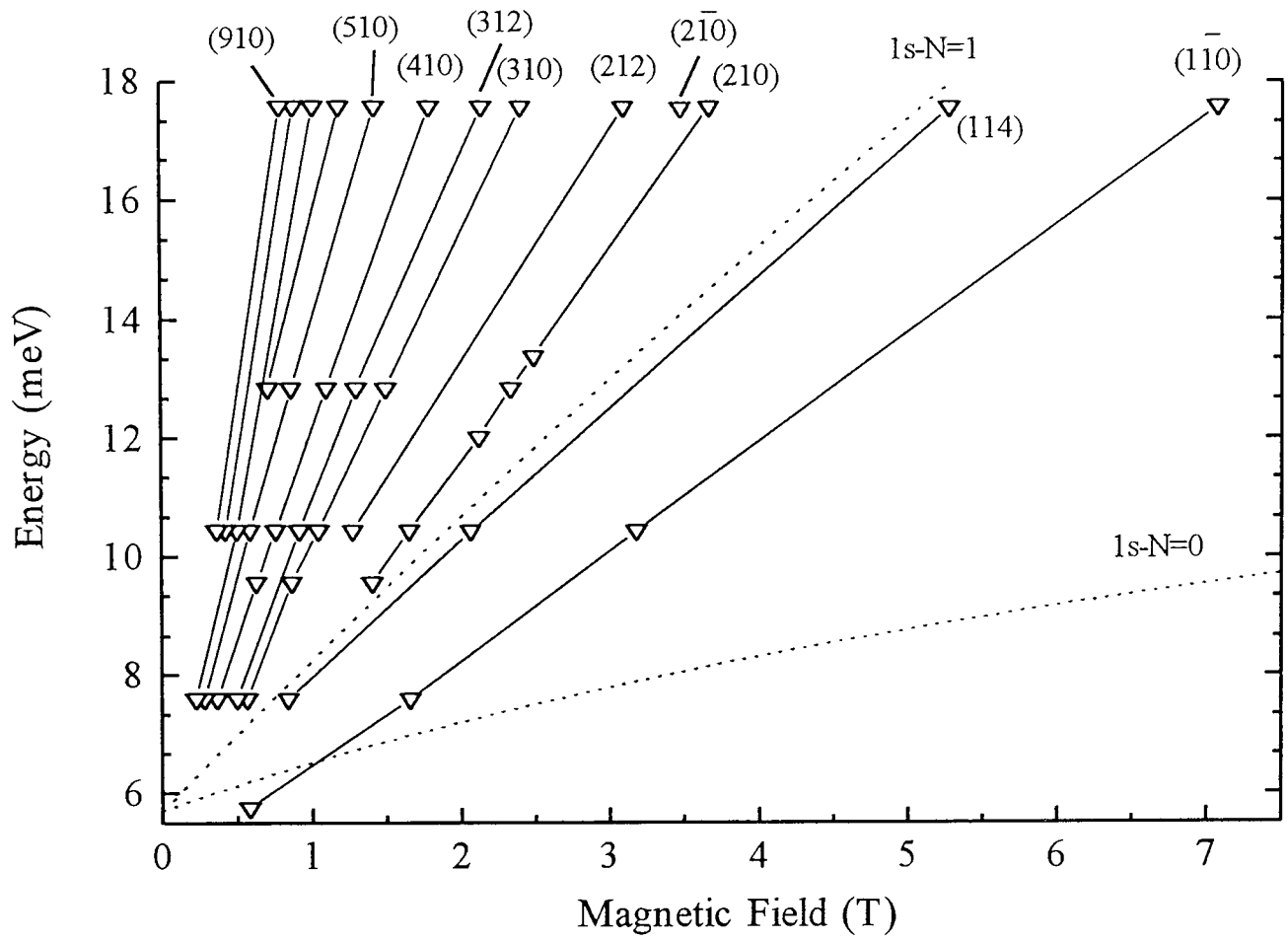

Figure 3.7: Transitions to states lying above the $1s - 3p_+$ impurity level. Solid lines are fits following the analysis of Simola and Virtamo[6].

resonance peak was seen (Figure 3.8). These have been observed previously in both ODCR[13, 14] and photoconductivity spectra[15] taken with strong incident FIR power and temperatures above 4 K. Following the analysis of Hawksworth *et al*[15] it is reasonable to assign these resonances as transitions from the $N = 0$ Landau level to metastable states. The broad shape is characteristic of a metastable transition and ODCR spectra match the photoconductivity trace, despite our colder base temperature which limited observation of such states in the Hawksworth experiment.

Despite the large magnitude of the $1s-2p_\pm$ impurity resonances, no transitions involving the D^- state were observed. The D^- is the analogue of H^-; for GaAs it has an effective Rydberg 5.5% of the Rydberg for the neutral donor. $D^- - N = 0$ LL transitions have been reported by Grimes *et al* among others, in recent photoconductivity studies as lying lower in field than the cyclotron resonance transition ([16] and references therein). The lack of D^- states probably results from neutralization of ionized donors by the visible laser radiation.

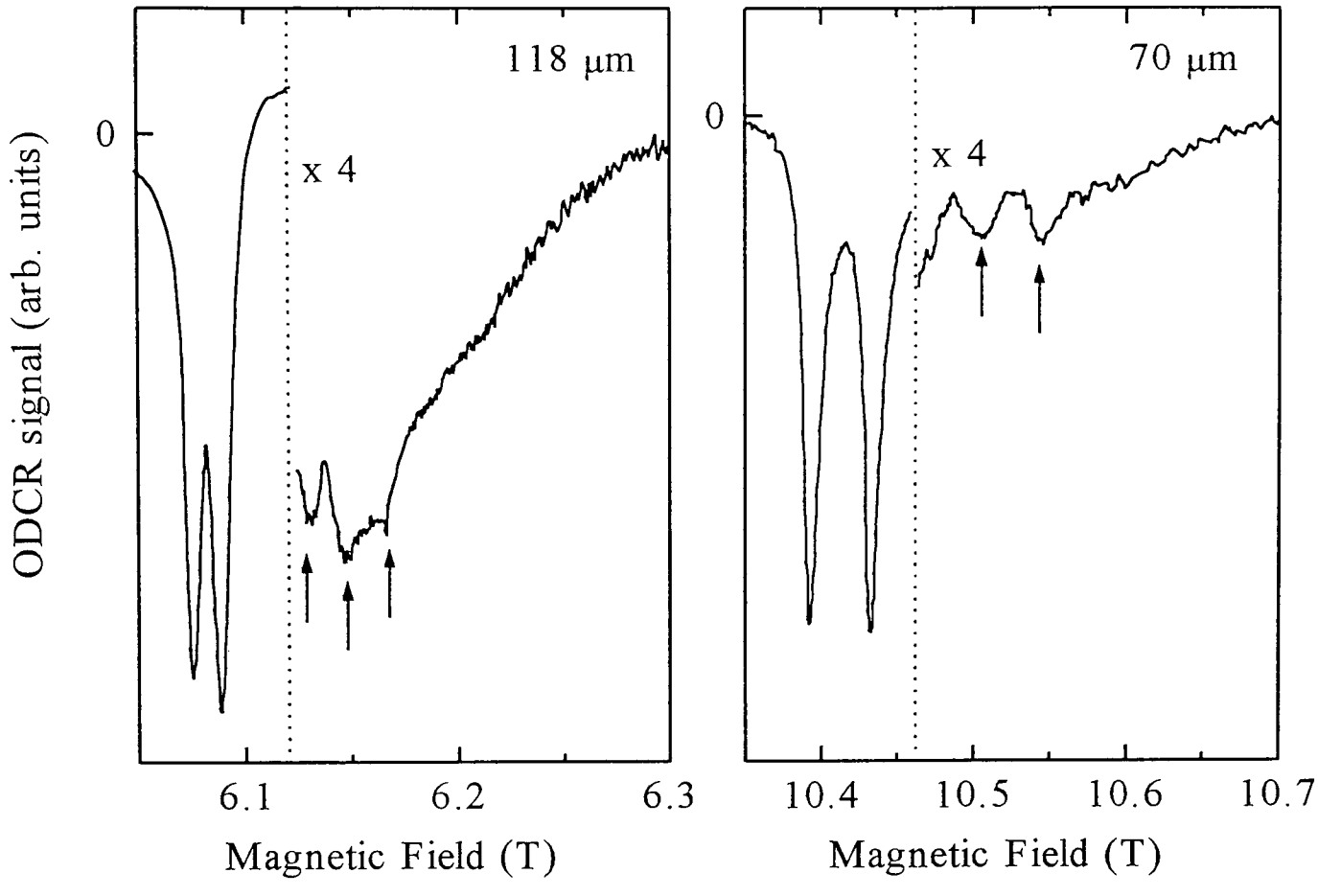

Figure 3.8: Transitions to metastable states from the $N = 0$ Landau level are visible in the tail of the free electron resonance for FIR wavelengths of 118 and 70 μm.

3.4 Mechanisms underlying ODCR

There are two distinct processes taking place simultaneously in an ODCR experiment: PL produced by the above band-gap radiation and absorption of the incident FIR radiation as in a standard CR experiment. The FIR radiation, from $4 - 25$ meV, results in donor-bound *electrons* being excited to higher energy levels. Detection of these transitions occurs through changes in the PL intensity which involves recombination of *excitons* bound to donor/acceptor sites at energies of ~ 1.5 eV. It is worth noting that all the observed resonances with the FIR energy were free or donor-bound single electron transitions rather than transitions within an excitonic complex. This is perhaps not surprising as excitons created by the visible laser illumination number much less than residual impurity electrons. The calculation that determines this is straightforward: 3 mW of diode illumination equals a power density of $4.2\,\mathrm{mW/cm^2}$ assuming a factor of ten loss in coupling to the fiber. An arreal population of 1.42×10^{16} photons $\mathrm{sec^{-1}\ cm^{-2}}$ is created. Given a penetration depth of 0.25μm and a 100 ns lifetime, this

results in a steady state exciton population of $\sim 5 \times 10^{13}\text{cm}^{-3}$ which is an order of magnitude below the estimated doping level.

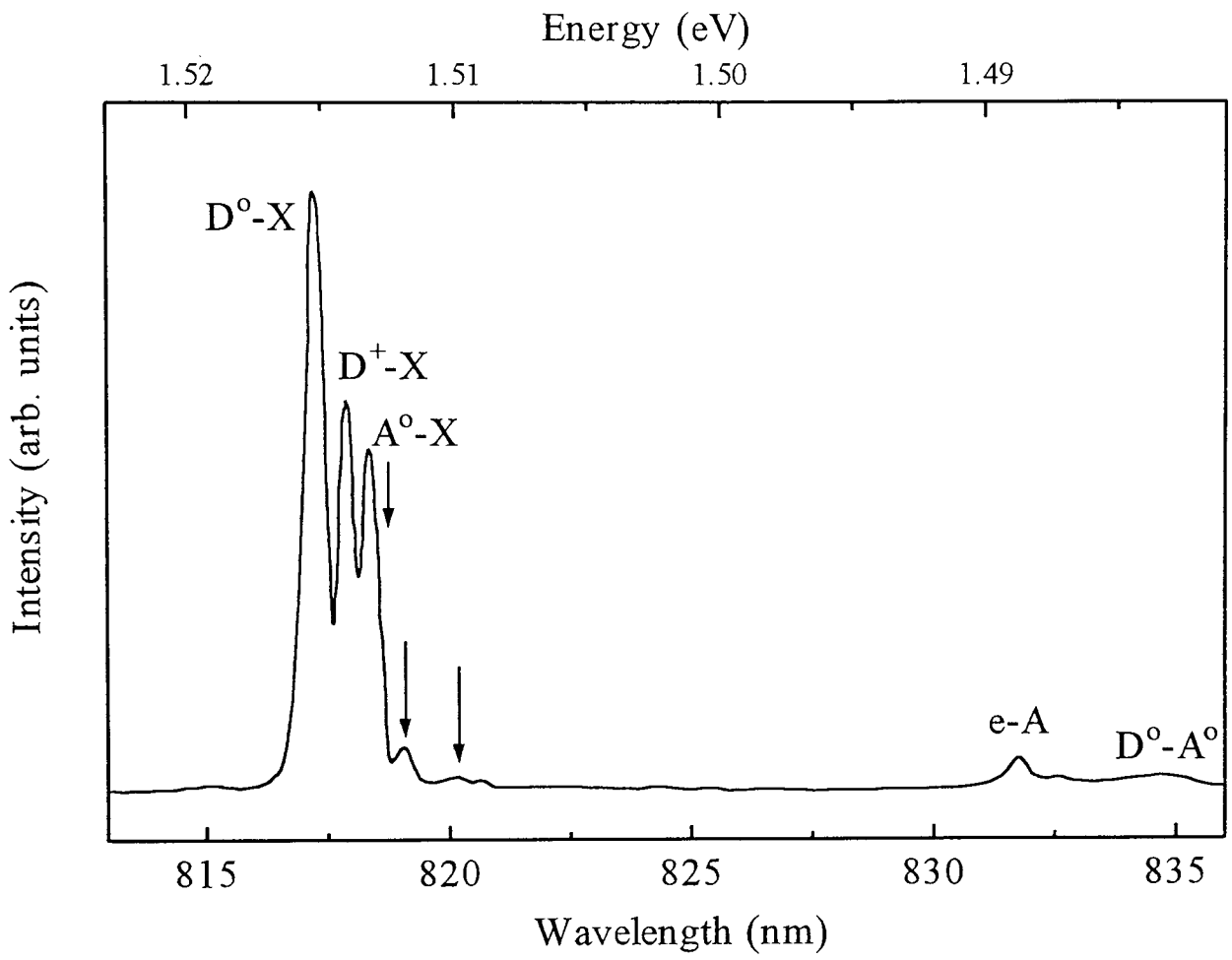

Figure 3.9: The PL spectrum of bulk GaAs taken at $B = 0$. The three arrows mark different rotational states of transitions involving excitons bound to neutral acceptors.

Since detection of the electron resonances is inextricably linked to the luminescence, it is necessary first to try to provide a qualitative description of the luminescence mechanism in bulk GaAs. PL measurements were taken over a range of magnetic fields and temperatures to aid in this process. Figure 3.9 shows the zero field, 2.2 K PL spectrum with the different transitions labelled. Peaks due to the radiative dissociation of excitons bound to neutral and ionized donors and acceptors (D^o, X), (D^+, X), (A^o, X) respectively, are prominent. Less intense are peaks due to free exciton recombination (X) and the free electron-neutral acceptor (e, A^o) /neutral donor-acceptor (D^o, A^o) complex at longer wavelengths[8][17]. The (D^+, X) complex is often is represented as (D^o, h), a hole binding to a neutral donor, which is an excited state representation of the (D^+, X) system.

A study by Bimberg *et al*[18] on the kinetics of recombination in GaAs indicates that excitonic creation is extremely rapid and essentially instantaneous on the scale of bound

excitonic lifetimes. Time-resolved luminescence studies show prominent free exciton and (D^o, X) peaks after pulses as short as 2 ns. Striking enhancement of donor-related photoluminescence has also been observed when the excitation energy lies just below the band gap, consistent with excitation of the free excitons[19]. Exciton capture then represents the dominant mechanism for (D^o, X) creation[20]. Formation of neutral acceptor complexes, however, is determined by the initial capture of holes by ionized acceptors, $A^- + h^+ \rightarrow A^o$; resulting in the neutral acceptor state to which the exciton then binds. This capture of minority charge carriers by ionized impurities is relatively slow when compared to formation of donor bound excitons.

The relative probability of binding to an ionized impurity depends on the effective mass ratio of electrons and holes; $\sigma = m_e^*/m_h^*$; if $\sigma < 0.38$ stable binding to ionized donors, (D^+, X) occurs[21]. GaAs meets this requirement with $m_e^* \ll m_h^*$ but the hole is considered to be very weakly bound. This complex competes with ionized acceptors for capture of holes, which generally disappear quickly due to their large capture cross-section[18][22].

The sample was heated up to $\sim 20\,\mathrm{K}$ in an attempt to increase emission of the free exciton luminescence. While the relative proportion of free exciton PL was increased, total luminescence intensity was drastically reduced, with the different recombination processes affected unevenly. In the temperature region from 2 to 12 K, a rapid decrease of the intensity of the (D^o, X) line with increasing temperature was accompanied by an increase in the free electron-acceptor (e, A^o) peak. These results are consistent with an earlier study [23] whose authors attributed differing behavior of the two transitions to an Auger-like process where (D^o, X) non-radiative dissociation results in promotion of the 'donor' electron up into the conduction band. Although the dominance of non-radiative processes in direct gap materials like GaAs has since been called into question [24], the temperature data indicates a strong link between the efficiency of (D^o, X) formation and the number of free electrons as signified by the strength of the (e, A^o) line. Failure to increase the amount of free excitonic recombination and the overall reduced levels of luminescence at higher temperatures led us to take all ODCR spectra at 2.2 K.

An applied magnetic field increases the complexity of luminescence originating from ex-

citons bound to impurities. The problem is similar to that of a single electron subjected to simultaneous Coulomb and magnetic forces discussed earlier, except that the exciton replaces the single carrier orbiting the donor complex. The energy spectrum of bound excitons is similarly quantized with selection rules governing the allowed transitions. Attempts to model the observed intensities of bound excitonic transitions in magnetic fields have characterized the binding energy between exciton and donor as a combination of existing theories for the H^- and H_2 hydrogen atom. In the former, the electron orbit will be smaller than the hole orbit and the two electrons can be assumed to pair in the $1s$ state of the donor, with the 'excitonic hole' some distance away; while the latter envisions the donor and exciton as two interacting H atoms[25][26]. Magneto-photoluminescence studies of GaAs have primarily attempted to separate transitions due to the presence of different donors[27] and identify the origin of satellite luminescence spectra[28]. In the present study, the spectrometer slit width was coarse when compared with these high resolution PL experiments. Nonetheless, changes in the spectra with field are attributable to reductions in the efficiency of bound excitonic creation and shifts of the underlying excitonic structure.

Figure 3.10 shows the effect of increasing field on the intensities of the (D^+, X), (A^o, X), $(e - A^o)$ and $(D^o - A^o)$ transitions relative to (D^o, X) intensity. A field strength of 13 T results in $\sim 70\%$ of the total integrated PL intensity being due to (D^o, X) dissociation, with little contribution from the other lines. The quenching of the (D^+, X) transition could be explained by the magnetic field limiting the extent of the donor wavefunction and increasing the binding energy. This would reduce the concentration of D^+ ions by increasing the probability of electron capture to a D^o state[29]. It is not as clear why the (A^o, X) transition diminishes in intensity at these high fields. Spectra taken by Driessen *et al*[28] on high purity GaAs samples show similar intensities of the (D^o, X) and (A^o, X) peaks at 7 T, although a direct comparison is difficult because of their use of selective line pumping. Formation of the exciton acceptor complex is dependent on the ability of ionized acceptors to capture free holes which, in turn is heavily dependent on the compensation ratio. The relatively low compensation ratio expected for a sample of this quality may explain the discrepancy as most of the available holes would be already bound to donors.

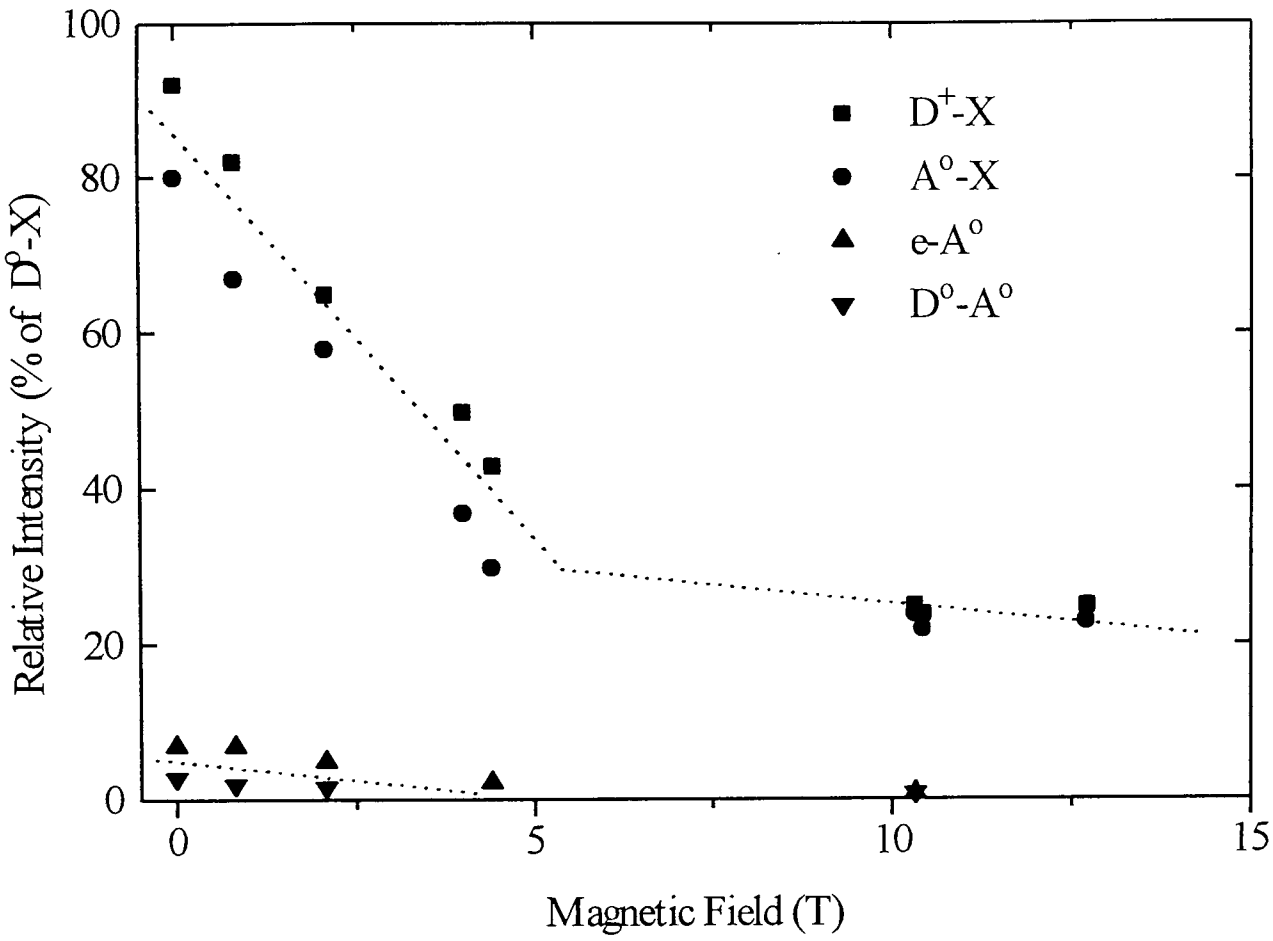

Figure 3.10: An increase in the magnetic field sharply decreases the intensity of the $(D^+ - X)$, $(A^o - X)$, $(e - A^o)$ and $(D^o - A^o)$ transitions *relative* to the $(D^o - X)$ transition. At fields above 10 T, 70% of the total integrated intensity is a consequence of the $(D^o - X)$ transition.

Absorption of the FIR may be viewed as a significant perturbation on this complex luminescence mechanism. ODCR resonances were classed as **negative** if the FIR resulted in a decrease of the PL intensity and **positive** if the PL intensity was increased at resonance. The free electron, higher energy impurity transitions (i.e. $m = +1, +2, etc.$) and transitions to metastable states all resulted in negative resonances. Lower energy impurity transitions (i.e. $m = 0, -1$) switched from producing a negative to positive ODCR signal at fields above 8 T. This phenomenon has not been reported in other ODCR studies. Negative and positive ODCR resonance signals are marked in Figure 3.5.

Most of the ODCR data was taken with a wide slit setting and the spectrometer centered on the luminescence due to excitonic recombination. This eliminated changes in PL intensity due to the diamagnetic shift and provided ample luminescence signal. It did not differentiate between different luminescence transitions; a negative ODCR signal results from a net decrease of the total PL with FIR illumination. Comparison of

the PL and IMPL traces, however, indicates how the FIR radiation impacts on the intensities of the differing PL transitions.

Figure 3.11 shows the PL and IMPL signals at the resonance field of the $1s - 2p_+$ transition for a FIR wavelength of 163 μm. Intensity of the (D^o, X), (D^+, X) and (A^o, X) complexes is sharply reduced when illuminated by the FIR. Attenuation of the PL intensity originating in this triplet of peaks often approached 50% under resonant conditions. An increase in PL intensity is observed for the free electron to acceptor transition, (e, A^o), at longer wavelengths. The increase in PL intensity for this transition is contrary to the findings of Wright *et al*[13] in their ODCR study of bulk GaAs but agrees with a parallel study by Moll *et al*[30]. The IMPL spectrum in Figure 3.11

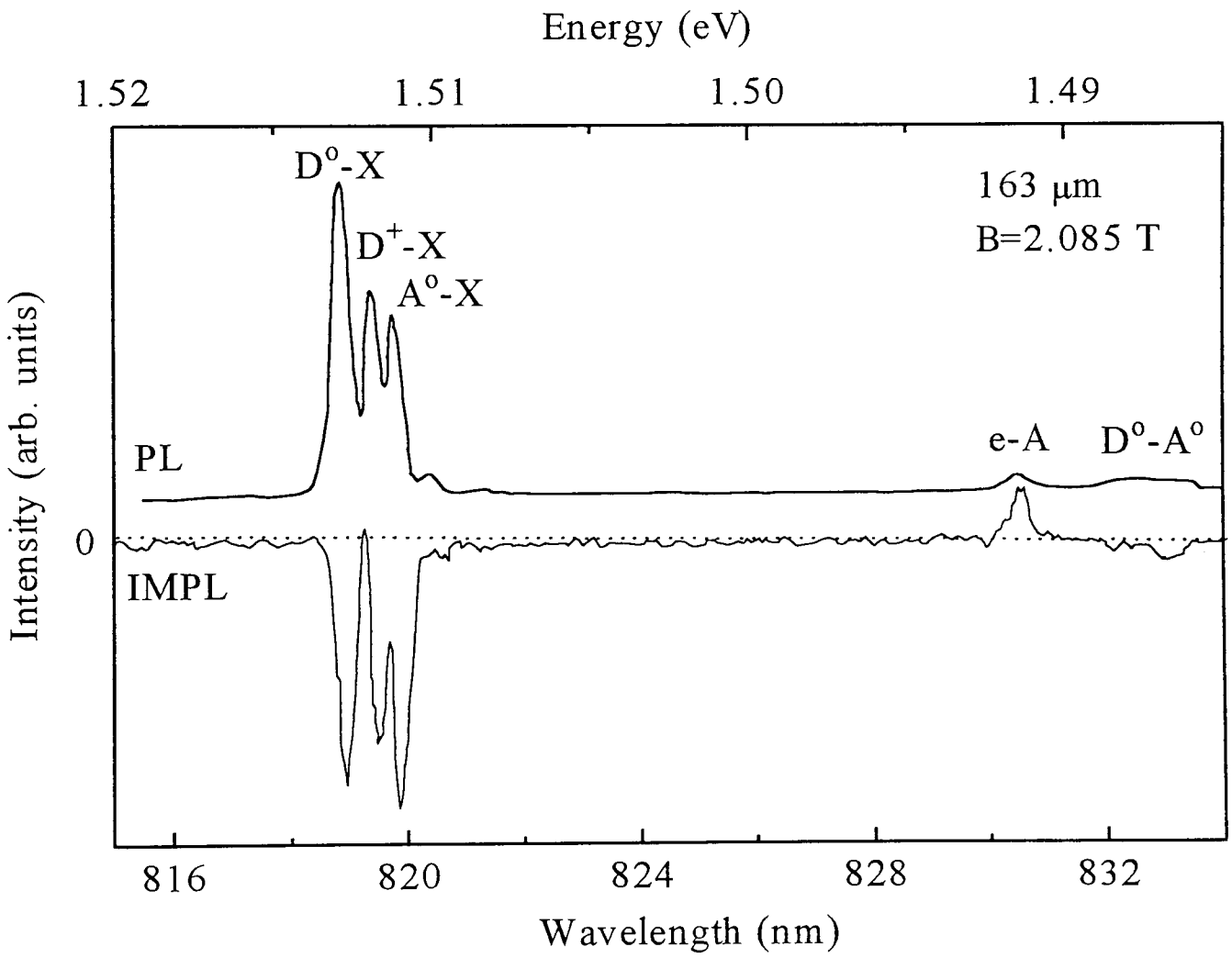

Figure 3.11: PL and IMPL traces for FIR wavelength of 163 μm taken at 2.085 T which corresponds to the $1s - 2p_+$ transition. The FIR radiation strongly attenuates the transitions involving bound excitons and the $(D^o - A^o)$ complex. An increase in the $(e - A^o)$ line indicates a greater number of electrons in the conduction band.

illustrates the principal mechanism at work in optically detected cyclotron resonance: donor electrons, excited by the FIR from the ground $1s$ level into higher impurity states, have an increased probability of being ejected into the conduction band by absorption of

phonons[31]. A greater number of free electrons will suppress the formation of excitons and increase the impact ionization process whereby an electron knocks the remaining bound excitons off their donor sites. This results in a decrease of the PL due to bound excitons. There is a visible enhancement of the (e, A^o) transition, signifying an increase in the number of conduction band electrons.

Support for this contention comes from photoconductivity measurements, where a current increase across a sample is seen at field values corresponding to impurity transitions [32, 33]. A luminescence study monitoring the influence of 10.6 μm radiation on edge luminescence in n-GaAs, attributed quenching of transitions involving both donor and acceptor bound excitons to the liberation of electrons and holes from their respective impurity centers by the near infra-red radiation[34]. Additional evidence is provided by luminescence intensity measurements as a function of electric bias voltage[35], which showed similar changes in individual peak intensity to those observed in the present study and indicated that weakly bound excitons are first to be ionized when the field strength is increased.

As noted earlier, high energy impurity transitions continue to give a negative ODCR signal throughout the field range, while lower energy impurity transitions produce positive ODCR signal above 8 T. I believe the cause for the changeover is twofold: Firstly, the magnetic field increases the magnitude of the (D^o, X) transition relative to the other excitonic transitions (cf. Figure 3.10). Changes to the (D^o, X) complex therefore more heavily influence the ODCR signal at higher fields. Secondly, the increase in field suppresses the photothermal ionization of carriers from lower lying impurity levels up to the conduction band. This has been shown in far-infrared photoresponse studies of high purity InP [36] and GaAs [37] where the application of field results in extremely long lifetimes of carriers confined in lower lying impurity states like the $2p_-$.

It is possible that carriers which are stuck in these 'bottleneck' states could lead to the formation of donor bound excitons directly in excited states. For example, a donor with its electron confined to the $2p_-$ level would capture an exciton and result in a state which could be labelled (D_{2p_-}, X). These excited donor bound excitons would provide the specific mechanism that results in the observed positive ODCR signals at

higher field. The larger extent of the donor electron wavefunction when excited by the FIR into a higher impurity state would increase the donor capture cross section and subsequent probability of exciton capture. An increase in luminescence intensity with FIR radiation would then be expected at high fields when the photothermal effect is only weakly operative. Additionally, the 'Auger'-like process used to explain the temperature dependence of luminescence peak intensity[23], could also contribute to the changeover from negative to positive ODCR signal. Interactive processes like the Auger effect, are usually confined to materials with extremely high carrier concentrations but in the case of an exciton bound to a neutral donor, the three required carriers are confined to the region surrounding the donor. The increasing size of the donor electron wavefunction with FIR illumination would also serve to weaken the overlap between the 'exciton hole' and 'donor electron'. The probability of the non-radiative 'Auger' process would be decreased leading to more radiative recombination and thus more luminescence.

The presence of excited donor bound exciton states with FIR illumination might be expected to slightly shift the luminescence recombination energy. The limit of maximum excitation of the donor electron to higher impurity states would be the (D^+, X) transition, where the exciton binds to a donor whose electron has been ionized. Evidence for excited donor bound exciton states would therefore occur in the portion of the (D^o, X) line which adjoins the (D^+, X) peak. Under FIR illumination, the excited donor bound exciton states would be expected to increase their radiative recombination, while the standard donor bound exciton line might slightly decrease due to the weakened photothermal effect. This is exactly what we observe. Pictured in Figure 3.12 are the PL and IMPL signals corresponding to the $1s - 2p_+$ resonance for 47 μm at 12.7 T. For the (D^+, X) and (A^o, X) peaks there is a direct correspondence between the PL and IMPL trace. The IMPL signal for the (D^o, X) transition, however, shows a positive signal close to the (D^+, X) peak and a slightly negative signal at shorter wavelengths. IMPL spectra of the lower energy $1s - 2p_-$ resonance for 251 μm (Figure 3.13) reveals only a positive (D^o, X) contribution to the ODCR signal. This again illustrates the role that lower lying donor states have in the process of excitonic recombination.

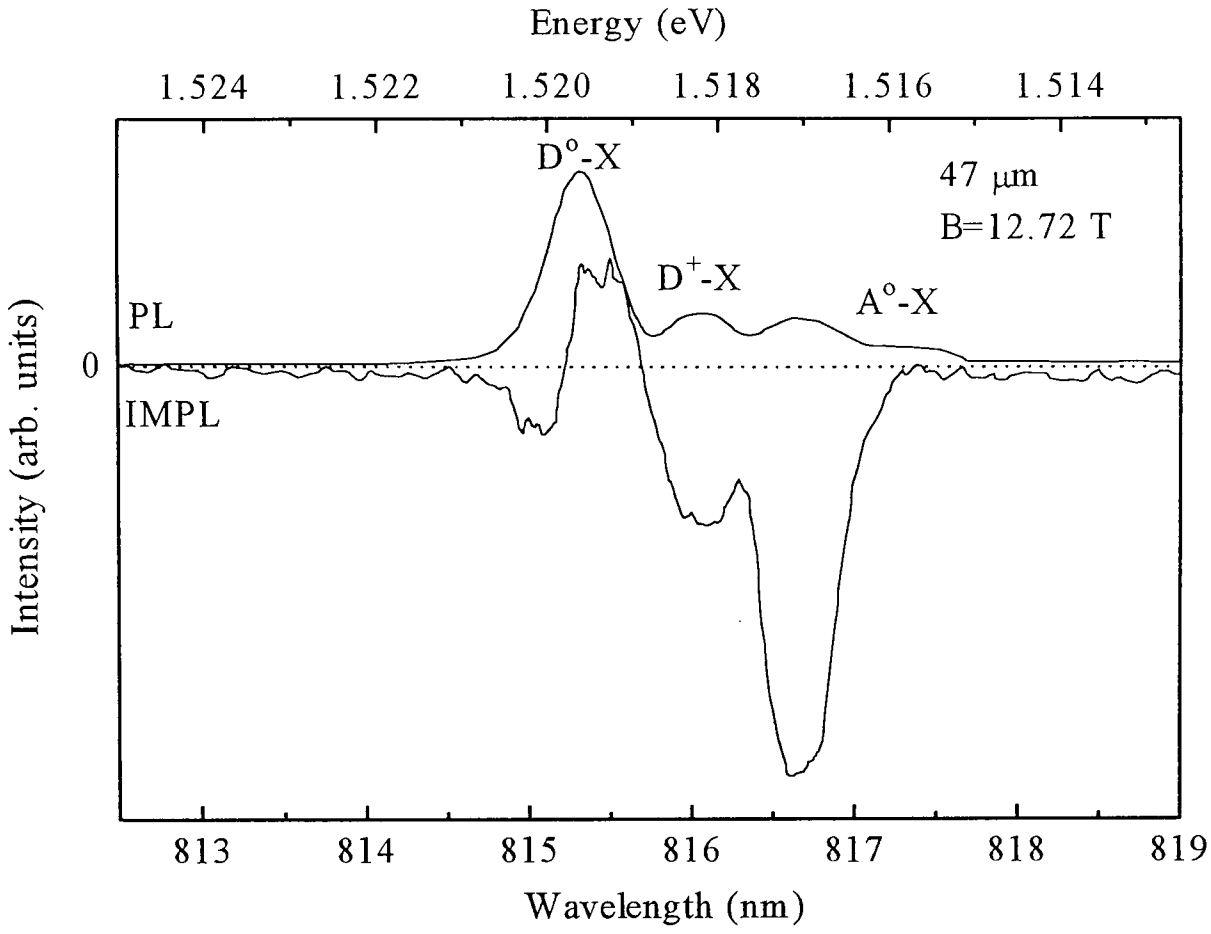

Figure 3.12: PL and IMPL traces for FIR wavelength of 47 μm taken at 12.72 T which corresponds to the $1s - 2p_+$ transition. FIR radiation attenuates the $(D^+ - X)$ and $(A^o - X)$ lines but has a differential effect on the $(D^o - X)$ transition.

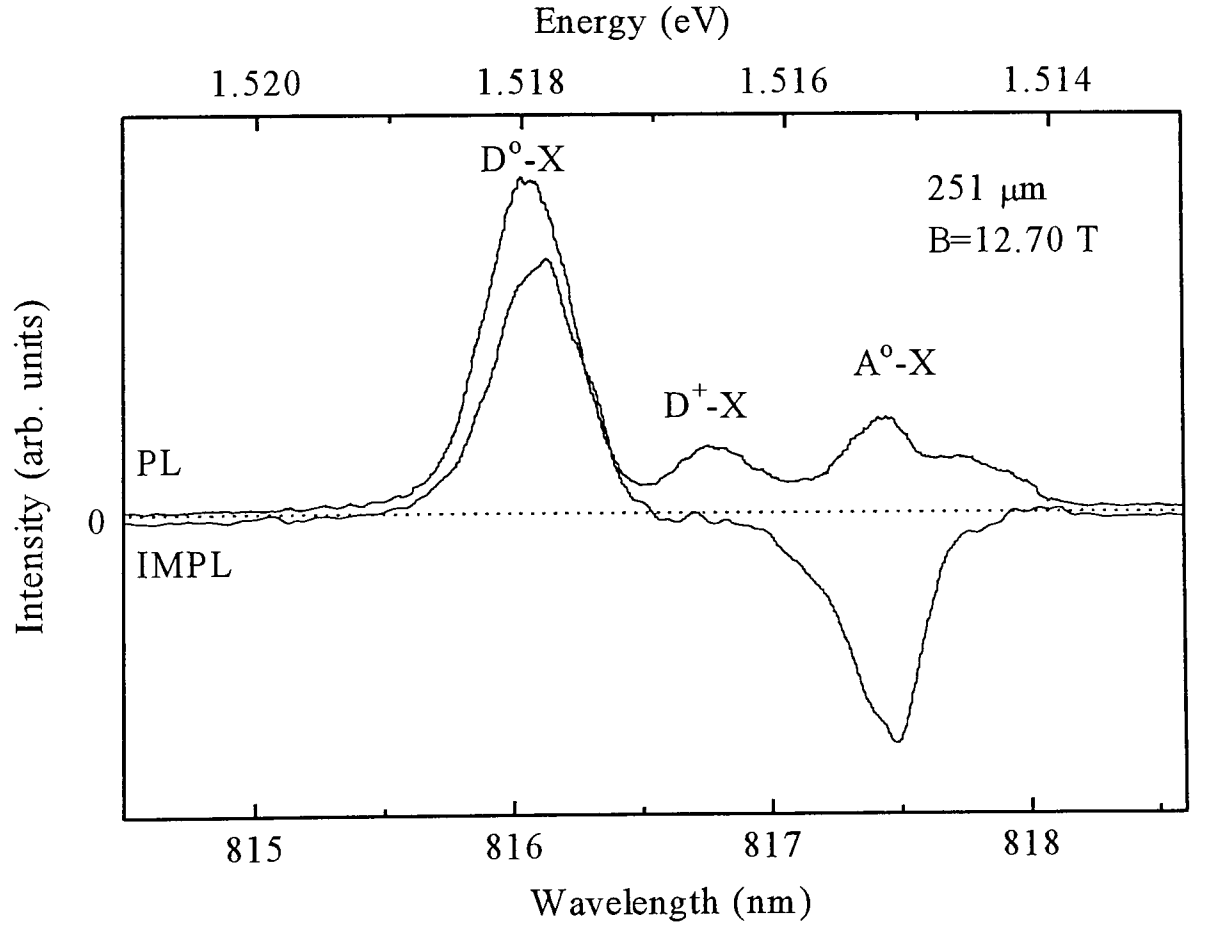

Figure 3.13: PL and IMPL traces for FIR wavelength of 251 μm taken at 12.703 T which corresponds to the resonant position of the Silicon impurity $1s - 2p_-$ transition. FIR radiation results in an enhancement of $(D^o - X)$ intensity but reduces the radiative recombination of the $(D^+ - X)$ and $(A^o - X)$ lines. An ODCR trace of this lower energy impurity resonance taken with wide slits, would produce an overall positive signal.

Differential-like IMPL signals have been previously observed in GaAs/AlGaAs quantum wells[38] and heterostructures[14][39]. Ahmed *et al* ascribed the positive portion to resonant heating of free carriers, thereby increasing free exciton and decreasing (D^o, X) emission. No increase in free exciton emission is observed in our data or in their bulk GaAs spectra[14], casting doubts on the validity of this hypothesis.

3.5 Conclusions

Optically detected cyclotron resonance has been performed on a high quality sample of bulk GaAs. Experimentally, ODCR is shown to be a viable experimental technique for free electron mass determination and impurity studies. Transitions from the impurity ground state to excited states with hydrogen-like analogues are described well by the energy levels predicted by Makado and McGill. Chemical shifts to these impurity levels due to different donors in the sample are completely resolved at full field. Metastable states exist, appearing as broad-shaped resonances, and are fitted using an existing theory. The ODCR signal is shown to be primarily due to the photothermal effect where larger numbers of electrons are freed by FIR illumination from donor sites into the conduction band. This increases the impact ionization of bound excitons and results in a decrease of luminescence intensity due to excitonic recombination and a corresponding increase in free electron related luminescence. At higher fields, a complex interaction between donor electrons and the donor bound exciton energy spectrum results in an enhancement of a portion of the (D^o, X) PL transition.

3.6 References

[1] P.C. Makado and N.C. McGill, J. Phys. C: Solid State Phys. **19**(1986)873-885.

[2] A. v.Klarenbosch, T.O. Klassen, W. Th. Wenckebach and C.T. Foxon, J. Appl. Phys. **67**(1990)6323

[3] H.P. Wagner and W. Prettl, Solid State Commun. **66**(1988)367

[4] C.J. Armistead, R.A. Stradling and Z. Wasilewski, *Semicon. Sci. Tech.* **4**, 1989 (557-564).

[5] R.T. Grimes, M.B. Stanaway, J.M. Chamberlain, M. Henini and O.H. Hughes, Semiconductor Sci. and Technol. **4** (1989)548

[6] J. Simola and J. Virtamo, J. Phys B: Atom. Molec. Phys. **11**(1978)3309

[7] P.E. Simmonds, J.M. Chamberlain, R.A. Hoult, R.A. Stradling and C.C. Bradley, J. Phys. C: Solid State Phys. **17**(1974) 4164

[8] C.R. Stanley, M.C. Holland and A.H. Kean, Appl. Phys. Lett. **58**(1991)478

[9] M.A. Hopkins, R.J. Nicholas, P. Pfeffer, W. Zawadzki, D. Gauthier, J.C. Portal and M.A. DiForte-Poisson, Semicond. Sci. Technol. **2**(1987) 568-577.

[10] H. Sigg, J.A.J. Perenboom, P. Pfeffer and W. Zawadzki, Solid State Commun. **61**(1987)685

[11] Z. Wasilewski and R. A. Stradling, Semicond. Sci. Technol. **1** (1986)264-274.

[12] S.R. Holmes, C.C. Phillips, R.A. Stradling, Z. Wasilewski, R. Droopad, S.D. Parker, W.T. Yuen, P. Balk, A. Brauers, H. Heinecke, C. Plass, M. Weyers, T. Foxon, B.A. Joyce, G.W. Smith and C.R. Whitehouse, Semicond. Sci. Technol., **4**(1989)782-90

[13] M.G. Wright, N. Ahmed, K. Mitchell, A. Koohian, C.R. Pidgeon, B.C. Cavenett, C.R. Stanley and A.H. Kean, Semicond. Sci. and Technol. **5** (1990)438-441.

[14] N. Ahmed, I.R. Agool, M.G. Wright, K. Mitchell, A. Koohian, S.J. Adams, C.R. Pidgeon, B.C. Cavenett, C.R. Stanley and A.H. Kean, Semicond. Sci. Technol. **7**(1992)352.

[15] S.J. Hawksworth, R.T. Grimes, E.P. Pearl, M.B. Stanaway, J.M. Chamberlain, J.L. Dunn, C.A. Bates, S.P. Najda, C.J.G.M. Langerak, J. Singleton and C.R. Stanley, Semicond. Sci. Technol. **7**(1992)1499-1503.

[16] R. T. Grimes, M. B. Stanaway, K. Singleton, C.J.G.M. Langerak, J. M. Chamberlain, C. R. Stanley and T. Cheng, Inst. Phys. Conf. Ser. No. 112:Chapter 4. 1990.

[17] U. Heim and P. Hiesinger, Phys. Stat. Sol. B **66**(1974)461.

[18] D. Bimberg, H. Munzel, A. Steckenborn and J. Christen, Physical Review B **31**(1985)7788.

[19] S. Zemon and G. Lambert, Solid State Commun. **70**(1989)855.

[20] C. J. Hwang, Phys. Rev. B **8**(1973)646.

[21] J. J. Hopfield, in *Proc.* 7^{th} *Int. Conf. Phys. Semicond.*, edited by Dunod, (Paris, 1964)725.

[22] T. Tomaru, T. Ohyama and E. Otsuka, Phys. Rev B. **46**(1992)9390.

[23] H. B. Bebb and E. W. Williams, in *Semiconductors and Semimetals 8*, edited by R. K. Willardson and A. C. Beer (Academic, New York, 1972), p. 182.

[24] C. J. Hwang and L. R. Dawson, Solid State Commun.**10**(1972)443.

[25] J. Rorison, D. C. Herbert, P. J. Dean and M. S. Skolnick, J. Phys. C:Solid State, **17**(1984)6435.

[26] P. J. Dean and M. S. Skolnick, J. Appl. Phys. **54**(1983)346.

[27] T. D. Harris, M. S. Skolnick, J. M Parsey, Jr. and R. Bhat, Appl. Phys. Lett. **52**(1988)389.

[28] F.A.J.M. Driessen, H.G.M. Lochs, S. M. Olsthoorn and L. J. Giling, J. Appl. Phys. **69**(1991)906.

[29] T. W. Hickmott, Phys. Rev. B **38**(1988)12404.

[30] A. Moll, C. Wetzel, B.K. Meyer, P. Omling, and F. Scholz, Phys. Rev. B **45**(1992)1504

[31] V. I. Sidorov and T. M. Lifshitz, Sov. Phys. Solid State; **8**(1966)2000.

[32] S.M. Kogan and B.I. Sedunov, Sov. Phys. - Solid State (8).

[33] E.A. Kurkova and V.I. Sidorov, Sov. Phys. Semicond. **9**(1975)850-853.

[34] A. V. Akimov and V. G. Shofman, Sov. Phys. Semicond., **25**(1991)961.

[35] W. Bludau and E. Wagner, Appl. Phys. Lett., **29**(1976)204.

[36] J. M. Chamberlain, A. A. Reeder, L. M. Claessen, G. L. Rikken and P. Wyder, Phys. Rev. B, **35**(1987)2391.

[37] G. R. Allan, A. Black, C. R. Pidgeon, E. Gornik, W. Seidenbusch and P. Colter, Phys. Rev. B, **31**(1985)3560.

[38] R. J. Warburton, J. G. Michels, R.J. Nicholas, C.T. Foxon and J.J. Harris, Phys. Rev. B **46**(1992)13394

[39] S. I. Gubarv, A. A. Dremin, I. V. Kukushkin, A. V. Malyavkin and M. G. Tyazhlov, JETP Lett., **54**(1991)355.

Chapter 4

The Influence of Light on the Confinement Potential of GaAs/GaAlAs Heterojunctions

4.1 Introduction

This chapter addresses the question of what happens to the shape of the confinement potential in very high mobility heterojunction samples when illuminated. The interest in this topic arose because of investigations into the fractional quantum hall effect and Wigner crystallization which used these and other similar samples. Many experiments relied on visible radiation to either alter the carrier concentration of electrons confined at the heterojunction interface or to excite photoluminescence. It was usually assumed in previous studies that the basic shape of the conduction band profile remained relatively unchanged with the additional perturbation of light. It will be shown that this is not the case and that the behavior of these samples indicates a delicate interplay between the depletion electric field in the GaAs, the channel density and the Fermi level in the AlGaAs barrier. As the wavefunction extent of electrons confined at the interface is determined by the potential shape, answers to this question are important in any discussion of the various possible states of such a two-dimensional system.

The work has both an experimental and theoretical component. Experimentally, the energy level spacings of the confined subbands of the two dimensional electron system (2DES) are determined by looking for resonant coupling with the Landau levels originating from different subbands when the sample is placed in a tilted magnetic field. Resonant coupling is marked by anticrossing behavior of the subbands, apparent from a dramatic enhancement of the cyclotron resonance linewidth accompanied by shifts and sometimes splitting of the resonance. These positions in energy correspond to the spacings between the subbands. A theoretical value of the subband spacing is then calculated by using a computer model to self-consistently solve the Schrödinger equation by adjusting a trial wavefunction and potential until a solution is reached. Comparison of theoretical and experimental values of the subband spacing allow a surface depletion field to be deduced. The value of the surface depletion field is then combined with the field contribution from the electrons trapped at the interface to provide the conduction band profile. The shape of the band through the depletion layer also enables analysis of what effect the inclusion of a superlattice prelayer has on the level of the Fermi energy through this region.

4.2 Resonant subband Landau-level coupling

Chapter 1 reviews the case where a magnetic field directed perpendicular to a 2DES results in a series of Landau levels for each of the discrete subbands. Cyclotron resonance occurs when the photon energy of incident light matches the characteristic energy splitting $E = \hbar\omega_c$ between Landau levels, with resonant frequency $\omega_c = eB/m^*$; B is the magnetic field strength and m^* the electron effective mass. When the field is tilted at an angle relative to the perpendicular, it then has components both parallel and perpendicular to the xy-plane. For a strictly two dimensional electron gas the energies of the Landau levels should depend only on the perpendicular magnetic field component ($B_\perp$). The cyclotron resonance (CR) then occurs at energy:

$$E = \frac{\hbar e B_\perp}{m^*} = \hbar\omega_c \cos\theta \tag{4.1}$$

where θ is the angle between the sample normal and magnetic field direction. The tilted field adds an extra term to the Hamiltonian that causes motion in the $xy-$plane to be coupled to that in the $z-$direction. The net result is a mixing between the electric subbands and the Landau levels leading to a hybridization of the electron wavefunction when Landau levels from different subbands cross. Hybridization is evident as the bands repel one another and demonstrate what is known as *anti-crossing* behavior. Figure 4.1[a] shows the mixing of Landau levels from the zeroth and first subbands. Usually, N refers to the Landau level index, while i=0,1 indicates the ground and first subbands respectively. Crossing of the Landau levels from these subbands leads to the $N = 1$ level of the $i = 0$ subband changing character and becoming essentially the $N = 0$ level of the $i = 1$ subband. A similar process transfers the $N = 0$ level of $i = 1$ to the $N = 1$ Landau level of the $i = 0$ subband. This process is referred to as resonant subband Landau-level coupling or RSLC. RSLC is the most convenient method for determining the intersubband spacing and thus the form of the confinement potential.

As the cyclotron resonance approaches the energy of the intersubband transition, it splits into two components or branches. The higher energy component usually gains in intensity while the lower energy component eventually disappears. These two transitions, marked by arrows in Figure 4.1[a], result in two peaks in the absorption spectra

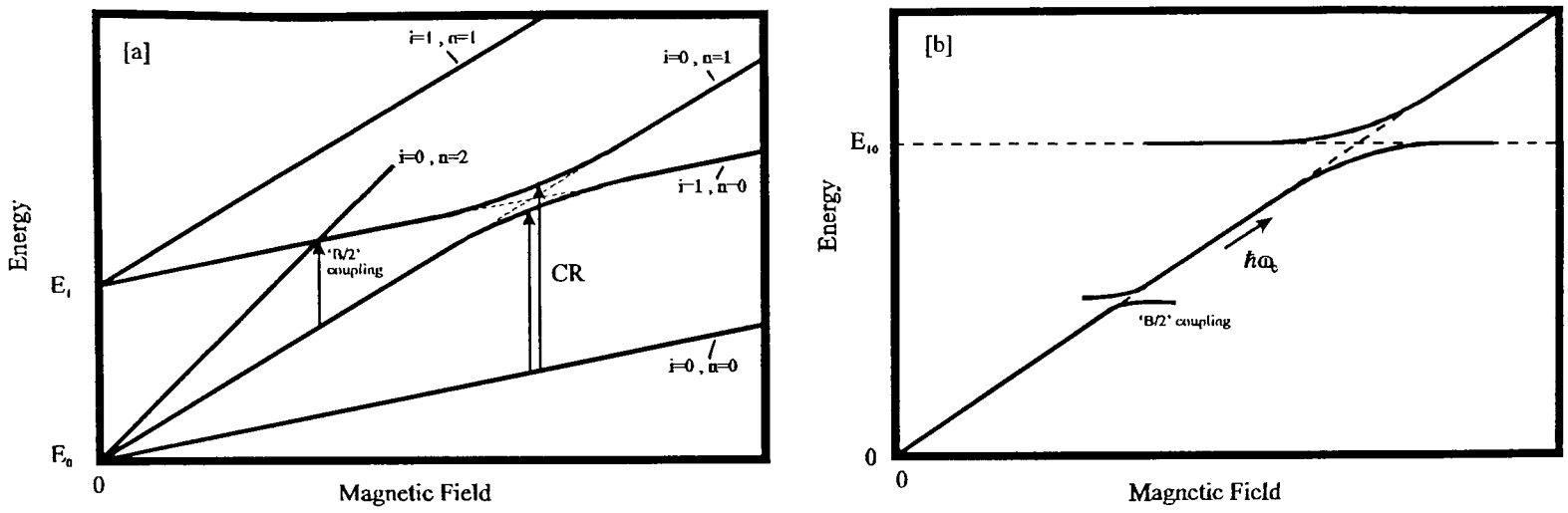

Figure 4.1: [a] Anticrossing Landau levels from different subbands. [b] The resultant cyclotron resonance energies. Taken from [4].

which anticross about the intersubband energy E_{10} as shown in Figure 4.1[b]. Also shown is a possible 'B/2' coupling, which only occurs when there is sufficient population of the $N = 1$ level of the ground subband, i.e. for $\nu > 2$, which is outside of the covered experimental range for these samples. From Figure 4.1[b] it can be seen that the upper branch is pinned to the energy separation E_{10} at low fields and tends to the cyclotron energy $\hbar\omega_c$ at high fields. The lower branch follows the cyclotron energy at low fields, but bends over at high fields to the subband energy separation. An analytical approach used to describe RSLC predicts that while the upper branch remains fixed to the energy E_{10} the lower branch actually becomes pinned to energy $E_{10}\cos\theta$ resulting in the formation of a small energy gap through the coupling[1]. Observations of RSLC in a GaAs/$Ga_{1-x}Al_xAs$ heterojunction tilted at large angles to the magnetic field have shown this to be the case[2]. For this reason, previous authors have tried to use the low field asymptote of the upper branch whenever possible to determine the subband coupling energy.

When the depletion field in the heterostructure is reduced either through a decrease in the residual doping level or (as will be shown) via illumination with light, the spatial extent of the higher lying subbands is increased relative to E_0 which remains tightly confined. A reduction in the overlap between the E_0 and E_1 wavefunctions can be seen by solution of the overlap integral $c_n = \int \Psi_0 \Psi_1 dz$. Another consequence of lowering the depletion field is to reduce the spacing between the higher subbands. This is illustrated

in Figure 4.2. Under these conditions, the anticrossing behavior is not as well defined. The reduction in subband spacing tends to mix E_{10} coupling with higher orders of subbands. Less overlap between the E_0 and E_1 wavefunctions sharply curtails the coupling strength.

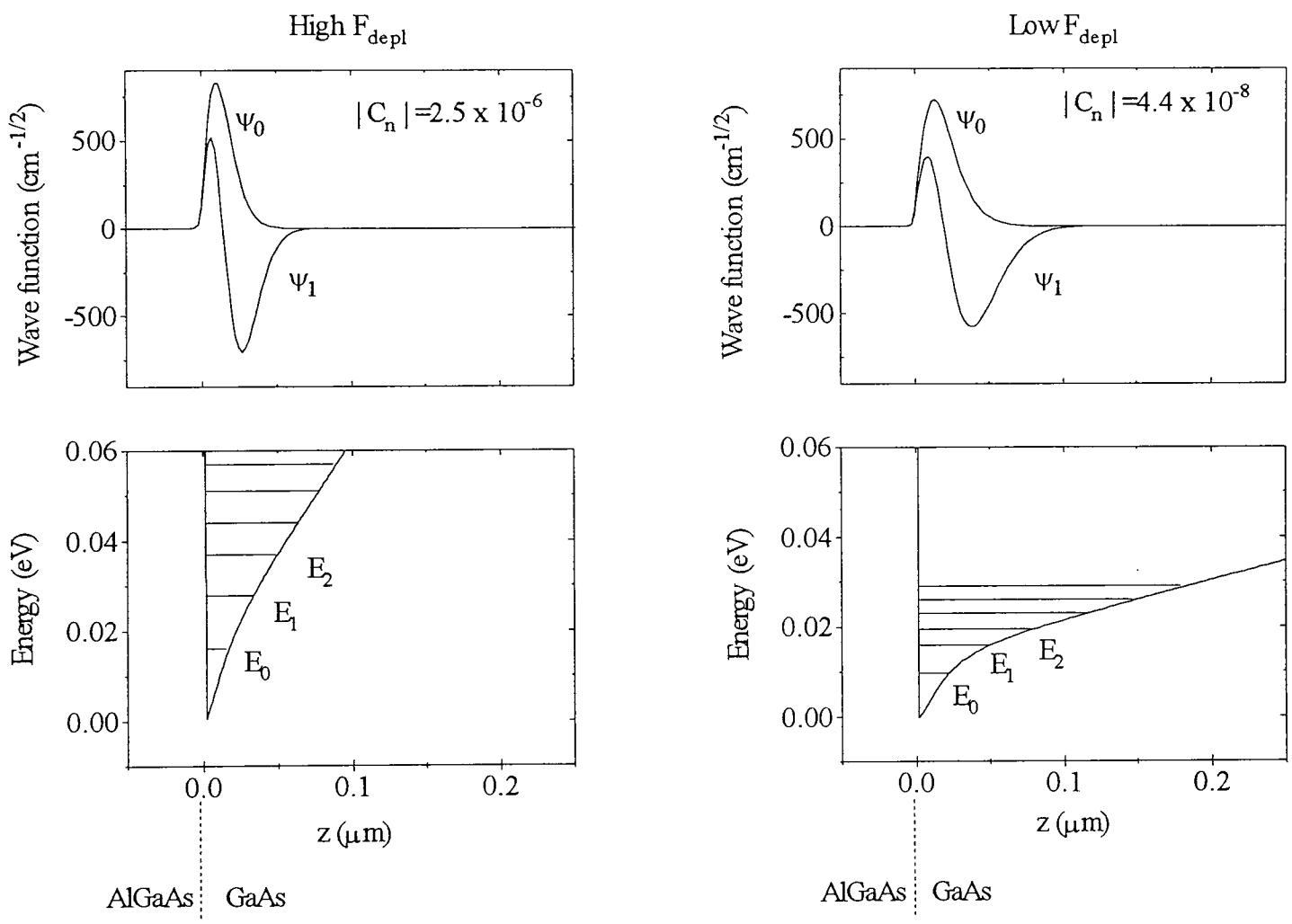

Figure 4.2: The conduction band profile and subband energy levels for a GaAs/GaAlAs heterostructure if [a] the depletion field F_{depl} is large (6×10^5 Vm^{-1}) or [b] F_{depl} is small (0.8×10^5 Vm^{-1}). The magnitude of the overlap integral c_n highlights the larger spatial extent of the E_1 subband relative to E_0 when the depletion field is lowered. The band profile, subband energy levels and wavefunctions are computed using the procedure outlined in Section 4.6 with experimental values of E_{10} and N_s.

When the coupling is weakly defined, the midpoint of the two resonances is taken as the coupling energy when the peaks are of equal intensity. Previous RSLC work has shown that only a slight discrepancy of ± 2 cm^{-1} exists between these two methods of determining the subband spacing when both methods could be employed[3]. The high levels of continuous illumination used in this thesis resulted in a very abrupt transition from the single cyclotron resonance at low energies to the split or broadened resonance

through the coupling. This forced determination of the subband spacing to be made as the midpoint of the two resonances when the peaks were of equal intensity.

There has been some debate over whether the intersubband energy determined from RSLC measurements is the actual subband spacing or if it is depolarisation shifted as direct intersubband excitations are. Direct intersubband transitions require the incoming light to be polarised perpendicular to the interface. RSLC has the electric field polarised essentially parallel to the interface and relies on coupling to the cyclotron resonance to view the intersubband transition. It is then unclear whether a depolarisation shift occurs in RSLC measurements. If this additional error does exist in the determination of the subband spacing, it has shown to be small for the low carrier densities studied here [3]. For an excellent review of RSLC, see G. Summers, D.Phil. Thesis [4].

4.3 Sample details

Most the work done for this chapter was performed on a single n-type GaAs/$Ga_{1-x}Al_xAs$ heterojunction: G640. This sample is part of the G64_ series grown at Philips Research Laboratories, described in detail in chapter 1, which arguably comprise the best set of low density, high electron mobility heterojunctions grown anywhere to date. These samples are identical except for variation of the spacer layer thickness which determines the residual carrier density in the 2DES. Also affecting the carrier density is any exposure of the samples to light. It will be shown that G640, and indeed all similar samples, exhibits four characteristic regimes of behavior. These are descriptively labelled as:

- non-illuminated
- saturated [dark]
- metastable equilibrium
- dynamic equilibrium.

G640 has a spacer layer thickness of 1200 Å which results in a transport measured carrier density of $6.7 \times 10^{10}\text{cm}^{-2}$ and mobility of $3.2 \times 10^{6}\text{cm}^{2}\text{V}^{-1}\text{s}^{-1}$ when the sample

is *non-illuminated.* This state is reached if the sample is protected from any stray light during a deliberately slow cool down to 4 K. The carrier concentration *saturates* to 12.2 $\times 10^{10}\text{cm}^{-2}$ when the sample is exposed to a very low level of illumination and then kept in darkness for several hours prior to measuring. Background room light or a short burst from a red LED is sufficient to cause the almost doubling of the carrier concentration. The period of darkness following illumination is necessary to allow the sample to reach an equilibrium state as there is an initial decay in the carrier concentration in the hours after the sample has been exposed to light. Continuous illumination with a HeNe laser whose power is sharply reduced by using neutral density filters, results in a maximum number of carriers in the 2DES and produces a *metastable* state. Finally, a high level of continuous illumination with the HeNe produces a *dynamic equilibrium* with a large number of electron-hole pairs created in the AlGaAs and a reduction of the channel electron density to levels slightly above the non-illuminated value.

G640 was chosen because the motivation for this project was to determine the shape of the confinement potential under conditions similar to those present in the cyclotron resonance measurements at millikelvin temperatures detailed in chapter 5[5]. G640 was one of the two samples in that experiment which detected the cyclotron resonance absorption of far-infrared radiation in order to probe phases of the two-dimensional electron system in the ultra-quantum limit. The electron carrier density of the samples was reduced from a saturated value by controlled amounts of HeNe laser illumination, as in the present experiment, while a far-infrared laser supplied the longer wavelength light. This far infra-red laser generates much more intensity for a given wavelength than is possible using the white light source of the fast-scan Fourier spectrometer employed for RSLC measurements. For this reason, the Fourier spectrometer measurements required a higher sample carrier density in order to provide an observable cyclotron resonance. G640's minimum carrier density value of $6 \times 10^{10}\text{cm}^{-2}$ meant that illumination with levels of *visible* light similar to those in the millikelvin experiment would leave enough carriers in the 2DES to hopefully allow for a detectable cyclotron resonance absorption. Previous experimental work at 2 K from three other of the G64_ series is also included to extend the range of carrier densities surveyed. These samples are G641, G647 and G648.

Sample,spacer layer thickness	Condition	4.2K Mobility ($\times 10^6 cm^2 V^{-1} s^{-1}$)	$N_s (\times 10^{10} cm^{-2}$
G640,1200	Dark	3.2	6.7
	Saturated	3.5	12.2
G641,1600	Dark	2.0	3.2
	Saturated	3.4	6.0
G647,3200	Dark	-	$< 0.5^{\dagger}$
	Saturated	2.5	4.41
G648,4800	Dark	-	$< 0.5^{\dagger}$
	Saturated	2.0	2.84

† Transport and optical measurements in the dark were unable to detect any carriers

Table 4.1: Transport measured values of the carrier concentration N_s and mobility for the four samples studied

Table 4.1 lists the non-illuminated and saturated values of the carrier concentration and mobilities.

Simultaneous transport measurements were not possible in the experimental arrangement so that the carrier density was determined from the absorption strength of the cyclotron resonance. Conversion of absorption strength to carrier concentration was made using the classical Drude absorption formula outlined in chapter 2. Optically measured values of carrier density have been matched to transport results for this sample and agree to within 5%[4][5].

4.3.1 D-X Centers and channel electron density

The earlier 2 K experiment revealed that the way the sample is cooled down critically influences the 'non-illuminated' value of the carrier density. In order to reach the minimum value of carrier density, the sample must be blocked from even the smallest amount of visible light and the cool down from room temperature to 150 K must happen very slowly - over a period of several hours. The value of the carrier concentration reached in this manner was shown to remain stable for periods of up to one week. It was also demonstrated that saturated values of the carrier density, achieved after a short burst of light from an LED, would initially decay by about 20% over a few hours but would then also remain constant for many days provided there was no change in the background

level of illumination.

These phenomena can mostly be explained by the existence of what are known as D-X centers formed by the silicon dopants in AlGaAs. The name arises from early explanations for the non hydrogen-like behavior of these centers as being related to a substitutional donor atom (D) and an unknown lattice defect (X). For AlGaAs with Al concentrations x, greater than 0.22, the D-X center is the lowest energy state of the donor atom and thus determines the conductivity of the material. Greater concentrations of Al result in an increase in the binding energy until a maximum is reached for $x \simeq 0.4$; the Philips samples have $x = 0.33 \pm .01$. Key features of D-X centers are a large binding energy setting the level $70 - 120\,\text{meV}$ below the Γ conduction band minimum, the existence of capture and emission barriers which control the flow of electrons to and from the D-X center, and the very large difference between the thermal and optical ionization energies (0.1 eV and 1.0 eV respectively)[6].

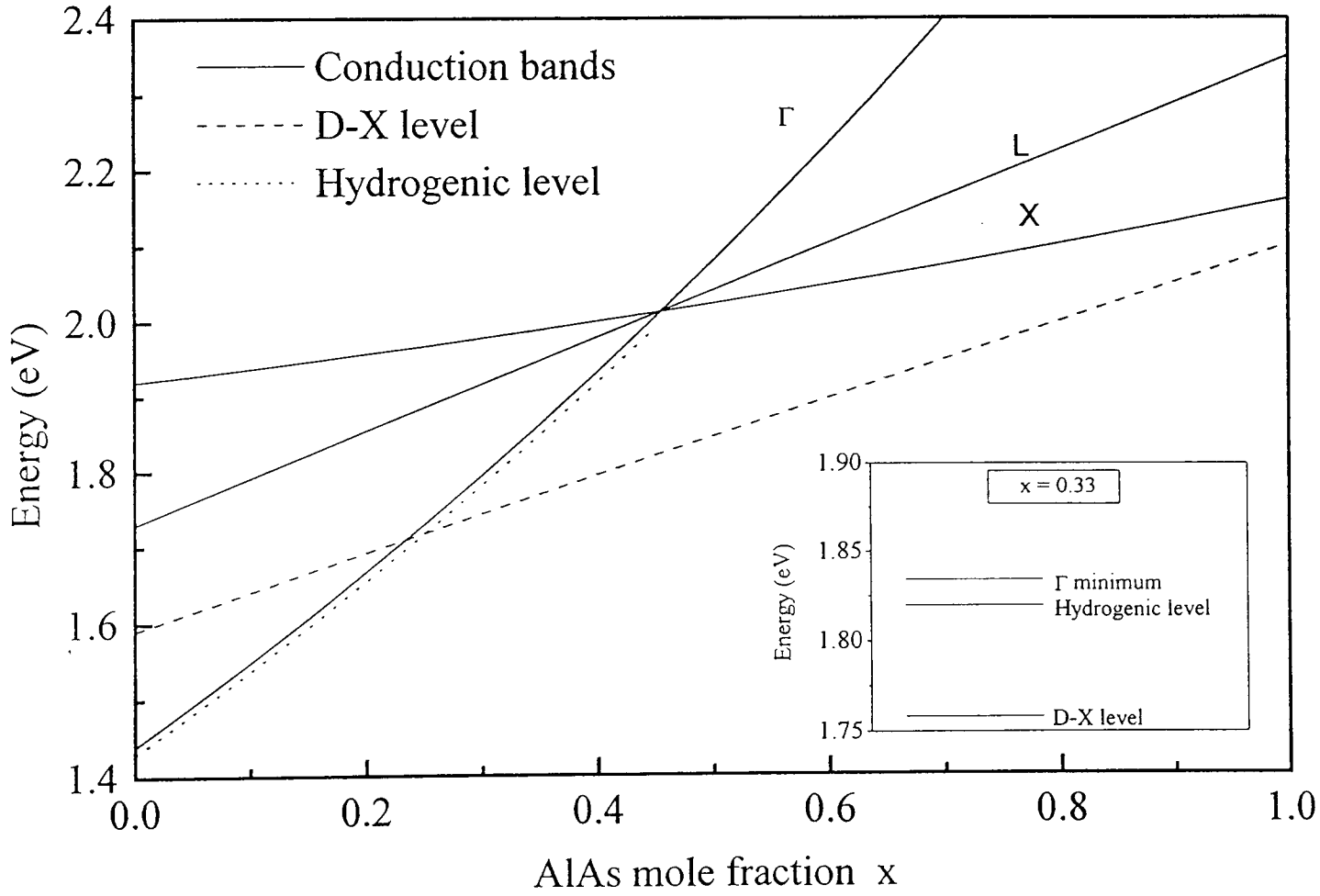

Figure 4.3: Schematic diagram showing energies of the three conduction band minima, the hydrogenic levels, and the D-X level as a function of the composition of the AlGaAs. Inset: The Γ conduction band minimum, shallow donor and D-X center levels for G640 with an *Al* concentration of 0.33.

The large binding energy has the effect of sharply reducing the number of ionized donors at low temperatures. This can be seen from an expression for the free electron concentration given by:

$$n \simeq \frac{1}{\sqrt{2}} \frac{(N_D N_C)^{1/2}}{2} \exp\left[-\frac{E_d}{2kT}\right] \tag{4.2}$$

E_d is the donor binding energy, N_d the donor concentration, and N_C the effective density of states in the conduction band, defined as

$$N_C = 2\left(\frac{2\pi m_{de} kT}{h^2}\right)^{3/2} M_C \tag{4.3}$$

Here, m_{de} is the density of states effective mass of the electron and M_C is the number of equivalent conduction band minima. For a shallow donor with E_d=10 meV, the term $\exp(-E_d/kT)$ is 0.68 at 300 K and 0.22 at77 K. Most of the donors are ionized at room temperature and the free carrier concentration decreases only by about a factor of 4 when the temperature decreases. For a deep donor, however, with a binding energy of 100 meV, the exponential term is 2.1×10^{-2} at 300 K and decreases by about three orders of magnitude to 2.8×10^{-5} at 77 K. So for the experimental temperatures described, only a negligible proportion of the D-X levels are ionized.

The situation is somewhat more complicated if the reduction in temperature between 300 K and 150 K is made rapidly. Then some of the ionized D-X centers at room temperature are not given the chance to relax back to the deep donor level and remain at shallow donor sites below the conduction band. This is due to the existence of capture and emission barriers especially prevalent at low temperatures preventing an 'easy' transfer of electrons between the shallow and deep donor levels. Explanation for this effect has shown to be consistent with a model of multiphonon capture and emission processes[7]. An analogous situation occurs if the sample is exposed to light at low temperatures, then some of the D-X centers ionize into the conduction band and decay only very slowly, over the period of several weeks while most remain trapped in the shallow donor states.

From this, it can be inferred that the minimum carrier density is achieved when all the electrons are trapped into the deep D-X level in the AlGaAs and remain there, unable to thermally excite up to the conduction band. A small amount of light is effective in ionizing many of the D-X centers up to the shallow donor levels where they can then

tunnel across the heterojunction interface and increase the channel electron density. The decay after several hours in the saturated carrier density is unlikely to be caused by D-X centers as the time scale involved is too large. Electrons able to overcome the capture and emission barriers to return to the deep donor levels, would do so in fractions of a second. After that period, it is unlikely that any further redistribution of charge would occur. It seems likely that the decay is caused by a change in the depletion field; possibly by the fixed acceptors in the depletion layer becoming neutralized through the capture of holes that have swept across the interface and up the valence band. Non-equilibrium depopulation of the 2DES also occurs under intense illumination but will be commented on later in the experimental results section.

4.4 Experimental setup

The experiments performed in this chapter were a series of cyclotron resonance transmission measurements using the fast scan Fourier transform spectrometer and ^{3}He cryostat and insert described in detail in chapter 2. The ^{3}He insert was specially modified with the insertion of an optical fiber down into the sample space to enable depopulation of the 2DES with visible illumination. This procedure was difficult as it involved threading a springy optical fiber through the innards of the refrigeration system, making sure that integrity of the different vacuum spaces was retained. A HeNe laser which emitted 5 mW of red light at 632 nm (1.96 eV) was directed down the fiber in order to reduce the channel electron density. Since its energy is greater than the band gap of the AlGaAs, illumination with this laser is capable of exciting electron and holes directly into the conduction and valence bands respectively. A green HeNe emitting 0.5 mW at 584 nm (2.1 eV) and a solid-state laser diode with 3 mW at 670 nm (1.85 eV), just below the AlGaAs band gap, were also tried separately on several runs to see whether there was any difference due to the type of light source. No variation in coupling energy was observed for similar power densities of the three lasers. The power density was altered through the use of externally placed neutral density filters. A maximum power density 10^{-3} W/cm^2 reduced the lower bound on the carrier density in G640 to 5 $\times 10^{10}$cm^{-2}.

Most of the measurements were attempted at the system's base temperature of 360 mK,

although over the course of a long automated run, there would be a slight drift upward as the cooling power of the ^{3}He slowly waned. This problem became much more acute when significant power densities were achieved on the sample surface using a HeNe laser directed down the fiber. For these experiments, the ^{3}He would be condensed into the sample chamber but not pumped down making the holding temperature $1.2 - 1.5\,\mathrm{K}$. The system was resilient at holding these temperatures over the course of an automated run, even with a 5 mW HeNe laser directed down the fiber without any neutral density filters cutting down the intensity.

The sample chamber was modified to allow the insertion of a wedge, introducing a tilt angle of the 2DES to the magnetic field direction. This tended to reduce the amount of transmitted far-infrared signal as the sample was no longer mounted exactly at the focal point of the collecting and collimating cones. The tilt angle also created difficulties getting the visible laser light into the 2DES. Gallium arsenide's high index of refraction will reflect most light that is not incident perpendicular to the sample surface. For this reason, the sample and fiber end had to be aligned as close to perpendicular as possible to maximize the amount of visible light actually transmitted into the sample. Efficiency in getting the HeNe radiation to the sample varied over the several different groups of experimental runs. Tilt angles up to $\sim 12^o$ were used and measured by shining visible laser light off the shiny epitaxial surface of the sample.

For these high mobility Philips samples, typical CR linewidths could be as low as $0.15\,\mathrm{cm}^{-1}$. The spectrometer was operated at a typical resolution of $0.5\,\mathrm{cm}^{-1}$ in order to maximize the signal to noise ratio. This setting enabled an accurate determination of peak position in energy without accentuating the noise that a higher resolution would bring. Relatively coarse when compared to the resolution of $0.12\,\mathrm{cm}^{-1}$ used in the 2 K measurement, this setting caused some smearing of possible fine splittings in the resonance peaks but was the best that could be used given the noise considerations.

Although the structural changes to the ^{3}He system are detailed in chapter 2, it is worth noting that this system required constant fiddling to minimize both the electrical and vibrational noise. These steps involved trying to shield the signal-carrying wires more effectively from residual r-f radiation and an endless effort to dampen vibrations

from attached pumps through the strategic placing of lead weights. The noise problem was partly a result of the low carrier concentrations which meant that CR absorption approaching a coupling was often less than 5%. This is compared to a minimum background residual noise of 3% when everything was working well. Despite all efforts, the ^{3}He system with its many more pumps and support systems never achieved the almost noise free spectra that a standard 2 K insert provided in earlier work[4].

Automated experiments were performed, whereby a series of CR traces were measured at different magnetic fields, usually from 8.5 T to 0 T at 0.25 T increments. Often 30 minutes was required for each field setting as a large number (n) of scans averaged together sharply reduces random noise with a $n^{1/2}$ dependence. Thus the total time of an automated run could last for over 16 hours. With some careful preparation, the experimental conditions could be maintained accurately over the course of the run.

4.5 Experimental results

4.5.1 Non-illuminated

The sample was cooled down in the dark, with both the light pipe and fiber end blocked off, but the sliding probe arrangement of the ^{3}He system made it extremely difficult to control the descent from room temperature to 77 K. This led to some of the carriers being prevented from relaxing into the deep D-X level and consequently, the minimum carrier density achieved was $8.55 \times 10^{10}\text{cm}^{-2}$. Comparison to the transport determined dark value of $\sim 6 \times 10^{10}\text{cm}^{-2}$ indicates that this density does not qualify the sample as being truly *non-illuminated* so a separate slow cooldown in a standard 2 K insert was used to provide the fully dark spectra. Figure 4.4 shows the cyclotron resonance (CR) spectra taken of sample G640 with the sample normal oriented at a 13.2^o tilt angle to the magnetic field direction using the 2 K insert. Fields every half Tesla up to 14.5 T were examined. The temperature was 3.5 K and the carrier density determined from the area of the resonant absorption curve was $7.0 \times 10^{10}\text{cm}^{-2}$

Two subband couplings are marked: E_{10} refers to coupling between the 0^{th} and 1^{st}

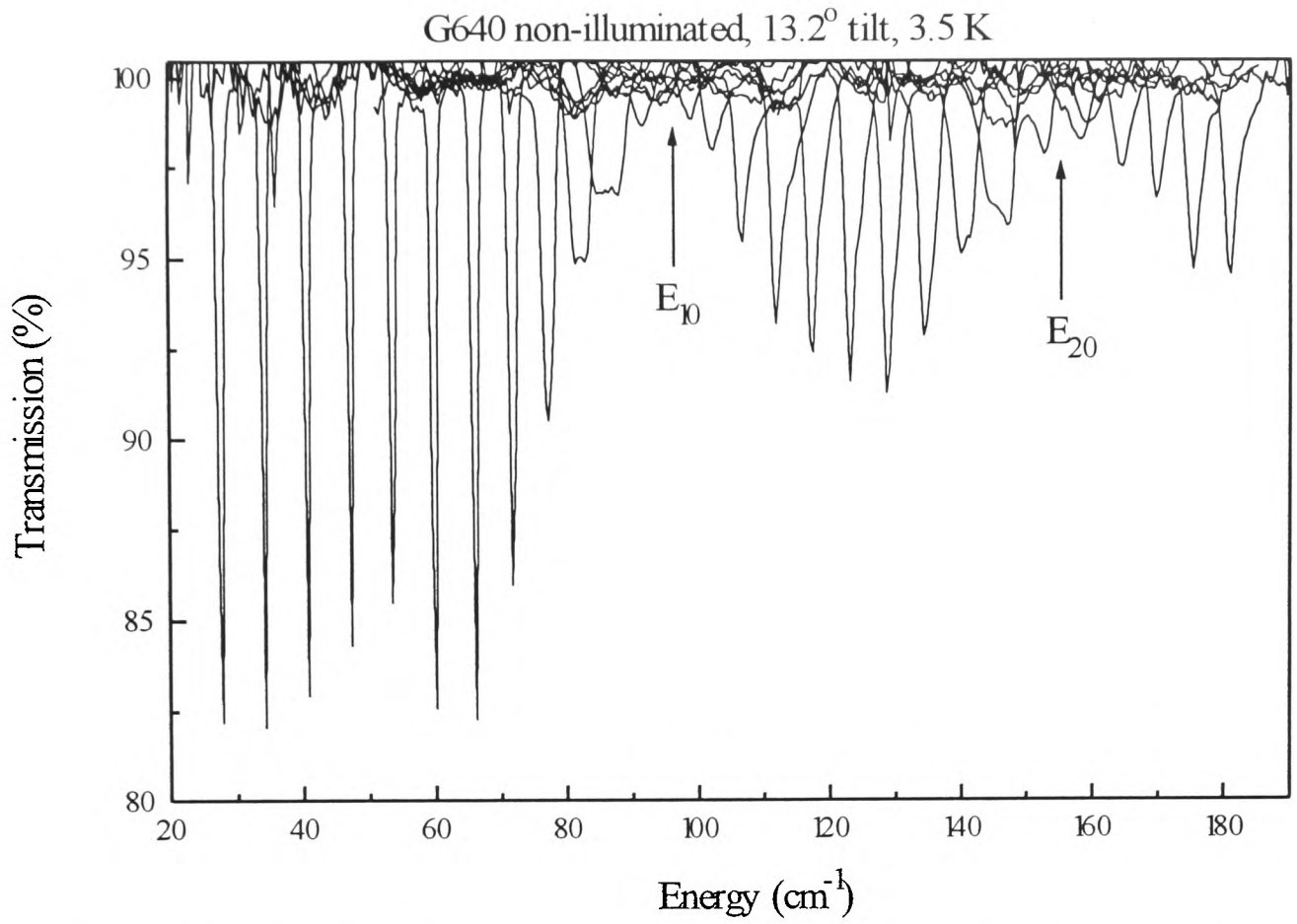

Figure 4.4: A series of cyclotron resonance specra taken in sample G640 at 13.2° tilt to the magnetic field direction. Fields up to 14.5 T were used. The sample temperature was 3.5 K. The arrows indicate the E_{10} coupling at 12.4 meV and the E_{20} coupling at 20 meV.

subband while E_{20} logically indicates coupling between the 0^{th} and 2^{nd} subband. Well away from any possible couplings the cyclotron resonance appears as a single sharp peak at the position determined from the resonance condition: $E = \hbar eB/m^*$, with $m^* = 0.07m_e$ for GaAs. As the energy of the coupling is approached, a broadening of the linewidth occurs with an accompanying decrease in the amount of transmission. Through the E_{10} coupling, the resonance splits and the intensity of carriers shifts from the low to high energy peak. The coupling energy is determined using plots of the CR position and effective mass pictured in Figure 4.5. The carrier effective mass is an extremely sensitive probe of any deviations in the peak position and discontinuities in m^* exhibit anti-crossing behavior. Also shown is a representative CR spectra pictured with the least squares Lorentzian fitted peaks superimposed. These fitted peaks provide the cyclotron resonance position, linewidth and absorption. Figure 4.5[c] shows that the product of the CR absorption and width stays roughly constant over the field range if the region around the two couplings is excluded. This is an indication that the carrier density N_s has remained fixed during the long experimental run.

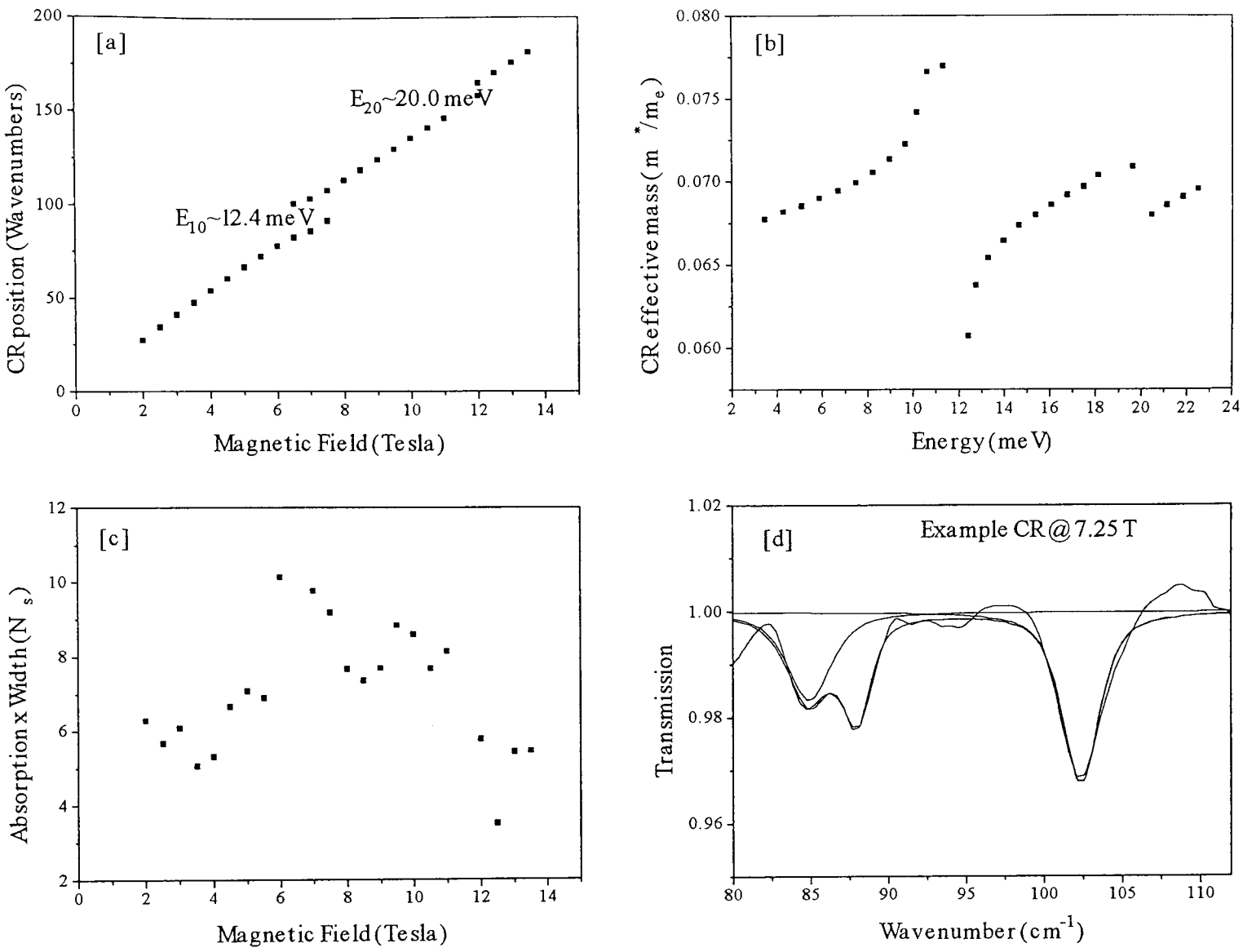

Figure 4.5: [a] CR position and [b] cyclotron effective mass with the non-illuminated sample at 13.2°. [c] The product of the absorption and width for each individual resonance is converted into a carrier density N_s and remains roughly constant except through the E_{10} and E_{20} coupling regions. [d] A representative spectra from Figure 4.4 showing the least squares fitted Lorentzian peaks to determine individual peak position, width and absorption.

4.5.2 Saturated

Saturated is a term that has been used in transport characterization of heterojunctions whose channel electron density is increased from the 'dark' value following a brief period of illumination. The mechanism underlying the increase of the carrier density is the ionization of the D-X centers by light. This is analogous to the persistent photoconductivity (PPC) observed at low temperatures in $Ga_{1-x}Al_xAs$ after a brief exposure to light. PPC is the result of the very slow recapture rate of the ionized electrons into the D-X levels from the conduction band. [6]. Following illumination there is an initial

$20 - 30\%$ decay in the carrier density as the depletion field changes. For this reason, the sample is left in darkness for several hours prior to measurement to allow it to reach equilibrium. The ^{3}He system was used for RSLC measurements of saturated sample behavior. The sample proved to be extremely sensitive with even the smallest amount of light causing a transition from the non-illuminated to saturated state. A reasonable estimate of the amount of the visible illumination needed to attain these carrier densities is 10^{-6} W/cm^2.

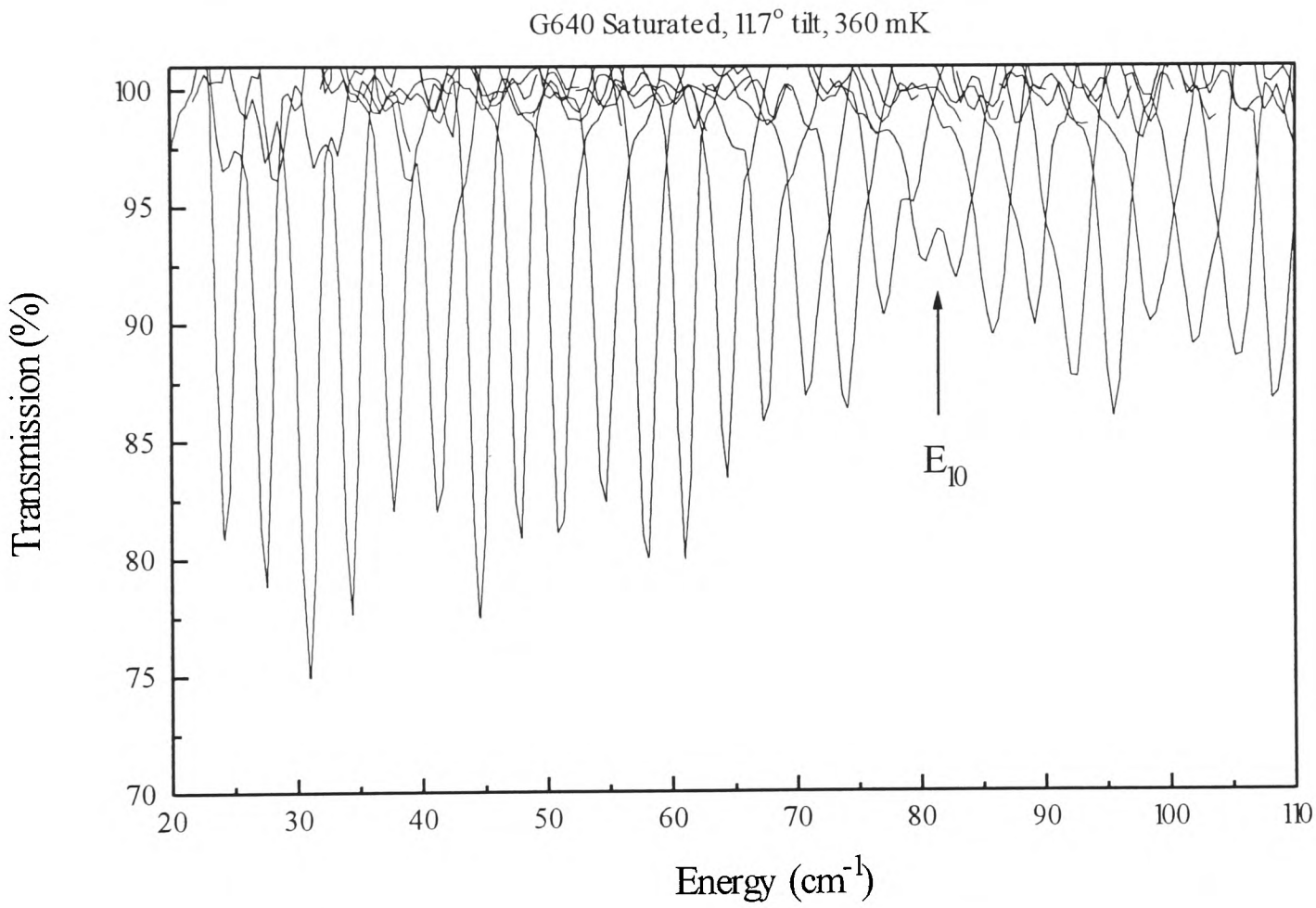

Figure 4.6: Transmission spectra for G640 where the sample was cooled down in the dark with the fiber uncovered. The sample was then left in the dark for several hours prior to taking the CR spectra. The channel electron density is 12.15×10^{10}cm^{-2}.

Figure 4.6 is representative of saturated sample behavior. The coupling at 10 meV ($80\,\mathrm{cm}^{-1}$) is marked by the arrow; evident from a partially split and broadened resonance where the intensity in each peak is roughly equivalent. An increase in the carrier density from 7 to 12×10^{10}cm^{-2} has decreased the coupling energy and corresponding subband separation. The transmission intensity at lower energies is roughly constant within noise fluctuations except at $30\,\mathrm{cm}^{-1}$ where a marked increase is seen. This energy corresponds to a filling factor $\nu = 2$ where there have been many reported observations

of anomalies in the cyclotron resonance of two dimensional systems[3]. These effects are often attributed to random potential fluctuations pinning a charge density wave (CDW) state and suggest the importance of electron-electron interactions. Above the E_{10} coupling a slight broadening of a peak occurs which could indicate a weak coupling to a higher subband although no discontinuity is present in a plot of the effective mass. The lack of clearly defined couplings above E_{10} is likely to be the result of the reduced coupling strength and an indication that the slope of the confinement potential has been reduced. Under these circumstances the already weakly coupled transitions to higher subbands are just too insubstantial to observe. The rapid changeover from resonances displaying a sharp and narrow profile to those broadened with very weak absorption strength also signals the presence of many overlapping couplings and points to a lessening of the depletion field (refer to Figure 4.2).

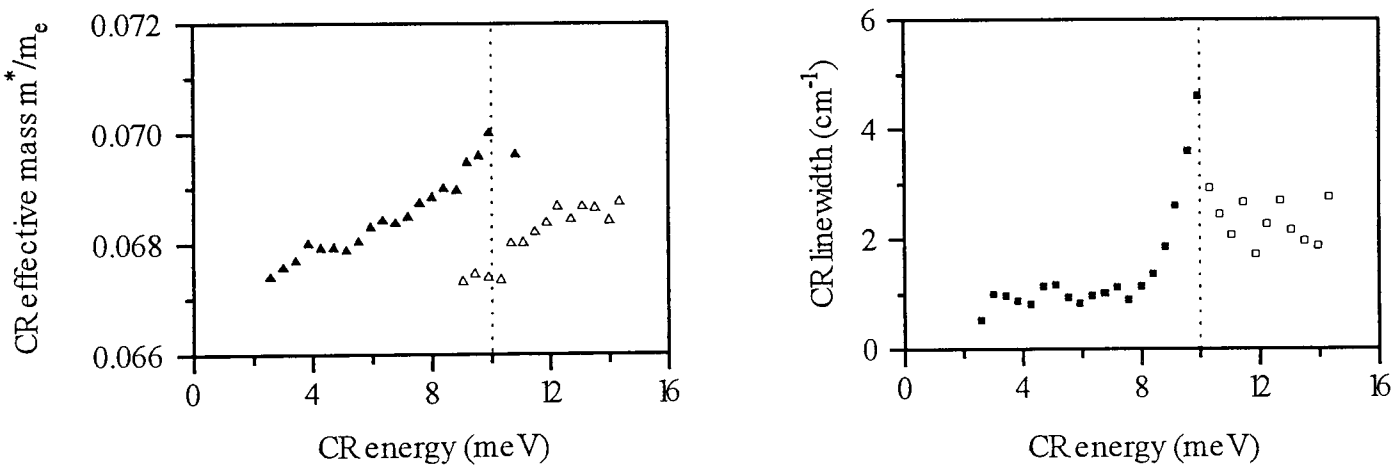

Figure 4.7: Effective mass and linewidth plots for the saturated case pictured in Figure 4.6.

Figure 4.7 shows the corresponding plots of the effective mass and linewidth as a function of CR energy for the experimental spectra pictured in Figure 4.6. From these plots, combined with a close examination of the transmission data, the exact coupling energy is determined. The estimated error in this determination was approximately 5%.

4.5.3 Metastable - low levels of continuous illumination

Low levels of continuous illumination increase the carrier density over saturated levels and further lower the coupling energy. I label this state metastable because it relies on the continuous above band-gap radiation to ionize the deep D-X levels. Should the sample be blocked from the light source, then the carrier density would slowly decay to the equilibrium of a saturated state over a period of hours.

Figure 4.8 shows a spectrum which typifies this metastable regime. The sample was cooled down in the dark and then continuously illuminated with the fiber opened to the background room light. The ^{3}He system's base temperature of 360 mK was maintained for the duration of the experimental run and the sample normal was orientated at 11.7° to the magnetic field direction. The carrier density of 14.85 $\times 10^{10}$cm^{-2} in the represen-

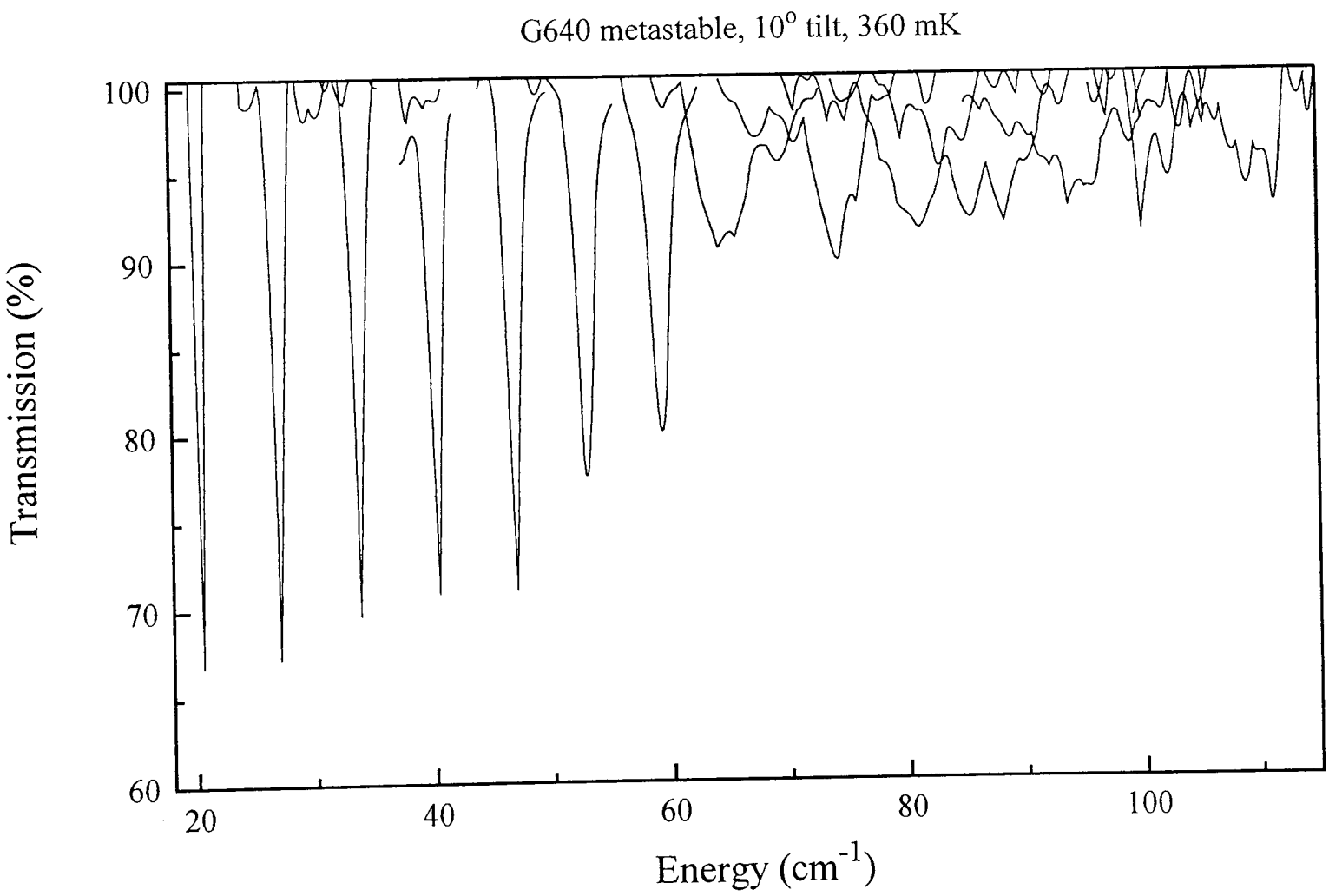

Figure 4.8: CR spectra taken with the fiber left open to the room lights. This low level of continuous illumination resulted in a peak channel electron density of 14.85 $\times 10^{10}$cm^{-2}.

tative trace is the maximum obtained for this sample. Transition from single peaks with 70% transmission to broadened linewidths and reduced transmission abruptly occurs in less than 0.5 T over the energy range from 60-70 cm^{-1}. Effective mass, linewidth and

absorption plots which aid in the determination of the coupling energy are presented in Figure 4.9. The absorption strength and CR linewidth exhibit opposing behavior: a decrease in the absorption through the coupling is matched by a corresponding increase in the linewidth. This information, combined with visual inspection of the CR spectra fixes the E_{10} coupling at 8.6 meV. No higher couplings are evident.

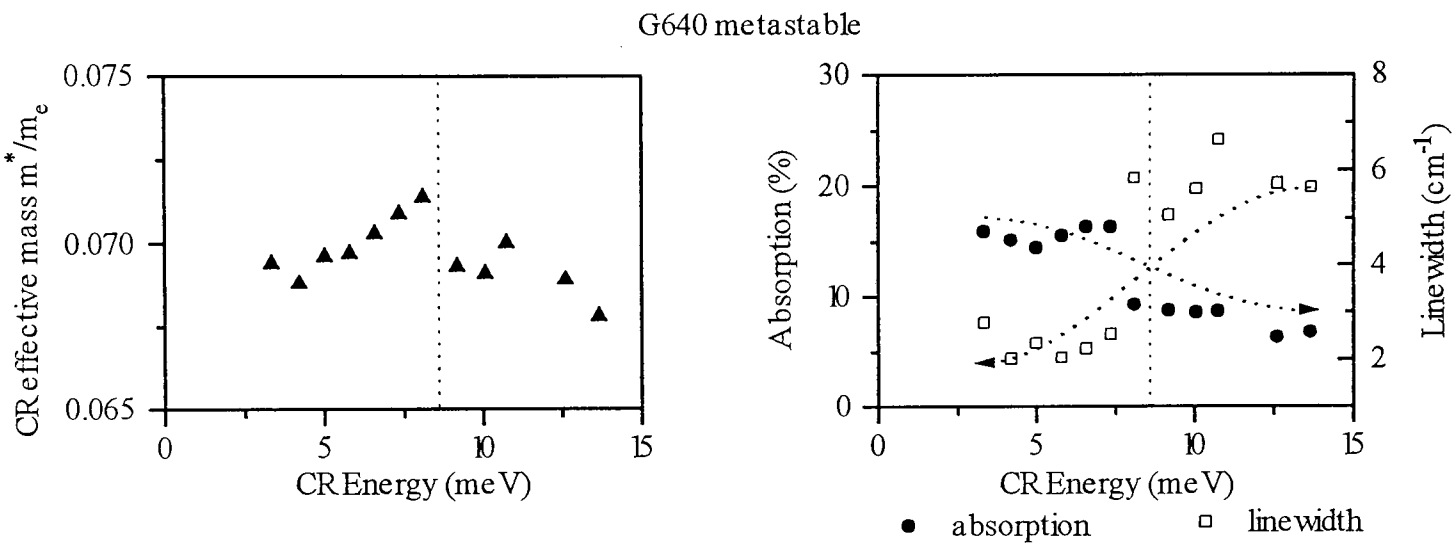

Figure 4.9: Effective mass and linewidth plots for the metastable case pictured in Figure 4.8. The dashed lines mark the subband coupling energy while the dotted lines are to guide the eye in observing the opposing behavior of the absorption and linewidth.

4.5.4 Dynamic equilibrium- high levels of continuous illumination

High levels of continuous illumination with the HeNe laser create a large number of electron-hole pairs in the AlGaAs. A dynamic equilibrium is very quickly reached under these circumstances where the optically generated electrons are repelled by the spacer layer potential and remain in the AlGaAs while the holes are swept into the GaAs recombining with the few remaining carriers in the 2DES. The stream of holes also serves to further neutralize the acceptors in the GaAs and hence reduces the depletion field.

Even with the relatively large amounts of laser power directed down the fiber and into the sample, the carrier temperature is increased by less than 1 K which means that the sample is still truly 'cold'. This is an estimate based on the power loss rates of electrons which has been extensively studied[8]. Using experimental results that cover

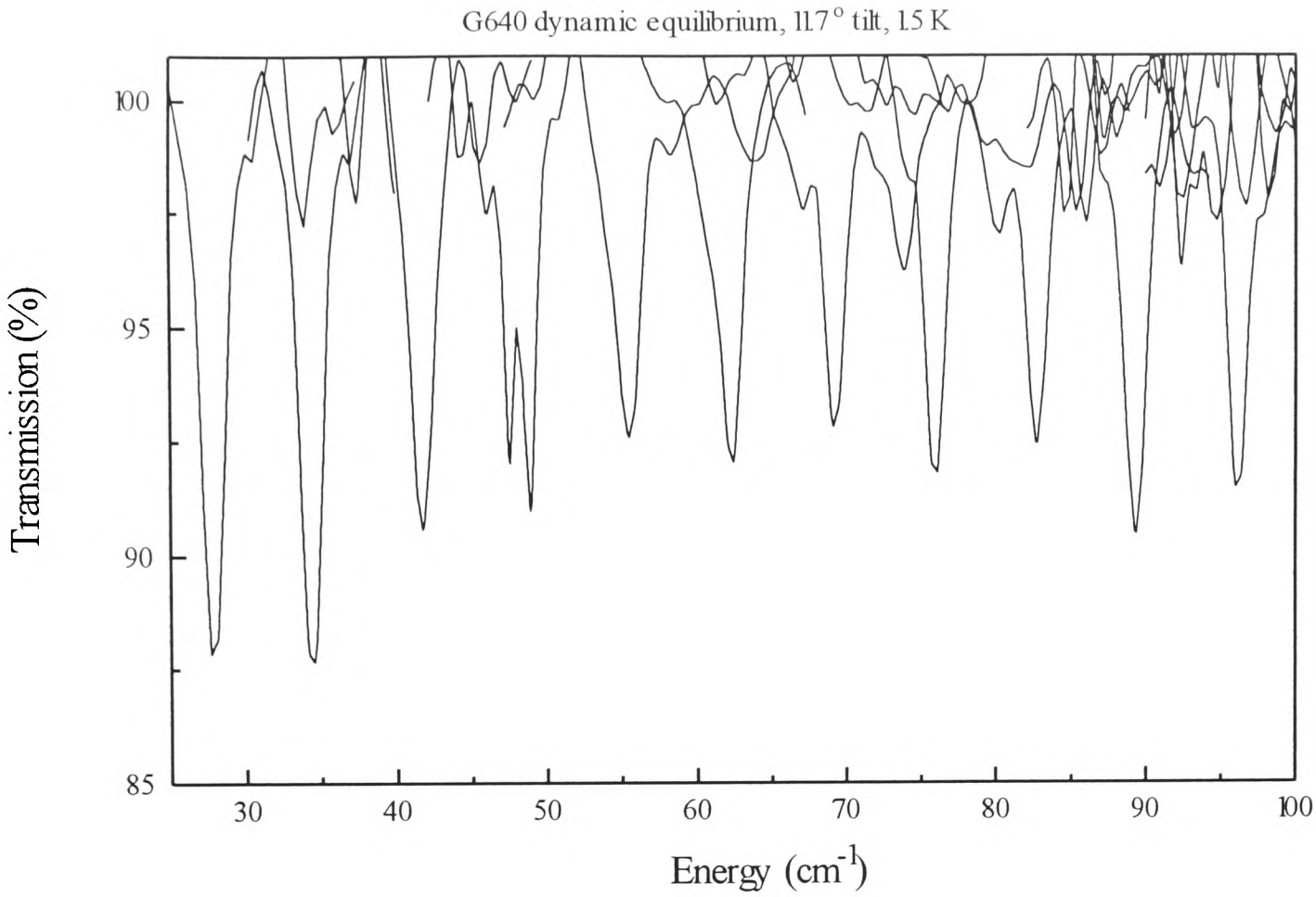

Figure 4.10: Transmission spectra for G640 where the sample was illuminated with the HeNe laser + ND1. Estimated power density at the sample surface is 10^{-3} W/cm^2 which resulted in a channel electron density of 5.0×10^{10}cm^{-2}.

over eighteen orders of magnitude, Leadley *et al* was able to derive the relation: energy loss rate per electron (in eV/s) equals $\alpha(T_e^3 - T_L^3)$ where $\alpha \sim 100$ eV/s/K^3, and T_e^3, T_L^3 are the electron and lattice temperature in Kelvin. Since the lattice temperature is small and cubed, it can be ignored. A maximal power density of 10^{-3} W/cm^2 results in 3×10^{15} photons/cm^2/s. With a 2DES density of 1×10^{11} cm^{-3} and assuming that each photon has an energy of 30 meV[1], gives $\sim 10^3$ eV/s per electron. Using the above relation, this would correspond to a lattice temperature increase of ~ 2 K. This calculation should only serve as an estimate; experimental proof that the sample is cold is contained in the simultaneous transport and optical measurements presented in chapter 5. There, the presence of near zero minimas in the diagonal resistivity corresponding to the fractional quantum Hall effect, are confirmation that the sample is cold despite the illumination by the visible laser (see Figure 5.5).

[1] Each electron-hole pair has an excess energy of ~ 0.4 eV which is reduced by very rapid LO phonon emission processes to less than one LO phonon energy.

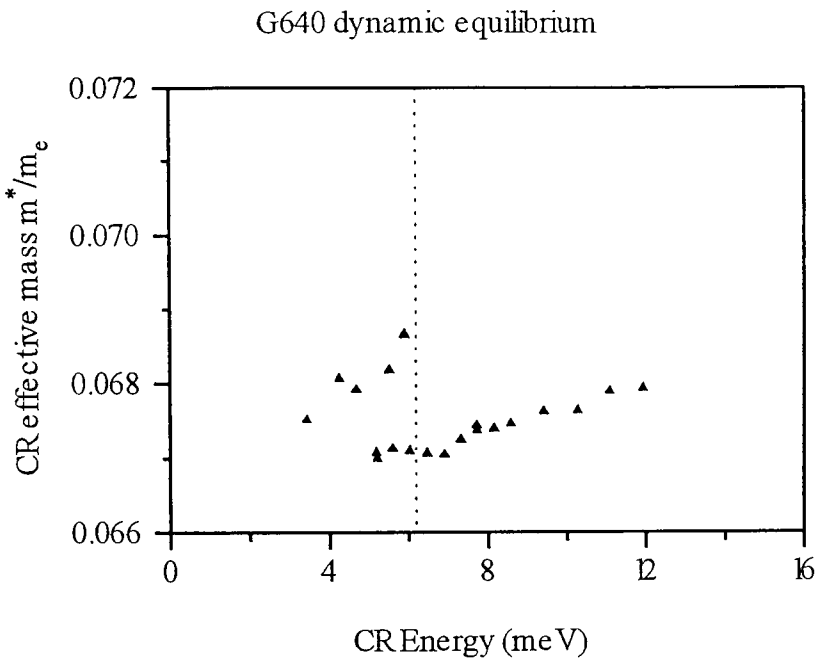

Figure 4.11: CR Effective mass for the dynamic equilibrium case pictured in Figure 4.10.

The small numbers of carriers in the 2DES combined with the deleterious effect that large amounts of light had on the staying power of the ^{3}He system made cyclotron resonance measurements of the dynamic equilibrium state difficult. Figure 4.10 shows the run which produced the lowest value for both the carrier density and the coupling energy. The estimated power density at the sample surface is $10^{-3}\,\mathrm{W/cm^2}$. The one clearly observable split peak defines the coupling energy at $6.2\,\mathrm{meV}(50\,\mathrm{cm^{-1}})$. A plot of the CR effective mass shows how weak the subband coupling is with the two branches overlapping in energy (Figure 4.11). Linewidth and absorption plots provided little information as there is very little change in either through the coupling region.

All the experimental data is pulled together in Table 4.2 which combines RSLC measured E_{10} energies, carrier density and a listing of the different experimental conditions.

4.6 Sketches of the confinement potential

Armed with values of E_{10} and N_s we now proceed to a calculation of the potential through the depletion layer. This is done by using a self-consistent approach developed by D. Symons[11] that first guesses the shape of the potential across the heterojunction and then finds the corresponding wavefunction. From this new wavefunction, a potential

Sample,θ	Illumination Conditions	N_s ($\times 10^{10}$cm^{-2}	E_{10} (meV)	F_{depl} ($\times 10^5$Vm^{-1}
G640,10^o	fiber open	11.25	8.2	1.25
	full green	11.7	7.6	0.8
	fiber covered	10.35	8.6	1.72
	full red	11.7	7.6	0.8
G640,6^o	red+ND1	9.9	9.0	2.1
	full red	11.25	8.8	1.7
	full laser diode	11.25	8.8	1.7
	fiber covered	11.25	8.8	1.7
G640,10^o	fiber covered	8.55	9.8	2.98
	fiber uncovered	14.85	8.6	0.9
	red+ND2	9.9	6.6	0.51
G640,10^o	red+ND1.3	11.7	8.0	1.04
	red+ND1	10.8	8.0	1.19
	red+ND0.3	11.25	8.0	1.12
	fiber covered	9.9	8.4	1.68
	red+ND1	13.05	8.0	0.82
G640,11.7^o	red+ND1	4.95	6.2	1.21
	red+ND2	8.1	7.0	1.06
	fiber uncovered	12.15	10.0	1.68
	red+ND3	9.0	6.8	0.78
2 K insert RSLC data				
G640,13.2^o	dark	7.0	12.4	5.5
G641,12.4^o	dark	3.2	12.28	6.92
	saturated	6.4	11.5	5.07
	red LED	8.7	7.53	1.29
G647,?	saturated	4.2	6.5	1.66
G647,?	red LED	4.4	6.1	1.36
G648,?	red LED	2.8	6.5	2.07

Table 4.2: RSLC determined values for the coupling energy E_{10} and the carrier concentration N_s. These values are used to provide a depletion field F_{depl} using the procedure outlined in Section 4.6.

is calculated. A percentage of the new potential is added to the old to create a composite potential from which a new wavefunction is generated. This cycle continues until the wavefunction and potential are self-consistent. This is signified by convergence of the lowest subband energy E_0 after several iterations. Once E_0 is fixed, E_1 can be calculated; the difference $E_1 - E_0 = E_{10}$ provides the theoretical subband spacing. Comparison of theoretical and experimental values of E_{10} allow a surface depletion field to be deduced.

4.6.1 Self-consistent calculation of the depletion field F_{depl}

In the GaAs/$Ga_{1-x}Al_xAs$ heterojunction shown schematically in chapter 1, the GaAs channel is nominally undoped. Past the 0.5 μm GaAs buffer a superlattice (SL) prelayer is added to help reduce the acceptor doping level due to impurities. The wider band-gap AlGaAs has a spacer region, also undoped and then a high level of doping further away from the interface. Variables that characterize this system are:

- N_s - the concentration of electrons per unit area confined at the interface
- N_{ac} - the net acceptor doping per unit volume in the GaAs depletion layer
- N_{depl} - the number of charges per unit area in the depletion layer whose thickness is z_d
- V_b - the interface barrier height
- m^* - the electron effective mass

For the calculation presented here, m^* is $0.07m_0$ in the GaAs and $0.09m_0$ in the AlGaAs. G640's 33% Al concentration results in an interface barrier of 0.27 eV. This value is reached by taking 60% of the difference between the AlGaAs band gap (1.97 eV at 4 K) and the GaAs gap (1.52 eV)[12]. The value of the net acceptor density is fixed at $5 \times 10^{13}\,cm^{-3}$ based on estimates made during sample growth[10][14]. This estimate is slightly reduced on a previously used figure of $1 \times 10^{14}\,cm^{-3}$ but is consistent with the effectiveness of the superlattice in capturing acceptors in the GaAs depletion layer[10] and has shown to result in only very small changes to the subband energy levels.

The relation between N_{ac} and N_{depl} is given by:

$$N_{depl} = N_{ac} z_d \tag{4.4}$$

$$z_d = \left[\frac{2\epsilon_0 \epsilon_r \phi_d}{e N_{ac}} \right]^{1/2} \tag{4.5}$$

where ϕ_d is the band bending associated with the depletion layer. At low temperatures, ϕ_d is given approximately by the difference between the bottom of the conduction band in the bulk GaAs and the Fermi level. In a normal GaAs/$Ga_{1-x}Al_xAs$ heterostructure that does not contain the SL prelayer ϕ_d will be approximately 1 V. If values are inserted into Equation 4.5, $\phi_d = 1$ V, $\epsilon_r = 11.7$, and N_{ac}=$\sim 5 \times 10^{13}$ cm^{-3}, we obtain $z_d = 5.1 \mu$m. This is obviously greater than the size of the buffer layer. Even including the SL buffer and substrate with a composite thickness of 2 μm does not provide enough room for the predicted depletion layer thickness. For this reason, it is not entirely correct to talk of a depletion density N_{depl} in these heterojunctions because the corresponding depletion length is larger than the sample extent. The concept of a depletion field, (F_{depl}) however, remains valid and will be used to characterize the shape of the band through the depletion layer.

In order to generate the band profile, the self-consistent theory begins with a solution of Poisson's equation:

$$\frac{d^2\phi(z)}{dz^2} = \frac{e\left(N_s \left|\Psi_i(z)\right|^2 + N_{depl}\right)}{\epsilon_r \epsilon_o} \tag{4.6}$$

Here, only the carrier concentration of electrons in the ground subband is included in N_s which assumes $kT = 0$ and as a result no higher subbands are occupied. Ψ is the solution of Schrödinger's equation of the form

$$\frac{d^2\Psi(z)}{dz^2} + \frac{2m^*}{\hbar^2}\left[E_i + e\phi(z)\right]\Psi(z) = 0 \tag{4.7}$$

where the potential $V(z) = -e\phi(z)$.

Because of the way in which the Schrödinger equation is coupled with Poisson's equation it is necessary to numerically solve these expressions to have a truly self-consistent approach. An iterative process is used, beginning with a triangular potential assumed for the inversion layer. In order to construct a partial wavefunction from this potential, the initial value of the wavefunction a picked distance z along from the interface is set to zero and its gradient set to a non-zero value. Using these two points, the Runge-Kutta

algorithm[13] generates successive points in the wavefunction that continue to satisfy the slope provided by the Schrödinger equation. The proper energy of the ground state is then determined by examining the number of zero-crossing points of the partial wavefunction contained within z. A wavefunction with energy less than E_0 will have no crossing points, while a wavefunction with energy greater than E_0 will cross zero once.

Energy values are stepped in 1 meV increments between 0 and 100 meV looking for the high and low boundaries to the correct energy. The distance along the growth direction z, is picked to be far enough away from the interface as to ensure that the wavefunction has gone through its turning point but close enough to prevent the values of Ψ from reaching values too large to handle numerically. Once bounded, the correct value for E_0 is found by halving the difference between the upper and lower bound until the wavefunction approaches zero far from the interface as would be expected. A correct value of the energy allows a complete wavefunction to be generated that extends into the barrier and across the depletion layer. From the complete wavefunction, a new potential, which includes the electron exchange potential, is computed. 30% is added to the initial triangular approximation to form a new 'composite' potential. This cycle is repeated until the potential and the wavefunction are self-consistent within a tolerance 1×10^{-4}meV in E_0. With E_0 established, E_1 is calculated by looking for higher bound states of the wavefunction through an identical process of stepping energy values in 1 meV increments, this time beginning from E_0. Inclusion of the exchange potential, which has its minimum centered on the charge distribution, has the effect of rounding out the potential near the interface since most of the charge is contained within 500 Å of the potential discontinuity. The self-consistent calculation was checked against published results[9] for known values of N_s and N_{ac}.

A previous study[4] used the triangle-potential approximation to calculate the depletion field This was accomplished by a plot of subband spacing E_{i0} as a function of subband index, with the depletion field varied until agreement between theoretical and experimental values for was reached. Excellent agreement between theory and result was achieved for non-illuminated data. A large positive energy offset was observed, however when fits were tried with illuminated data. This discrepancy confirms that the triangle-potential approximation is reasonable when there is little or no charge in the inversion

layer but fails when $N_s \geq N_{depl}$ which is usually the case under continuous illumination.

4.6.2 Four regimes of sample behavior

The experimental value of N_s for each run was entered into the program along with an initial estimate of the depletion field. The depletion field was subsequently varied until the program's self-consistent E_{10} matched the experimental value. The calculated values of the depletion field are included for each of the different experimental runs in Table 4.2. Also included in the table is the experimental data from 2 K measurements on the other Philips' samples.

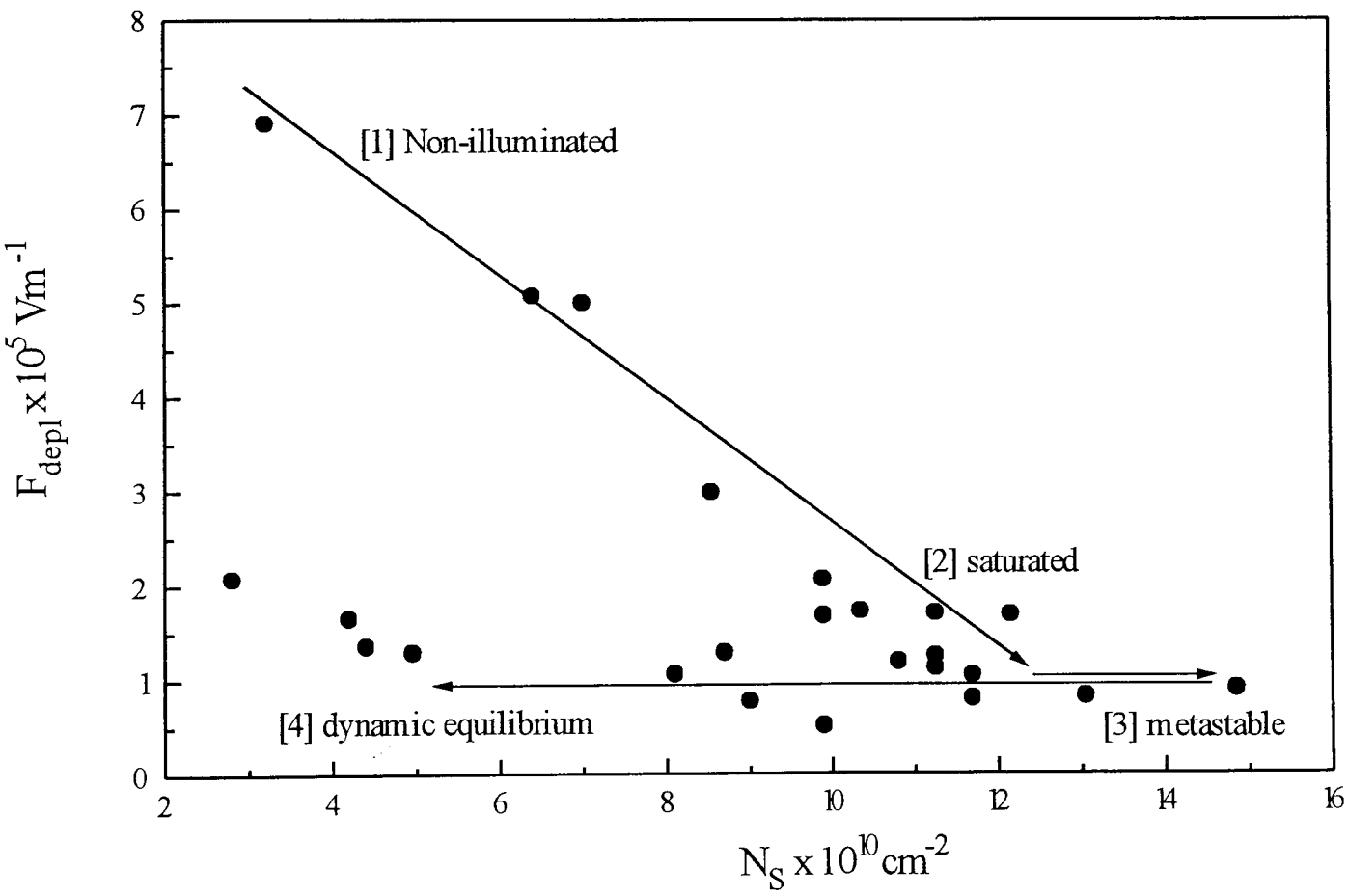

Figure 4.12: Calculated values of the depletion field F_{depl} against the carrier density N_s. Four regimes of sample behavior are marked.

An illustrative way of presenting the data is to plot the depletion field F_{depl} as a function of the channel electron density N_s. This is done in Figure 4.12. Evident is a progression from a minimum channel electron density and high depletion field towards a maximum channel electron density and reduced depletion field. Increasing levels of illumination then depopulate the 2DES while the depletion charge density stays roughly constant.

This sequence is marked by the solid lines superimposed on the data points. In this progression, the four different regimes of sample behavior are more clearly defined.

A non-illuminated state is reached by cooling slowly under conditions of total darkness resulting in a minimum of the channel electron density and high depletion field. A short burst of illumination followed by a long period [many hours] of total darkness results in a saturated state with an enhanced channel density but a somewhat reduced depletion field. Maximum, metastable channel electron density and minimum depletion field is obtained with low levels of persistent illumination. Finally, for high levels of continuous illumination, of order $10^{-3}\mathrm{Wcm}^{-2}$, the channel electron density drops to similar values to those observed in the non-illuminated case, but the depletion field stays relatively low.

4.6.3 Confinement potentials for the four states

Conduction band profiles are deduced from F_{depl}, spacer layer thickness, N_s and the self-consistent calculation. The field at the interface is equal to the sum of the depletion field and field due to charge in the inversion layer. The self-consistent calculation provides the potential through the GaAs from the interface out to an arbitrary point, chosen to be $0.5\,\mu$m, corresponding to where the SL prelayer begins. On the AlGaAs side, the field at the interface is dropped linearly across the spacer layer thickness (1200 Å for G640, 1600 Å for G641) which is assumed to be free of any significant charge density. Out of the spacer layer, the band is assumed to be flat. Transition from the spacer layer to doped region is plotted as occurring abruptly, although in reality this probably takes place in the relatively short space of 20 Å.

Also included are the energy levels for E_0, E_1, and E_f, the Fermi energy calculated using the general expression:

$$E_f = \frac{\pi\hbar^2 N_s}{m^*} + E_0 \tag{4.8}$$

where E_0 is the energy level of the ground subband. E_f is not pictured in the dynamical equilibrium case because, as will be shown later, the concept of a Fermi energy is not applicable to a system where the location of charge is governed by different recombination rates and processes involving both electrons and holes.

The conduction band profiles for the non-illuminated, saturated, metastable and dynamic equilibrium states are pictured in Figure 4.13 deduced using the procedure outlined above. Clearly evident is the dramatic change in the slope of the potential under different illumination conditions.

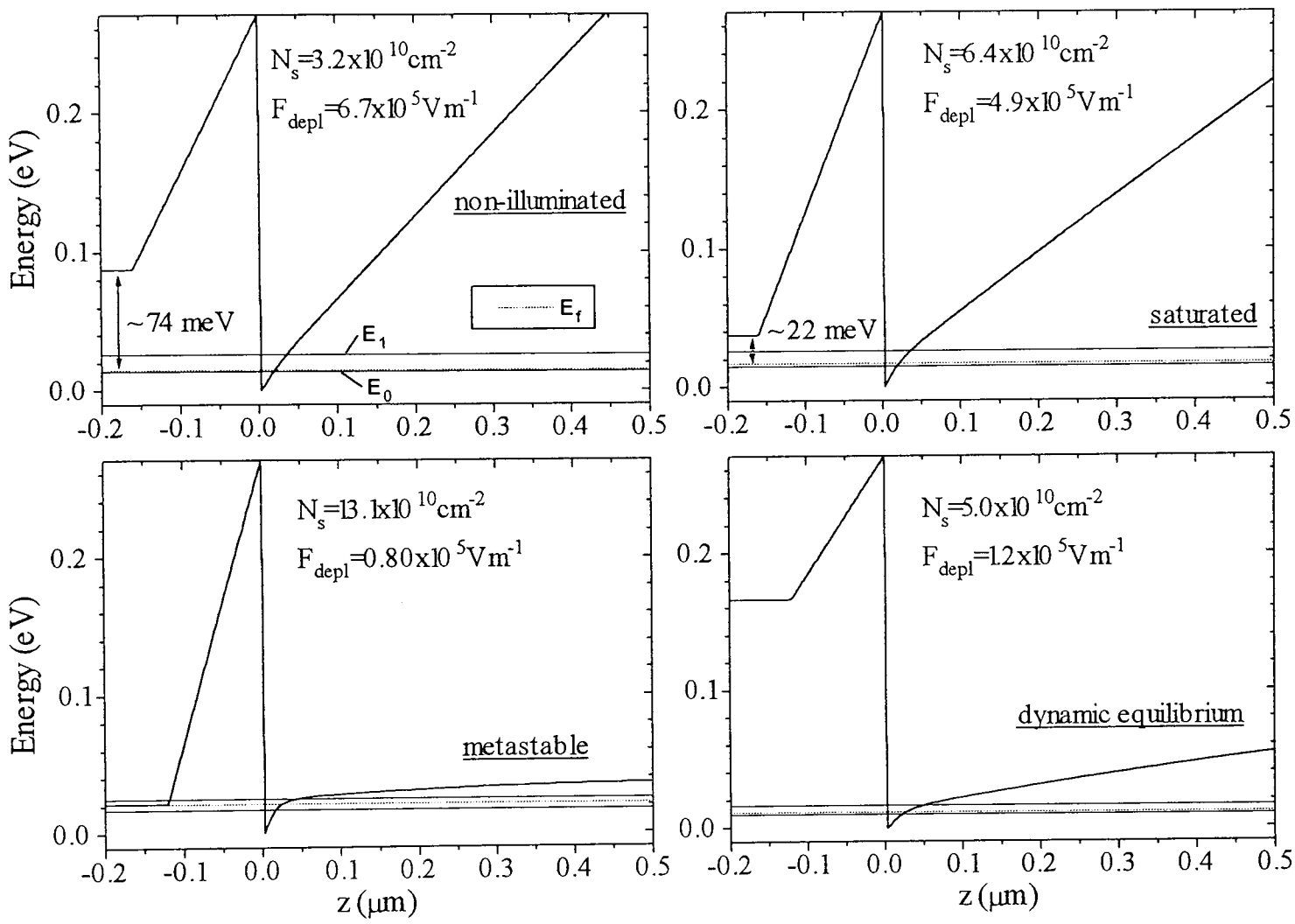

Figure 4.13: Conduction band profiles for the four itemized illumination conditions.

The representative graph for an non-illuminated case, shows the conduction band minima set at 74 meV above the Fermi energy. The field due to the inversion layer is small when compared to the depletion field. This results in very little band bending through the region of the depletion layer where the electrons are confined and an almost triangle-like potential. The level of the Fermi energy is consistent with predicted values for the D-X center[6][7] which means that, as expected, almost all of the electrons are trapped at these deep donor sites.

When a small amount of light is allowed to strike the sample, followed by a long period of darkness, the value of N_s increases while F_{depl} is reduced. In the AlGaAs, the conduction

band is now only 22 meV above the Fermi level, indicating that the light has ionized the electrons from the D-X states up into the shallow donor states lying just below the conduction band. These carriers are then able to tunnel through the spacer layer and into the heterojunction. 22 meV is almost the exact value of the ionization energy for these shallow hydrogen-like donors predicted in a recent study[15].

Low levels of persistent illumination pull the conduction band down coincident with the Fermi energy and further increase the channel electron density. The depletion field is flattened by the minimal charge remaining in the GaAs. A possible explanation for this is that the continuous illumination results in charge separation of electron-hole pairs in the AlGaAs. The electrons are repelled by the spacer layer potential, while the holes are swept into the GaAs and neutralize the acceptor charge.

The fourth state caused by high levels of continuous illumination, results in a further decrease of the channel electron density while the depletion field remains low. The additional influx of holes, once the GaAs potential is flat, is thought to further depopulate the channel. The sample should be in dynamic equilibrium with the shape of the potential reflecting the charge distribution throughout the heterojunction. There would be several different competing processes at work in the dynamic equilibrium case. A model of the complex processes that would occur when the sample is strongly illuminated would have to include

- photoexcitation rate of electrons and holes in the $Ga_{1-x}Al_xAs$
- tunnelling rate of electrons into the 2DES from the $Ga_{1-x}Al_xAs$
- recombination between electrons in the 2DES and holes bound to acceptors in the GaAs
- recombination between electrons in the 2DES and free holes
- contributing effect of the electrons and holes photoexcited in the GaAS.

In a soon to be published study of optically induced 2DES depletion in structures containing a δ-doped layer with Be acceptors the authors[18], conclude that the number of free holes in the GaAs governs the depletion effect for high levels of illumination.

Although the structure of the samples is different from the Philips' configuration, this report emphasizes the importance of the acceptor sites in setting the charge distribution throughout the sample. Another effect that has been observed when using similar levels of continuous illumination on this sample was a metastable population of the higher energy spin$\downarrow$ state associated with the $N = 0$ Landau level in the millikelvin CR experiment described in chapter 5 [5].

4.6.4 Comparison with earlier work

RSLC measurements have also been performed on the other Philips samples using a 2 K insert[4]. This experimental setup allowed for a controlled sample cooldown making it possible to reach the minimum carrier densities of the non-illuminated state. Above band gap radiation was provided only by a small red LED rather than directing a HeNe laser down an optical fiber. Sample G641 with a spacer layer of 1600 Å and a residual carrier density of $3 \times 10^{10}\text{cm}^{-2}$, exhibited identical behavior as G640. A brief burst of light from the LED raised N_s to a saturated value of $6 - 7 \times 10^{10}\text{cm}^{-2}$ and lowered the depletion field. Continuous illumination by the LED provides a metastable, maximum carrier density of $8.7 \times 10^{10}\text{cm}^{-2}$ and further reduces the depletion field. An equivalent of the dynamic equilibrium state was never reached due to the low level of illumination provided by the LED when compared to the HeNe laser employed in the ^{3}He experiment. Values for the depletion field were arrived by using the triangular-well approximation detailed in [17]. As noted earlier, this fitted the 'dark' data well but an offset was observed for the illuminated case. This discrepancy is to be expected as the light reduces the depletion field and serves flattens the band away from the interface. The potential then only approximates a triangle for the lowest confined subband.

4.7 Conclusions

The coupling between the Landau levels of adjacent subbands promoted by using tilted field measurements has been used to generate the conduction band profile in $GaAs/Ga_{1-x}Al_xAs$ heterojunction subjected to above band gap illumination. Despite

the very low carrier densities which resulted in weakly observable coupling, values of the depletion field have been calculated by comparing experimental and theoretical predictions for the value of the lowest subband coupling. A self-consistently generated potential has shown to be superior to the triangular well approximation especially under the experimental conditions studied where the density of carriers trapped in the 2DES is greater than the fixed space charge of the depletion layer. Four regimes of sample behavior have been outlined. The level of the shallow donor and D-X center impurity levels in the AlGaAs have shown to be critical in understanding possible physical mechanisms contributing to these different regimes. High levels of continuous illumination, however, cause a dynamic equilibrium which can only be qualitatively examined. This is true also for speculation as to the shape of the potential through the superlattice prelayer and into the substrate.

4.8 References

[1] R.Merlin, *S.S. Comm.* **64**, 99 (1987).

[2] S. Huant, M. Grynberg, G. Martinez and B. Etienne, *Semicon. Sci. Tech.* **65**, 457 (1988).

[3] G. C. Wiggins, *D.Phil thesis, Oxford*, (1990)

[4] G. M. Summers, *D.Phil thesis, Oxford*, (1993)

[5] J.G. Michels, S. Hill, R.J. Warburton, G.M. Summmers, P. Gee, J. Singleton, R.J. Nicholas, C.T. Foxon and J.J. Harris, *Surface Science* **305**, 33 (1994).

[6] M. Mooney, *J. Appl. Phys.* **67**, r1 (1990).

[7] P. Bhattacharya, *Semicon. Sci. Tech.* **3**, 1144 (1988).

[8] D.R. Leadley, *D.Phil thesis, Oxford*, (1989)

[9] F. Stern and S. Das Sarma, *Phys. Rev.* B **30**, 840 (1984).

[10] C.T. Foxon, J.J. Harris, D. Hilton, J. Hewett and C. Roberts, *Semicon. Sci. Tech.* **4**, 582 (1989).

[11] D.M. Symons, M. Lakrimi, R.J. Warburton, R.J. Nicholas, N.J. Mason and P.J. Walker, *Phys. Rev.* B **49**, 16614 (1994).

[12] S. Adachi, *J. Appl. Phys.* **58**, R1 (1985).

[13] W.H. Press, B.P. Flannery, S.A. Teukolsky and W.T. Vetterling, *Numerical Recipes*, Cambridge Univ. Press, 550,(1986)

[14] J.J. Harris, C.T. Foxon, K.W.J. Barnham, D.E. Lacklison, J. Hewett and C. White, *J. Appl. Phys.* **61**, 1219 (1987).

[15] G.Oelgart, G.Grummt, G.Lippold, R.Pickenhain, R.Schwabe and L.Lehmann, *Semicon. Sci. Tech.* **5**, 894(1990).

[16] F. Stern, *Phys. Rev.* B **12**, 4891 (1972).

[17] F. Stern and W.E. Howard, *Phys. Rev.* **163**, 816 (1967).

[18] M. Hayne, A. Usher, A.S. Plaut and K. Ploog, to be published in *Phys. Rev.*B.

Chapter 5

Cyclotron resonance to 100 mK of a GaAs heterojunction in the extreme-quantum limit

5.1 Introduction

The discovery of the quantum Hall effect in 1980 marks the point where growth techniques were able to produce structures whose physical behavior was governed by the properties of a two dimensional electron system (2DES). Further advances in growth technologies, reflected by vast increases in carrier mobility, preceded the discovery of the fractional Quantum Hall effect. These phenomena spurred investigation into the ground state of the 2DES at very low temperatures and large magnetic fields. Subsequent studies have provided evidence for competing phases of solid, liquid and gas-like behavior of the electrons which makes this topic both interesting and complex. This chapter details an optical investigation of the 2DES present in extremely high mobility $GaAs/Ga_{1-x}Al_xAs$ heterojunctions using cyclotron resonance (CR) absorption of far-infrared light. CR is shown to be a valuable tool for the study of these systems in the extreme quantum limit, when only the lowest Landau level is occupied and electrical transport measurements become impossible. Additionally, an important aspect of this investigation is that by using a Helium dilution refrigerator, the temperature range is extended below where the electrons are predicted to condense into an ordered solid or Wigner crystal, named after its proposer Eugene Wigner[1].

A two dimensional electron system is a specific type of plasma. Accordingly, the chapter begins with a brief discussion of plasmas, which focuses on their unique property of exhibiting a response to an external perturbing fluctuation that is dependent on the wavelength of the stimuli. This principle is then applied to the specific example of a two-dimensional electron system in a magnetic field which supports three classes of plasma excitation: inter-Landau level, spin resonance and intra-Landau level. Cyclotron resonance is an inter-Landau level excitation which is also referred to as the magnetoplasmon or magneto-exciton. A review of experimental and theoretical work on the magnetoplasmon highlights discrepancies between the two and the failure of any model to offer a convincing explanation for recently observed anomalies in the CR that are the subject of this chapter. A new theory by Nigel Cooper and John Chalker, which differs from earlier work by considering the Coulomb interactions between spin states of the lowest Landau level, is presented. Despite making some simplified assumptions,

the Cooper and Chalker model provides a convincing explanation for the experimental results.

A description of the setup for CR measurements at millikelvin temperatures precedes presentation of the experimental results. The results section is divided into three subsections based on the filling factor or occupancy of the Landau levels which marked different regimes of system behavior. In presenting the experimental data, the language of the Cooper and Chalker model is used to emphasize the excellent agreement between theory and experiment. Ending the chapter will be a discussion of a reasonable interpretation of the CR data and how this fits into the larger picture of a phase diagram for the 2DES in a perpendicular magnetic field.

5.2 Cyclotron resonance and the magnetoplasmon

A plasma is a collection of relatively mobile, charged particles that interact with one another via the Coulomb force. Intuitively, a plasma is pictured as an electrified gas or fluid that responds strongly to magnetic or electrical perturbations. Not so obvious perhaps, are solid state plasmas that are formed in the presence of a neutralizing background of positive charge from the donor and ionic charges that exist in semiconductors. A unique feature of plasmas is that despite the relative weakness of individual electron-electron interactions, the overall effect of Coulomb interactions can be large if the plasma is perturbed in a coherent way. This can be seen by consideration of the expression for the potential energy of a system of charged particles

$$V = \frac{1}{2}\int \frac{\rho(\mathbf{r})\rho(\mathbf{r}')d^3r d^3r'}{\epsilon_0 \left|\mathbf{r}-\mathbf{r}'\right|} \tag{5.1}$$

where $\rho(r)$ is the charge density at position $\mathbf{r}$. If the excitation is a charge density fluctuation of the form

$$\rho(\mathbf{r}) = \rho_{\mathbf{k}}\left(e^{ik\cdot r} + e^{-ik\cdot r}\right) \tag{5.2}$$

then the potential energy calculated from Equation 5.1 is

$$V_k = \left|\rho_k\right|^2\left(4\pi/\epsilon_0 k^2\right). \tag{5.3}$$

When the plasma is perturbed by a long-wavelength (short k) disturbance, the Coulomb energy according to Equation 5.3 is relatively large and forces the plasma to behave in

a collective way. If the perturbation has a sufficiently short wavelength (large k) then the Coulomb energy is small and the plasma behaves as a system of non-interacting particles.

The collective response of the plasma to a long wavelength perturbation occurs at the plasma frequency, ω_p. For bulk or three-dimensional semiconductors, the plasma frequency approaches a finite value as k goes to zero. In two-dimensions, however, $\omega_p \rightarrow 0$ when $k \rightarrow 0$. This can be seen from the expression for the 2D plasma frequency given by

$$w_p = \left[\frac{2\pi N_s k}{m^*}\right]^{1/2} \tag{5.4}$$

where N_s is the electron density and m^* the effective mass. When the 2D electron system is placed in a magnetic field, Landau quantization of the energy levels occurs and the plasma excitation modes occur close to integral multiples of the cyclotron frequency ω_c. At long wavelength the lowest of these modes is plasmon-like and is referred to as the magnetoplasmon. The magnetoplasmon mode is equivalent to the formation of a *magnetic-exciton*, which would correspond to the energy required to promote an electron from an occupied Landau level to unoccupied Landau level leaving a hole behind in the lower level. As a result, the dispersion relation of a 2DES in a perpendicular magnetic field can be expressed as

$$E(k) = \hbar\omega_c + \delta E(k) \tag{5.5}$$

with $\hbar\omega_c$ the cyclotron energy and $\delta E(k)$ the energy of the magneto-exciton which is due to the correlation between electrons. Pure cyclotron resonance corresponds to the zero k-vector limit of this dispersion.

For a system that is translationally invariant, cyclotron resonance is independent of any electron-electron interactions: the system resonates at a single frequency $\omega_c = eB/m^*$. This result is known as Kohn's theorem[3] and follows from the fact that the long wavelength electric field couples only to the center of mass motion. Kohn's theorem leads to the conclusion that $\delta E(k) \rightarrow 0$ as $k \rightarrow 0$. This has been confirmed by several calculations of the magnetoplasmon mode made by various authors[4]-[12]. However, translational invariance can be broken by dopant impurities, lattice defects or nonparabolicity of the conduction band, which could cause the $k \neq 0$ modes to mix with the cyclotron mode at

$k = 0$. Mode mixing can lead to changes in the effective mass and resonance linewidth.

The amount of mode coupling and its effect on the cyclotron resonance spectrum has been the topic of spirited debate over the past ten years. Theoretical treatment of the magnetoplasmon mode began with Kallin and Halperin[4] who examined a system with completely filled Landau levels and derived a dispersion relation pictured in Figure 5.1. $\delta E(k) = E - \hbar\omega_c$ goes to zero as k approaches zero which agrees with Kohn's theorem. For small values of k-vector, $\delta E(k)$ increases linearly from the origin. Further work

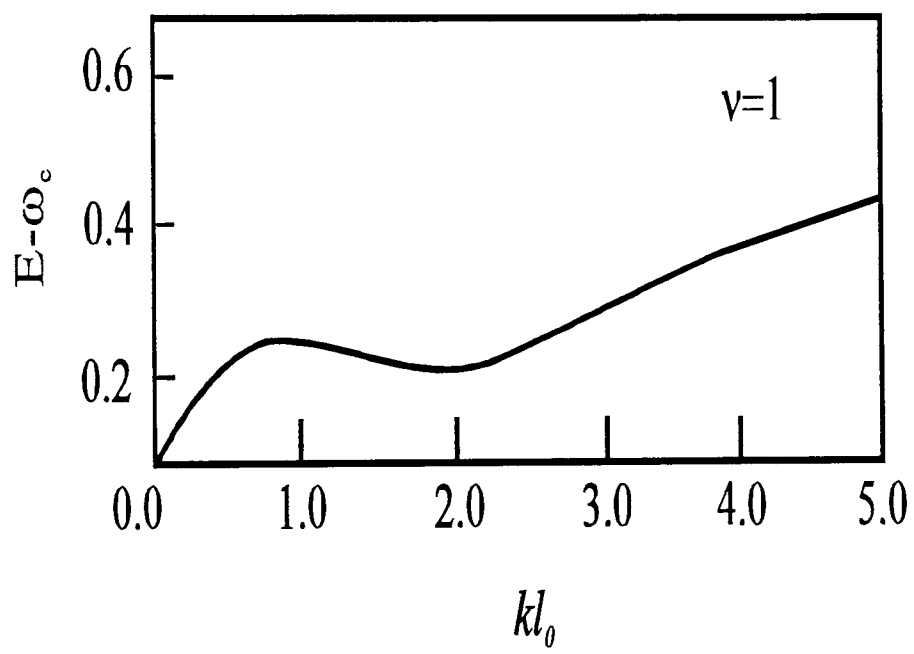

Figure 5.1: Exciton dispersion curve near ω_c for $\nu = 1$ for the case where all the electrons have the same spin. Taken from Reference [4].

by the same authors introduced the possibility of mode coupling caused by impurity centers in the lattice [5] which seemed to explain experimentally observed shifts to lower frequencies in the position of the CR and a narrowing of the resonance profile[6].

Calculations have also been performed for fractional filling values[7] using an approximation employed in descriptions of intra-Landau level collective excitations of the fractional quantum Hall effect states. The magnetoplasmon excitation energies for fractional filling factors $\nu = \frac{1}{m}$, $m = 1, 3, 5, 7$ are plotted in Figure 5.2. The dispersion curves reflect differences in the strength of the electron correlation function as ν is changed. The apparent stiffening of the magnetoplasmon modes when compared to integral filling was predicted to cause a narrowing of the CR linewidth at fractional filling factors.

Also predicted by studies of the magnetoplasmon for fractional values of ν was a huge enhancement of the effective g-factor that sets the magnitude of the Zeeman splitting; again due to the strong electron-electron interaction[8]. This effect would be particu-

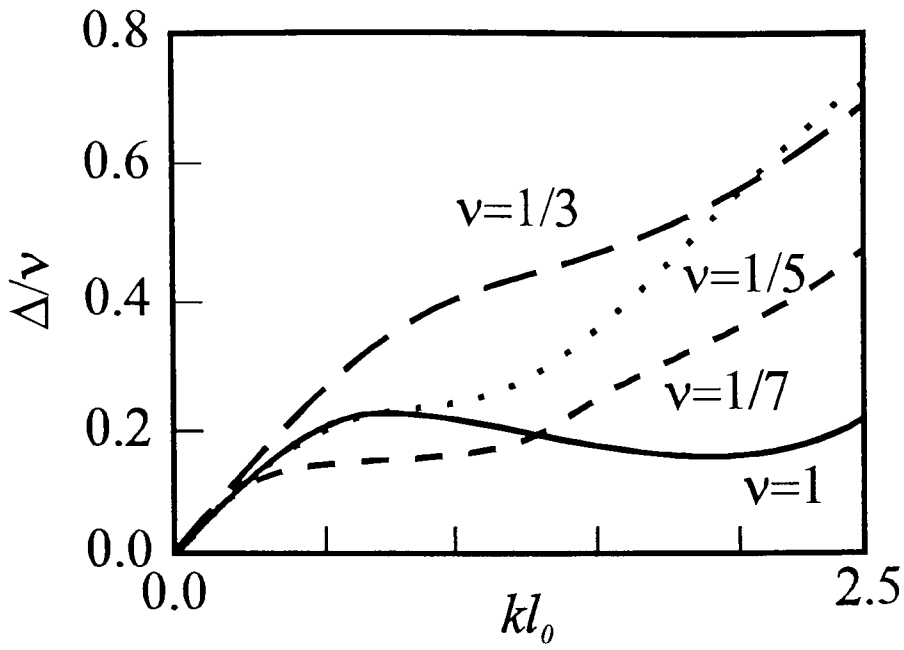

Figure 5.2: Magnetoplasmon excitation energies measured from $\hbar\omega_c$ (in units of $\nu e^2/l_0$ where l_0 is the larmor radius) for $\nu = 1$ (solid line), $\nu = 1/3$ (long-dashed line), $\nu = 1/5$ (dotted line), and $\nu = 1/7$ (short-dashed line). Taken from Reference [7]

larly strong for $\nu > 2$ when both $N = 0 \rightarrow 1$ and $N = 1 \rightarrow 2$ Landau level transitions are possible. An increase in the Zeeman splitting between the spin states would reduce the population of the upper or minority spin unless matched by significant rise in temperature because the relative population of both spin states is thermally activated. Exchange enhancement of the effective g-factor was often used as an explanation as to why only a single CR peak was seen at integral filling factors when both spin states were thought to be occupied[9].

Identification of band nonparabolicity as a cause behind the mixing of $k \neq 0$ modes to those at $k = 0$ was made by MacDonald and Kallin[10]. Even the smallest amount of band nonparabolicity was shown to allow the strong influence of electron-electron interactions to be revealed. In a result that will be important in the later section on the Cooper and Chalker model, the authors found that coupling between the two spin states of the lowest Landau level, could be activated by disorder or nonparabolicity. Despite the possibility of anomalies in the CR spectrum due to an exchange interaction between the spin states, MacDonald and Kallin calculated that any effects would be negligible since the coupled mode would be only weakly infra-red active.

Predictions of possible Wigner crystallization at low filling factors have led to very recent studies of the magnetoplasmon where the magnetic length is kept small relative to the interparticle spacing. Salkola[11] has predicted a shift and splitting of the CR line shape due to the pinning of the periodic crystal potential by potential fluctuations. Côté and

MacDonald find that for $\nu \leq \frac{1}{3}$ exchange effects become small and the strength of the collective excitation decreases as the occupancy is reduced[12].

5.3 The Cooper and Chalker model for CR in the extreme quantum limit

The most recent theoretical approach to explain the CR spectra of a two dimensional electron system in the extreme quantum limit was made here in Oxford by Nigel Cooper and John Chalker[13]. Their formalism is a marked departure from those detailed above in that it considers a *non-degenerate* system where Coulomb interaction between the two different spin states is taken into account. MacDonald and Kallin only ever considered degenerate systems where a Landau level (or spin state) was completely filled. Since coupling between Landau or spin levels requires an empty state in both the initial and final level of the electron transition, no coupling would be expected in a degenerate system. The Cooper and Chalker C&C model makes the following assumptions:

- carriers are placed on the sites of a triangular lattice; the exchange energy contribution is ignored because its effect would be negligible at the small filling fractions involved

- low temperatures mean that only the two spin states of the lowest Landau level are occupied; spin states separated by the Zeeman energy are pictured as being equivalent to a system with two types of carriers, each with a parabolic dispersion relation and slightly different effective masses

- population of the spin states is set by the physical temperature of the system through the Boltzmann distribution function

- the two spin states (or different type carriers) couple with each other through the Coulomb force; the strength of the coupling is proportional to the carrier density

- the cyclotron resonance transition involves transitions only into the corresponding spin states of the adjacent Landau level

- the negative g-factor of GaAs results in the spin↑ lying lowest in energy and therefore is the favoured or majority spin (Figure 5.4). The minority spin state resonates at a lower frequency and can be thought of as randomly distributed 'heavy' impurities in a sea of majority spin state.

Using these assumptions, C&C begin with the Hamiltonian of an interacting two component plasma where ground state is taken to be the Wigner solid with the electrons located at the sites of a triangular lattice. The eigenvalue equation for this harmonic system reduces to solving

$$\omega a_i = \delta\omega_i a_i + I \sum_j M_{ij} a_j \tag{5.6}$$

for the eigenvalues a_i. The frequency ω is measured relative to the cyclotron frequency of the majority spin state ω_c, in units of the splitting $\delta\omega_c$ so that $\delta\omega_i = 0, 1$ for the majority and minority spins respectively. I is the dimensionless interaction strength given by

$$I = \frac{e^2 l^2}{8\pi\epsilon\epsilon_0 a^3} \frac{1}{\hbar\delta\omega_c} = \frac{e}{\pi\epsilon\epsilon_0\kappa} \left(\frac{\sqrt{3}\nu e}{8hB}\right)^{3/2} \tag{5.7}$$

with the lattice constant $a = \left[\left(\sqrt{3}/2\right) N_s\right]^{-1/2}$ and $\delta\omega_c = \kappa B^2$. The matrix for Coulomb interactions is

$$M_{ij} = \begin{cases} \sum_{k\neq i} |\mathbf{R}_i - \mathbf{R}_k|^{-3}, & i = j, \\ -|\mathbf{R}_i - \mathbf{R}_j|^{-3}, & i \neq j. \end{cases} \tag{5.8}$$

where $\mathbf{R_i}$ is the equilibrium position of the i^{th} electron using units of the lattice constant. The form of the matrix reflects a co-ordinate transform that expands the potential about a minimum which is taken to be zero.

In order to examine behavior of the system over the entire range, C&C diagonalized Equation 5.6 numerically. A considerable amount of insight, however, can be gained from a simplified model which replaces the long range Coulomb interactions with an infinite interaction where each electron is coupled equally to all others regardless of relative position. Analytic expressions for the two supported frequency modes from this model enable quantitative evaluation of the experimental data within the C&C framework.

The simplified model begins by assuming infinite range interactions with a coupling constant α which is inversely proportional to the total number of particles N. Under

these conditions, the coupling matrix becomes

$$M_{ij} = \begin{cases} \frac{\alpha}{N}(N-1), & i = j, \\ -\frac{\alpha}{N}, & i \neq j. \end{cases} \tag{5.9}$$

By inspection, the matrix can be expressed as

$$IM_{ij} = \alpha \mathbf{1} - \frac{\alpha}{N}\mathbf{K} \tag{5.10}$$

with $\mathbf{K}$ a vector of the form

$$\mathbf{K} = \begin{pmatrix} 1 & 1 & . & . & 1 \\ & & . & & \\ 1 & & . & & 1 \end{pmatrix} \tag{5.11}$$

Solutions are of two types: those where the particles resonate independently of one another and those where there is collective or center of mass motion of the particles. Independent motion of the particles has an oscillator strength of zero and so are 'optically inactive.' The two 'optically active' modes have finite oscillator strength and reflect collective behavior of the system.

The system of N electrons is divided into the two spin states with $(1-p)N$ spin$\uparrow$ (majority spins) and pN spin$\downarrow$ (minority spins) where p is the concentration of minority spin. Considering only the optically active modes, we guess solutions u, v for the spin$\downarrow$ and spin$\uparrow$ states respectively

$$a_i = \begin{cases} u & 1 < i < (1-p)N \\ v & (1-p)N < i < N. \end{cases} \tag{5.12}$$

Equation 5.6 provides two coupled equations

$$\omega u = \alpha u - \alpha([1-p]u + pv) \tag{5.13}$$

$$\omega v = -v + \alpha v - \alpha([1-p]u + pv) \tag{5.14}$$

which are then expressed in matrix form

$$\begin{pmatrix} \alpha p - \omega & -\alpha p \\ -\alpha(1-p) & \alpha(1-p) - 1 - \omega \end{pmatrix} \begin{pmatrix} u \\ v \end{pmatrix} = 0. \tag{5.15}$$

Diagonalizing and solving gives the two optically active modes which represent the in-phase and out-of-phase oscillations of the two spin populations, with frequencies

$$\omega_{in} = [\alpha - 1 - \sqrt{(1-\alpha)^2 + 4\alpha p}]/2, \tag{5.16}$$

$$\omega_{out} = [\alpha - 1 + \sqrt{(1-\alpha)^2 + 4\alpha p}]/2. \tag{5.17}$$

The oscillator strength is given by

$$S = \frac{1}{N} \frac{\left(\sum_n a_n\right)^2}{\sum_n a_n^2} \tag{5.18}$$

which reduces to

$$S_{in} = 1 - S_{out} = \frac{\omega_{out} + p}{\omega_{out} - \omega_{in}}. \tag{5.19}$$

A comparison of the simple model to the full numerical calculation requires that $\alpha = 11.034I$ which means that the sum of the interaction matrix over all neighbors is the same as that obtained when the position of the electrons is taken into account.

Experimental results are presented in terms of temperature, carrier density and the splitting between the two resonance positions. A move from the C&C terminology to the experimental parameters is straightforward. The temperature in Kelvin determines the proportion of electrons with minority spin using the simple Boltzmann relation

$$p = \frac{1}{1 + e^{\frac{E_z}{kT}}} \simeq exp(-E_z/kT) \tag{5.20}$$

where the Zeeman energy $E_z = \mu_B(g^* + g^{'}B)B$. B is measured in Tesla and $g^{'} = 0.004T^{-1}$ represents the slight field dependence of the g factor. The total carrier density N_s enters the interaction strength I with $I \propto N_s^{3/2}$. The splitting of the CR corresponds to

$$\omega_{in} - \omega_{out} = \sqrt{(1-\alpha)^2 + 4\alpha p}. \tag{5.21}$$

There is a critical value of $\alpha = 1$, corresponding to the density at which the splitting will go to zero at low temperatures, and which will give a single strong collective resonance at higher temperatures. This will be used later to define a critical occupancy ν_c which separates a radical difference in the system's response to changes in temperature.

In the experimental results section, it should become clear that the Cooper and Chalker model successfully reproduces the temperature and density dependence of the CR spectra obtained in the extreme quantum limit. The success of this model is primarily due to the insight that it is the Coulomb interaction between electrons residing in the different spin states underlying the observed change from a single resonance at high densities to a split resonance at low densities. All previous models failed because they considered only the completely filled Landau or spin levels of degenerate systems.

5.4 Experimental setup

The experiments described here consist of monitoring the transmission of radiation through high mobility GaAs/$Ga_{1-x}Al_xAs$ heterojunctions as a function of either frequency or magnetic field, using either a far-infrared laser or Fourier transform spectrometer. Chapter 4 outlines the ^{3}He system used in conjunction with a Fourier transform spectrometer so only the experiments which employed the dilution refrigerator and far-infrared laser will be covered in this section. The extension of cyclotron resonance experiments into the millikelvin temperature and magnetic field range where Wigner crystallization is predicted to occur presents a formidable problem. The silicon bolometer which serves as a highly sensitive infra-red detector must be positioned in such a way as to allow it to capture the maximum amount of light transmitted through the sample without having its output influenced by changes in the magnetic field.

There is the additional problem of getting the far-infrared (FIR) radiation from the CO_2-pumped laser to the sample deep in the innards of a helium dilution refrigerator, which lies in the bore of a 17.5 T magnet. For this purpose, a highly polished, evacuated brass light pipe was inserted down through the many vacuum spaces into the sample chamber. Thermal conduction was minimized by dividing the pipe into sections corresponding to the room temperature, 77 K, 4 K and 1 K portions of the refrigerator and isolating each section with insulating material. Internal light pipe filters also had to be added at these stages to exclude the large black body heat load which is peaked around $10-20\,\mu$m but still let through the measurement wavelengths of $50-1000\,\mu$m. A series of crystalline quartz and black polythene filters were used such that only wavelengths longer than $\sim 50\,\mu$m passed through, essentially blocking all but the long wavelength tail of the room temperature Planck distribution, and conveniently just letting through the $57\,\mu$m laser line needed to match the cyclotron frequency for fields of $\sim$ 13 T. Even so, a specially designed cold finger had to be made from high conductivity copper in order to maximize the cooling power of the refrigerator and enable it to keep the sample below 100 mK. The cold finger assembly with the FIR lightpipe and the bolometer arrangement is shown schematically in Figure 5.3.

These steps enabled the dilution refrigerator to hold base sample temperatures of nearly

50 mK, as measured with RuO_2 resistors. Cyclotron resonance measurements were made in the range from $50 - 1000$ mK on high mobility GaAs/$Ga_{1-x}Al_xAs$ heterojunctions grown by MBE at Philips Research Laboratory, Redhill [14]. The samples had spacer layer thicknesses of 4800, 1600 and 1200 Å with carrier densities after illumination from 12 to 3 $\times 10^{10}$cm^{-2}. Continuous reduction of the density by up to 70% was achieved *in situ* by using above barrier illumination from a red or green HeNe laser carried to the sample by a 1 mm glass optical fiber. With energy greater than the AlGaAs band gap, this light served to further depopulate the 2DES; a power density of 10^{-3} W/cm^2 reduced the lower bound on the carrier concentration to 1 $\times 10^{10}$cm^{-2}. The power density was altered through the use of externally placed neutral density filters. Little difference in resultant carrier concentration was observed between equivalent power densities of the red and green HeNe. The dilution refrigerator was reasonably tolerant of this additional source of heat, holding base temperature for all but the largest power densities, with a full HeNe power of 0.5 mW.

Electrical contacts allowed simultaneous transport measurements to be made on the high density sample, enabling a precise comparison of optical and transport measurements of the carrier density. Conversion of absorption strength to carrier concentration was made using the classical Drude absorption formula as in previous ^{3}He cryostat experiments [15][16] that used both the CO_2-pumped FIR laser and a Fourier transform spectrometer. No differences in CR position or intensity were detected between data taken at comparable densities and temperatures, either between measurements with different samples, different illumination conditions, or different refrigeration systems.

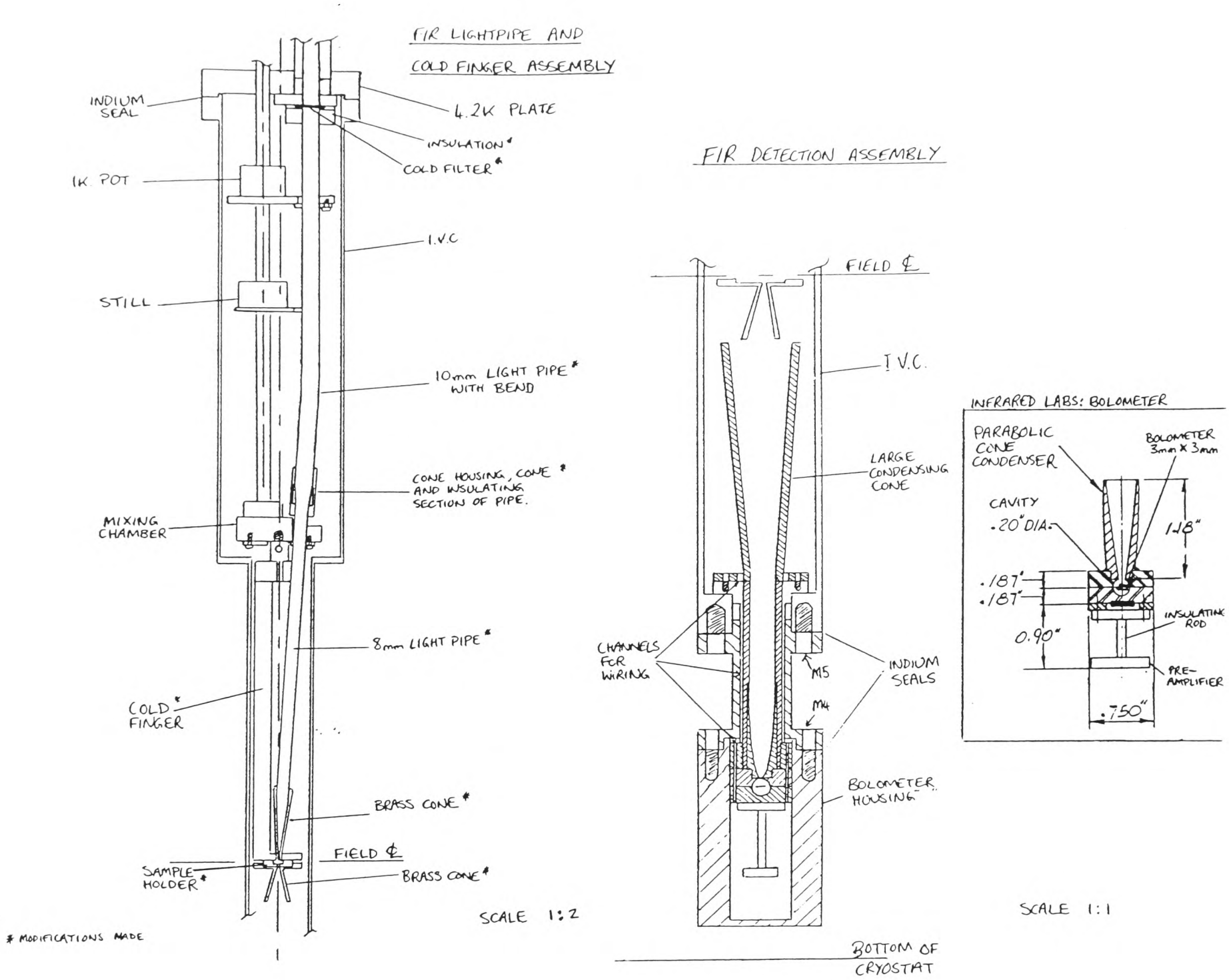

Figure 5.3: [a] A schematic diagram of the FIR lightpipe and cold finger assembly. [b] Detail of the sample mounting and silicon bolometer placement.

5.5 Cyclotron resonance in the quantum limit

The dilution refrigerator measurements are an extension of previous CR experiments performed in Oxford[15][16] and elsewhere[17][18]. These studies demonstrated that there was a considerable population of both spin states in the extreme quantum limit which was surprising given the failure to observe a split resonance at higher densities and temperatures. Motivation for using the dilution refrigerator was to lower the plasma temperature well below the classical Wigner solid melting temperature T_c, to see if the temperature and density dependence of the CR splitting observed at higher temperatures continued. The data and consequent analysis are best understood within a framework where the range of filling factors is divided into three regions: $1 < \nu < 2$, $\frac{1}{6} < \nu < 1$, and $\nu < \frac{1}{6}$. While this chapter concerns itself with data taken in the extreme-quantum limit ($\nu \ll 1$), it relies to a large extent on previous experimental and theoretical work in each of the listed regimes.

5.5.1 Two spin regime $1 < \nu < 2$

Generally, spin splitting of the Landau levels is the result of the Zeeman interaction but only manifests itself in CR measurements because of the energy dependence of the g-factor, which changes the magnitude of the splitting for successive Landau levels. This leads to two possible transitions for an electron going from the $N = 0$ to $N = 1$ Landau level as shown schematically in Figure 5.4. The expected single particle behavior of a 2DES should be identical to that found in high purity, low carrier concentration bulk GaAs, which has a $N = 0$ g-factor of ~ -0.4. resulting in two spin-conserving transitions split by 60 mT (3 K) at 13 T with the spin$\uparrow$ state lowest in energy. For lattice temperatures below 2 K this means that the spin$\uparrow$ transitions become dominant. The spitting also has a characteristic B^2 dependence because the magnetic field enters both the Zeeman energy difference between the spin levels and the g-factor difference between the ground and first Landau level. The predicted field location of the spin$\uparrow$ and spin$\downarrow$ transitions is carrier concentration dependent due to band nonparabolicity

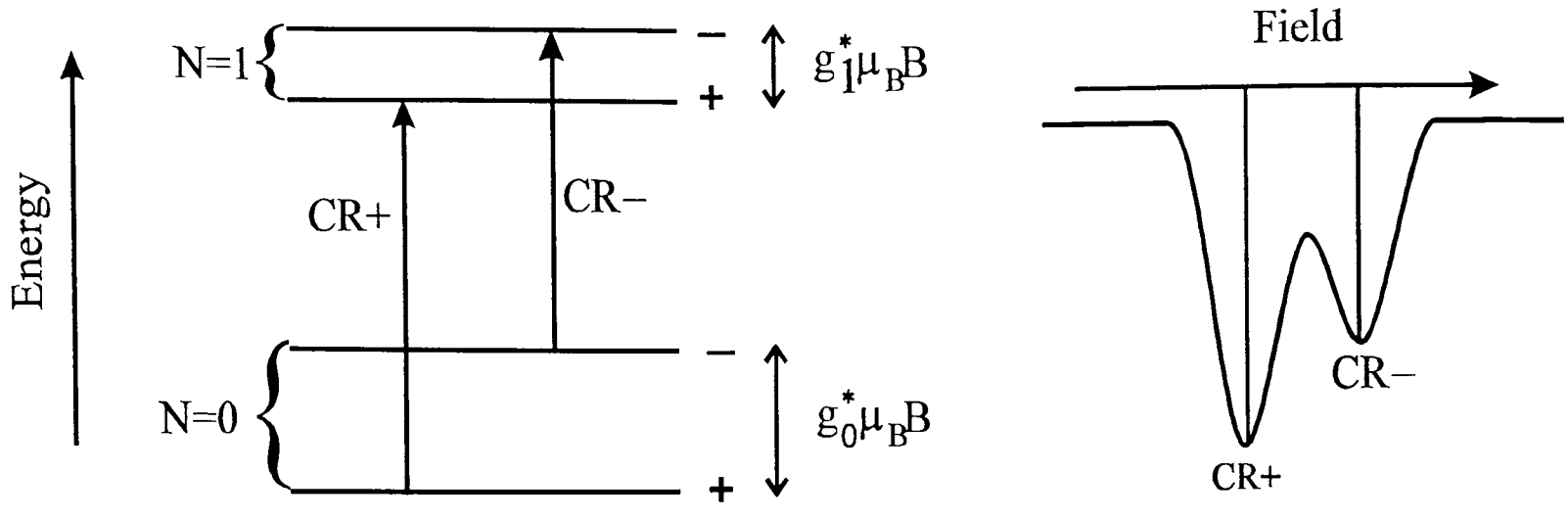

Figure 5.4: possible CR transitions from the $N = 0$ Landau level and the resultant spin splitting of the CR absorption spectrum

and can be calculated by the formula

$$m^* = m_0 \left[1 - \frac{2K_2}{E_g}(E_{CR}+ < T_z >)\right] \tag{5.22}$$

where K_2 is the slope of the effective mass when plotted as a function of energy, m_0 is the band edge effective mass, $< T_z >$ is the kinetic energy due to shape of the 2DES confinement potential, E_{CR} the cyclotron energy and E_g the GaAs band gap[19][20]. Whereas previous studies estimated $< T_z >$ from the Fang-Howard variational wave function, the resonant subband Landau-level coupling work detailed in Chapter 4 has enabled a more accurate determination of this parameter and a better fit between the C&C model and experimental results than had been previously thought.

Initial experiments [9] in very high mobility GaAs/AlGaAs heterojunctions for $1 < \nu < 2$ where both spin states are populated, failed to observe a splitting of the CR, despite experimental linewidths that were considerably smaller than the expected splitting. The observation of a single sharp resonance was attributed to plasma mode mixing or hybridization of the two spin transitions [9], resulting in a single coupled resonance although mixing of the spin states was predicted to be weak and only activated by disorder[10]. By contrast, recent work in InAs quantum wells, where the g-factor is much larger (-15), does show separately resolved resonances from different spin states of the same Landau level [21]. This splitting disappears, however, for the sample with highest mobility, leading the authors to conclude that the lower amount of disorder in high mobility samples results in a system with strong translational symmetry leading

to a likely hybridization of the two spin states. This suggestion becomes applicable in discussion concerning the origin of the two observed CR peaks in the extreme-quantum limit.

5.5.2 The fractional regime $\frac{1}{6} < \nu < 1$

Transport data showing several well defined fractional quantum Hall states in this region led researchers to try and correlate shifts in cyclotron resonance positions or changes in absorption linewidths to filling factors associated with the FQHE. In reports on high mobility GaAs heterojunctions, Seidenbusch *et al*[22] and Rikken *et al*[23] have suggested that there was a small oscillation in the CR linewidth at 4.2 K, which is rather high for observation of the FQHE. These studies have been countered by other workers [24]-[26] who could find no significant effects. Taken as a whole, experimental results of this controversial topic provide no *conclusive* evidence for the observation of the FQHE by CR, although the majority of experiments have been performed between 0.5 and 2 K, where the FQHE features are not particularly strong.

Recent ^{3}He data on the very high mobility Philips samples demonstrated that deviations in the linewidth and effective mass over a large field range were very small indeed[27]. The dilution fridge provided the capability to extend this work down to 100 mK. A comparison of the cyclotron masses for a large wavelength range ($1223 - 57\,\mu$m) with simultaneous transport measurements in a sample which shows a clearly resolved series of FQHE features, is shown in Figure 5.5. No anomalies in the effective mass are seen at fields corresponding to fractional filling factors, and a single resonance is always seen for $\nu > \frac{1}{6}$. Both of these results provide evidence for the insensitivity of the CR to the electron-electron interactions responsible for the FQHE.

While not finding any evidence of FQHE states, recent CR measurements in this regime [15][16] have found a systematic shift in resonance position as the temperature is varied. This temperature dependence appears to have an onset at $\nu \sim \frac{1}{3}$ and becomes more pronounced towards smaller filling factors. Changing the temperature from 2 K to 300 mK for $\nu = \frac{1}{3} \rightarrow \frac{1}{6}$ resulted in a continuous shift of the resonance position downwards in field. The total shift in position was up to half of the single particle spin splitting.

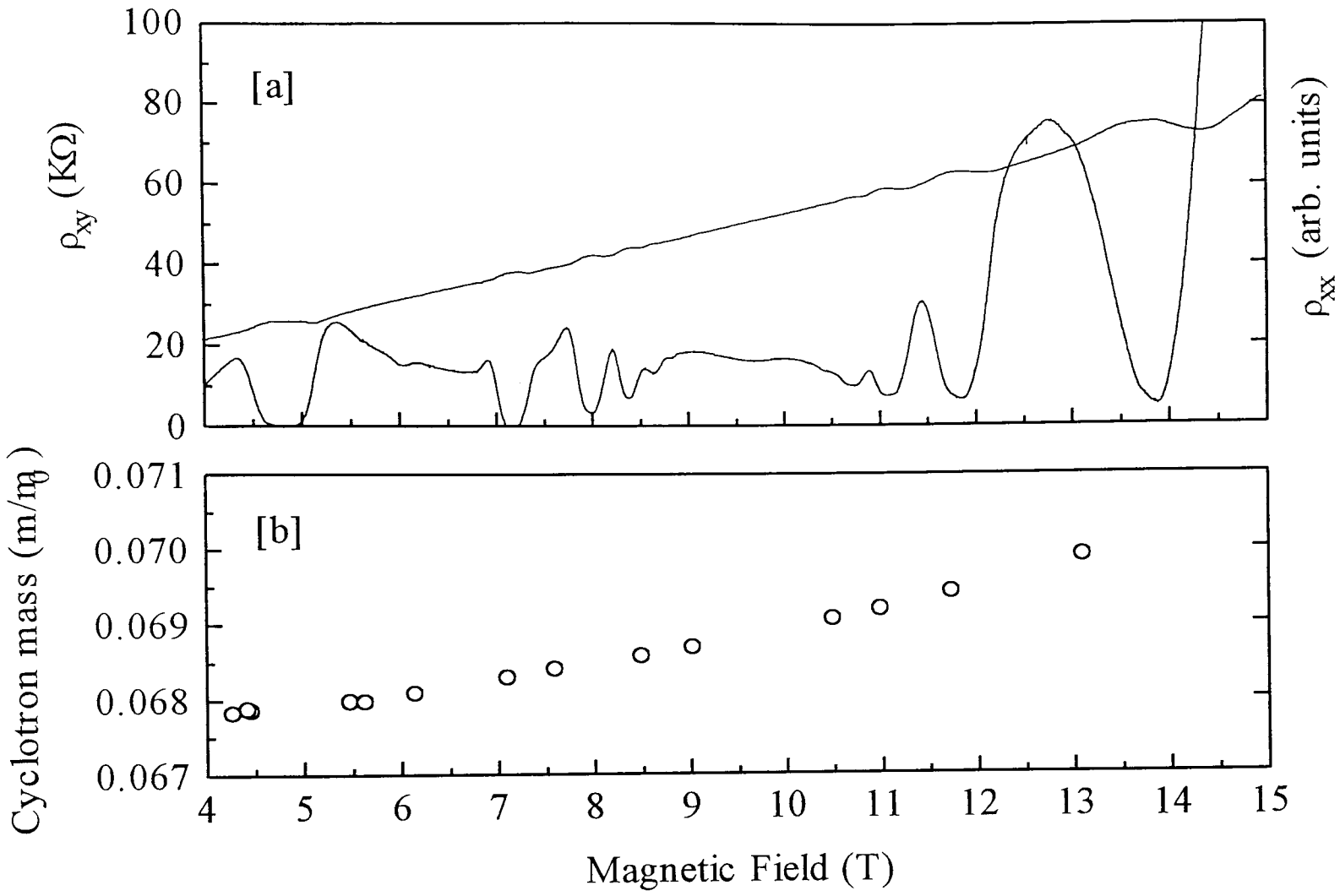

Figure 5.5: [a] Hall and diagonal resistivity traces for the sample with 1200 Å spacer layer thickness. Note the well defined FQHE effect features at $\nu = 1/3, 2/5, 3/7, 3/5, 2/3$. [b] The cyclotron effective mass increases linearly with increasing field if the slight contribution from band nonparabolicity is ignored.

5.5.3 The extreme quantum limit $\nu < \frac{1}{6}$

5.5.3.1 Magnetic field dependence

Significant and unusual features in the CR spectrum do begin to occur once the occupancy falls below $\nu = \frac{1}{6}$. The appearance of a second resonance was reported independently by two groups [16][17], and although initially cited as evidence for the Wigner solid, Nicholas et al. [16] quickly demonstrated that the magnitude of the observed splitting at very low densities ($\nu \rightarrow 0$) was identical to that of high purity bulk GaAs. This interpretation was strengthened by pulsed magnetic field measurements of the Philips' heterojunctions up to 90 T where the splitting was found to accurately follow the expected B^2 dependence[16][29]. The possibility of impurity shifted CR, thought to have influenced earlier measurements on less pure samples[26][28], was discounted due

to the highly systematic dependence of resonance positions and intensities on carrier density. This correspondence is continuous from one sample to the next, and independent of other factors such as spacer layer thicknesses, illumination states and cool-down history.

5.5.3.2 Temperature dependence

An important clue that CR was influenced by intra-Landau level electron-electron interactions was provided in a series of measurements that plotted the position and intensity of the dual peaks as a function of temperature and filling factor. Summers *et al*[15] showed that the position and intensity of the resonance peaks were strongly carrier density and temperature dependent and that these differences could not be explained in a single-particle picture. A critical occupancy ν_c of $\sim \frac{1}{10}$ divided regions differing dramatically in their response to changes in temperature (Figure 5.6). This behavior was interpreted in terms of a competition between a weakly interacting gas-like phase separated at ν_c from a more strongly interacting liquid-like phase.

Below ν_c, the resonance peak positions vary little with decreasing temperature but the *intensity* of the spin↑ transition is increased relative to the spin↓ so that, at low temperatures, most of the carriers are seen to reside in this lower energy state. In the low density limit (i.e. $\nu \rightarrow 0$) the absolute positions of both resonances correspond very accurately (± 5 mT) to the field positions in bulk GaAs, measured with the same system. Above ν_c, the resonance peak positions merge together with decreasing temperature to join into a single resonance also close to the predicted spin↑ transition.

The temperature dependent behavior of the CR either side of ν_c is almost uncannily duplicated by C&C numerically generated spectra pictured in Figure 5.7. When comparing the two figures remember that the ordering of the peaks is reversed between a magnetic field sweep (experiment) and an energy sweep(theory). The best fit was reached with values of the interaction strength $I = 0.05$ and 0.1 which are slightly down on the experimental densities that give $I = 0.1, 0.17$. This discrepancy is attributed to the finite thickness of the 2D electron gas which is thought to reduce the strength of the electron-electron interaction. Similar results have been seen previously in models

of the fractional quantum Hall effect[30] which indicated that a finite layer thickness causes a reduction in the energies of the quantum liquid by factors of order $0.5 - 0.7$. No adjustment was made in the conversion from experimentally recorded temperatures to p, the population of the higher energy minority spin state. In the low temperature limit, the C&C theory faithfully reproduces the experimental result of having almost all the electrons in the favoured spin$\uparrow$ state located at $\omega = 0$. At high temperatures, the single-particle picture remains valid (Figure 5.7[a]) as nearly equal population of the two spin states is seen at the highest experimental temperature of 1.7 K.

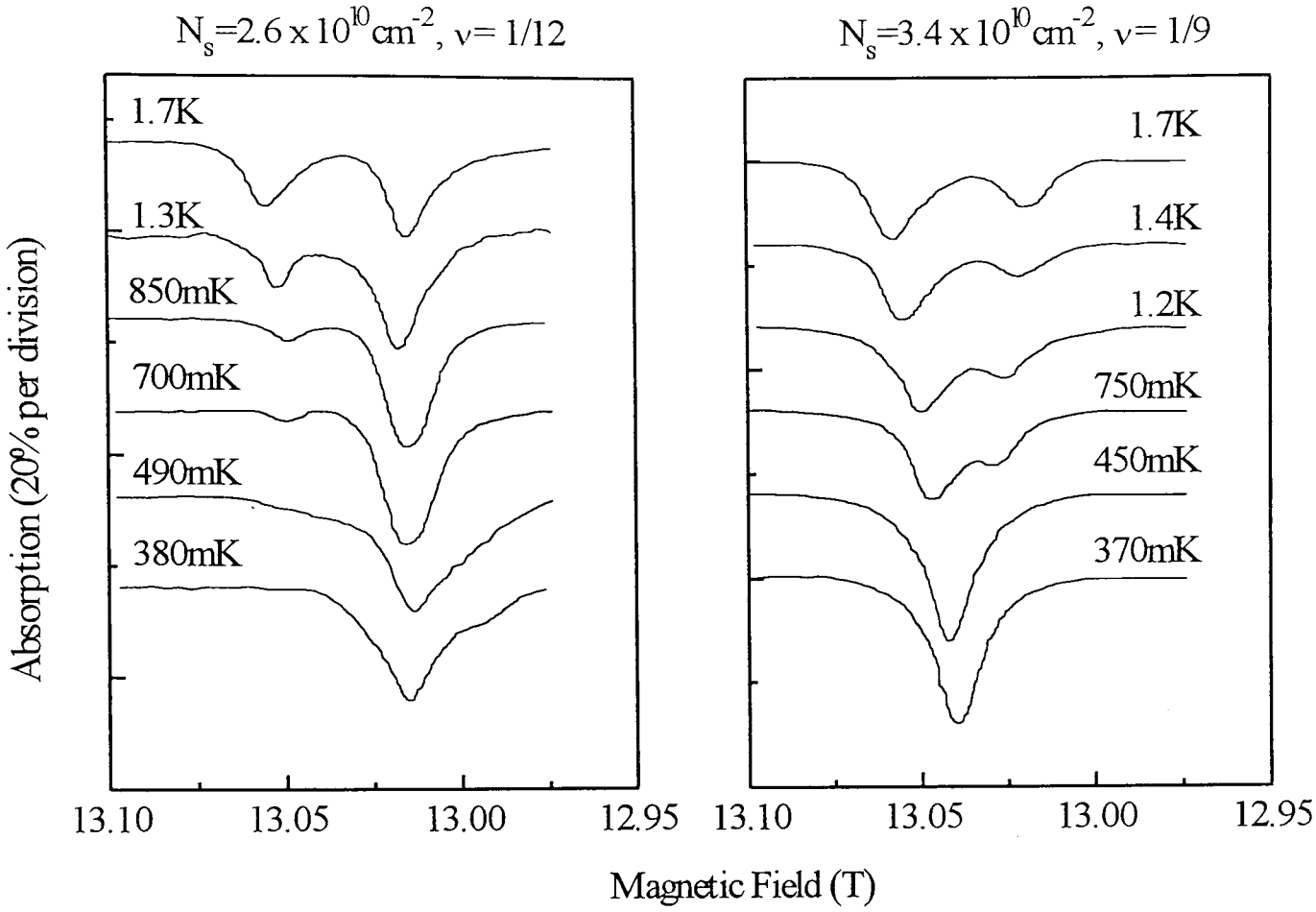

Figure 5.6: CR traces are shown as a function of temperature for occupancies $\nu = \frac{1}{12}$ and $\frac{1}{9}$, either side of $\nu_c = \frac{1}{10}$.

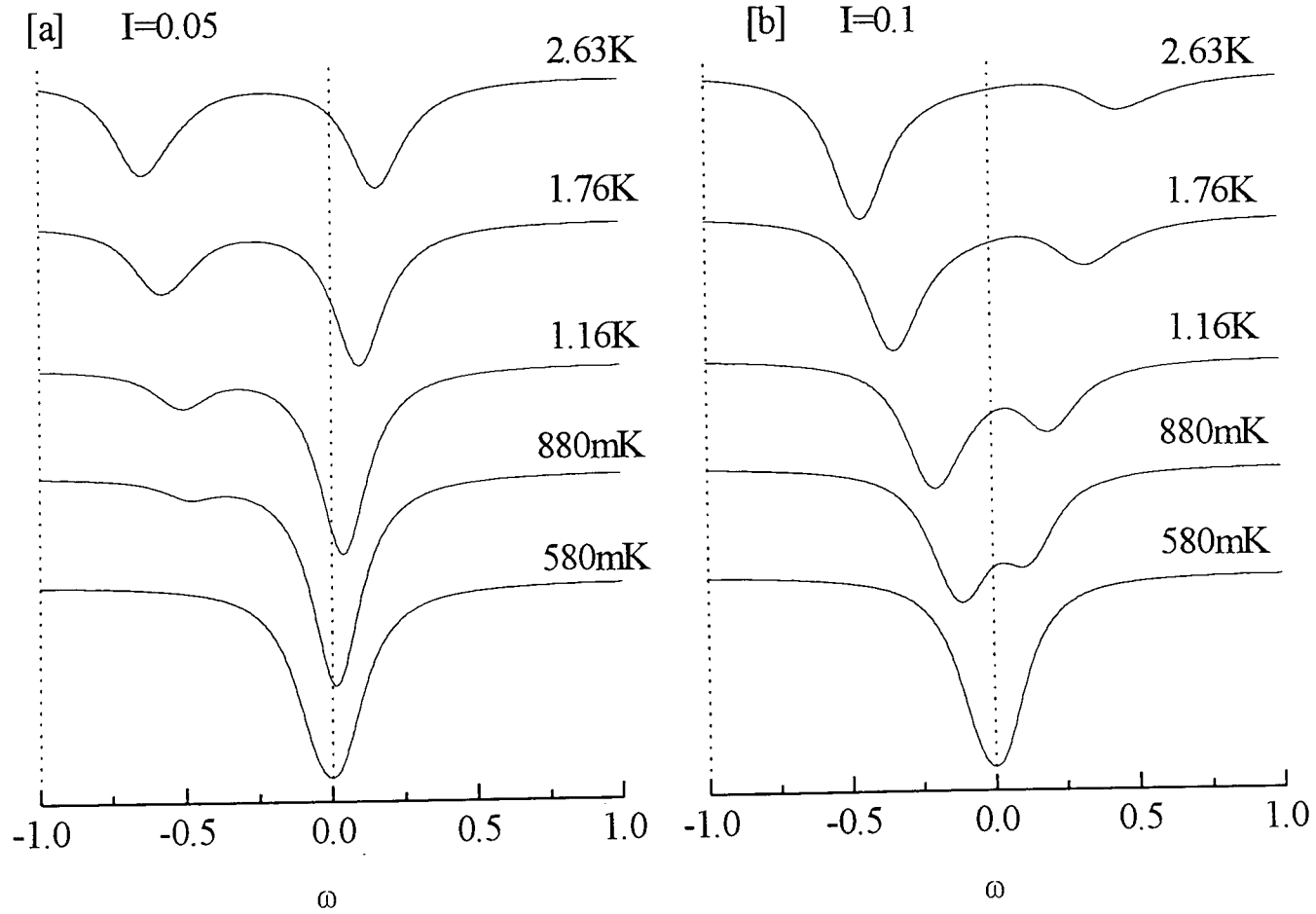

Figure 5.7: Theoretical CR spectrum calculated with [a] $I = 0.05$ and [b] $I = 0.1$. The spin populations for a given temperature are set by the Zeeman splitting using the single-particle g-factor.

Dilution refrigerator experiments demonstrate the continued existence of a critical occupancy to temperatures below 100 mK. Data was recorded at a fixed carrier density, controlled by the level of continuous illumination, as a function of increasing temperature. Figure 5.8 shows transmission spectra obtained for a FIR wavelength of 57 μm at a filling factor which is [a] just above $\frac{1}{8}$, [b] just below $\frac{1}{18}$, and [c] at the critical occupancy of $\frac{1}{10}$. These traces were taken in the dilution refrigerator and are the extension of Figure 5.6 to lower temperatures. Analysis of the peak intensities indicates that the total carrier density is constant and independent of temperature and magnetic field.

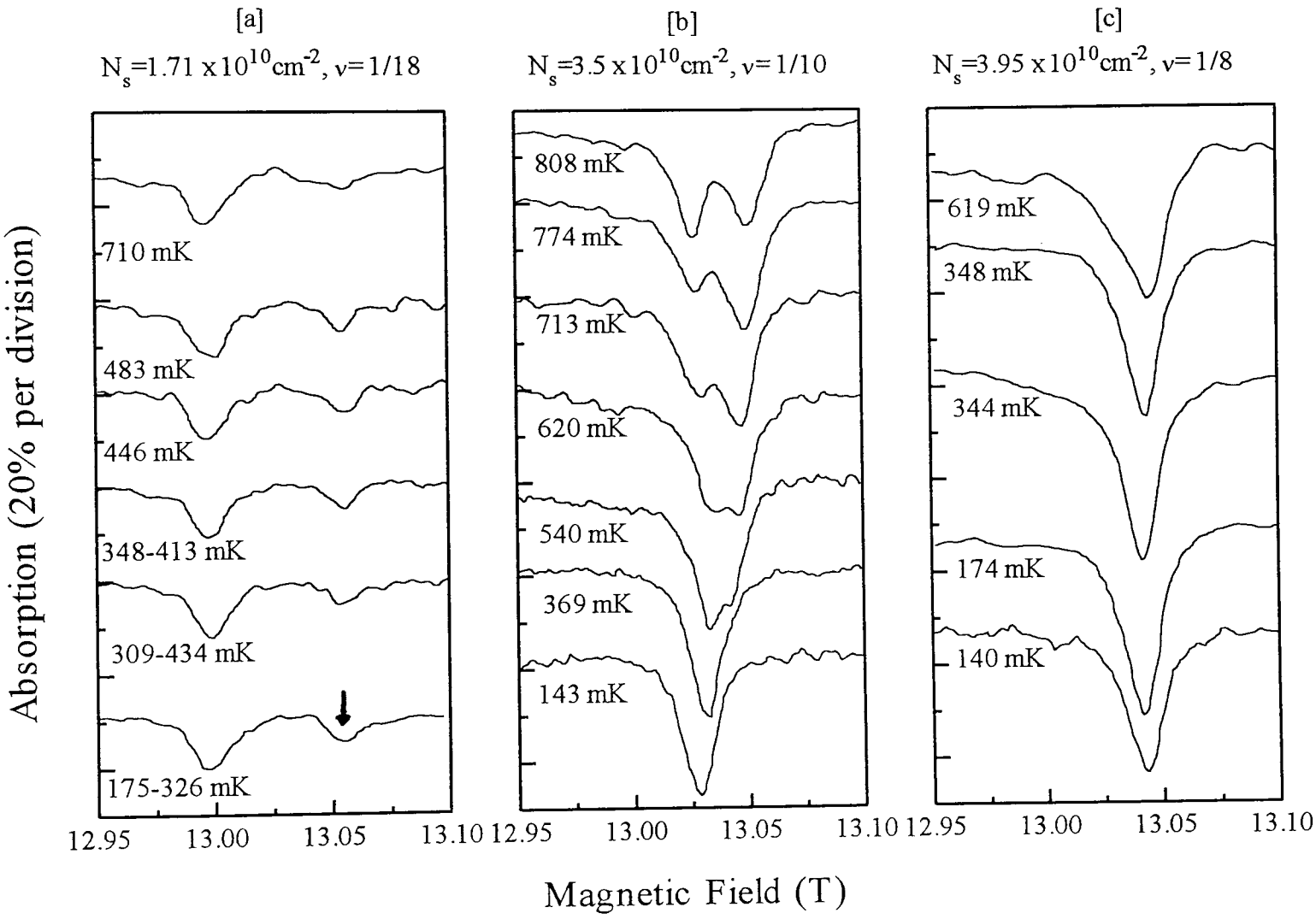

Figure 5.8: Experimental traces from the dilution refrigerator down to 140 mK for an infrared wavelength of 57 μm and filling factors of 1/18, 1/10 and 1/8 which is [a] below, [c] just above and [b] at the critical occupancy of 1/10.

Very little temperature dependence is seen below the critical occupancy (Figure 5.8[a]), with most of the carriers contained in the low field (spin$\uparrow$) transition. The weak high field resonance (indicated by an arrow in Figure 5.8[a]) is probably an experimental artifact due to a metastable population of the spin$\downarrow$ state; a consequence of the high illumination intensity used to depopulate the heterojunction and the relatively long

spin relaxation time. For $\nu = \frac{1}{8}$ (Figure 5.8[c]), there is little visible shift in resonance position for the single peak as the temperature is lowered. This is due only to our high temperature limit of $\sim 600\,\mathrm{mK}$ which fails to show a shift that principally occurs from $500\,\mathrm{mK}$ to $2\,\mathrm{K}$.

At the critical occupancy of $\frac{1}{10}$ (Figure 5.8[b]), a decrease in temperature results in the same merging of the resonances as was observed for the higher range of temperatures of the ^{3}He experiment and at $\sim 540\,\mathrm{mK}$ a single resonance is formed. A further reduction in temperature slightly shifts this single resonance towards lower field. The temperature influence on the field positions of the two spin resonances is more clearly shown in Figure 5.9, which is a composite picture of the resonance positions as a function of temperature, for a range of occupancies $\nu = \frac{1}{9} - \frac{1}{11}$ *close* to the critical occupancy. The range of the plot ($60\,\mathrm{mT}$) is equal to the single particle spin splitting, and demonstrates that the splitting is already well below this value by $1\,\mathrm{K}$, and that the two resonances collapse to a single peak at temperatures below $\sim 540\,\mathrm{mK}$. The temperature, $540\,\mathrm{mK}$, at which the resonances in Figure 5.9 collapse together corresponds to a temperature of approximately 1.5 times the classical Wigner solid melting temperature for these densities.

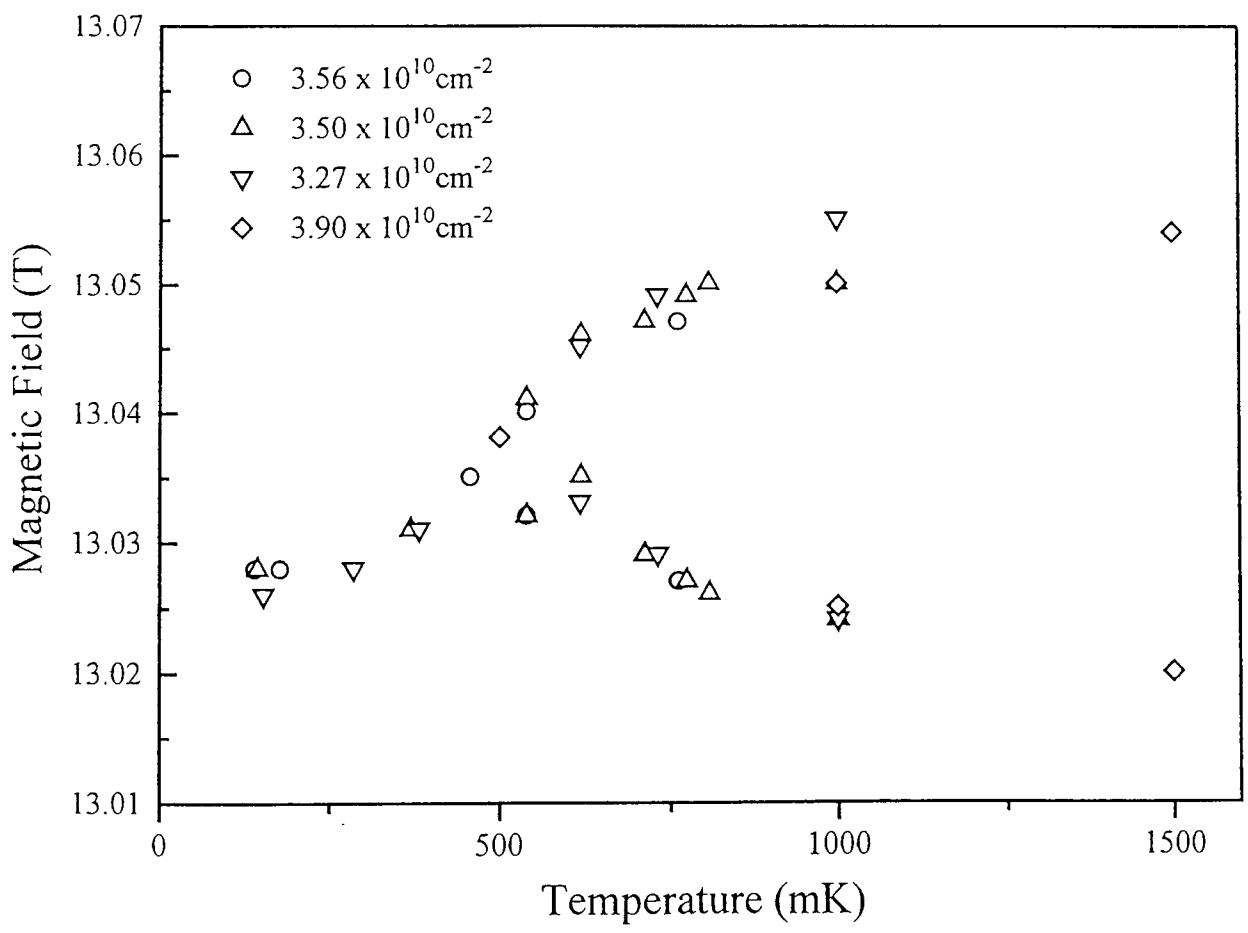

Figure 5.9: A composite picture of the resonance positions for a range of carrier concentrations, close to the critical occupancy of $\nu = \frac{1}{10}$.

5.5.3.3 Density dependence

The density dependent behavior of the system for a fixed temperature is shown in Figure 5.10[a] at 16 T and 2.2 K, where the occupancy is varied from $\sim \frac{1}{50}$ to $\sim \frac{1}{3}$. Above $\nu = \frac{1}{6}$ the absorption spectrum consists of a single peak but further reduction in the occupancy results in the appearance of a second peak which gradually gains in intensity. The field position of the second resonance at lower densities corresponds to the majority spin↑ state. Figure 5.10[b] shows the Cooper and Chalker generated CR

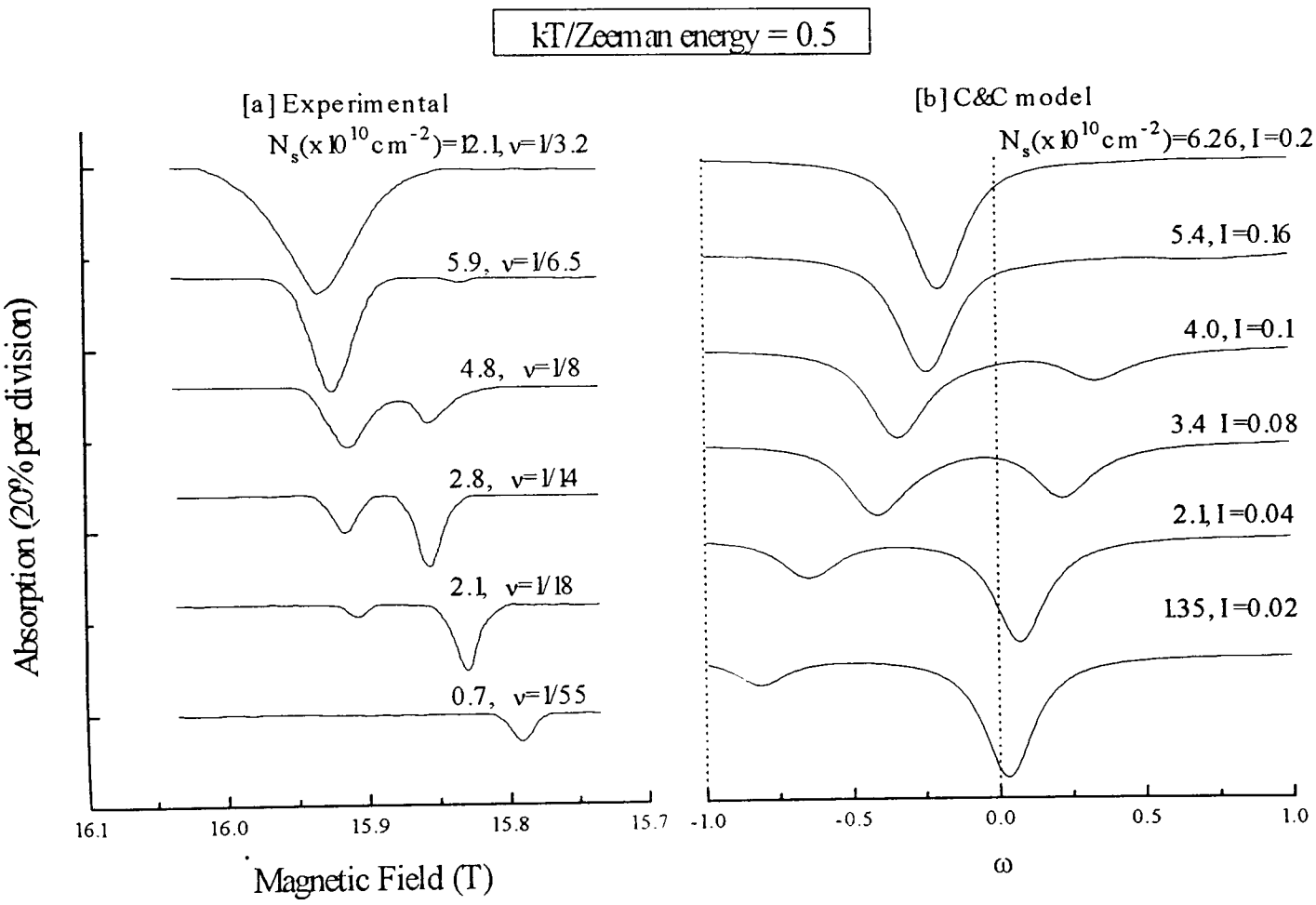

Figure 5.10: [a] The density dependence of the CR at 16 T and 2.2 K covering the occupancy range $\frac{1}{50}$ to $\frac{1}{3}$. [b] Cooper and Chalker predicted CR spectra when $T = 0.5$. The slight shift in resonance position with density due to nonparabolicity is not included in the theoretical calculation.

spectra keeping the temperature fixed as the interaction strength is varied. The dotted line marks the position of the favoured spin↑ transition at $\omega = 0$. In comparing these two pictures, the effect of band nonparabolicity which shifts the resonance positions as the density is varied during the experiment, must be taken into account. Even with this complication, an excellent agreement between theory and experiment is reached.

The existence of a critical occupancy below which complete spin polarization occurs, continues at the low temperatures achieved by the dilution refrigerator. Figure 5.11 shows CR traces taken at $\sim 150\,\mathrm{mK}$ where the occupancy is varied from $\sim \frac{1}{18}$ to $\sim \frac{1}{8}$. Starting at densities near the critical filling factor, there is a small continuous shift in the single resonance position due to the normal effect of band nonparabolicity. At very low densities two resonances are observed with the lower field spin↑ resonance as the most intense and the second, weaker resonance just below the field expected for the spin↓ transition in bulk GaAs. As mentioned previously, the small high field peak is probably a result of the high levels of continuous illumination used to depopulate the heterojunction.

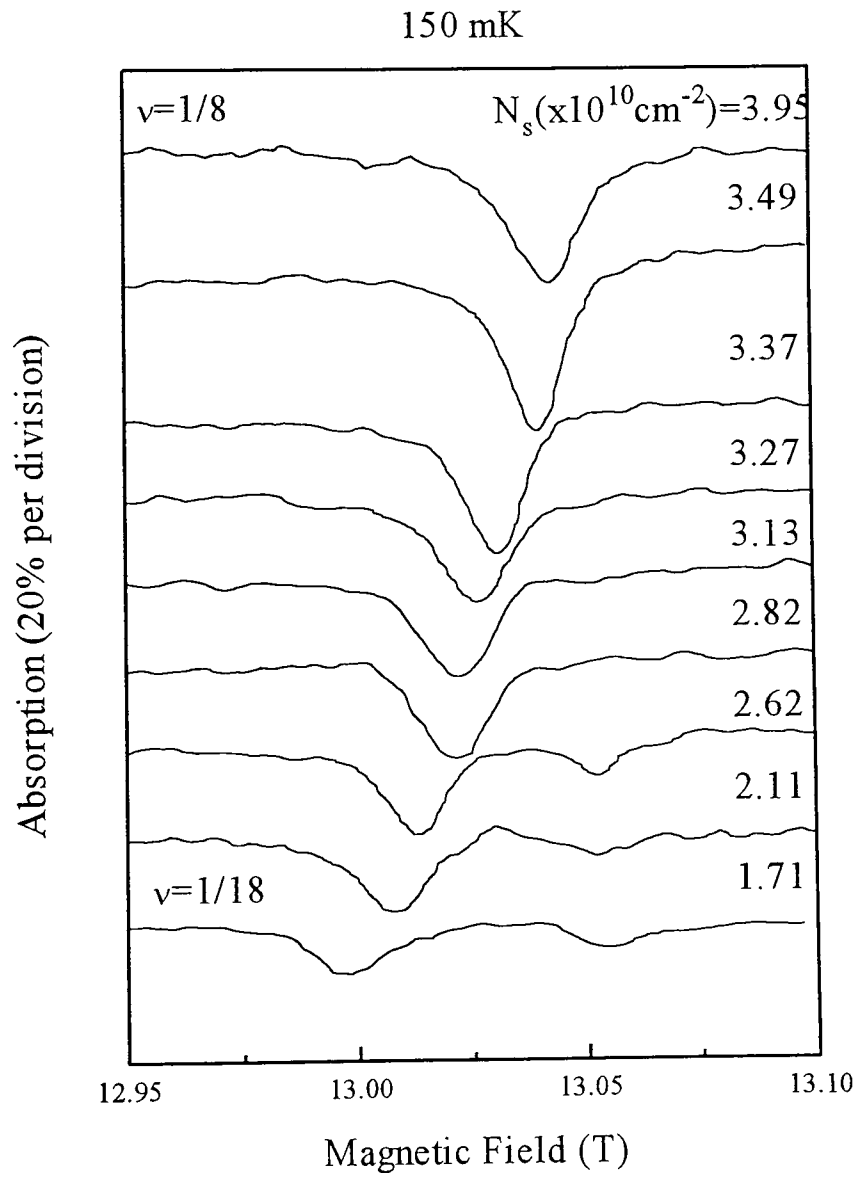

Figure 5.11: CR traces taken at 150 mK. The resonance position of the single peak changes as a function of density due to the effect of band nonparabolicity. Almost complete spin polarization is seen below the critical occupancy at very low temperatures.

When defining a critical occupancy that separates single-particle and collective behavior of the CR, it is important to have an accurate prediction of the spin↑and spin↓ resonance field position. In the absence of electron correlation, this is given by Equation 5.22 which includes the effect of band nonparabolicity. The problem with this formula is that it depends on a value of $< T_z >$ which is the kinetic energy due to confinement of the electron wavefunction in the z-direction. Previously published data employed the Fang-Howard variational wavefunction to estimate $< T_z >$[31]. As was shown in Chapter 4, the shape of the confinement potential and hence $< T_z >$, is very sensitive to the amount of visible illumination. The variational approach is a poor approximation especially when large amounts of visible illumination have flattened the conduction band through the depletion layer, which is the case in all the low density measurements.

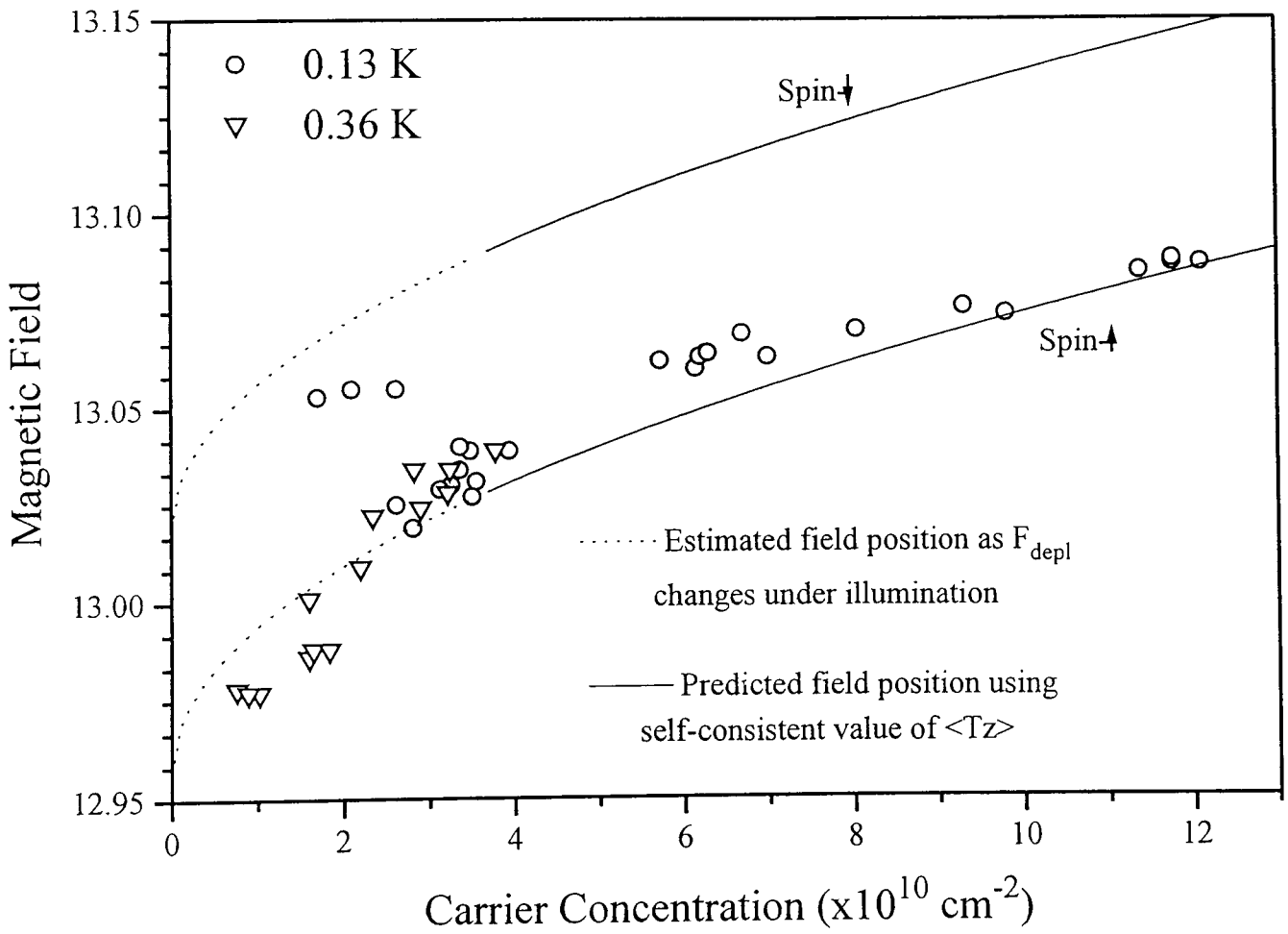

Figure 5.12: A composite picture illustrating the shift in resonance position with carrier concentration. The solid lines show the expected behavior of the spin-states due to band nonparabolicity with a self-consistent value for $< T_z >$. An accurate value for $< T_z >$ is not known for small N_s so a reasonable estimate of the kinetic energy is used to give the dotted lines (see text).

A self-consistently generated potential from the resonant subband Landau level coupling

measurements in Chapter 4 has enabled a much more accurate determination of $< T_z >$. Using these values for the kinetic confinement energy, experimental CR field positions are shown to lie close to the spin↑ resonance position in the low temperature limit as is predicted in the Cooper model. Intuitively this makes sense because regardless of the interaction strength due to the carrier density, coupling between the two spin states can only occur when there is a thermally activated population of the higher energy spin. Figure 5.12, shows dilution refrigerator data combined with previous ^{3}He work at 360 mK. Solid lines mark the predicted shift in resonance position with band nonparabolicity using self-consistent values of $< T_z >$. At very low densities, with $N_s < 4 \times 10^{10}$ cm^{-2}, the depletion field is no longer constant. These carrier concentrations are outside of the range surveyed in Chapter 4, so an approximation is made where the depletion field drops linearly with the carrier concentration. This is indicated by the dotted lines.

5.6 Comparing theory and experiment

The many cyclotron resonance experiments performed at different temperatures and densities, have provided an enormous quantity of data. In the previous section, the data was divided into into three groups corresponding to different values of the filling factor and then further subdivided by experiment; *i.e.* density held constant while temperature was varied, etc. Visual inspection of experimental traces when compared to the Cooper and Chalker model showed excellent agreement between the two spectra. It would be preferable, however, if there was a way to combine data taken at different densities and temperatures and present it using the Cooper and Chalker formalism. The analytic expressions derived from the simplified model allow for such a comparison. An overview of the process involves three steps:

- Seven different density values were selected spanning the range from $3.5 - 0.5 \times 10^{10}$cm^{-2}. For each density, the magnitude of the spin splitting for a given temperature was recorded. These points were then fitted to Equation 5.21 to derive a value of α which is the interaction strength of the simplified model.

- The interaction strength is then plotted against density.
- A critical density $\nu_c(T)$ which corresponds to the point at which the splitting is a minimum is defined. Since this also corresponds to the point where the two peaks swap intensities, it allows for a differentiation between gas-like and strongly correlated liquid behavior of the plasma.

It should be clear following this analysis, that the Cooper and Chalker model provides an excellent description of cyclotron resonance in the ultra-quantum limit.

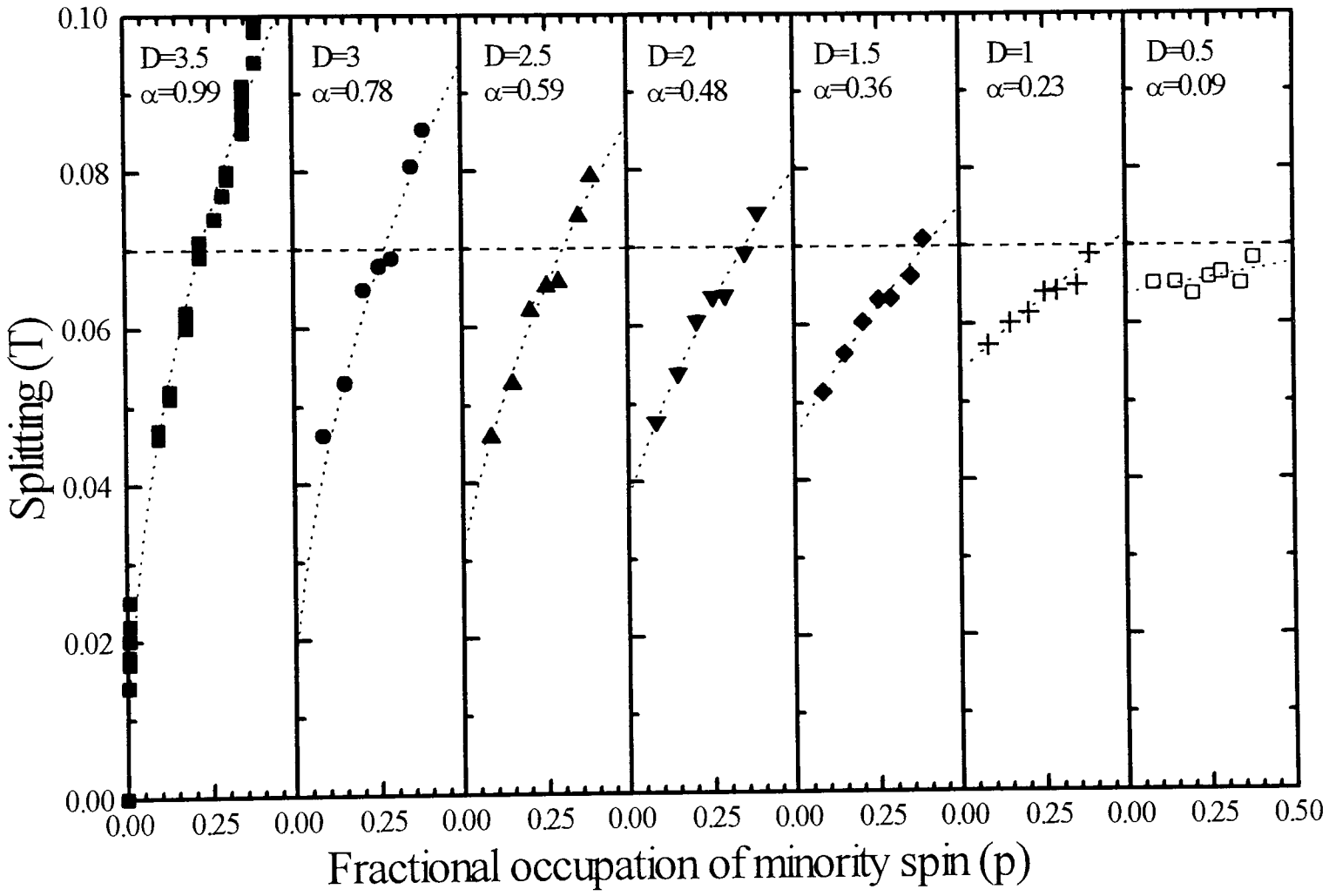

Figure 5.13: Temperature dependence of the two cyclotron resonance spin-split transitions measured at 13 T, for a series of densities. The splitting is fitted using Equation 5.21 with the spin population calculated from the Boltzmann factor. The horizontal dashed line shows the single particle spin splitting which is 70 mT.

Figure 5.13 plots the magnitude of the splitting for data from .3 to 8 K as a function of fractional occupation of minority spin, assuming that the value of p is given only by the Boltzmann factor calculated using Equation 5.20. The splitting is fit to Equation 5.21 with α as the fitting parameter, recalling from Section 5.3 that α is the coupling constant of the simplified model. The interaction strength of the full matrix diagonalization

$I = (\alpha/11.034)$ is then plotted against the experimental density in Figure 5.14. The solid line shows the values for α calculated from Equation 5.7 assuming a reduction in the electron-electron interaction strength by a factor F= 0.65. This reduction was used as a fitting parameter and agrees with the estimated effect of the finite thickness of the 2DES in the experiment. As mentioned earlier, studies of the FQHE [30] have indicated that the finite layer thickness of the 2DES causes a reduction in the energies of quantum liquids by factors of order $0.5 - 0.7$.

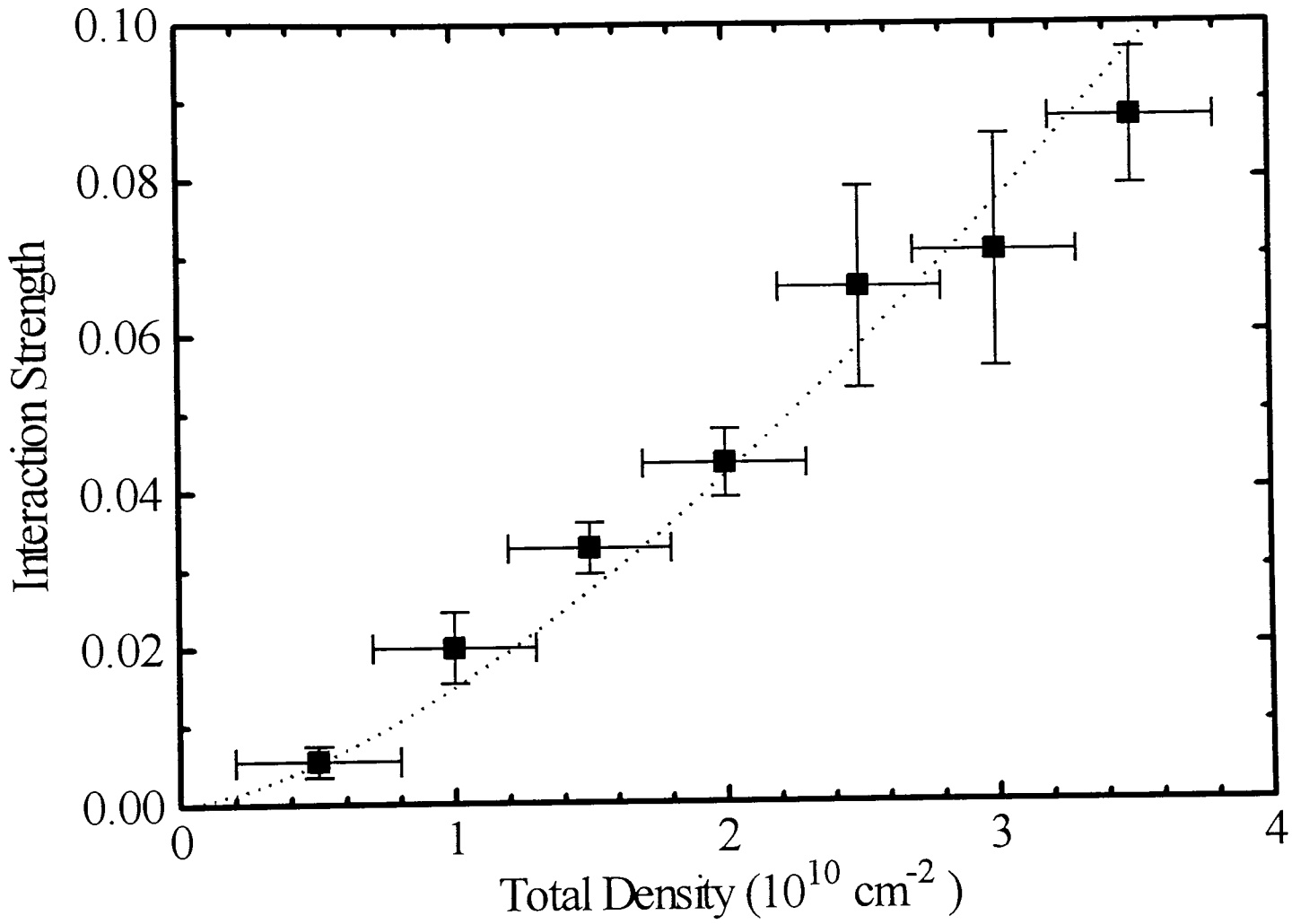

Figure 5.14: The fitted values for the interaction strength given by $I = \alpha/11.034$ are plotted as a function of density deduced from the splittings shown in Figure 5.13. The dashed line shows the predictions of Equation 5.7 if the interaction strength is scaled down by a factor of 0.65.

The critical occupancy $\nu_c(T)$, is defined as the density at which the observed splitting is a minimum ($\alpha = 1 - 2p$ from Equation 5.21) which also corresponds to the point of equal resonance intensity ($S_{in} = S_{out}$).

$$\nu_c = \left(\frac{\pi \epsilon \epsilon_0 \kappa (1-2p)}{11.034 e \hbar F} \right)^{2/3} \frac{8hB}{\sqrt{3}e} = 8.14 \times 10^{-3} (1-2p)^{2/3} B \qquad (5.23)$$

$F = 0.65$ is the reduction in interaction strength due to the softening of the Coulomb potential by the wavefunction extent in the z direction. For GaAs at 13 T, Equation 5.23

gives $\nu_c(T) = 0.106(1-2p)^{2/3}$.

Figure 5.15 shows the predicted phase boundary from Equation 5.23 compared with critical occupancies measured from the experimental minimum splitting at 13 T. There is an excellent agreement between the theoretical line and experimental points. The Wigner solid boundary deduced from earlier measurements is also shown[32, 33].

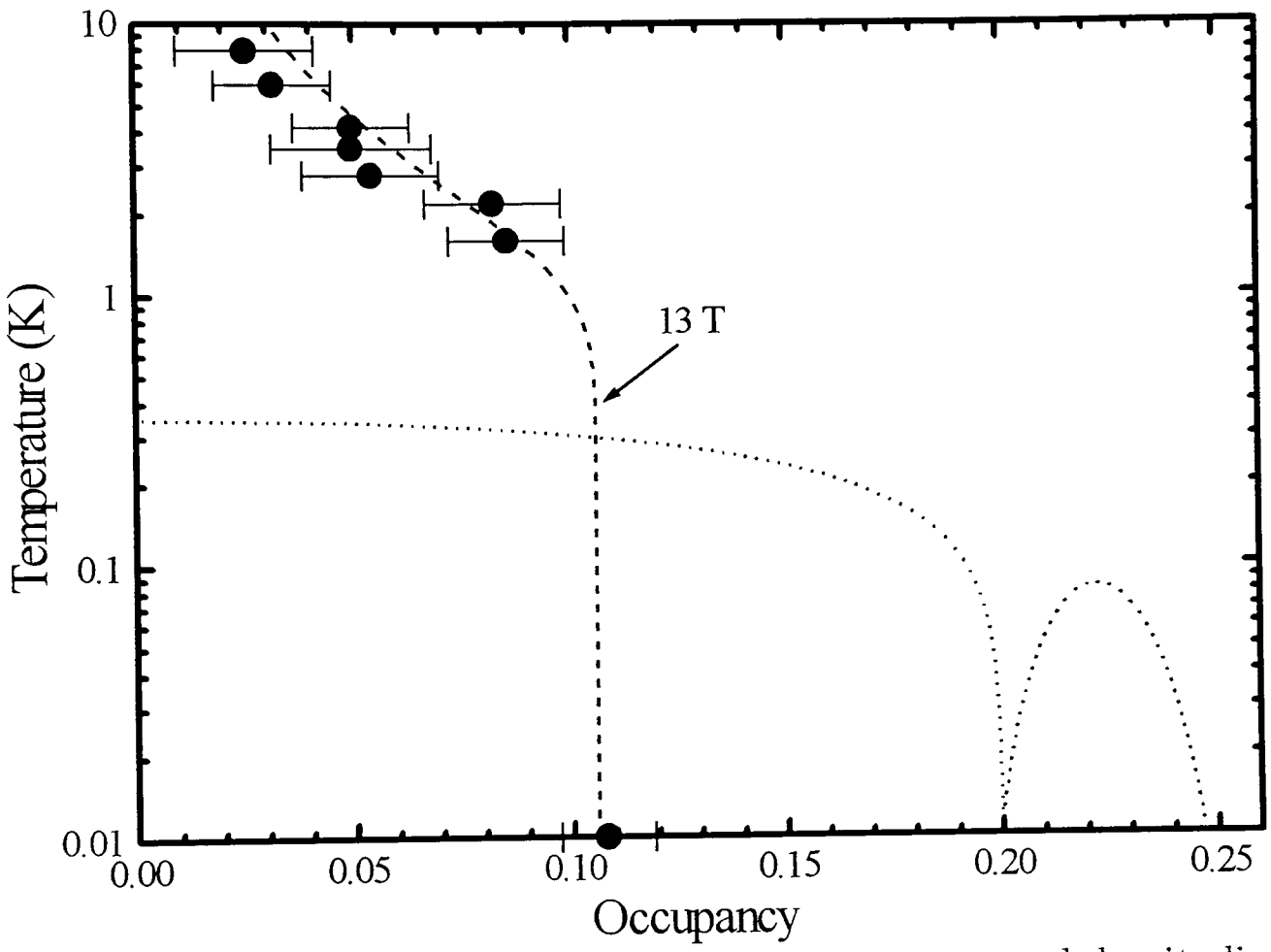

Figure 5.15: A diagram of the 2DES in the low temperature and density limit showing the theoretically predicted critical occupancy for GaAs at 13 T. The points are taken from an experimental determination of the minimum splitting for a given density. The dotted line is a schematic picture of the Wigner solid phase as proposed in references [32, 33].

$\nu_c(T)$ defines a boundary between the single particle gas-like behavior and collective liquid-like behavior. For filling factors less than $\nu_c(T)$, two CR peaks are seen with a splitting close to that seen in bulk GaAs. The intensity of the carriers in each peak as a function of temperature is satisfactorily explained by single-particle statistics indicating a gas-like excitation. The low temperature and low occupancy region is characterized by almost complete spin polarisation with the majority of the carriers in the lower energy spin$\uparrow$ state. Occupancies greater than ν_c act as a liquid, characterized by the interplay between the Coulomb force and Zeeman energy which results in the striking temperature dependence.

5.7 Discussion

I will now discuss the origin of the behavior seen in the CR and how it relates to the wider topic of the phase diagram of the 2DES at low temperatures and densities. It seems clear especially after the convincing duplication of experimental CR spectra by the Cooper and Chalker model, that the spin states of the electrons play a central role in determining inter-Landau level excitations. Simple disorder or impurity effects can be discounted because of the very high mobility of the samples and the consistent behavior of different samples when measured at comparable density and temperature.

The origin of spin-splitting of the Landau levels lies in the nonparabolicity which lifts the spin degeneracy of the conduction band through the inclusion of a k^4 term identified as the k-dependent contribution to the g-factor[34]. Nonparabolicity is also the culprit behind the slight shift in g-factor that results in a difference between the $N = 0 \rightarrow 1$ spin$\uparrow$ and spin$\downarrow$ transitions. Either disorder or nonparabolicity is sufficient to overcome the restrictions of Kohn's theorem, which allows the CR to be influenced by the electron-electron interactions.

While the CR is evidently not measuring single particle behavior of the 2DES it is an accurate probe of the spin composition of the ground state of the interacting electron system as a function of temperature and density. The fact that the splitting at very low densities is equal to the single particle spin splitting suggests that the very low density limit corresponds to pure spin states. A single peak observed at high densities and the coalescing of two peaks at the critical occupancy presents a more complicated problem. Prior to publication of the Cooper and Chalker formalism, a spin pairing mechanism was proposed as a possible explanation[27],[31]. The merging of the two resonances into one is suggestive of a realignment of spin orientation or possibly the formation of a state where the spins are aligned in plane of the 2DES which would lead to either $S = 0$ or $S_z = 0$. Theoretical[35] and experimental[36] studies have indicated that a mixed spin state can occur for certain fractional quantum Hall liquid states notably at $\nu = 2/3$ and $2/5$. A recent calculation of low density 3D electron systems by Moulopoulos and Ashcroft [37] indicates that an $S = 0$ spin-singlet arrangement is energetically favorable except at very low densities to the Wigner crystal which is antiferromagnetic. The au-

thors postulate that a reduction to two dimensions would increase the tendency toward a spin pairing. The major problem with the spin paired interpretation is that there is no clear analogue to another system where spin behavior exhibits both a density and temperature dependence. Cooper and Chalker did investigate possible exchange mechanisms without conclusive results either in support or contradiction of this premise[38].

If the experimental data taken at intermediate densities is ambiguous, the low density behavior is not and leads to the conclusion that two different types of particles are involved to produce the independent resonances. Perhaps a closer look should have been made of the early Appel and Overhauser study of Si inversion layers[39]. The conduction band of Si contains two minima which lie close in energy. When uniaxial stress is applied, the cyclotron resonance changes from having a single peak to a split peak. These structures were described as being composed of two different electron systems interacting through electron scattering processes. The computationally generated CR spectra bears a close resemblance to that from the GaAs heterojunctions; strongly supporting the Cooper and Chalker insight that the spin states define the two systems with an interaction supplied by the Coulomb force rather than particle collisions.

Although it is likely that the Appel and Overhauser model could be adjusted so that it managed to reproduce the experimental CR spectra, the Cooper and Chalker model is superior as it is an absolute calculation of the interaction strength. After C&C's initial assumption that the electrons rested on triangular lattice sites, no other parameters such as electron scattering rates, required fiddling. Only experimentally measured variables such as temperature and carrier density are entered. As for the validity of the C&C model in placing the electrons on triangular lattice sites of the Wigner crystal even when computing for temperatures well above the predicted crystal melting point, the authors did perform a calculation for a fixed liquid configuration. Comparison to the crystal lattice configuration showed that there was little difference between the generated spectra. Intuitively this makes sense as the peculiar long range nature of the Coulomb interaction diminishes the importance of correlation between the particles. This fact also underscores the insensitivity of the CR to the highly correlated states of the fractional quantum Hall effect.

With these ideas in mind the concluding task of the chapter is to place the CR data in the wider context of the possible states of a 2DES placed in a perpendicular magnetic field. I hesitate to use the term 'phase diagram' as the CR measurements examine an excitation property of the system. While it is valid to then characterize this property as gas or liquid-like, another leap of faith is needed before commenting on whether the electrons have crystallized into the Wigner lattice. This is especially true given the lack of any clear signature in the CR spectra that would indicate a phase change. Additionally, the insight gained from the Cooper and Chalker model has shown that it makes little difference as to whether the electrons are fixed at lattice sites or allowed to move in a strongly correlated liquid.

5.8 Conclusions

In conclusion, the technique of cyclotron resonance has shown to be uniquely suited to probing the spin composition of the 2DES in large perpendicular magnetic fields. Millikelvin experiments have confirmed that even at the lowest achieved sample temperatures that there is significant population of both spin states of the lowest Landau level. A theoretical calculation of CR spectra by Cooper and Chalker convincingly reproduces experimental results, using a model that considers the interaction between interacting, non-degenerate spin states. The temperature dependence is accounted for in terms of the thermal population of the two spin states, without invoking exchange interaction. Changes in the spectra with occupancy are seen to be the result of changing from single particle behavior at low densities to a single mode dominated by Coulomb interactions at higher densities.

Comparison between experiment and the Cooper and Chalker model clearly shows that there is now a good quantitative understanding of the cyclotron excitations of the interacting two-dimensional system. These excitations can be divided by a critical density which separates single particle behavior at low temperatures from a system with coupled excitations at higher densities. The critical density is a function of the spin population and the carrier density.

5.9 References

[1] E.P. Wigner, *Phys. Rev.* **46**, 1002 (1934).

[2] P.M. Platzman and P.A. Wolf, *Waves and Interactions in Solid State Plasmas*, Solid State Physics vol. **13**, Academic Press (1973)

[3] W. Kohn, *Phys. Rev.* **123**, 1242 (1961).

[4] C. Kallin and B.I. Halperin, *Phys. Rev.* B **30**, 5655 (1984).

[5] C. Kallin and B.I. Halperin, *Phys. Rev.* B **31**, 3635 (1985).

[6] Z. Schlesinger, J.C.M. Wang, P.M. Platzmann, and N. Tzoar, *Phys. Rev.* B **30**, 435 (1984).

[7] A.H. MacDonald, H.C. Oji and S.M. Girvin, *Phys. Rev. Lett.* **55**, 2208 (1985).

[8] H.C.A. Oji and A.H. MacDonald, *Phys. Rev.* B **33**, 3810 (1986).

[9] M. Watts, R.J. Nicholas, N.J. Pulsford, J.J. Harris and C.T. Foxon in *Proceedings of the Twentieth International Conference on the Physics of Semiconductors,* edited by E.M. Anastassakis and J.D. Joannopoulos (World Scientific, Singapore, 1991), p. 1465.

[10] A.H. MacDonald and C. Kallin, *Phys. Rev.* B **40**, 5797 (1989).

[11] M. Salkola, *Phys. Rev.* B **43**, 1190 (1991).

[12] R. Côté and A.H. MacDonald, *Phys. Rev.* B **44**, 8759 (1991).

[13] N.R. Cooper and J.T. Chalker, *Phys. Rev. Lett.* **72**, 2057 (1994).

[14] C.T. Foxon, J.J. Harris, D. Hilton, J. Hewett, and C. Roberts, *Semicon. Sci. Tech.* **4**, 582 (1989).

[15] G.M. Summers, R.J. Warburton, J.G. Michels, R.J. Nicholas, J.J. Harris and C.T. Foxon, *Phys. Rev. Lett.* **70**, 2150 (1993).

[16] R.J. Nicholas, G.M. Summers, M. Watts, R.J. Warburton, J.G. Michels, R.A. Lewis, J.J. Harris and C.T. Foxon in *Low Dimensional Electronic Systems, New Concepts,* Springer Series in Solid-State Sciences Vol. 111 (Springer-Verlag, Berlin, 1992), p. 232.

[17] M. Besson, E. Gornik, C.M. Engelhardt and G. Weimann, *Semicon. Sci. Tech.* **7**, 1274 (1992).

[18] C.M. Englehardt, E. Gornik, M. Besson, G. Böhm and G. Weimann, *Surface Science* **305**, 23 (1994).

[19] M.A. Hopkins R.J. Nicholas, P. Pfeffer, W. Zawadzki, D. Gauthiers, J. Portal and M.A. DiForte-Poisson, *Semicon. Sci. Tech.* **2**, 568 (1987).

[20] H. Sigg *et al*, *S.S. Comm.* **48**, 897 (1983).

[21] J. Scriba, A. Wixforth, J.P. Kotthaus, C. Bolognesi, C. Nguyen and H. Kroemer, *Semicon. Sci. Tech.* **8**, S133 (1993).

[22] W. Seidenbusch, E. Gornik and G. Weimann, *Phys. Rev.* B **36**, 9155 (1987).

[23] G.L.J.A. Rikken, H.W. Myron, P. Wyder, G. Weiman, W. Schlapp, R.E. Horstman and J. Wolter, *J. Phys. C: Condens. Matter* **18**, L175 (1985).

[24] R.J. Nicholas, D.J. Bares, R.G. Clark, S.R. Haynes, J.R. Mallett, A.M. Suckling, A. Usher, J.J. Harris, C.T. Foxon and R. Willett, in *High Magnetic Fields in Semiconductor Pysics II*, G. Landwehr (ed.), Springer-Verlag, Berlin, 115 (191988)

[25] M.J. Chou, D.C. Tsui and G. Weimann, *Phys. Rev.* B **37**, 848 (1988).

[26] Z. Schlesinger, W.I. Wang and A.H. MacDonald, *Phys. Rev. Lett.* **58**, 73 (1987).

[27] G.M. Summers, *D.Phil thesis, Oxford*, (1993)

[28] J.P. Cheng and B.D. McCombe, *Phys. Rev. Lett.* **64**, 3171 (1990).

[29] R.J. Nicholas, D.J. Barnes, N. Miura, J.J. Harris and C.T. Foxon, *J. Phys. Soc. Jpn.* **62**, 1267 (1993).

[30] A.H MacDonald and G.C. Aers, *Phys. Rev.* B **29**, 5976 (1984).

[31] J.G. Michels, S. Hill, R.J. Warburton, G.M. Summers, P.Gee, J. Singleton, R.J. Nicholas, C.T. Foxon and J.J. Harris, *Surface Science* **305**, 33 (1994).

[32] E.Y. Andrei, G. Deville, D.C. Glattli and F.I.B. Williams, *Phys. Rev. Lett.* **60**, 2765 (1988).

[33] H.W. Jiang, R.L. Willet, H.L. Stormer, D.C. Tsui, L.N. Pfeiffer and K.W. West, *Phys. Rev. Lett.* **65**, 633 (1990).

[34] G. Lommer, F. Malcher and U. Rössler, *Phys. Rev. Lett.* **60**, 728 (1988).

[35] T. Chakraborty, P. Pietiläinen and F.C. Zhang, *Phys. Rev. Lett.* **57**, 130 (1986).

[36] J.P. Eisenstein, H.L. Stormer, L.N. Pfeiffer and K.W. West, *Phys. Rev. Lett.* **62**, 1540 (1990).

[37] K. Moulopoulos and N. W. Ashcroft, *Phys. Rev. Lett.* **69**, 2555 (1992).

[38] N. Cooper, *2nd Year Report*, unpublished, 1994.

[39] J. Appel and A.W. Overhauser, *Phys. Rev.* B **18**, 758 (1978).

Chapter 6

Optically detected cyclotron resonance of GaAs quantum wells

6.1 Introduction

This chapter details an optically detected cyclotron resonance (ODCR) study of a GaAs quantum well series composed of four samples each with a different well width. The conduction band mass was measured as a function of well width, and the data agrees with a simple formula based on **k.p** theory, as derived by Ekenberg [1]. A further result concerns an offset in the cyclotron resonance energy when the magnetic field is extrapolated to zero. The offset is shown to be strongly dependent on well width, scaling as $\mathrm{d}\varepsilon/\mathrm{d}L$ where ε is the electron confinement energy and L the quantum well width. This behavior indicates that the offset is caused by the localization of electrons by monolayer width fluctuations.

The ODCR technique was especially well suited for this experiment because it allowed for the use of undoped samples. This allowed the effective mass to be compared to *flat band* calculations, and makes the interpretation of the offset effect unambiguous. For doped samples, band bending must be taken into account, and the interpretation of the offset effect is confused in this case because the potential from the ionised donors can also localize electrons in the quantum limit.

ODCR from two GaAs quantum wells has been previously reported by Ahmed *et al*[2]. However, these authors used only a single cyclotron energy, and so did not observe the offset effect.

6.2 Experimental Details

The ODCR experimental setup is detailed in Chapter 2. A 3 mW solid state laser diode operating at 670 nm was used to excite the luminescence, and the optically pumped molecular gas laser supplied the far-infrared (FIR) radiation. All measurements were made with the sample at ~ 2.2 K in an 18 T superconducting magnet.

The 670 nm radiation arrived at the sample by means of one arm of a bifurcated fiber bundle; the second arm was used to collect the luminescence. The power density at the sample was $\sim 5\,\mathrm{mW/cm^2}$, which gives an estimated carrier density in each quantum

well of $< 10^6$ cm^{-2}. This is very small compared to typical doping concentrations of $\sim 10^{11}$ cm^{-2}. The luminescence was dispersed with a 0.5 m spectrometer, and detected with a GaAs photomultiplier tube.

In a similar manner as the bulk GaAs ODCR experiment, the FIR radiation travelled through an evacuated light pipe and then was guided through two 45° reflections underneath the sample, bringing the FIR incident on the sample substrate. The throughput of the FIR was continuously monitored by a bolometer placed next to the fiber bundle as to not interfere with the visible radiation striking the sample surface. Care was taken to ensure that the visible and FIR radiation were aligned on either side of the sample. Ten FIR laser lines, with wavelengths between $\sim$ 300 and 70 μm, were used in an attempt to match the cyclotron frequency for magnetic fields up to 18 T.

The samples for the experiment were high quality GaAs quantum wells, grown at Philips, Redhill. Each is a multi–quantum well, consisting of sixty nominally identical $GaAs/Al_{0.36}Ga_{0.64}As$ wells. Extensive characterization details can be found in Orton *et al*[3]. The sample well widths are listed in Table 6.1. The samples have been previously used for inter-band magneto-optic experiments [4, 5] which confirm that they are of high quality. The 25.7 Å sample was also used in a pump-probe experiment [6], in which electrons were excited with a red LED, and cyclotron resonance detected by the photoconductivity response to light from a FIR laser.

6.3 Results

Figure 6.1 shows the photoluminescence and the ODCR signals as a function of detection energy for the 56 Å quantum well at the resonance field. The luminescence spectrum consists of a single line due to free exciton-hole recombination in the quantum well. The ODCR spectrum roughly follows the derivative of the photoluminescence spectrum. The overall ODCR response, integrated over energy, is positive (i.e. when the FIR is allowed to strike the sample, there is an increase in the photoluminescence intensity). Similar curves to Figure 6.1 were obtained away from resonance, but with a smaller ODCR signal. The integrated ODCR signal was at best +1.0% with the strongest laser line,

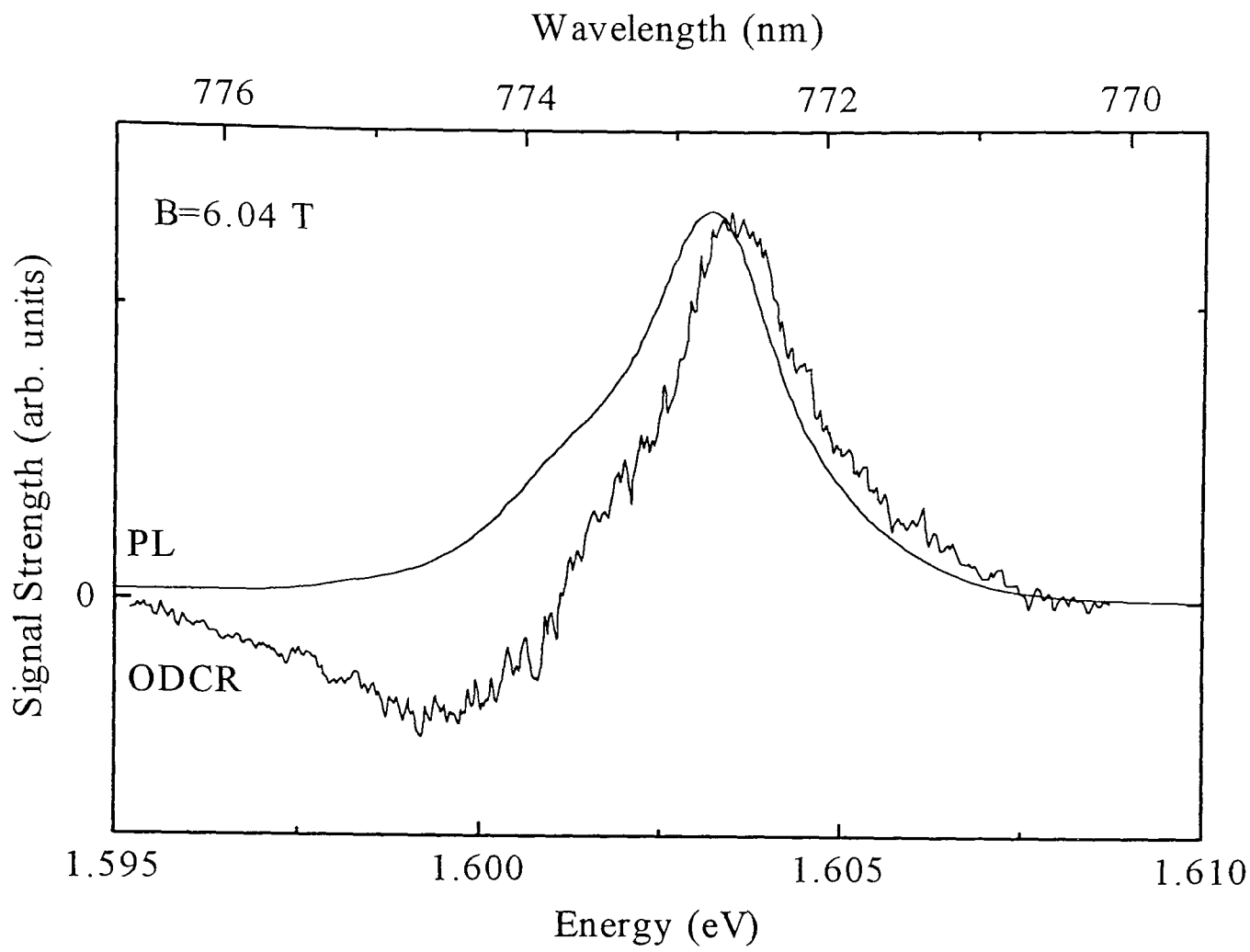

Figure 6.1: Photoluminescence (PL) and optically detected cyclotron resonance (ODCR) signals versus detection energy for sample G57, a 56 Å $GaAs/Al_{0.36}Ga_{0.64}As$ quantum well. The ODCR spectra is for 118.8 μm which matches the electron cyclotron frequency at a field of 6.04 T.

118.8 μm. Most of the data was taken with the spectrometer slits opened to 5 mm, with resolution comparable to the diamagnetic shift of the luminescence peak at high magnetic field. The wide slit width maximized the luminescence signal and made it unnecessary to continually adjust the detection wavelength when sweeping the field.

A representative ODCR trace, where the luminescence intensity is monitored while the field is swept, is shown in Figure 6.2 from sample G51, taken with the 118.8 μm far-infrared line. The prominent peak is the electron cyclotron resonance. The peak is fairly broad (half-width 0.3 T) which is largely caused by well-to-well fluctuations in the well width. Figure 6.2 also shows that the background response, which is quite large at zero field, decays rapidly in the first few Tesla, but returns at high field to approximately the zero field level. The background was less noticeable at wavelengths longer than $\sim$ 150 μm. Unfortunately, no cyclotron resonances from sample G50, the 25.7 Å well sample were observed. There was an ODCR signal for some short wave-

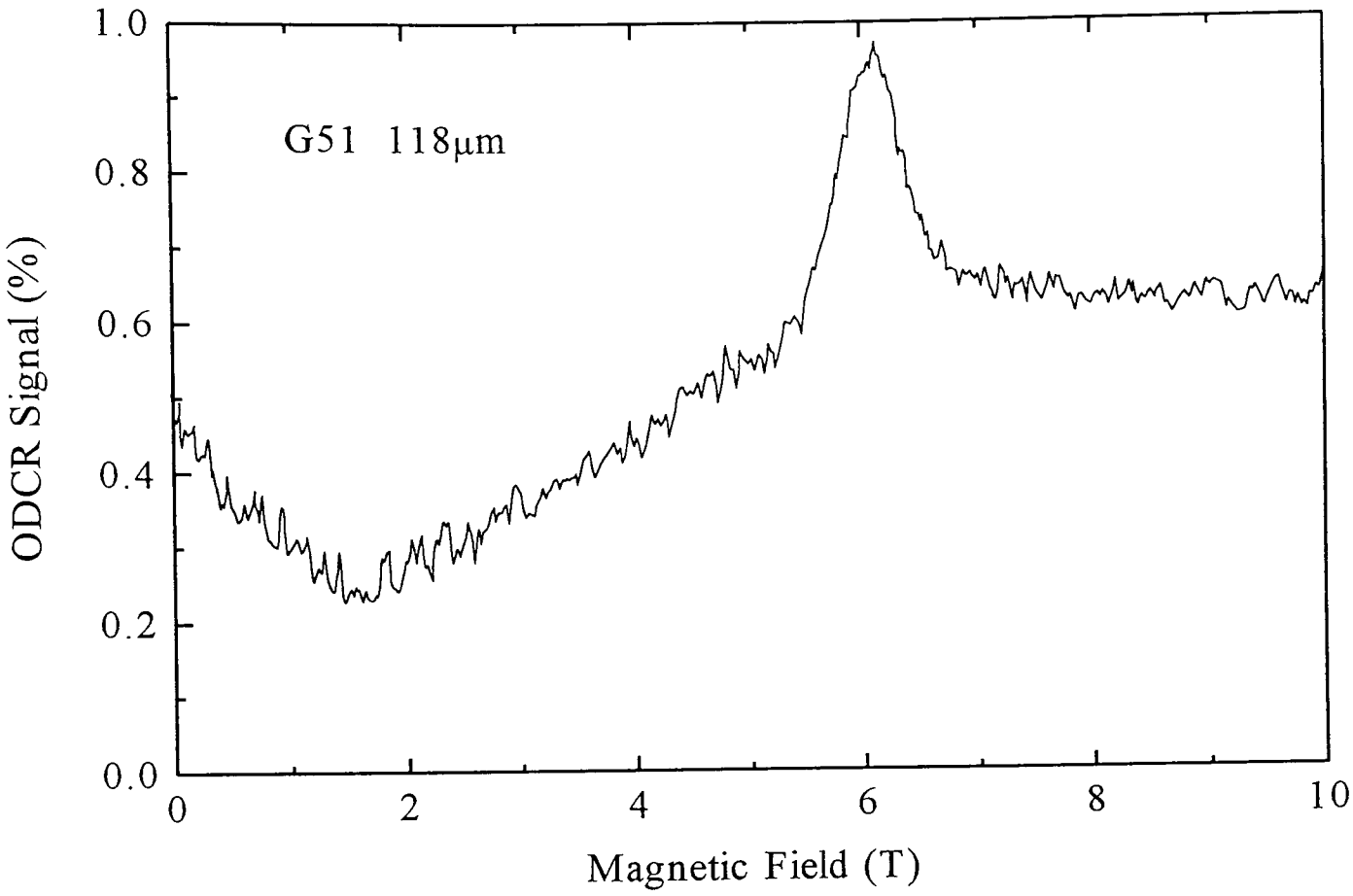

Figure 6.2: Integrated ODCR signal versus magnetic field for sample G51, a 73.4 Å quantum well, with FIR wavelength 118.8 μm. The prominent peak is the electron cyclotron resonance.

lengths (eg. 70.5 μm), but it consisted only of the background response without any resonant features. It is not clear why this should be, as the 25.7 Å sample is certainly of high quality. Experimentally, this result is consistent with the work of Ahmed *et al*[2] who could also find no ODCR from narrow GaAs quantum wells. It is curious that the pump-probe experiment of Singleton [6] was only successful for the 25.7 Å quantum well and not for the wider wells, so the two techniques, pump-probe and ODCR, are apparently complementary for these samples.

Cyclotron resonance data for samples G57, G51 and G55 are collected together in Figure 6.3, a plot of the cyclotron energy, E_{CR}, against magnetic field, B. The data were fitted to:

$$E_{CR} = E_o + E_1 B + E_2 B^2 \tag{6.1}$$

E_1 determines the slope at low field, and hence the band edge mass of the quantum well, $m^* = e\hbar/E_1$. Figure 6.3 shows how the slope decreases, and hence the mass increases,

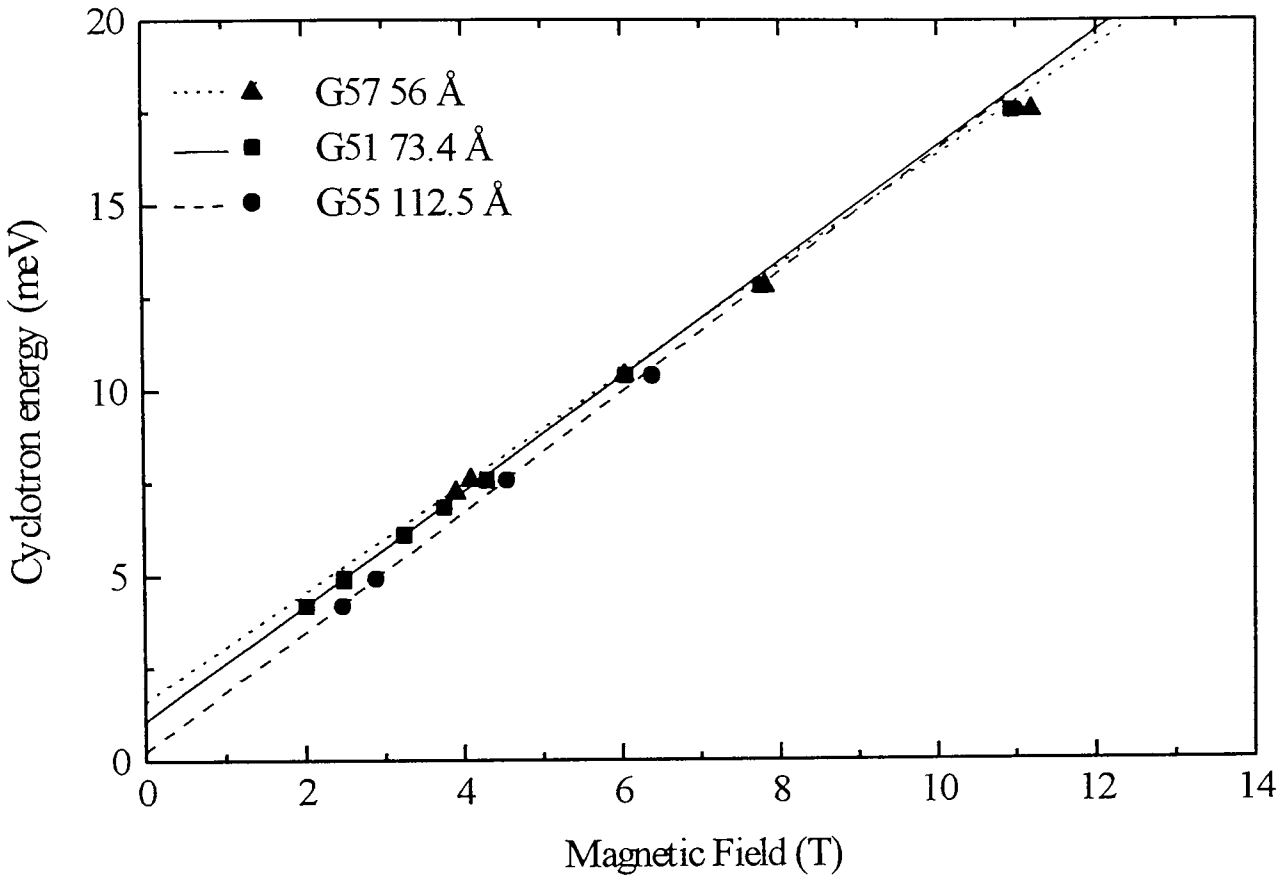

Figure 6.3: The data collected by ODCR at several FIR wavelengths for the quantum well samples, plotted as cyclotron energy versus magnetic field. The plot shows how the low field slope decreases and the offset (the cyclotron energy extrapolated to zero field) increases as the well width decreases.

with decreasing well width. The explanation is that as the well width decreases, the confinement energy increases, giving a larger nonparabolicity correction to the bulk GaAs mass. The term E_2 in Equation 6.1 arises from nonparabolicity in the quantum well in-plane dispersion relation. To within experimental error, E_2 was the same for the three samples. The value of E_2 provided by the fit matches theoretically predicted values for band nonparabolicity found in Equations 6.2 and 6.5. Both expressions are found in section 6.3.1 as part of the analysis of the electron effective mass as a function of well width. The energy E_o is the offset energy. Figure 6.1 shows clearly how the offset increases for decreasing well width.

The dependence of the effective mass and offset energy on well width is plotted in Figure 6.4[a] and [b]. Figure 6.4[a] includes the band edge mass of the 25.7 Å sample as deduced from the pump-probe experiment. Note that with these samples it is essential to take into account the offset energy to reliably determine the effective mass. If the mass were deduced simply from $m^* = e\hbar B/E_{CR}$ then large errors would arise. For

instance, Figure 6.3 shows that if the masses were measured only, say, with $E_{CR} = 7.6$ meV (163 μm), then one would conclude that the mass decreases with decreasing well width!

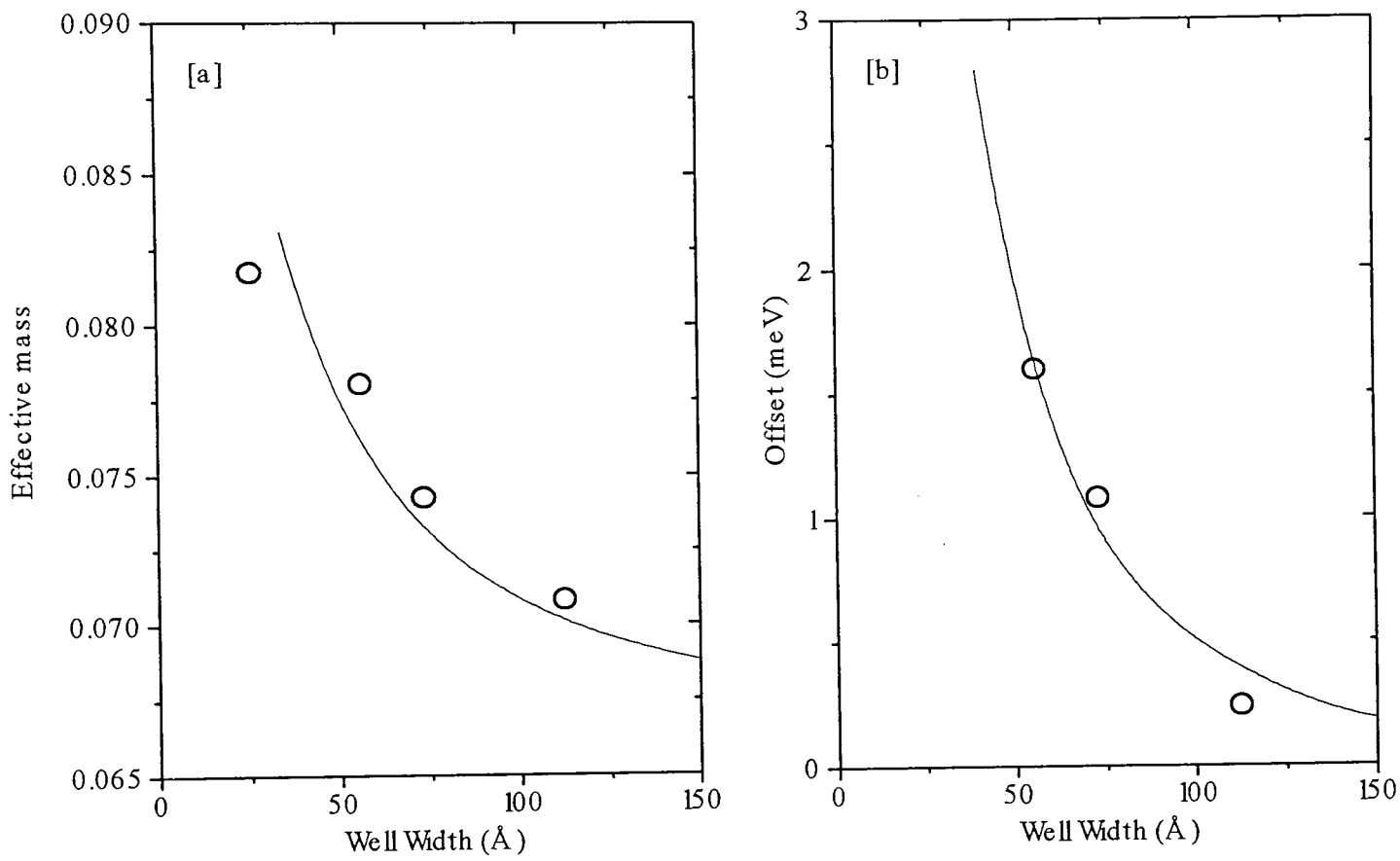

Figure 6.4: [a] Effective mass (in units of the free electron mass) versus quantum well width. The solid line is the theory of Ekenberg, as discussed in the text. [b] Cyclotron resonance offset energy versus quantum well width. The solid line is Equation 6.10 with $\gamma = \frac{1}{3}$.

6.3.1 The effective mass

To calculate the effective mass as a function of well width, the confinement energy must be evaluated, and then from this the nonparabolicity enhancement to the bulk GaAs mass, m_o^*. Band nonparabolicity arises from interaction of the Γ_1^c conduction band with the Γ_5^v valence band and with the higher Γ_5^c conduction band. Rössler [7] has shown that the $\Gamma_1^c - \Gamma_5^c$ interaction must be included for energies more than ~ 50 meV above the band edge. This is the energy range here, because the confinement energy is ~ 80 meV for the 57 Å quantum well. Ekenberg [1] has considered both sources of

Sample	G50	G57	G51	G55
Width[a] (Å)	25.7	56	73.4	112.5
Measured m^* ($\times 10^{-3} m_e$)	81.8[b]	78.1	74.3	70.8
Measured ε (meV)	198[c]	78	50	29
m^* from measured ε ($\times 10^{-3} m_e$)		76.8	73.1	70.3

[a]X–ray measurements (Ref. [3])

[b]Ref. [6]

[c]Ref. [4]

Table 6.1: The well widths, measured masses, measured confinement energies, and the calculated masses. The calculated masses come from Equation 6.2 using $m_o^* = 0.0665$ and the measured confinement energies.

band nonparabolicity and derived that for an infinitely deep well, to first order in the confinement energy ε,

$$m^* = m_o^* [1 + (2\alpha' + \beta')\varepsilon] \tag{6.2}$$

where $\alpha' = -(2m_o^*/\hbar^2)^2 \alpha_o$, $\beta' = -(2m_o^*/\hbar^2)^2 \beta_o$, with α_o and β_o band parameters from Rössler [7]. Numerically for GaAs [1, 8], $\alpha' = 0.64$ eV^{-1} and $\beta' = 0.70$ eV^{-1}, so that, for ε in eV,

$$m^* = m_o^* [1 + 1.98\varepsilon] \tag{6.3}$$

Ekenberg [1] also showed that Equation 6.2 still applies in the case of a finite well, providing that the penetration of the wave function into the barriers is small. Numerically, Equation 6.2 works well for a 50 Å GaAs/$Al_{0.3}Ga_{0.7}As$ quantum well compared to a theory that also includes the effects of the boundary conditions at the interfaces[1].

In order to test Equation 6.2 the confinement energies ε were measured experimentally. This eliminates any errors in the calculation of ε which would arise through uncertainties in the actual well widths. There are also problems in the effective mass approach, in that there is no unique choice for the envelope function boundary conditions, and different choices can give significantly different results. For instance Ekenberg [1] considered three different boundary conditions, which, for a 50 Å well, give confinement energies differing by as much as 14 meV in a confinement energy of $\sim$ 75 meV. The confinement energies ε were evaluated from the photoluminescence peak position E_{PL}, the exciton binding energy E_B, the GaAs band gap E_g (=1.519 eV), and the heavy hole confinement

energy E_{HH}:

$$\varepsilon = E_{PL} + E_B - E_g - E_{HH} \tag{6.4}$$

E_{PL} was measured in our experiment; E_B is known from photoluminescence experiments by Moore *et al*[9] on these samples, E_B deduced from an observation of $2s$ exciton recombination; and E_{HH} was calculated using the X-ray widths[3]. ε is determined to about ± 3 meV error. The values of ε are listed in Table 6.1 and from these values we have calculated the masses from Equation 6.2 which are also included in Table 6.1. The calculated masses can be compared with the experimentally measured points in Table 6.1, and in Figure 6.5, a plot of m^* versus ε. The theory can be seen to give a good fit to the experimental data.

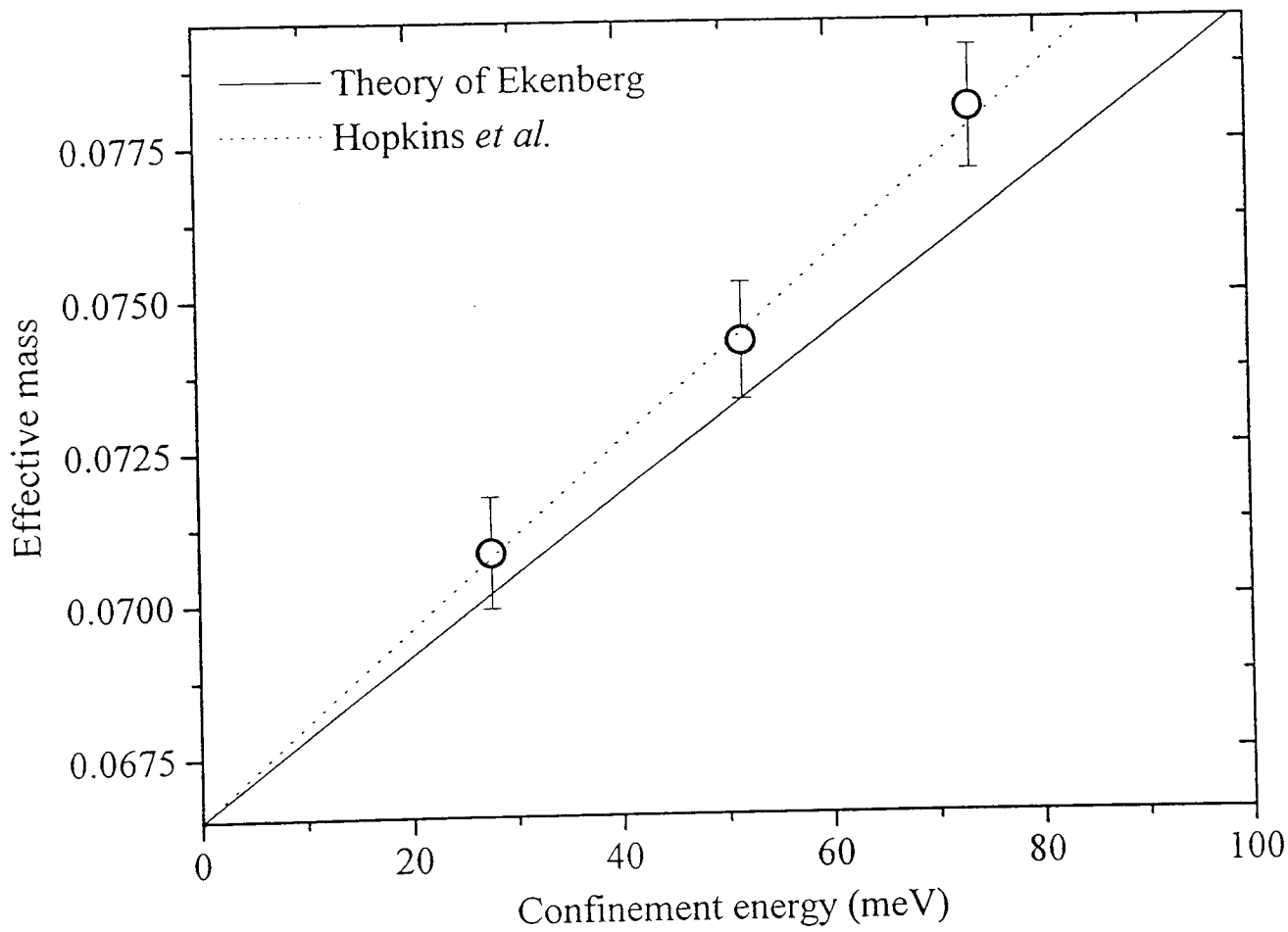

Figure 6.5: A plot of measured effective mass versus measured electron confinement energy for the 56, 73.4 and 112.5 Å quantum wells. The data is modelled according to $m^* = m_o^*[1 + k\varepsilon]$ with $k = 1.98$ eV^{-1} (solid line) from the theory of Ekenberg (ref. [1] and Equation 6.2), and with $k = 2.30$ eV^{-1} (dashed line) from the cyclotron resonance results on bulk GaAs of Hopkins *et al* (ref [11] and Equation 6.5-6.6).

Figure 6.5 shows that we have a linear variation of m^* with ε, but with a gradient slightly steeper than Equation 6.2 predicts. The residual discrepancy could be caused by a

number of factors, such as the omission of polaron enhancements in the theory, an error in the GaAs non-parabolicity at high energies above the band edge, or some additional error in the experimental data points. The polaron effect is known to be stronger in an ideal two-dimensional system than in an equivalent three-dimensional system [10], but this is not obvious in experiments on quasi two-dimensional GaAs because of penetration of the wave function in the third dimension (and by screening in doped samples). A strong dimensionality dependence, i.e. a ε dependence, of the polaron enhancement is therefore not expected. In an attempt to model the data including both band and polaron nonparabolicity, the results of both Hopkins *et al*[11] and the Chapter 3 ODCR study of bulk GaAs are extrapolated to the quantum well case. The effective mass at low E_{CR} is fitted to

$$\frac{1}{m^*} = \frac{1}{m_o^*}\left[1 + \frac{2K_2}{E_g}E_{CR}\right] \tag{6.5}$$

with $K_2 = -1.75$ (an average of the two spin-split transitions). Replacing E_{CR} with ε, and inverting Equation 6.5, gives

$$m^* = m_o^*\left[1 + 2.30\varepsilon\right] \tag{6.6}$$

Figure 6.5 also includes this expression for the mass, and fits the data very well [12]. For GaAs heterojunctions, Hopkins *et al*[13] used Equation 6.5 but found $K_2 = -1.4$, reduced in magnitude from the bulk value because the degenerate electron gas screens out the polaron effect. $K_2 = -1.4$ implies $-2K_2/E_g \simeq 1.8\ \mathrm{eV}^{-1}$, which is essentially the same as Equations 6.2-6.3, the difference being caused by the isotropic conduction band used in the derivation of Equation 6.5. For the present case, the carrier concentration is so low that the polaron is not screened. It is likely then that the small discrepancy with Ekenberg's theory in Figure 6.5 is caused by the polaron effect.

Figure 6.4[a] is a plot of m^* versus quantum well width L. The solid line shows Equation 6.2 using ε calculated with the three band Kane model[14], using the boundary conditions of Bastard[15]. The L's of the data points plotted in Figure 6.4[a] have been adjusted from their X-ray values such that the Kane model reproduces the measured confinement energies. No more than a one monolayer adjustment was necessary. For wells where $[(2\alpha' + \beta')\varepsilon \ll 1]$, then Equation 6.2 applies and successfully relates the parallel mass and the confinement energy. For the 25.7 Å sample, $(2\alpha' + \beta')\varepsilon \simeq 0.4$,

which is no longer small compared to 1, and Equation 6.2 is no longer valid. However, Ekenberg [1] considered this sample as a special case and calculated $\varepsilon = 205$ meV and $m^* = 0.080$ including the effects of the boundary conditions. These numbers agree well with the measured values of $\varepsilon = 198$ meV and $m^* = 0.082$, although this may be fortuitous given the absence of any polaron enhancement in the theory, and given the experimental uncertainty in the well width.

Finally, the importance of including the nonparabolicity from the $\Gamma_1^c - \Gamma_5^c$ interaction to model the experimental results should be noted. Neglecting this coupling, by putting $K_2 = -1$ in Equation 6.5, considerably underestimates the measured masses.

6.3.2 The offset

Offset effects have been observed and studied in ordinary cyclotron resonance with doped samples [16]-[20]. The offset energy tends not to arise until the quantum limit is reached, when the electrons (or holes [20]) condense into the localized states of the $N = 0$ level, and it is this extra localization energy that gives rise to the offset. At lower fields more than one Landau level is occupied, and so the effect of the localizing potential is averaged out. Two models have been presented to analyse the offset energy. The first is that the observed cyclotron energy E_{CR} is perturbed from the intrinsic value E_{CR}^o by a constant term:

$$E_{CR} = E_{CR}^o + \delta \tag{6.7}$$

as for the binding energy of a shallow impurity. Alternatively, one may suppose that the carriers are bound into a parabolic potential within the layers. For a one-dimensional potential $V(x) = \frac{1}{2}m^*(\delta/\hbar)^2x^2$ (with the growth direction along the z axis) one finds [21] that:

$$(E_{CR})^2 = (E_{CR}^o)^2 + \delta^2 \tag{6.8}$$

The potential that causes this localization phenomenon can arise from several sources, for instance the random potential from ionised donors, alloy disorder effects, or monolayer interface fluctuations. The potential need not be particularly large, and so can arise even in ultra-high mobility heterojunctions [19].

In the present case, the density of electrons is very small and so we are in the quantum limit for all fields at which a resonance was recorded. The samples are of high quality and are nominally undoped, so there is no ionised donor potential to localize the carriers. The electron concentration is so low that it might be possible for each electron to bind onto a residual impurity in the wells. However, this is very unlikely from the offset energies. Experimental [22] and theoretical [23] studies of donor species in quantum wells have shown that the $1s - 2p_+$ energy increases relative to bulk GaAs, whereas all our offsets are less than this (Figure 6.4[b], compared to a $1s - 2p_+$ energy of 4 meV for bulk). The remaining possibility is that the carriers are bound by monolayer width fluctuations. The carriers localize in regions of the quantum well where the well is widest and hence the confinement energy is lowest. An offset can arise if the spatial extent of the step (in the layer plane) is larger than the cyclotron radius of the $N = 0$ level. The $N = 1$ Landau level is perturbed less because it has a larger cyclotron radius and hence averages over a wider area. As a result, an offset in the cyclotron energy appears. A strong well width dependence arises because a monolayer width fluctuation changes the confinement energy more for a narrow well than for a wide well. This is precisely the trend in Figure 6.4[b], where the offset increases rapidly with decreasing well width.

The cyclotron resonance data was analysed using Equation 6.7 rather than Equation 6.8, as it is not clear how a monolayer fluctuation can be modelled with a parabolic potential. The offset will be at most

$$\frac{\mathrm{d}\varepsilon}{\mathrm{d}L}\delta L \tag{6.9}$$

where $\delta L \simeq 3$ Å, which assumes that only the $N = 0$ level is perturbed. This will not be the case in practice, and the offset will be smaller than this because the energy of the $N = 1$ level will also be pulled down, but to a lesser extent. Plotted in Figure 6.4[b] is:

$$\delta = \gamma \frac{\mathrm{d}\varepsilon}{\mathrm{d}L}\delta L \tag{6.10}$$

with $\gamma \sim \frac{1}{3}$, which can be seen to reproduce the data remarkably well.

For this picture to be accurate, the extent in the plane of the well width step d must be larger than the $N = 0$ cyclotron radius, otherwise the electrons would average out the perturbation in the course of their orbits. Also, d cannot be much larger than the

$N = 1$ cyclotron radius, otherwise the offset would not appear at all. The lowest field we used was ~ 2 T, which implies roughly that $200 \leq d \leq 1000$ Å.

6.4 Conclusions

Optically detected cyclotron resonance has been performed on a series of undoped GaAs quantum wells. The results show that:

- the band edge mass for in-plane motion can be related to the confinement energy with the theory of Ekenberg [1], based on **k.p** theory. It is important to include the nonparabolicity from both $\Gamma_1^c - \Gamma_5^v$ and $\Gamma_1^c - \Gamma_5^v$ interactions in the band structure of bulk GaAs.

- the samples have monolayer width fluctuations, extending over $\sim$ 500 Å, which localize the carriers, giving rise to an offset energy in the cyclotron energy.

6.5 References

[1] U. Ekenberg, Phys. Rev. B **40**, 7714 (1989).

[2] N. Ahmed, I. R. Agool, M. G. Wright, K. Mitchell, A. Koohian, S. J. A. Adams, C. R. Pidgeon, B. C. Cavenett, C. R. Stanley, and A. H. Kean, Semicond. Sci. Technol. **7**, 357 (1992).

[3] J. W. Orton, P. F. Fewster, J. P. Gowers, P. Dawson, K. J. Moore, P. J. Dobson, C. J. Curling, C. T. Foxon, K. Woodbridge, G. Duggan, and H. I. Ralph, Semicond. Sci. Technol. **2**, 597 (1987).

[4] D. C. Rogers, J. Singleton, R. J. Nicholas, C. T. Foxon, and K. Woodbridge, Phys. Rev. B **34**, 4002 (1986).

[5] A. S. Plaut, J. Singleton, R. J. Nicholas, R. T. Harley, S. R. Andrews, and C. T. B. Foxon, Phys. Rev. B **38**, 1323 (1988).

[6] J. Singleton, R. J. Nicholas, D. C. Rogers, and C. T. B. Foxon, Surf. Sci. **196**, 429 (1988).

[7] U. Rössler, Solid State Commun. **49**, 943 (1984).

[8] F. Malcher, G. Lommer, and U. Rössler, Superlatt. Microstruc. **2**, 267 (1986).

[9] K. J. Moore, P. Dawson, and C. T. Foxon, Phys. Rev. B **34**, 6022 (1986).

[10] F. M. Peeters and J. T. Devreese, Phys. Rev. B **31**, 3689 (1985).

[11] M. A. Hopkins, R. J. Nicholas, P. Pfeffer, W. Zawadzki, D. Gauthier, J. C. Portal, and M. A. DiForte–Poisson, Semicond. Sci. Technol. **2**, 568 (1987).

[12] Hopkins et al. (ref. [11]) measure the band edge mass of bulk GaAs to be 0.0660, whereas Ekenberg takes 0.0665 (ref. [1]). For consistency with Ekenberg's theory, both curves in Figure 6.5 use 0.0665.

[13] M. A. Hopkins, R. J. Nicholas, M. A. Brummell, J. J. Harris, and C. T. Foxon, Phys. Rev. **36**, 4789 (1987).

[14] E. O. Kane, J. Phys. Chem. Solids **1**, 249 (1957).

[15] G. Bastard, Phys. Rev. B **24**, 5693 (1981); **25**, 7584 (1982).

[16] H. Sigg, D. Weiss, and K. v. Klitzing, Surf. Sci. **196**, 293 (1988).

[17] G. Wiggins, R. J. Nicholas, J. J. Harris, and C. T. Foxon, Surf. Sci. **229**, 488 (1990).

[18] J. Richter, H. Sigg, K. v. Klitzing, and K. Ploog, Phys. Rev. B **39**, 6268 (1989).

[19] R. J. Nicholas, M. A. Hopkins, D. J. Barnes, M. A. Brummell, H. Sigg, D. Heitmann, K. Ensslin, J. J. Harris, C. T. Foxon, and G. Weimann, Phys. Rev. B **39**, 10955 (1989).

[20] R. J. Warburton, R. J. Nicholas, L. K. Howard, and M. T. Emeny, Phys. Rev. B **43**, 14124 (1991).

[21] J. P. Kotthaus, G. Abstreiter, J. F. Koch, R. Ranvaud, Phys. Rev. Lett. **34**, 151 (1975).

[22] N. C. Jarosik, B. D. McCombe, B. V. Shanabrook, J. Comas, J. Ralston, and G. Wicks, Phys. Rev. Lett. **54**, 1283 (1985).

[23] R. L. Greene and K. K. Bajaj, Phys. Rev. B **31**, 913 (1985).

Chapter 7

Electron Orbits and Impurity States in InGaAs/GaAs Superlattices

7.1 Introduction

A superlattice (SL) is the term used to describe a system with periodically alternating thin layers of different materials. The material with the wider band gap serves as a barrier, while the narrow gap material sandwiched between barrier material functions as a quantum well. A superlattice that displays real periodic behavior consists of quantum wells sufficiently close together so that there is an overlap between the electron (or hole) wavefunctions in adjoining wells. The main effect of the periodicity is the division of the Brillioun zone into subzones at wavevectors $q = n\pi/L$ where L is the period of the superlattice. Minigaps are created within each subzone at the zone edge which either reflect or allow transmission of carriers through the barrier. As a result there is a band dispersion along the growth axis of the superlattice which allows for transport in the SL direction. This gives the system a three dimensional nature but the narrow width of the miniband ($\sim 100\,\mathrm{meV}$) when compared to bulk materials makes superlattices really quasi two dimensional.

The Lorentz force of a magnetic field applied parallel to the growth direction of a SL will compel the electrons to execute cyclotron orbits in the plane of the layers while a field applied perpendicular to the growth axis will force electrons to tunnel through the barriers. The latter case can be pictured semi-classically because of the band dispersion in the growth direction. However, once the cyclotron diameter, $2r_c$ ($r_c = \sqrt{\hbar/eB}$), is smaller than, or comparable to, the superlattice period, L, then the effective mass picture breaks down.

The transition from semi-classical to a strongly quantum mechanical behaviour when $2r_c \sim L$ has received only limited experimental coverage. Belle and co-workers [1] observed a weakening of photoluminescence excitation energy (PLE) features when a Landau level's energy exceeded the top of the miniband. Determination of the miniband width was based on theoretical calculations which indicated that the energy range of 'flat' Landau levels, defined as those with a dispersion less than half the average spacing, coincides with the width of the miniband in zero magnetic field. Only carriers that reside in these relatively flat Landau levels can hope to tunnel through several barriers and complete their cyclotron orbit while carriers in levels with a wider dispersion fall

within the minigaps and are reflected back by the barriers leading to position dependent Landau levels.

There is great advantage in probing the modes directly with far infra-red (FIR) radiation, as has been reported by Duffield *et al*[2, 3] for GaAs/AlGaAs superlattices. These authors made cyclotron resonance experiments for $2r_c > L$, modelled successfully within a semi-classical picture, but for $2r_c < L$ a new mode, corresponding to a state bound to the barriers, was observed.

The binding energy of impurities within a superlattice geometry is also of interest, as the binding energy can depend strongly on the position of the impurity, being a minimum when the impurity lies in the middle of the barrier, and a maximum when the impurity lies in the middle of the well [4]. If the impurities are spread evenly throughout the superlattice then there are two peaks in the density of states, leading to characteristic absorption edges [5]. Experimental work has in general concentrated on well-bound impurities [6, 7, 8].

This chapter presents measurements on a series of $In_{0.05}Ga_{0.95}As/GaAs$ superlattices with the field $\mathbf{B}$ either $\mathbf{B} \parallel \mathbf{z}$ (Faraday) or $\mathbf{B} \perp \mathbf{z}$ (Voigt), where $\mathbf{z}$ lies along the SL growth direction. There are a number of differences to previous work. Most importantly, the electron band offset in $In_{0.05}Ga_{0.95}As/GaAs$ is only ~ 40 meV, giving sizeable miniband widths for relatively large barrier widths, L_b. This should be compared to the more familiar GaAs/AlGaAs system in which superlattice behaviour is only apparent for very thin barrier widths, $L_b \leq 20$ Å. With $In_{0.05}Ga_{0.95}As/GaAs$ it was possible to achieve not only $2r_c < L$ when the semiclassical model is no longer valid, but also $2r_c < L_b$ where the electron is confined to the barrier width. Secondly, the technique of optically detected cyclotron resonance (ODCR) described in Chapter 2 was employed. This allowed cyclotron resonance experiments at low temperature, without the constraints of impurity freeze-out. ODCR proved to be an excellent tool for the study of these samples and provided signals for the free electron and impurity resonances in both the Faraday and Voigt field orientations. Finally, measurements were made on what proved to be *barrier*-centered $1s - 2p_+$ impurity transitions, also in both field orientations. The striking behavior of the impurity transitions as a function of barrier width and field

orientation is conclusive proof of the superlattice nature of the samples.

7.2 Experimental details

The samples were grown at Philips, Redhill, and consist of twenty periods of nominally undoped $In_{0.05}Ga_{0.95}As/GaAs$ with nominal well/barrier thicknesses (L_w/L_b) 50/50, 50/100, 50/150 and 50/200 Å. Measurements on these samples, confirming their high quality, have already been published, notably a PL and PLE study [9] to determine the miniband widths and exciton binding energies. The PL from each sample, excited with a 3 mW HeNe or solid state diode laser, consisted of a single line due to free exciton recombination within the GaAs quantum wells. As in the other optically detected cyclotron resonance experiments, the change in PL intensity induced by far infra-red radiation was monitored. The sign of the ODCR signal was found not to depend on the exact detection wavelength, and so a wide slit width was set on the spectrometer to give as large a PL signal as possible. The sample was cooled to 2 K, and fields up to 15 T were applied. The arrangement for holding the sample in the Faraday configuration was identical to that used in the bulk GaAs (Chapter 2) and GaAs quantum well (Chapter 6) experiments. For measurements in the Voigt configuration, a new sample holder was machined which employed a small glass prism to bring the visible laser light to the sample surface, now rotated 90° to make the field lines perpendicular to the growth direction. The FIR, now directed through only one 45° reflection, was brought incident to the sample substrate as before. At resonance, there was up to a 20% reduction in the PL signal due to the FIR from the optically-pumped gas laser. It is worth noting that the ODCR signal may not have a straightforward relation to the absorption of FIR.

7.3 Experimental results

7.3.1 Faraday configuration

Typical ODCR traces in the Faraday orientation, taken with the 96 μm FIR laser line, are shown in Figure 7.1[a]. There are two main features for each of the samples: one

at lower field due to a $1s - 2p_+$ impurity resonance, and one at higher field due to the electron cyclotron resonance (CR). The impurity transitions are thought to be related to a low density of residual donors distributed throughout the superlattice. There are also, particularly for the 50/150 and 50/200 samples, sharp features of opposite sign. The field values of these sharp features, and their independence from sample to sample, suggest that they arise from $1s - 2p_+$ and CR transitions in bulk GaAs, most probably from the GaAs capping layer, where any FIR absorption could affect the transfer of electrons into the superlattice and influence the ODCR signal.

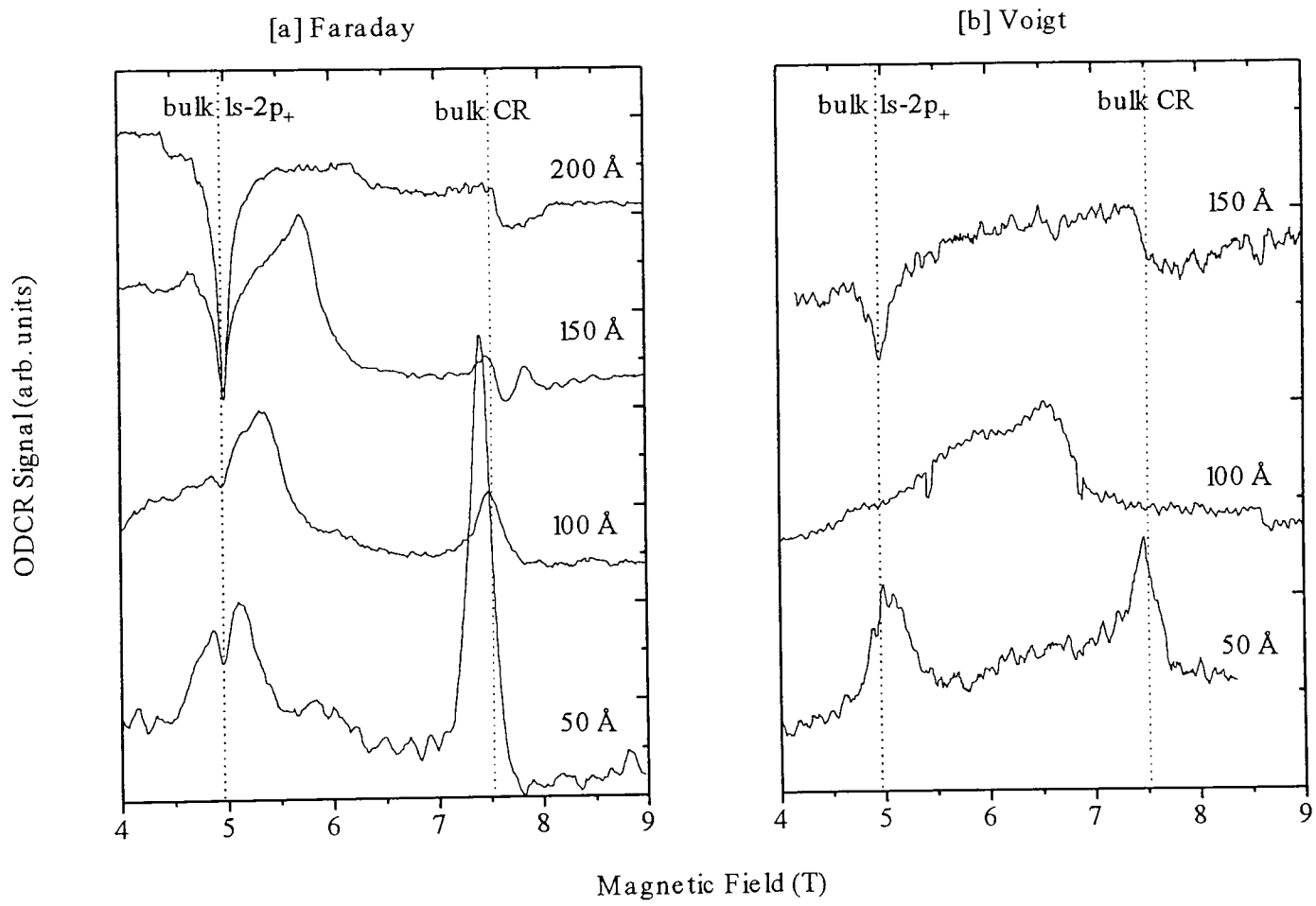

Figure 7.1: ODCR traces taken with the 96 μm laser line for the four samples labelled with the nominal barrier widths in both Faraday [a] and Voigt [b] orientation. The dashed lines show the fields of the bulk GaAs $1s - 2p_+$ and cyclotron resonance transitions. Arrows indicate the position of the superlattice impurity transitions,

The CR field for the 50/50 sample occurs at a lower field than for bulk GaAs, but the field increases as the barrier width increases. This means that the cyclotron mass, $m^* = e\hbar B/E$, increases for increasing L_b, a consequence of a reduction in inter-well coupling. As the wells couple to form a superlattice, the confinement energy of the first electron level (E_1) decreases, causing a reduction in the nonparabolicity enhancement

to the band edge mass. Nonparabolicity was taken into account with an eight band k.p calculation developed by Richard Warburton[10]. The agreement with the data is good for cyclotron energies above ~ 8 meV (see Table 7.1), but at lower energies the measured masses fall to anomalously small values. This is reminiscent of CR from conventional GaAs quantum wells where a similar effect has been observed [11] and attributed to shallow localizing potentials from well width fluctuations.

As the period of the superlattice increases, there is a notable decrease in the intensity of the free electron CR and the lineshape becomes asymmetric. These factors combined to make determination of the CR peak position more difficult. The reason for the change of the CR in the Faraday orientation is not clear. A possible explanation is that the majority of the carriers in the well are provided for by the visible laser light that strikes the sample surface and ionizes bound impurities in the capping layer. As the barrier width increases, fewer of the freed electrons are able to tunnel through the barrier into the well. This is marked by a decrease in the strength of the CR and a corresponding increase in the $1s - 2p_+$ bulk GaAs signature from the capping layer where the ionized electrons are quickly recaptured by the impurity centers.

Figure 7.1[a] shows two effects concerning impurity resonances: with increasing barrier width the field increases, implying a reduction in the binding energy, and the line shape becomes asymmetric with the signal falling rapidly on the high field side. Both factors point to impurities that are primarily in the barriers, although the broadness of the impurity resonance compared to the CR does mean that there is a distribution of impurities throughout the superlattice. The high field (low energy) absorption edge comes from the peak in the density of states from impurities in the middle of the barrier. As the barrier width increases, the superlattice potential draws the electron wave function further away from the impurity centers and reduces the binding energy as observed. Calculations of the shallow donor $1s-2s$ energies give reasonable agreement with the $B = 0$ energies estimated experimentally (see Table 7.1).

L_b	Δ	m_F^{expt}	m_F^{calc}	$1s-2p$	$1s-2s$	$r_c = L_b$
55.0	36.7	0.0665	0.06680	4.3	5.3	21.8 T
104.1	12.7	0.0671	0.06699	4.2	4.7	6.1 T
146.0	5.9	0.0677	0.06714	3.6	4.3	3.1 T
202.7	2.5	–	0.06725	3.0	3.5	1.6 T

Table 7.1: A summary of sample details and some results. L_b is the barrier width in Å; Δ is the electron miniband width in meV; m_F^{expt} (m_F^{calc}) is the measured (calculated) effective mass at energy 10.43 meV in the Faraday orientation; $1s-2p$ ($1s-2s$) is the $B = 0$ impurity energy estimated experimentally (theoretically); and $r_c = L_b$ defines the magnetic field at which the cyclotron radius, r_c, is equal to the barrier thickness.

7.3.2 Voigt orientation

ODCR traces in the Voigt geometry are plotted in Figure 7.1[b], again for the 96 μm FIR laser line. Placing the axis of the superlattice perpendicular to the direction of the field forces the electrons to tunnel through the barriers and samples the new periodic band structure. There is a clear CR only from the 50/50 sample, which occurs at higher field than in the Faraday geometry of Figure 7.1[a]. With the 50/50 sample, the cyclotron diameter is always larger than the superlattice period for the fields used here, so it is valid to use a semi-classical quantization of the miniband dispersion to model the data. This requires solution of the Schrödinger equation for the special case where there is a periodic one-dimensional potential, often referred to as the Krönig-Penney potential. A general solution to the Krönig-Penney model can be found in *Physics and applications of semiconductor heterostructures* by Jaros[12].

When the magnetic field has quantized the energy spectrum into Landau levels we begin with the superlattice dispersion $E(q)$ where q is the wave vector along the superlattice direction

$$E(q) = \frac{\hbar q^2}{2m^*} = (N + 1/2)\frac{e\hbar B}{m^*}. \tag{7.1}$$

Cyclotron resonance promotes the electron from the $N = 0 \rightarrow 1$ Landau level so that E_{CR}, the cyclotron energy, is given by $E_{CR} = E(q_1) - E(q_0)$ with q_0 and q_1 the values of Equation 7.1 for $N = 0$ and $N = 1$ respectively. This leads to a cyclotron mass of

$$m_{zz} = \frac{e\hbar B}{E(q_1) - E(q_0)}; \quad q_0^2 = \frac{eB}{\hbar}; \quad q_1^2 = \frac{3eB}{\hbar}. \tag{7.2}$$

Usage of the term m_{zz} reflects the fact that the measured mass m^* is actually the geometric average of m_{zz} and m_{xx} where m_{xx} is the mass for in-plane motion. $E(q)$ was

calculated with the eight band program, although the result is not significantly different from the straightforward Krönig-Penney model. Figure 7.2 is a plot of $(m^*)^2/m_{xx}$, using the m_{xx} measured in the Faraday orientation for the same FIR energy, and shows how this semi-classical model gives good agreement with the data.

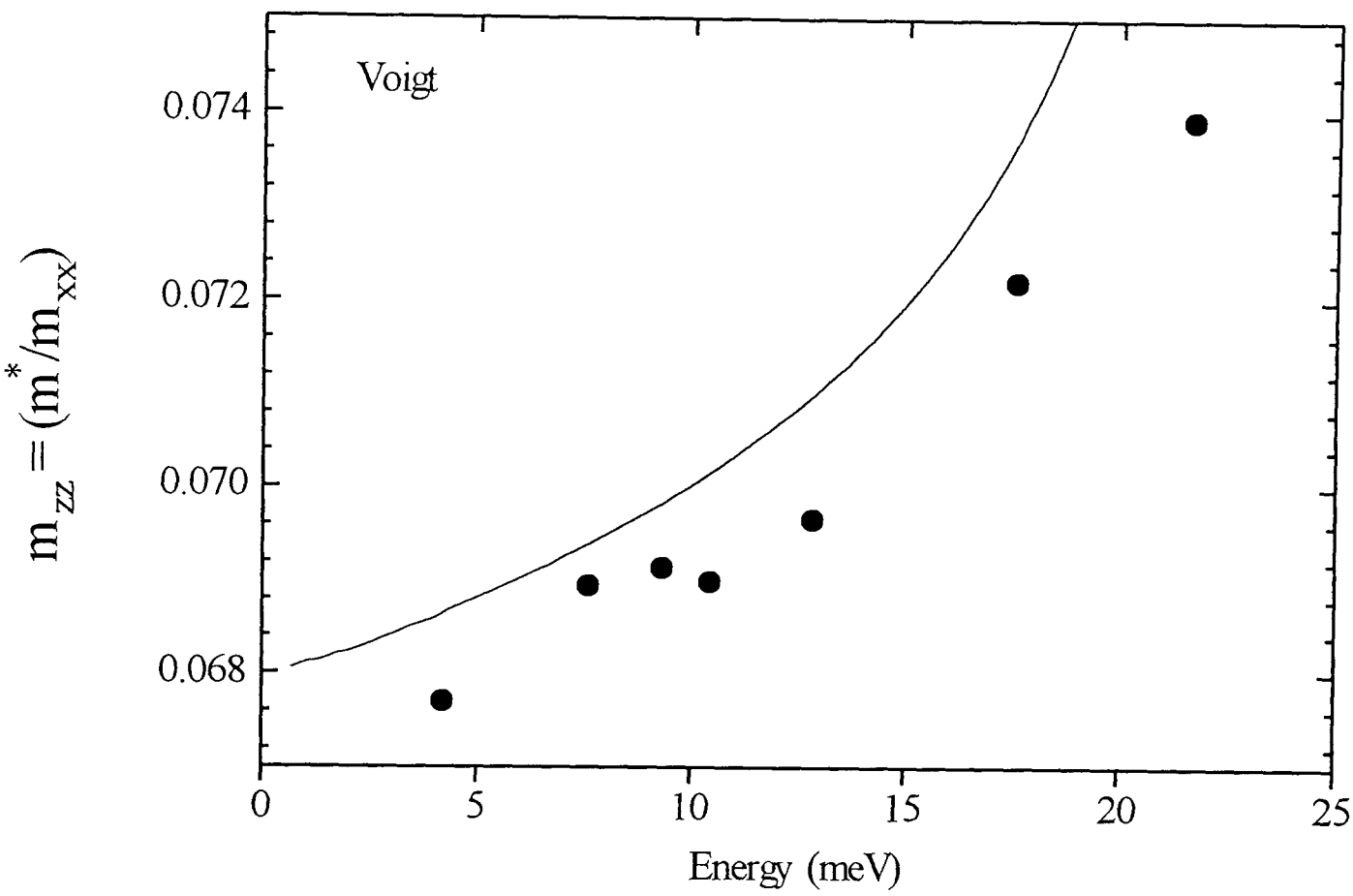

Figure 7.2: m_{zz} deduced experimentally by $(m^*)^2/m_{xx}$ (solid circles) where m_{xx} is the mass due to in-plane motion whose value is known from the Faraday measurements. The solid line is the mass calculated using the semi-classical quantization model.

The semi-classical approach breaks down when q_1 approaches π/L, the minizone edge. In real space, the breakdown can be interpreted as the point at which the E_1 energy becomes dependent on the orbit center. Calculations will shortly be presented indicating that this happens at $r_c = L_b + \frac{1}{2}L_w$. The cyclotron radius satisfies this condition at 9.7, 3.7, 2.0 and 1.2 T for the 50,100,150 and 200 Å barrier widths of the samples. This explains the failure to observe clear CR for all the samples except the 50/50. New modes corresponding to well-bound, barrier-bound or skipping orbits that have been seen in other studies[3, 5], were not observed. These modes might have been expected at high fields for the 50/100, 50/150 and 50/200 samples.

The impurity resonance displays dramatic shifts in the Voigt orientation, moving with

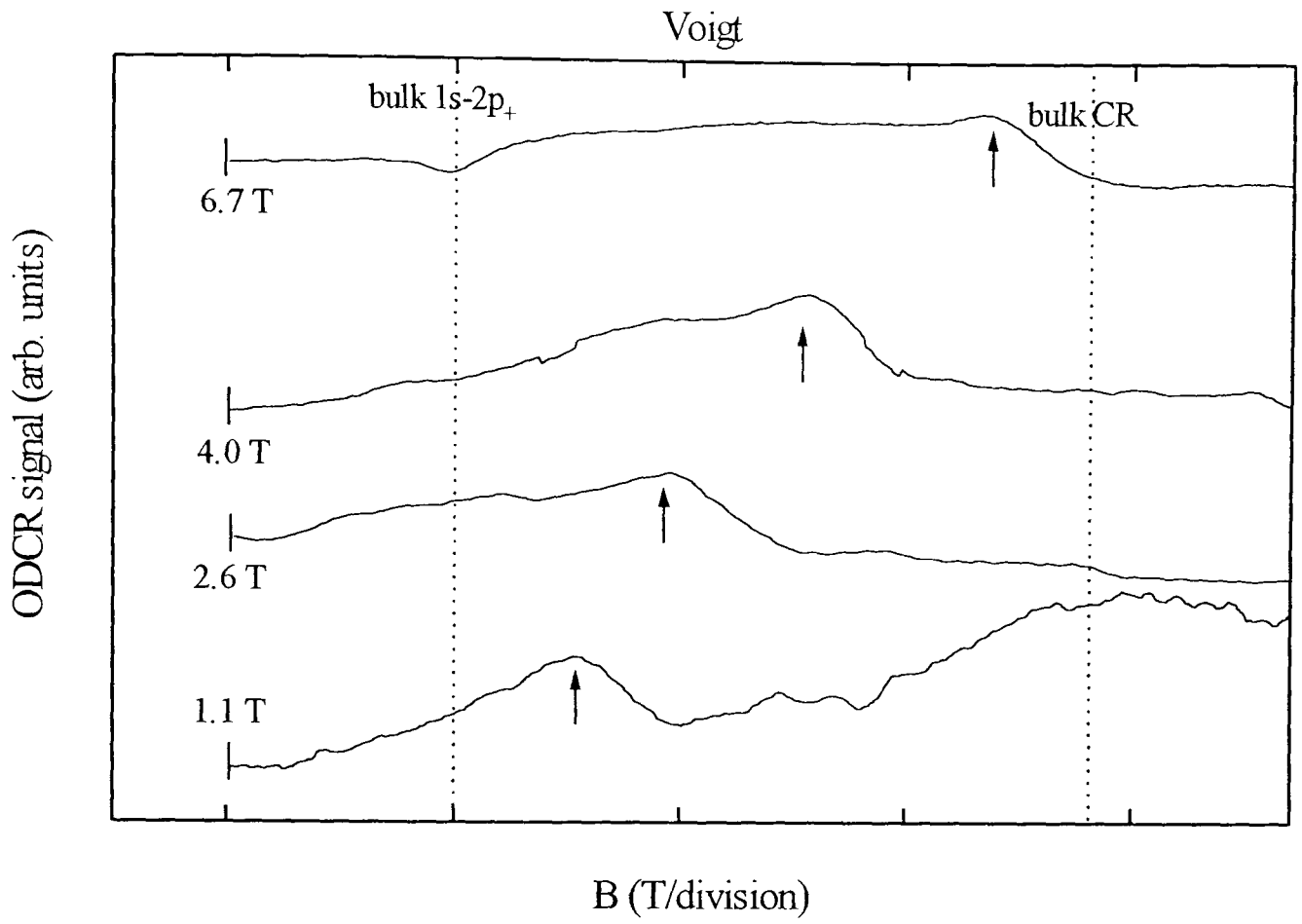

Figure 7.3: ODCR traces from the 50/100 sample, for four different laser wavelengths, 163, 118, 96 and 70 μm illustrating the shift in the $1s - 2p_+$ superlattice impurity transition with increasing barrier width. The field has been offset such that the bulk $1s - 2p_+$ fields (2.1, 3.6, 5.0 and 7.7 T respectively) are coincident.

increasing barrier width from close to the bulk GaAs $1s - 2p_+$ field for $L_b = 50$ Å, to close to the bulk GaAs CR for $L_b = 150$ Å. Figure 7.3 contains data from the 50/100 sample for different FIR wavelengths, illustrating how the impurity transition moves towards the bulk CR with increasing field.

In order to include all the samples and wavelengths of the Voigt data on a coherent graph, the peak position of each superlattice impurity resonance relative to the free electron CR for the same FIR wavelength is 'normalized' through division by the difference between the bulk free electron and impurity resonance. All the Voigt impurity data is brought together in Figure 7.4, a plot of

$$100 \times \left(\frac{B(\lambda) - B_{1s-2p}(\lambda)}{B_{fe}(\lambda) - B_{1s-2p}(\lambda)} \right) \quad \text{vs.} \quad \frac{L_b}{r_c} \tag{7.3}$$

where $B(\lambda)$ is the measured field, and $B_{1s-2p}(\lambda)$, $B_{fe}(\lambda)$ the fields for bulk GaAs $1s-2p_+$ and free electron CR respectively, all for the same FIR wavelength λ. Figure 7.4 shows how, for $L_b/r_c \ll 1$, the resonance is close to the bulk $1s - 2p_+$ field; but for $L_b/r_c > 1$

the resonance moves to the free electron CR field, being exactly midway between the two when $L_b/r_c = 1$. It will be shown later that the origin of this effect is a concentration of the wave function into the well closest to the impurity as the field is increased.

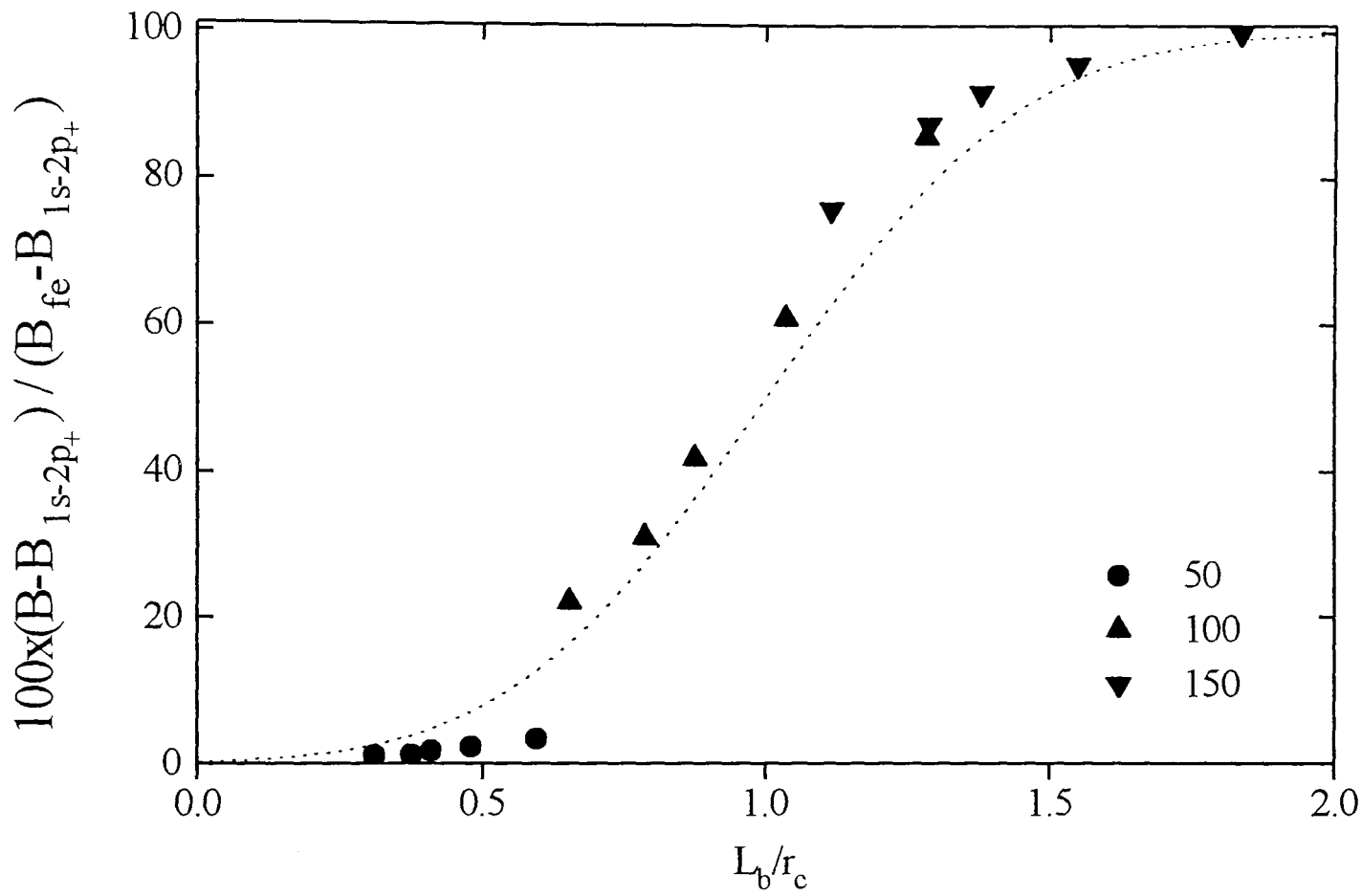

Figure 7.4: A summary plot of the experimental impurity resonances taken in the Voigt orientation. The dashed line is a guide to the eye (based on an error function). See the text for an explanation of the character notation.

A theoretical basis for the experimental results was formulated by Richard Warburton and Philip Peyla working here in Oxford who calculated the E_1 and $1s$ energies in the Voigt geometry by adapting the exciton calculation of Leavitt and Little [13]. The Hamiltonian for the system is given by:

$$H = \frac{1}{2m}\left(\underline{p} + e\underline{A}\right)^2 + V(z) - \frac{e^2}{4\pi\varepsilon_o\varepsilon_r\sqrt{x^2+y^2+(z-z_I)^2}}. \tag{7.4}$$

The magnetic field is directed along the x-axis: $\underline{B} = (B, 0, 0)$, which leads to a vector potential of $\underline{A} = (0, -zB, 0)$. The wave function is expanded following the procedure used by Leavitt and Little,

$$\Psi(\underline{r}) = \phi(z)g(\rho, z - z_I). \tag{7.5}$$

where $\phi(z)$ is the general superlattice solution from the Krönig-Penney model and $\rho = \sqrt{x^2 + y^2}$. The Hamiltonian operating on the wavefunction provides a differential equation for g which was then integrated numerically to provide a solution. With a known value of g it is now possible to calculate the impurity energy E given by evaluating the integral:

$$E = \int_{-\infty}^{+\infty} |g(z)|^2 E(z - z_I) dz \tag{7.6}$$

As would be expected, the eigenvalues E are dependent on the position of the orbit center $z - z_I$. Here, the impurity was taken to lie in the middle of a barrier within the superlattice.

Leaving the details of the calculation aside, the magnetic field can intuitively be though of as adding a quadratic term

$$\frac{e^2 B^2}{2m} (z - z_o)^2 \tag{7.7}$$

to the superlattice and impurity potentials in the effective Hamiltonian, where z_o is the orbit center. As the field strength is increased, the extent of the E_1 wave function is squeezed inwards by the field term until it is concentrated in the well adjacent to the barrier. This is shown more clearly in Figure 7.5 for the 50/100 sample, with the orbit center either at the middle of the well or at the middle of the barrier. Figure 7.5[a] shows that for $B < 6$ T, the $1s$ well- and barrier-centered states are almost degenerate, but the energies diverge at higher field. The divergence occurs at precisely the field when $r_c = L_b$ (6.1 T), the critical point observed experimentally in Figure 7.4. An examination of the impurity wave function, Figure 7.5[b], reveals that there are appreciable nodes in at least four wells at low field, but at high field these nodes disappear and the wave function is Gaussian-like, centered close to the middle of the well adjacent to the impurity.

The critical field, defined by $r_c = L_b$, can be understood semi-classically, as the coupling from one well to the next is much reduced once the cyclotron orbit centered on one well does not extend into the neighbouring well. This gives $r_c \simeq L_b + \frac{1}{2} L_w$, or, assuming that all the curvature of the orbit lies in the barrier, $r_c \simeq L_b$. The important point is that the field concentrates the wave function into the well, *not* the barrier. In the latter case the critical field would be $r_c \simeq L_b/2$ which is not observed experimentally.

The model could not easily include the $2p$ levels which made the exact transition energies

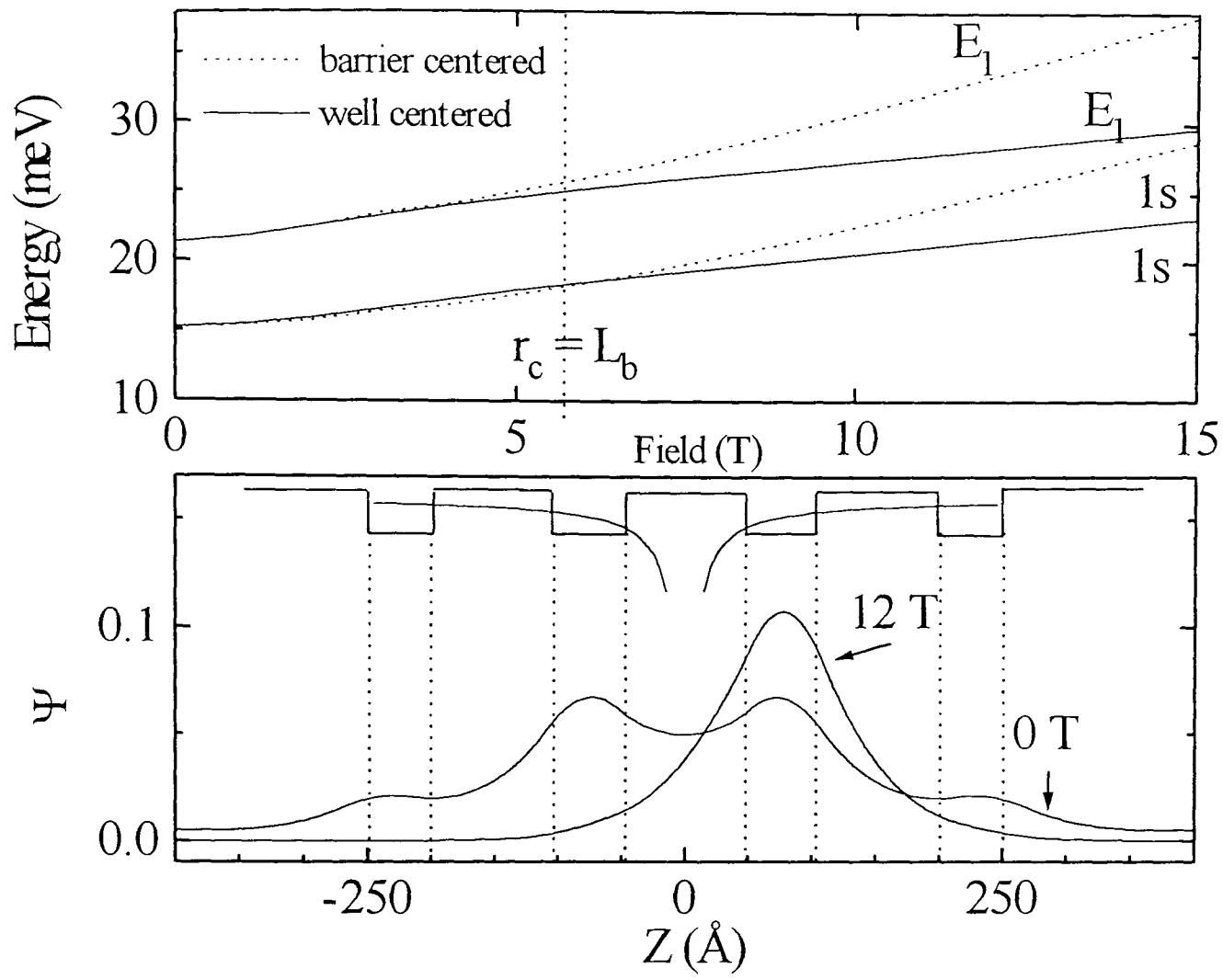

Figure 7.5: [a] The calculated $1s$ and E_1 energies for the 50/100 superlattice in the Voigt orientation. The orbit center lies either at the center of the well or at the center of the barrier. The energies diverge at the field when $r_c = L_b$. [b] The calculated wave functions, at 0 T and 12 T, for the *well*-centered $1s$ state. The impurity lies at $z = 0$, and the superlattice and impurity potentials are sketched.

impossible to calculate. However, it appears likely that the divergence of the well- and barrier-centered $1s$ energies at $r_c = L_b$, and the associated concentration of the ground state wave function, is the cause of the experimental behaviour as it successfully reproduces the critical point at $r_c = L_b$. In fact the well-centered $1s$ wave function is very similar to the first Landau eigenfunction (a Gaussian), suggesting that the transition energy for $r_c \ll L_b$ may well be that of a harmonic potential, i.e. the bulk cyclotron resonance energy. In this region, the cyclotron resonance would be a subband-like transition between quantum well states contained within the barrier width[5].

7.4 Conclusions

In summary, measurements on a series of $In_{0.05}Ga_{0.95}As/GaAs$ superlattices have been made using optically detected cyclotron resonance (ODCR) in both the Faraday and Voigt orientation. When the field is directed perpendicular to the growth axis (Voigt), the electrons are forced to tunnel through the barriers and become dependent on the dispersion relation through the superlattice. The ODCR measurements in the Voigt orientation confirm a well defined superlattice band structure that is altered by the strength of the inter-well coupling. A magnetic field directed parallel to the growth axis allows measurement of the in-plane mass, which is also shown to be sensitive to inter-well coupling. Mid-barrier impurities are investigated, and found to have a binding energy which is reduced by increasing barrier width. In the Voigt orientation, the transition energy of the mid-barrier impurity decreases rapidly when the cyclotron radius equals the barrier width which is explained as a concentration of the wave function into the quantum well adjacent to the impurity.

7.5 References

[1] G. Belle, J.C. Maan and G. Weimann, *S.S. Comm.* **56**, 65 (1985).

[2] T. Duffield, R. Bhat, M. Koza, F. DeRosa, D.M. Hwang, P. Grabbe and S.J. Allen, *Phys. Rev. Lett.* **56**, 2724 (1986).

[3] T. Duffield, R. Bhat, M. Koza, F. DeRosa, K.M. Rush and S.J. Allen, *Phys. Rev. Lett.* **59**, 2693 (1987).

[4] P. Lane and R.L. Greene, *Phys. Rev.* B **33**, 5871 (1986).

[5] T. Duffield, R. Bhat, M. Koza, M.C. Tamargo, J.P. Harbison, F. DeRosa, D.M. Hwang, P. Grabbe and S.J. Allen, *S.S. Comm.* **60**, 557 (1986).

[6] N.C. Jarosik, B.D. McCombe, B.V. Shanabrook, J. Comas, J. Ralston and G. Wicks, *Phys. Rev. Lett.* **54**, 1283 (1985).

[7] G. Brozak, B.D. McCombe and D. M. Larsen, *Phys. Rev.* B **40**, 1265 (1989).

[8] M. Helm, F.M. Peeters, F. DeRosa, E. Colas, J.P. Harbison, and L. T. Florez, *Phys. Rev.* B **43**, 13983 (1991).

[9] K.J. Moore, G. Duggan, A. Raukema, and K. Woodbridge, *Phys. Rev.* B **42**, 1326 (1990).

[10] R.J. Warburton, R.J. Nicholas, L.K. Howard and M.T. Emeny, *Phys. Rev.* B **43**, 14124 (1991).

[11] R.J. Warburton, J.G. Michels, R.J. Nicholas, J.J. Harris and C. T. Foxon, *Phys. Rev.* B **46**, 13394 (1992).

[12] M. Jaros, *Physics and applications of semiconductor microstructures*, ?, 93,(1989)

[13] R.P. Leavitt and J.W. Little, *Phys. Rev.* B **42**, 11774 (1990).